Charakterisierung und gezielte Eliminierung von toxischen Proteinaggregaten

Inaugural-Dissertation

Zur Erlangung des Doktorgrades der Mathematisch-Naturwissenschaftlichen Fakultät der Heinrich-Heine-Universität Düsseldorf

Vorgelegt von

Oleksandr Brener

Aus Nikolaew

Düsseldorf 2014

Aus dem Institut für Physikalische Biologie der Heinrich-Heine Universität Düsseldorf

Abgabedatum: 23.06.2014
Tag der mündlichen Prüfung: 17.07.2014

Gedruckt mit der Genehmigung der Mathematisch-Naturwissenschaftlichen Fakultät der Heinrich-Heine-Universität Düsseldorf

Referent: Prof. Dr. Dieter Willbold
Korreferent: Prof. Dr. Georg Groth

Eidesstattliche Erklärung

Hiermit erkläre ich an Eides statt, dass ich diese Arbeit selbständig verfasst und keine anderen als die angegebenen Quellen und Hilfsmittel benutzt sowie Zitate kenntlich gemacht habe.

Düsseldorf, den

Oleksandr Brener

Wo damals die Grenzen der Wissenschaft waren, da ist jetzt die Mitte.

Georg Christoph Lichtenberg (1742–99)

Danksagung

Für meine Doktorarbeit schulde ich sehr vielen Menschen einen herzlichen Dank. Zuerst möchte ich Prof. Dr. Dieter Willbold danken, dass diese Arbeit in seinem Institut angefertigt werden konnte. Ein besonderer Dank gilt meiner Betreuerin Dr. Luitgard Nagel-Steger, Dr. Lothar Gremer und nochmal Prof. Dr. Dieter Willbold. Sie brachten mir sehr viel Geduld entgegen, sorgten mit wertvollen (bis genialen) Ratschlägen für das Gelingen dieser Arbeit und haben nicht nur in fachspezifischen, sondern auch in privaten Gesprächen immer dafür gesorgt, dass ich meinen Geist anstrenge.

Bei allen Mitgliedern und ehemaligen Mitgliedern des Instituts für Physikalische Biologie, in deren Gesellschaft ich viele wundervolle Jahre verbracht habe: Henrik Müller, Jendrik Marbach, Giannantonio Panza, Ewa Mirecka, Ümit Pul, Tommy Agyenim, Timo Piechatzek, Gerhard Steger, Lars Lüers, Hamed Shaykhalishahi, Shantha Elter, Mario Schneider, Philipp Neudecker, Janine Kutzsche, Dagmar Jürgens, Oliver Bannach, Wolfgang Hoyer, Aziz Gauhar, Michael Wördehoff, Heidi Gruber, Martin Wolff, Christina Decker, Thomas Karcher, Steffen Hübinger, Ilka Ostermann, Elke Reinatz, Barbara, Filipp Oesterhelt, Stefanie Schiefer, Anna Bronder, Arpita Roychoudry, Meriem Jabnoun, Adeline Bieker, Clara Grüning, Eva Brinkmann, Henrike Heise, Fabian Dreßen, Kornelia Linnenbrik, Bernd Esters, Manuel Etzkorn. Daniel Frenzel, Dirk Bartnik, Aileen Funke, Sabine Arens, Stefan Klinker, Rolf Wagner, Zihni Arslan und Nadine Rösener. Alle hier genannten haben nicht nur zu meiner fachlichen, sondern auch kulturellen und menschlichen Bereicherung beigetragen.

Ein besonderer Dank gilt meinen Eltern, meiner Schwester (*Родители-это богатство! И кем бы я только был без вас?!*) und allen meinen Freunden, die mich immer unterstützt haben. Und Familie Kogolovsky.

Inhaltsverzeichnis

Abbildungsverzeichnis

Abkürzungsverzeichnis

Abkürzung	**Bedeutung**
AD	Alzheimer-Krankheit (Alzheimer's disease)
ADDL	*Amyloid-beta derived diffusible ligands*
AFM	Atomkraftmikroskop **(***atomic force microscope***)**
AKH	Amyloid-Kaskaden-Hypothese
APP	*Amyloid precursor protein*
Aβ	Amyloid-β Peptid. Wenn nicht ausdrücklich anders erwähnt, ist $A\beta_{1-42}$ gemeint.
Cryo-EM	Cryo-Elektronenmikroskopie
CSF	Liquor *cerebrospinalis* (*cerebrospinal fluid*)
DGZ	Dichtegradientenzentrifugation
EGCG	Epigallocatechingallat
EM	Elektronenmikroskopie
EphB2	Ephrin-Type-B Rezeptor 2
FAD	familiäre Alzheimer-Krankheit
FcγRIIB	Immunoglobulin G Fcγ Rezeptor II-b
HFIP	Hexafluoroisopropanol
HIV	Das Humane Immundefizienz-Virus
LilrB2	Leukozyt-Immunoglobulin-ähnlicher Rezeptor B2
LPR-1	*Low Density Lipoprotein receptor-related protein-1*
MD	Molekulardynamik
NMDA-Rezeptor	*N*-Methyl-$_D$-Aspartat-Rezeptor
NMR	Kernspinresonanz (*Nuclear Magnetic Resonance*)
PICUP	*photo-induced cross-linking of unmodified proteins*
PirB	Immunoglobulin-ähnlicher Rezeptor B
PMC-1	*pericentriolar material-1 protein*
PrP^c	das zelluläre Prion-Protein
QIAD	*quantitative determination of interference with aggregate size distribution*
SAD	spontane Alzheimer-Krankheit
SANS	*small-angle neutron scattering*
SAXS	*small-angle X-ray scattering*
SDS-PAGE	*sodium dodecyl sulfate polyacrylamide gel electrophoresis*
SEC	Größenausschluss-Chromatographie

1 Einleitung

1.1 Neurodegenerative Erkrankungen

Neurodegenerative Erkrankungen bilden eine Gruppe von Krankheiten, die spontan oder genetisch bedingt ausgelöst werden können und deren Hauptmerkmal die meist langsam fortschreitende irreversible Schädigung von neuronalem Gewebe ist. Die Symptomatik dieser Erkrankungen umfasst eine Vielzahl an neurologischen Erscheinungen. Mit Fortschreiten der Krankheit entwickelt sich meist eine starke Demenz. Bei einigen neurodegenerativen Erkrankungen lassen sich auch Bewegungsstörungen diagnostizieren. Die neurodegenerative Prozesse führen letztendlich zum Tod des Erkrankten. Zu den häufigsten neurodegenerativen Erkrankungen des Menschen zählen unter andern die Alzheimer-Krankheit (AD), die Parkinson-Krankheit und die weniger verbreitete Creutzfeldt-Jakob-Krankheit.

Allen drei angeführten Krankheiten ist gemeinsam, dass im zentralen Nervensystem der Betroffenen Ablagerungen mindestens eines fehlgefalteten körpereigenen Proteins nachgewiesen werden. Im Fall von AD handelt es sich um das β-Amyloid (Aβ), bei Parkinson-Krankheit sind Ablagerungen von α-Synuclein zu finden und bei Creutzfeldt-Jakob-Krankheit lässt sich das fehlgefaltete Prion-Protein nachweisen (Soto and Estrada 2008).

1.2 Proteinfehlfaltungserkrankungen

Durch den Begriff Proteinfehlfaltungserkrankungen wird die o.g. Gruppe der neurodegenerativen Erkrankungen stärker eingegrenzt. Hierbei ist das notwendige und besondere Merkmal der Krankheit die fehlerhafte oder alternative Faltung von körpereigenen Proteinen. Bei den meisten bekannten Proteinfehlfaltungserkrankungen ist es möglich, sie in zwei Untergruppen einzuteilen (Winklhofer et al. 2008). Bei der ersten Untergruppe führt die Fehlfaltung selbst oder die dadurch ausgelöste Proteindegradation zu einem Verlust der physiologischen Funktion („*loss-of-function*“), wodurch eine Krankheit ausgelöst wird. Die zweite Untergruppe umfasst die Krankheiten, bei denen fehlgefaltete Proteine oder deren aggregierte Formen toxisch wirken („*gain-of-toxicity*“) und folglich zu einer Proteinfehlfaltungserkrankung führen. Ein weiteres Merkmal der zweiten Untergruppe sind zahlreiche Ablagerungen von fehlgefalteten Proteinen, so genannten „Plaques“, die im Gewebe nachgewiesen werden. Zu letzteren Gruppe zählen auch die o.g. Alzheimer-, Parkinson- und Creutzfeldt-Jakob-Krankheit (Chiti and Dobson 2006).

1.2.1 Proteinfaltung

Die Aminosäuresequenz eines Proteins bestimmt seine native dreidimensionale Faltung und definiert somit auch die Proteinfunktion. Das Durchlaufen einer Energielandschaft ist eine visualisierte Darstellung von thermodynamischen Prozessen, die bei der Faltung einer ungeordneten Aminosäurekette zu einem funktionalen Protein stattfinden (Abbildung 1). Meistens wird am Ende die native Proteinkonformation erreicht. Diese Proteinkonformation entspricht der thermodynamisch stabilsten.

Die „astronomisch"-große Anzahl an möglichen Konformationen auf dem Weg von einem ungefalteten Zustand zur nativen dreidimensionalen Struktur steht im Widerspruch zur kurzen Zeit, die ein Protein *in vivo* braucht, um diese Konformation zu erreichen. Dieses Phänomen beschreibt das Levinthal-Paradox sehr anschaulich (Zwanzig et al. 1992). Dabei wird der

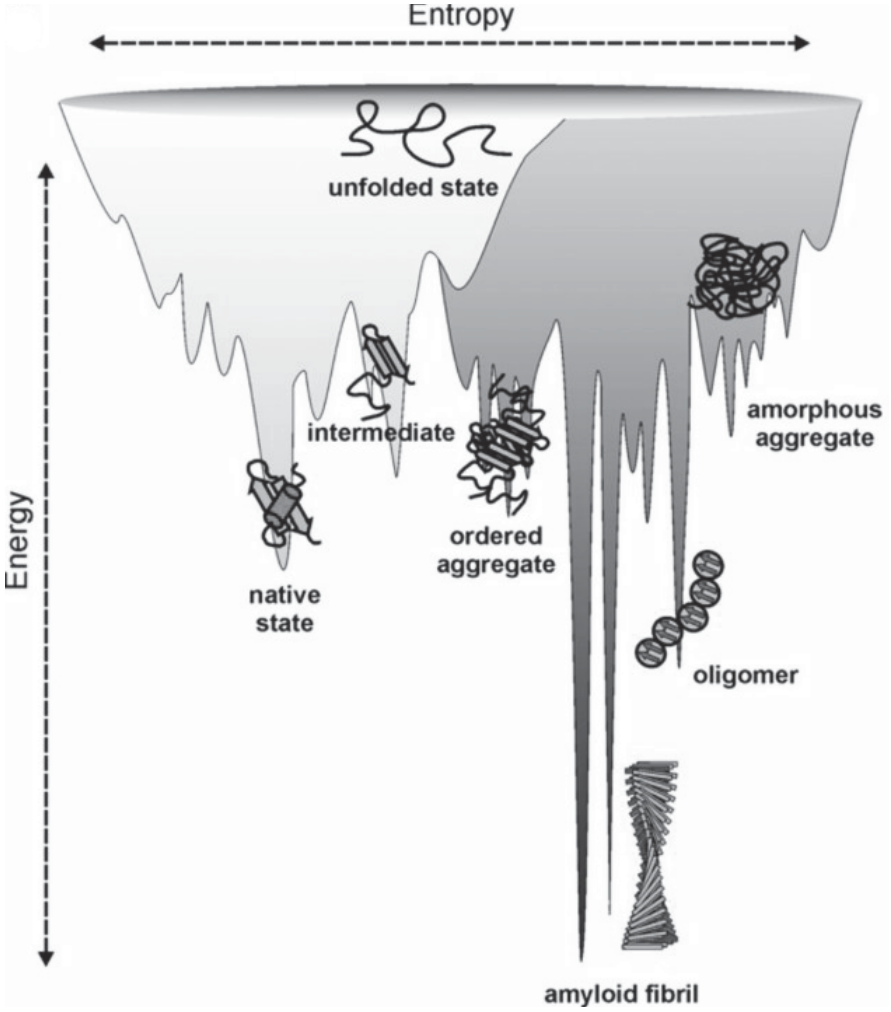

Abbildung 1 – Faltung und Aggregation der Proteine.
Schematische Illustration der Proteinfaltungsenergielandschaft. Die Entropie der Proteine ist von der dem System zur Verfügung stehenden Energie abhängig. Durch das Durchlaufen der Energielandschaft entstehen entlang des Faltungstrichters verschiedene Zwischenstufen der Proteinkonformationen. In der hellgrauen Hälfte ist der native Faltungsweg eines Proteins dargestellt. In der dunkelgrauen sind unterschiedliche Aggregationswege dieses Proteins veranschaulicht. Abbildung verändert nach (Jahn and Radford 2005).

Faltungsprozess eines Proteins rein mathematisch betrachtet. Das dahinterstehende kombinatorische Prinzip postuliert, dass die Anzahl der möglichen Faltungen eines Proteins mit der Länge der Aminosäurekette exponentiell zunimmt. Sogar bei einer simplifizierten Betrachtung, wo jeder Aminosäurerest nur 2 Zustände annehmen könnte, benötigt ein Protein bestehend aus 150 Aminosäuren ca. 1024 Jahre, um die optimale (native) Konformation zu finden. Das Levinthal-Paradox ist aber im Grunde kein wissenschaftliches Problem, sondern eine pädagogische Veranschaulichung, um die Komplexität der Proteinfaltung darzustellen. In Wirklichkeit faltet sich das Protein schon während seiner Synthese am Ribosom. Folglich nimmt jedes Kettenglied nach Aufnahme in die Sequenz die energetisch günstigste Konformation ein. Auf diese Weise falten sich benachbarte Sequenzabschnitte spontan und sehr schnell zu kleineren stabilen strukturellen Domänen. Also nur ein Bruchteil aller möglichen

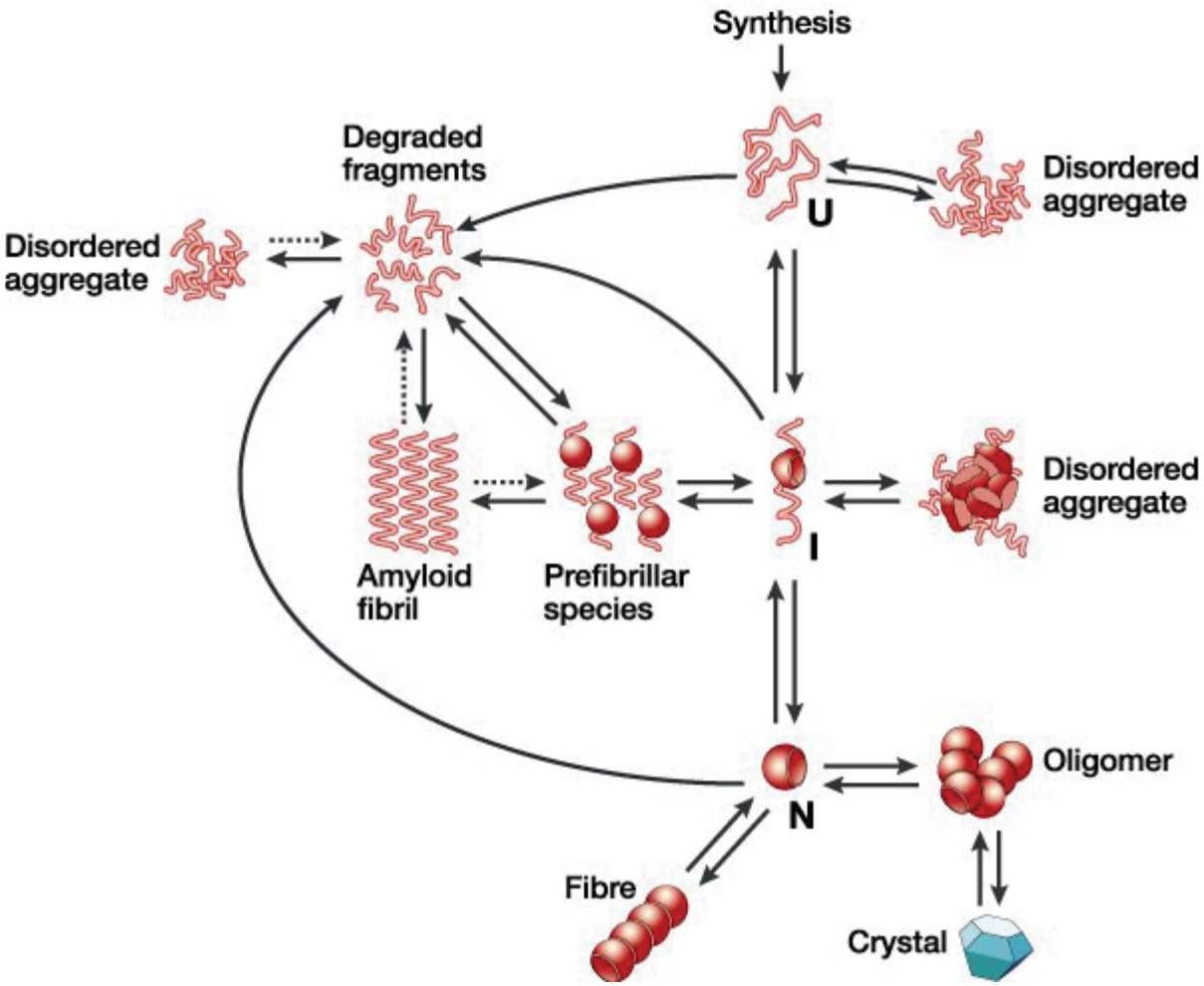

Abbildung 2 – Faltungswege von Proteinen und ihre Zustände
Am Ribosom wird das ungefaltete Protein (U) synthetisiert. Es kann über Zwischenstufen (I) die native Proteinstruktur (N) einnehmen. Bei einer Fehlfaltung entstehen amorphe Aggregate (*disordered aggregate*) oder Protofibrillen. Diese können degradiert werden oder aggregieren weiter zu amyloiden Fibrillen. Ausgehend vom nativen Proteinzustand N können sich durch Aggregation Oligomere, Fasern oder Kristalle bilden. Abbildung nach (Dobson 2003).

Proteinfaltungen muss durchlaufen werden, um zur nativen Struktur zu gelangen (Wolynes et al. 1995).

Des Weiteren stellen Chaperone und „Faltungskerne“ unterstützende Mechanismen der Faltungsprozesse dar. Auch das „*molten globule*“ wird als ein Intermediat zwischen denaturiertem und nativem Zustand vieler Proteine beschrieben. Dieser Zwischenzustand, der zum ersten Mal bei Cytochrom c entdeckt wurde, weist gleiche und stabile Sekundärstrukturelemente des nativen Proteins und eine relativ variable Tertiärstruktur auf (Kuroda et al. 1992).

Wenn Proteine eine nicht native Struktur haben, können sie als fehlgefaltete Proteine bezeichnet werden. Amorphe Aggregate, Fibrillen und manche oligomere Konformationen zählen auch zu fehlgefalteten Proteinen. Amyloide Proteinfibrillen stellen sehr stabile Formen dar (Abbildung 2). Einige Fibrillen und Oligomere haben eine toxische Wirkung, wobei der/die genauen Wirkmechanismen dieser Proteinaggregate in Bezug auf Toxizität noch nicht bekannt sind.

1.2.2 Amyloide Proteinaggregate

Die Bezeichnung „amyloid“ wurde bereits im Jahre 1854 von Rudolf Virchow eingeführt, um mit Jod anfärbbare makroskopische Gewebeanomalien zu bezeichnen. Wegen der positiven Jodfärbung nahm Virchow irrtümlicher Weise an, es würde sich um Zellulose- oder Stärkeablagerungen handeln, und gab ihnen den vom lateinischen *amylum* und altgriechischen *amylon* abgeleiteten Namen „amyloid“. Erst später stellte sich heraus, dass es sich um proteinöse Ablagerungen handelt (Sipe and Cohen 2000). Der Begriff Amyloid wurde benutzt, um spezifische Anomalien in Organen oder Gewebe, welche bei der Autopsie entdeckt wurden, zu bezeichnen. Amyloide Ablagerungen korrelieren mit einer Fülle von klinischen Syndromen, die primär als Idiopathien oder Myelom-assoziiert und sekundär als endokrin-, altersassoziiert oder erblich klassifiziert wurden.

Bei Analysen von ultradünnen Amyloid-Gewebeteilen mit Elektronenmikroskopie (EM) wurde im Jahre 1959 festgestellt, dass diese Strukturen aus Fibrillen bestehen (Cohen and Calkins 1959). Die klassische histopathologische Definition von amyloiden Aggregaten besagt, dass es sich um Proteinablagerungen handelt, die Proteine mit einer β-faltblattreichen Sekundärstruktur enthalten und mittels Kongorot-Färbung unter polarisiertem Licht eine grün-gelbe Doppelbrechung aufweisen (Puchtler and Sweat 1965). Neuere Definitionen schließen neben *in vivo* existierenden auch *in vitro* erzeugte Proteine ein und betrachten die Kongorot-Doppelbrechung nicht als zwingendes Kriterium (Harrison et al. 2007).

Um eine genauere *post mortem* Diagnose stellen zu können werden heutzutage Gewebeschnitte mit amyloiden Ablagerungen immunologisch gefärbt (Abbildung 3).

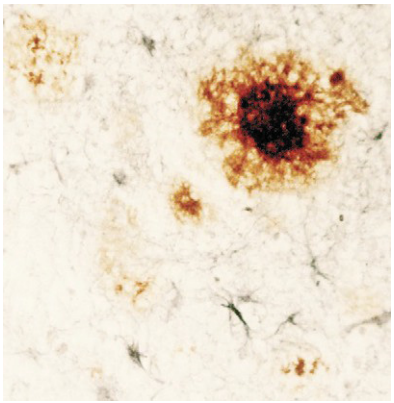

Abbildung 3 – Plaques im Hirngewebe eines Alzheimerkranken Patienten
Plaques in dünnen Autopsie-Gewebeschnitten aus dem Gehirn eines AD-kranken Patienten, visualisiert durch Immunofärbung mit Antikörpern gegen Aβ. Abbildung modifiziert nach (Nordberg 2004).

Wegen der immer größer werdenden sozialen Bedeutung amyloider Erkrankungen, vor allem der Alzheimer-Krankheit, werden in vivo Detektionsverfahren für amyloide Strukturen entwickelt und eingesetzt. Diese Detektionsmethoden, wie z.B. Positronen-Emissions-Tomographie, sollen eine Frühdiagnostik für AD-Patienten ermöglichen.

1.3 Die Alzheimer-Krankheit

Die Alzheimer-Krankheit, auch Alzheimersche Demenz (AD) genannt, ist eine neurodegenerative Erkrankung, die in ihrer häufigsten Form bei Personen über dem 65. Lebensjahr auftritt und für ungefähr 60 Prozent der Demenzerkrankungen verantwortlich zeichnet (Ferri et al. 2005).

Durch die Bevölkerungsentwicklung in den westlichen Industrienationen (auch Japan) mit immer älter werdenden Bürgern steigt daher auch die Alzheimer-Prävalenz. Unter den 65-Jährigen sind etwa 0,9 % betroffen, bei den 75-Jährigen sind es bereits 4,2 % und bei den 85-Jährigen zeigen etwa 15 % Symptome der Krankheit (Brookmeyer et al. 2007). Über dem 85. Lebensjahr nimmt der Anteil der Betroffenen wieder ab, da die zuvor Erkrankten nur selten dieses Lebensalter erreichen. Der jüngste bisher bekannte Alzheimer-Patient erkrankte mit 27 Jahren und starb mit 33.

Laut Prognosen der Weltgesundheitsorganisation (englisch *World Health Organization*, WHO) wird im Jahre 2050 weltweit 1 von 85 Menschen von Alzheimer-Krankheit betroffen sein. Dies würde je nach Entwicklung der Weltbevölkerung ca. 115 Millionen AD-kranken entsprechen. All diese Patienten werden pflegebedürftig sein, wobei ihre Pflege eine

extremgroße finanzielle Belastung für die Gesellschaft sowie eine vielleicht noch größere psychische Belastung für die Familienangehörigen sein wird. Somit spielt die Alzheimer-Krankheit eine nicht zu unterschätzende gesellschaftliche und politische Rolle.

Die AD wurde das erste Mal 1906 von Alois Alzheimer beschrieben. Neben den Symptomen von fortschreitendem Gedächtnisverlust und dem Rückgang allgemeiner kognitiver Eigenschaften, erwähnte er die Präsenz sogenannter intraneuronaler gewundener Faserbündel und extrazellulärer amyloider Ablagerungen in den von der Krankheit geschädigten Hirnbereichen (Alzheimer 1907).

Die Patientin trug den Namen Auguste Deter und wurde von Alois Alzheimer (Abbildung 4) nach der Aufnahme in der Frankfurter Nervenklinik medizinisch begleitet. Die offizielle Bezeichnung der Alzheimer-Krankheit wurde im Jahre 1910 von Emil Kraepelin eingeführt, der die Erkrankung in der achten Ausgabe seines *Lehrbuch der Psychiatrie* nach Alois Alzheimer benannte.

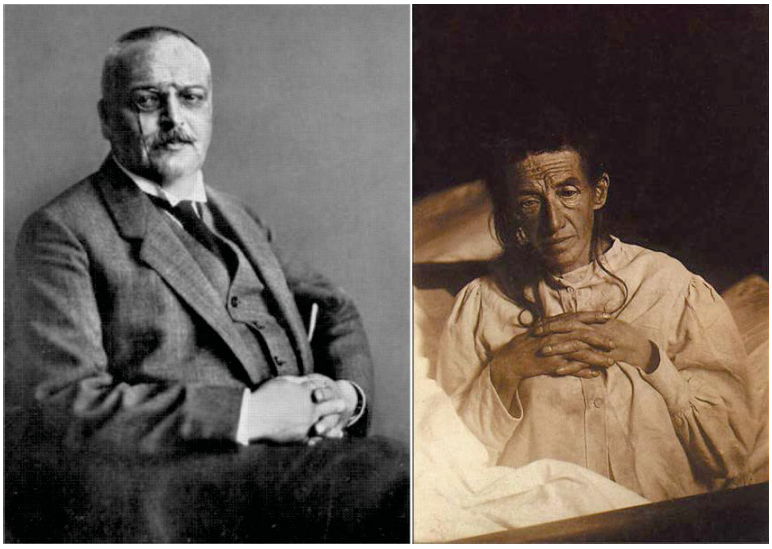

Abbildung 4 – Dr. Alois Alzheimer (links) und Auguste Deter (rechts)
Abbildung Auguste Deter aus http://commons.wikimedia.org/wiki/File:Auguste_D_aus_Marktbreit.jpg
Abbildung Dr. Alois Alzheimer aus http://www.findagrave.com/cgi-bin/fg.cgi?page=pv&GRid=10688

Da die von Alois Alzheimer betreute Patientin mit 50 Jahren relativ jung war, beschrieb er die Erkrankung als präsenile Demenz. Erst später erkannte man, dass dieselben histologischen Veränderungen auch bei älteren Demenz-Patienten auftreten. Zur Abgrenzung gegenüber dem 'echten' (präsenilen) Morbus Alzheimer bezeichnet man die Erkrankungsform des älteren Menschen als Senile Demenz vom Alzheimer-Typ. Im Jahre 1997 wurden originale Mikroskop-Präparate von Alois Alzheimers Arbeit in München wiederentdeckt und neu evaluiert (Graeber et al. 1997). 2013 wurde in dem Material eine Präsenilin-Mutation nachgewiesen (Muller et al. 2013).

Bis zum Ende des 20. Jahrhunderts blieben Proteine, die die Schlüsselrolle in der Alzheimer-Krankheit spielen unbekannt. Erst im Jahre 1984 konnten George Glenner und Cai'ne Wong

zwei Peptide, aus denen die charakteristischen Plaques bestehen, identifizieren und nannten sie α- und β-Peptid (Glenner and Wong 1984, Masters et al. 1985). Der in weitaus höherem Maße vorkommenden Komponente galt ihr weiteres Forschungsvorhaben. Sie wurde von ihnen als Amyloid-β (Aβ) bezeichnet.

Im Jahre 1991 konnte die Arbeitsgruppe um Ross Jakes die ebenfalls für die Alzheimer-Krankheit charakteristischen, intrazellulär gelegenen Neurofibrillenbündel entschlüsseln, indem sie die Hyperphosphorylierung der gepaarten helikalen Tau-Filamente nachgewiesen haben (Jakes et al. 1991).

1.3.1 Das Amyloid-Precursor-Protein und die „Amyloid-Kaskaden-Hypothese“

Das Amyloid-Precursor-Protein (APP) ist ein integrales Typ I Transmembran-Glycoprotein. Das Gen liegt auf Chromosom 21, ist hoch konserviert und besteht aus 18 Exons mit mehr als 170 kb(Robakis et al. 1987). Die Aβ-kodierende Region liegt auf Exon 16 und 17. Die Sequenz von β-Amyloid-Peptid (Aβ) ist zwischen 39-43 Aminosäuren lang und erstreckt sich über die Ecto- und Transmembrandomäne des APP (Selkoe 2001a, Suh and Checler 2002).

Das APP wird durch drei Proteasen gespalten, und zwar durch die α-, β- und γ-Sekretase. Die Prozessierung des APP und die dadurch entstehenden Fragmente sind in der Abbildung 5 schematisch dargestellt.

Die α-Sekretase gehört zur ADAM-Proteinfamilie und schneidet das APP teils innerhalb und teils auf der extrazellulären Seite der Membran. Diese Spaltungsstelle liegt mitten in der Aβ-Sequenz, somit verhindert die Prozessierung von APP durch Alpha-Sekretase die Bildung des Aβs und damit die Entstehung von Alzheimer. Das dadurch entstehende Spaltungsprodukt heißt sAPP (sezerniertes APP) oder auch APPsα (Lammich et al. 1999). Dieses Peptid ist gut wasserlöslich und hat neurotrophische und -protektive Wirkung (Bell et al. 2008).

Die β-Sekretase auch BACE1 (β-site of APP cleaving enzyme) genannt, ist eine transmembrane Protease, die das APP etwas weiter N-terminal (also weiter von der Membran entfernt) als die α-Sekretase schneidet. Durch die Spaltung des APP durch die β- und darauf folgende γ-Sekretase entsteht Aβ.

Die γ-Sekretase ist ein aus vier Untereinheiten bestehender Proteinkomplex (Kaether et al. 2006), der in die Membran integriert ist und verschiedene Funktionen hat. Das bekannteste Substrat der γ-Sekretase ist das APP. Des Weiteren ist der Proteinkomplex in mehrere Signalwege mitinvolviert, u.a. in den Notch- (De Strooper et al. 1999) und E-Cadherin-Signalweg (Marambaud et al. 2002). Durch die Spaltungen von APP durch die β- und γ-Sekretase entsteht Aβ. Dabei hat die γ-Sekretase eine gewisse „Ungenauigkeit“. Somit variiert

die Länge des Aβ-Peptids zwischen 17 und 46 Aminosäuren (Portelius et al. 2006, Portelius et al. 2011, Seubert et al. 1992, Zhao G. et al. 2007). Dabei spielen die $Aβ_{1-40}$- und $Aβ_{1-42}$-Isoformen die Schlüsselrolle in der AD. $Aβ_{1-40}$ stellt die Hauptkomponente der fibrillenreichen, neuritischen Plaques dar, die auch einen kleineren Anteil an $Aβ_{1-42}$ aufweisen. Die diffusen Plaques dagegen weisen nur einen geringen bis gar keinen Anteil an $Aβ_{1-40}$, sondern bestehen fast ausschließlich aus $Aβ_{1-42}$ (Selkoe 2001b). Einige Studien besagen, dass neuritische Plaques fast gar keinen Anteil an $Aβ_{1-40}$ aufweisen, sondern aus einer $Aβ_{1-42}$- und $Aβ_{1-43}$-Mischung (Karran et al. 2011, Welander et al. 2009) bestehen. Käme ausschließlich in „normalen" Stoffwechselwegen vor und hätte sogar eine Plaques-inhibierende Wirkung.

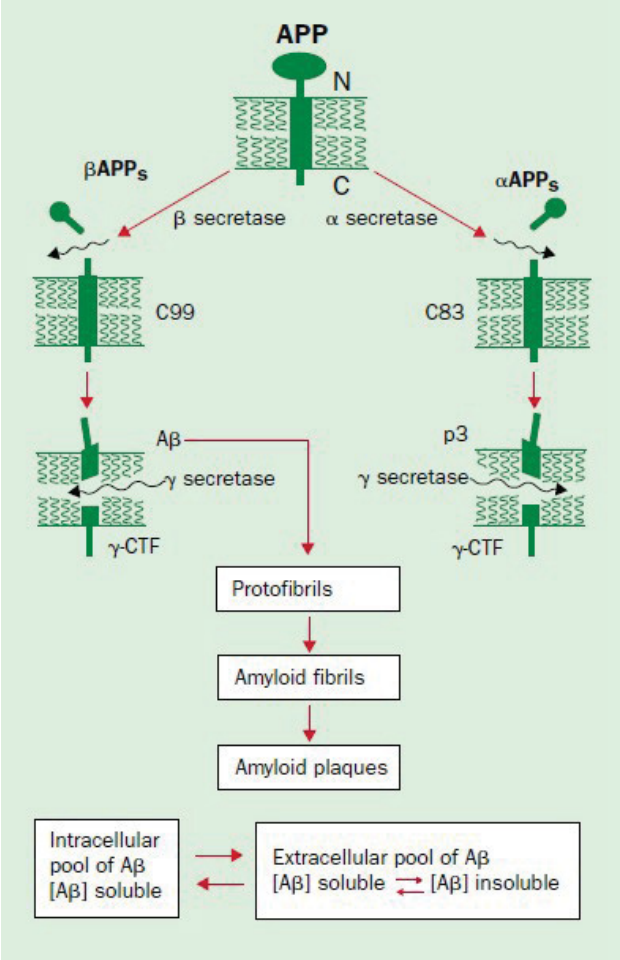

Abbildung 5 – APP-Prozessierung und dadurch entstehende Fragmente
APP wird durch α- oder β- und γ-Sekretase gespalten. Durch diese Prozessierung können unterschiedliche Peptide oder Proteine entstehen. Z.B. Aβ, welches 17 und 46 Aminosäuren lang ist. Aβ aggregiert zu Protofibrillen und Fibrillen, die den Hauptbestandteil der amyloiden Plaques darstellen. Abbildung aus (Nordberg 2004).

Aβ-Aminosäurensequenz:

DAEFR HDSGY EVHHQ KLVFF AEDVG SNKGA IIGLM VGGVV$_{40}$(IA)$_{42}$

Die normale (nicht pathogene) Rolle von Aβ ist zum heutigen Zeitpunkt nicht gut verstanden (Hiltunen et al. 2009) und wird in wissenschaftlichen Kreisen intensiv diskutiert. Tiermodelexperimente habe gezeigt, dass die Abwesenheit von Aβ zu keiner Beeinträchtigung physiologischer Funktionen führt (Luo et al. 2003). Es gibt Hinweise, dass Aβ unterschiedliche Funktionen haben und in mehrere Stoffwechselwege involviert sein könnte. Es wurde berichtet, dass Aβ eine antimikrobielle Funktion hat (Soscia et al. 2010), gegen oxidativen Stress schützt (Zou et al. 2002), Cholesterintransport reguliert (Igbavboa et al. 2009), etc.

Die molekularen Ereignisse, die schließlich in der Demenz münden, werden durch die Amyloid-Kaskaden-Hypothese (AKH) beschrieben. Sie wurde zum erstem mal von John A. Hardy und Gerald A. Higgins im Jahre 1992 formuliert und besagt, dass Aβ-Ablagerungen (Plaques) den Kausalfaktor der pathologischen Prozesse während der Alzheimer-Krankheit darstellen (Abbildung 6). Des Weiteren besagt die Theorie, dass sowohl die Neurofibrillenbündel (Tau-*Tangles*), der vaskuläre Schaden, die Beeinträchtigung der Ca^{2+} Homöostase, Zelltod und schließlich die fortschreitende Demenz durch Aβ-Ablagerungen in den Plaques verursacht wird (Hardy and Higgins 1992). Dabei wurde angenommen, dass Aβ auf einem endosomal-lysosomalen Wege aus dem APP prozessiert wird.

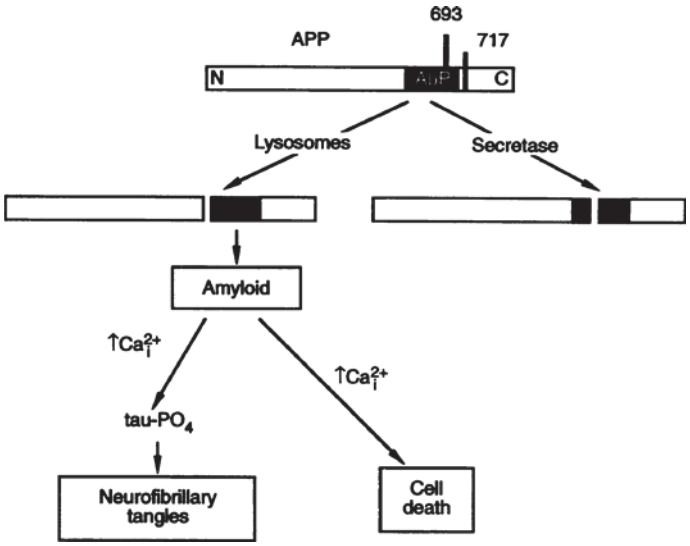

Abbildung 6 – Die Amyloid-Kaskaden-Hypothese
APP-Prozessierung ist auf zwei unterschiedlichen Wegen möglich. 1. Durch die Sekretasen-Spaltungen entstehen nicht amyloidogene Peptide oder 2. Endosomal-lysosomale Prozessierung und Entstehung des intakten Aβ, welches aggregiert und präzipitiert. Das aggregierte Aβ verursacht Bildung der Neurofibrillenbündel und den Zelltod und somit die AD. Abbildung aus (Hardy and Higgins 1992).

In folgenden Jahren wurde die AKH mehrfach modifiziert, wobei in diese immer neue experimentelle Ergebnisse eingeflossen sind. Sie rückte, wenn auch nur sehr langsam, von der anfänglichen Bedeutung der Plaques ab. Knapp 10 Jahre später nach der Ersterscheinung der

Hypothese bekamen die diffusen Plaques eine Größere Bedeutung als sich im Gehirn verbreitende *seeds* für die daraus entstehenden neuritischen Plaques (Abbildung 7). Da die diffusen Plaques fast ausschließlich aus $A\beta_{1-42}$ bestehen, wurde daraus schlussgefolgert, dass das initiierende Ereignis eine erhöhte Produktion des $A\beta_{1-42}$ sei. Im Falle der sporadischen AD wären die Gründe dafür ungeklärt, während im Falle der familiären AD (FAD) Mutationen in *APP*- und *Presenilin*-Genen verantwortlich für die erhöhte Produktion von $A\beta_{1-42}$ sind. Nachfolgend würde $A\beta_{1-40}$ mit unterschiedlichen aggregierenden Kofaktoren an diese diffusen Plaques andocken. Dieser Prozess würde dann schließlich zur Entstehung neuritischer Plaques führen, die dann die gleiche Rolle wie in der ursprünglichen Version der AKH spielen (Selkoe 2001b).

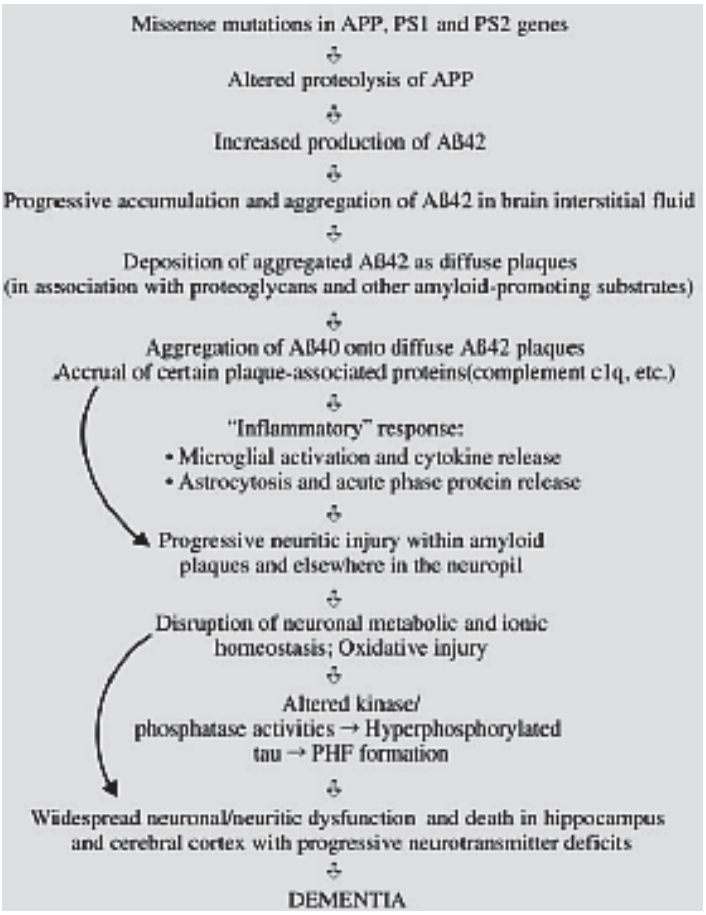

Abbildung 7 – modifizierte Amyloid-Kaskaden-Hypothese
Mutationen in den *APP*- und *Presenilin*-Genen bei FAD oder eine veränderte Prozessierung von APP bei SAD führen zu einer erhöhten Produktion von $A\beta_{1-42}$, die die Entstehung diffuser Plaques zu Folge hat. Neuritische Plaques entstehen beim Andocken von $A\beta_{1-40}$ an diffuse Plaques. Neuritische Plaques verursachen wiederum Prozesse, die in der AD münden. Abbildung modifiziert aus (Selkoe 2001b).

Zu dieser Zeit wurde schon die Rolle von $A\beta_{1-42}$-Oligomeren diskutiert, wobei sie zu dem Zeitpunkt noch keinen Platz in der AKH fanden und ihre Rolle eher unklar und gering geschätzt wurde. Auch die Möglichkeit einer Bindung der $A\beta_{1-42}$-Oligomere an spezifische

Zellrezeptoren und somit das Auslösen einer Signalwegkaskade wurde diskutiert, aber mangels experimenteller Beweise verworfen (Selkoe 2001b).

Die späteren Versionen der AKH diskutieren die zunehmende Bedeutung von $A\beta_{1-42}$-Oligomeren und erkennen deren zentrale Rolle in der AD an (Haass and Selkoe 2007). Ein wichtiger Aspekt beim Auslösen der Amyloid-Kaskade und somit der AD ist ein relatives Erhöhen des $A\beta_{1-42}/A\beta_{1-40}$-Verhältnisses (Haass and Selkoe 2007, Karran et al. 2011). Dieser Punkt erscheint im Licht einer neuen Rolle von Aβ-Oligomeren besonders wichtig, da Aβ-Oligomere fast ausschließlich aus $A\beta_{1-42}$ bestehen.

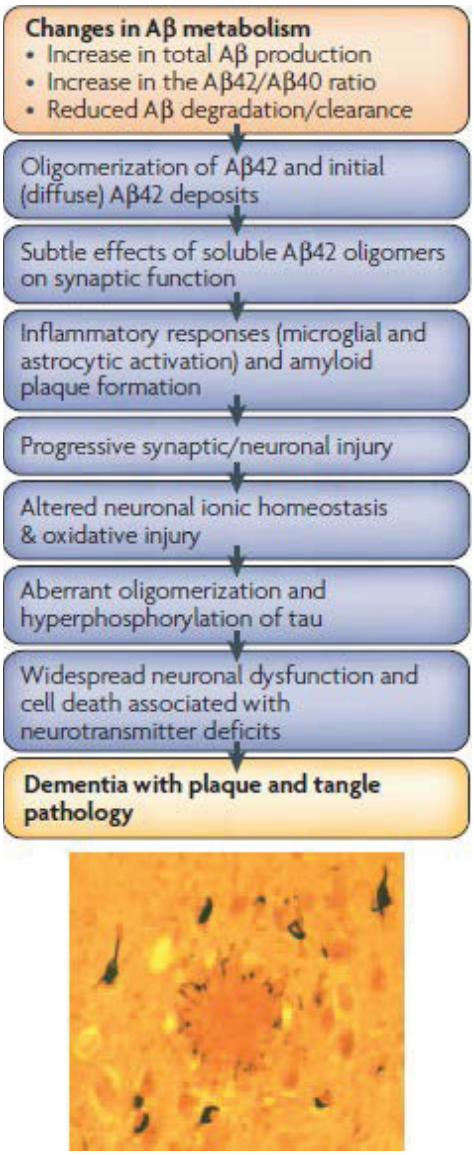

Abbildung 8 – spätere Version der Amyloid-Kaskaden-Hypothese
Erhöhte Aβ-Produktion, schwächere Aβ-Degradierung und erhöhtes Verhältnis von $A\beta_{1-42}$ zu $A\beta_{1-40}$ führen zu Oligomerisierung von Aβ. Diese beeinträchtigt synaptische Funktionen, was zu entzündlichen Reaktionen und Plaque-Bildung führt. Über Schädigung von Synapsen und Neuronen führt gestörte ionische Homöostase und oxidativer Stress wird die Hyperphosphorilierung von Tau ausgelöst. Diese führt zum Absterben von neuronen.
Abbildung modifiziert aus (Haass and Selkoe 2007).

Aβ-Oligomere beeinträchtigen synaptische Funktionen, wobei genaue Wirkungsmechanismen noch ungeklärt sind. Darauf folgende Prozesse decken sich mit früheren Versionen der AKHs (Abbildung 8). Die neuritischen Plaques verlieren die ihnen früher zugeschriebene Rolle, verantwortlich für die Entwicklung der AD zu sein, und werden als Folgen oder Symptome der AD eingestuft. Mit Hilfe von Analogien zu anderen Krankheiten, z.B. Huntington-Krankheit, wird sogar eine neuroprotektive Funktion der Plaques diskutiert (Haass and Selkoe 2007).
Auslöser für die Abwandlung der AKH waren Studien, in denen keine eindeutige Korrelation zwischen der Menge an amyloiden Ablagerungen und dem Grad des kognitiven Verfalls feststellbar waren. (Naslund et al. 2000). Amyloide Ablagerungen fanden sich bei Menschen ohne jegliche Demenz. Der Grad der Demenz korreliert deutlich besser mit biochemisch detektierbaren Aβ-Oligomeren als mit dem histologischen Befund der Plaques (Lue et al. 1999, McLean et al. 1999, Naslund et al. 2000, Wang et al. 1999).

1.3.2 Aβ-Oligomere und mögliche Mechanismen ihrer Wirkung

Das Forschungsfeld der Aβ-Oligomere ist heutzutage vielleicht eines der umfangreichsten aber gleichzeitig auch eines der unübersichtlichsten. Die seit mehr als anderthalb Jahrzehnten aufgestellte Hypothese, dass Aβ-Oligomere als Hauptursache der AD zu betrachten sind, fand in darauf folgenden Jahren immer mehr Unterstützer und Befürworter, die u.a. mit zahlreichen experimentellen Daten diese Hypothese belegt haben. Der Nachteil dieser Datenfülle ist die Schwierigkeit sie zu überblicken. Die größten Komplikationen in diesem Forschungsgebiet entstehen durch eine große zum Teil kontroverse Heterogenität dieser Daten. Der Hauptgrund dafür liegt wahrscheinlich in weniger präzisen oder unterschiedlichen Definitionen (Selkoe 2008). Z.B. werden „β-Amyloid-Kugeln“, die einen Durchmesser bis 200 µm aufweisen und vermutlich aus vielen Tausenden monomeren Einheiten bestehen, auch als Aβ-Oligomere bezeichnet (Westlind-Danielsson and Arnerup 2001). Viele Gruppen definieren und charakterisieren ihre Oligomere gar nicht, obwohl es bekannt ist, dass praktisch alle Parameter (Temperatur, pH, Ionenstärke etc.) einen sehr großen Einfluss auf Aβ-Oligomere haben. Diese starke Beeinflussung von Aβ-Oligomeren durch viele Faktoren wird oft als eine Entschuldigung oder Rechtfertigung für weniger präzise oder fehlende Definitionen benutzt und nicht selten von anderen Forschern auf diesem Feld akzeptiert.
Bis heute konnte keine hochauflösende Struktur eines Oligomers aufgeklärt werden. Ursache: fehlende Verfahren, um ein spezifisches Oligomer in ausreichender Menge herzustellen. Aβ-Oligomere bestehen *in vivo* hauptsächlich aus $A\beta_{1-42}$ (Haass and Selkoe 2007, Karran et al. 2011), obwohl die Länge des natürlich produzierten Aβ-Peptids im Gehirn, CSF oder

Zellkulturen variabel ist (Busciglio et al. 1993, Iwatsubo et al. 1994, Saido et al. 1995, Selkoe 2008). Aus diesem Grund werden die meisten Aβ-Oligomer-Studien *in vitro* überwiegend mit $Aβ_{1-42}$ durchgeführt. Viele unterschiedliche Konformationen der synthetischen Aβ-Oligomere wurden im Laufe der letzten zwei Jahrzehnte beschrieben. Ihnen wurden folgende Namen gegeben: Aβ-derived diffusible ligands (ADDLs), Aβ*56, Globulomere, donut-ähnliche (annular) Partikel (Selkoe 2008). Auch kleinere Aβ-Oligomere wie Di- bis Hexamere wurden beschrieben. Dabei wurde eine Hypothese aufgestellt, dass Penta- und Hexamere als Grundbausteine für höhere Aggregationsstufen und Aggregationskeime, sogenannte „paranuclei" fungieren (Roychaudhuri et al. 2009). Die Annahme, dass Aβ-Hexamere Bausteine weiterer Aβ-Strukturen sind, wird durch die Existenz oben erwähnter Aβ-Oligomere unterstützt: ADDLs, Aβ*56, die laut Literatur Dodecamere seien, sowie Aβ-Octadecamere. Sie alle stellen ein Vielfaches der Aβ-Hexamere dar (siehe Abbildung 9).

Die Präparation der ADDLs gelang nach einer Aβ-Inkubation mit Clusterin in Anwesenheit einiger Komponenten des Zellkulturmediums (Lambert et al. 1998). Die Clusterin-abgeleiteten ADDLs wurden mit AFM untersucht und hatten eine globuläre Struktur und einen Durchmesser von 5 - 6 nm. Man muss aber anmerken, dass Peptide, die in Abwesenheit von Clusterin präpariert wurden, zu einer eher fibrillären Struktur tendierten. In folgenden Jahren wurden ADDL-ähnliche Aβ-Oligomere aus *post mortem* AD-Gehirnen extrahiert. Ihre Anwesenheit korrelierte mit dem Gedächtnisverlust (Gong et al. 2003).

Aβ*56 wurde in Hirn-SDS-Extrakten von transgenen Mäusen detektiert (Lesne S. et al. 2006). Seine Form ähnelt einem länglichen Sphäroid. Der dritte Typ der Aβ-Dodecamere sind die Globulomere (Gellermann et al. 2008). Sie werden *in vitro* in Gegenwart von SDS gebildet.

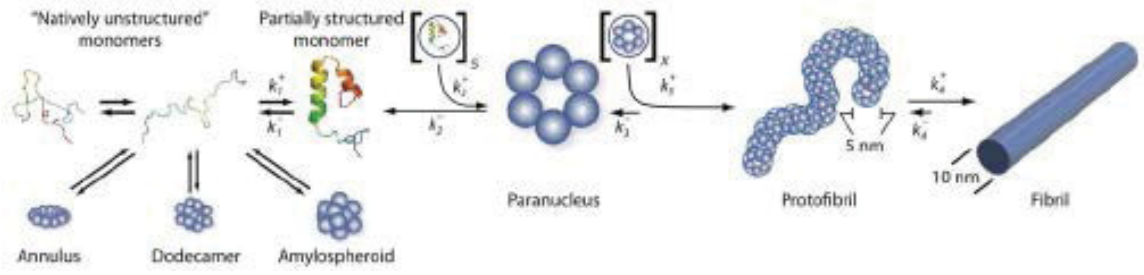

Abbildung 9 – Aβ-Oligomere, die als Aggregationskeime fungieren
Ein Aβ-Monomer kann Hexamere oder das Vielfache von ihnen bilden. Auf dem „off-pathway" der Fibrillogenese entstehen Dodeca- oder Octadecamere. Auf dem „on-pathway" Protofibrillen, die schließlich zu Aβ-Fibrillen reifen. Abbildung modifiziert aus (Roychaudhuri et al. 2009).

Für die Hypothese der hexameren Paranuclei sprechen auch die Dimensionen der Protofibrillen, sogenannter Fibrillenvorläufer. Sie wurden als Perlenketten beschrieben. Jede von diesen

Perlen hat einen Durchmesser von ca. 5 nm. Die meisten dieser Strukturen sind kürzer als 150 nm (Caughey and Lansbury 2003).

Mit einem Verfahren zur Vernetzung der Monomeren in den Aggregaten, namens PICUP (*photo-induced cross-linking of unmodified proteins*), konnten die Bausteine von Aβ-Oligomeren und Fibrillen stabilisiert werden. Auf diese Weise wurden Aβ-Pentamere und Hexamere, sowie eine geringere Menge an Di-, Tri- und Tetrameren, nachgewiesen (Bitan and Teplow 2004).

Die Verlässlichkeit vieler dieser Daten ist aufgrund von experimentellen Unzulänglichkeiten eingeschränkt. So basieren die meisten Erkenntnisse bezüglich der Größe kleiner Oligomere auf denaturierenden SDS-Gelen. Einer Meinung nach handelt es sich bei den detektierten Globulo-, Di-, Tri- und Tetrameren um SDS-resistente Moleküle (Podlisny et al. 1995, Selkoe 2008). Einer anderen Meinung nach sind es SDS-induzierte Artefakte (Bitan et al. 2005, Hepler et al. 2006, Lesne S. E. 2013). Die letztere Meinung hat sich heutzutage durchgesetzt.

Einige wichtige Ergebnisse können von anderen Gruppen nicht reproduziert werden. Dabei kommt eher raus, dass unterschiedliche Techniken inkonsistente Ergebnisse liefern und beim genauen Hinschauen es sich bei vermeintlich gut definierten Aβ-Oligomeren um Aggregatgemische oder ganz andere Spezies handelt. Dies betrifft z.B. die ADDLs (Lesne S. E. 2013).

Bei all diesen Problematiken der Aβ-Oligomer-Charakterisierung stellt sich natürlich die Frage, ob der komplette Wirkungsmechanismus von Aβ-Oligomeren in der Entwicklung der AD aufgeklärt werden kann. Mittlerweile gibt es aber dies bezüglich eine Menge Erkenntnisse und Hypothesen. Die Aβ-Oligomer-Forschung konzentriert sich in den letzten Jahren auf zwei Modelle der Aβ-Pathogenese. Ein nimmt an, dass Aβ-Oligomere mit der Zellmembran der Neuronen interagieren und diese dabei stören. Das andere besagt, dass Aβ-Oligomere einen Rezeptor oder Korezeptor der Neuronen bindet und somit eine Signalkaskade auslöst, die letztendlich zu Apoptose führt.

Die Störung oder Beeinträchtigung der Membranfunktion setzt voraus, dass das relativ lipophile Aβ in oligomeren Form an die Membran bindet und sie invaginiert (Zhao L. N. et al. 2012), sodass die ionische Homöostase gestört wird. Dabei können Aβ-Oligomere einer Art Pore oder Ionenkanal in der Membran bilden (Lin et al. 2001). Für diese Vorstellung eignet sich am besten das oben erwähnte Donut-ähnliche Oligomer, da es bereits eine Öffnung in seiner vermeintlichen Struktur besitzt (Caughey and Lansbury 2003, Haass and Selkoe 2007). Die porenähnliche Struktur mit einem Außendurchmesser von 8- 12 nm hat eine Porengröße von 2 - 2,5 nm. Es gibt auch molekular-dynamische (MD) Simulationen, die zeigen, dass ein nicht

porenähnliches Aβ-Oligomer bei Membranbindung sich umformt und eine Pore bildet (Shafrir et al. 2010). Eine wichtige Rolle spielen dabei die Lipide selbst, da es bekannt ist, dass sie einer Art Katalysator der Amyloidogenese sind (Berthelot et al. 2013).

Die Arbeitsgruppe um Jan hat demonstriert, dass die Aβ-Toxizität weniger von einem spezifischen Aggregatzustand, sondern mehr von der Möglichkeit den Wachstumsprozess der Fibrillen durchzuführen abhängt (Jan et al. 2011).

Ein strittiger Punkt bei der dargelegten „Porentheorie" ist, wie sich in nanomolaren Konzentrationen im Gehirn befindende Aβ so viel Schaden allein durch Störung der Ionen-Homöostase anrichten kann. Das Model der Rezeptorbindung durch Aβ-Oligomere und dadurch ausgelöste apoptotische Signalkaskade hat dieses Problem nicht.

Viele Rezeptoren wurden als mögliche Bindepartner für Aβ-Oligomere in Betracht gezogen. Z.B.: Ionotrope Rezeptoren wie *N*-Methyl-$_D$-Aspartat (NMDA)-Rezeptor oder α7-Acetylcholin-Rezeptor, Rezeptor-Tyrosinkinasen wie Insulin R oder EphB2, „*Receptor for Advanced Glycation Endproducts*", Immunoglobulin-ähnlicher Rezeptor B (PirB) und das zelluläre Prion-Protein (PrP^c) (Benilova and De Strooper 2013).

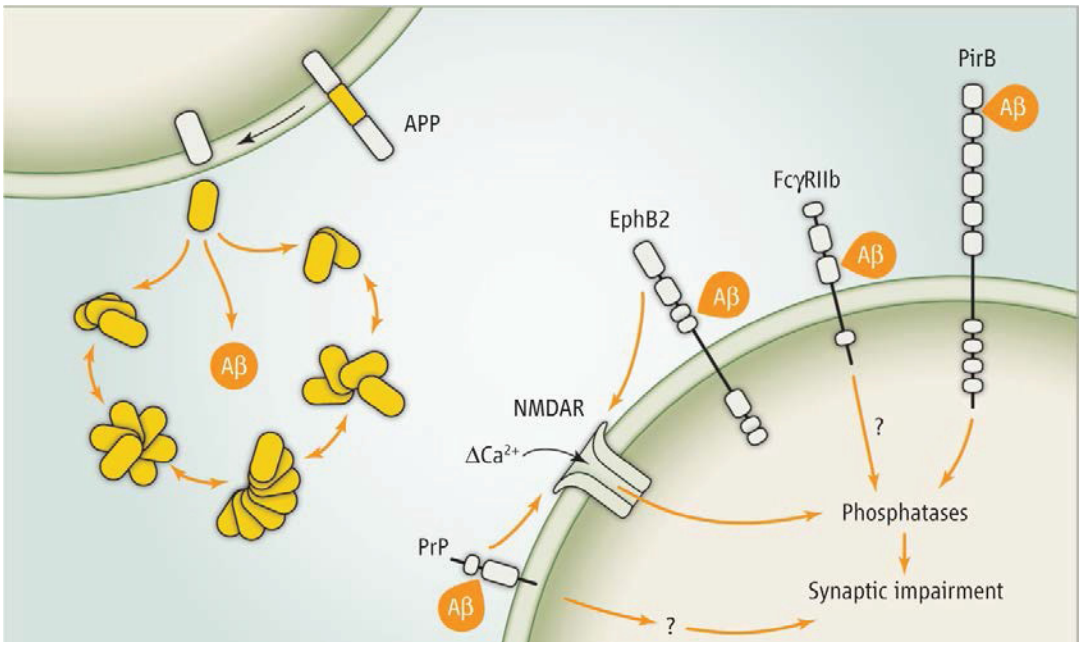

Abbildung 10 – Rezeptorvermittelte synaptotoxische Signalwege des Aβ-Peptids
Aβ-monomere prozessiert aus APP formen Oligomere unbekannter Konformationen. Diese wechselwirken mit mehreren vermeintlichen Rezeptorkandidaten. Orange Pfeile zeigen die vermeintlichen Aβ-Oligomer-Bindestellen der Rezeptoren. Im Gegensatz zu PrP^c- und EphB2-Signalwegen, die eventuell den NMDA-Rezeptor und Ca^{2+} Einstrom beeinflussen, neuroimmune Rezeptoren FcγRIIB und PirB/LilrB2 sind direkt in Signalkaskaden involviert, die zu synaptischer Beeinträchtigung führen.
Abbildung modifiziert aus (Benilova and De Strooper 2013).

Die entscheidende Wichtung dem PrP^c brachten die Experimente der Arbeitsgruppe um Strittmatter. Die Arbeitsgruppe konnte zeigen, dass transgene Mäuse, die normalerweise AD-ähnliche Symptome entwickelt hätten, beim „ausknocken“ des PrP^c keinerlei Anzeichen der AD zeigten (Gimbel et al. 2010, Lauren et al. 2009). Diese Ergebnisse blieben eine Zeit lang kontrovers basierend vor allem auf dies widerlegenden Versuchen der Arbeitsgruppe um Stravalaci (Balducci et al. 2010). Andere Gruppen konnten dennoch die entscheidende Verbindung zwischen PrP^c und der AD in Tiermodelen bestätigen (Lesne S. E. 2013). Es wurde auch gezeigt, dass Aβ-Oligomere an PrP^c in nanomolaren Konzentrationen bindet. Die Schlüsselrolle bei der Bindung spielt der N-Terminus des PrP^c (Fluharty et al. 2013).

Die Bindung von Aβ-Oligomeren an PrP^c soll eine Signalkaskade über die Fyn-Kinase auslösen, die in der Beeinträchtigung der neuronalen Funktion mündet (Lesne S. E. 2013, Rushworth et al. 2013). Da aber das PrP^c aber kein transmembranes Protein ist, also kein Rezeptor im klassischen Sinne sein kann, kann es nicht eigenständig das Signal der Aβ-Oligomer-Bindung transduzieren. Es wird postuliert, dass PrP^c das transmembrane “*Low Density Lipoprotein receptor-related protein-1*“ nach seiner Interaktion mit Aβ-Oligomeren bindet und dadurch eine Signalkaskade der Fyn-Kinase aktiviert (Rushworth et al. 2013).

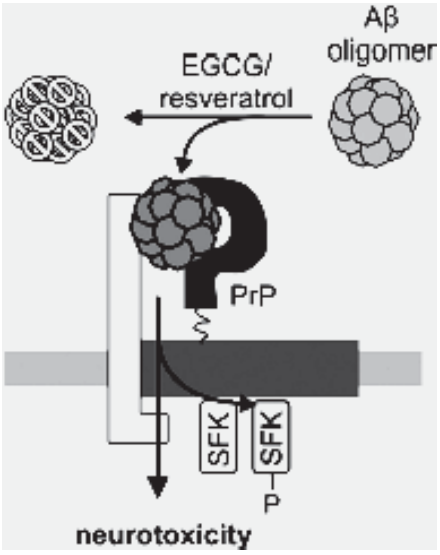

Abbildung 11 – Vermeintliches Model der Bindung von Aβ-Oligomeren an PrP^c mit darauf folgender Signalkaskade und Neurotoxizität
Fibrilläre Aβ-Oligomere binden an das PrP^c transmembrane „*Low Density Lipoprotein receptor-related protein-1*“(LRP1). Diese Bindung verstärkt die Cluster-Bildung von LRP1 in *lipid rafts*, was zu aktivierung der Fyn-Kinase und Neurotoxizität führt. EGCG remoduliert Aβ-Oligomere und verhindert somit die Bindung an PrP^c. Abbildung modifiziert aus (Rushworth et al. 2013).

Die These der Aβ-Oligomer-PrP^c-Bindung als eines entscheidenden Faktors fürs Auslösen der AD fand eine mittlerweile eine breite Akzeptanz in der Alzheimer-Forschung. Viele Gruppen benutzen die o.g. Bindung fürs Finden AD-relevanter Aβ-Oligomere und die Entschlüsselung

derer Bedeutung in unterschiedlichen Entwicklungsphasen der AD. So wurde festgestellt, dass Aβ-Oligomere aus *post mortem* Hirngewebe der AD-Patienten mit dem molekularen Gewicht von ca. 150 kDa an PrP^c binden (Dohler et al. 2014). In primären kortikalen Neuronen nur Aβ-Di- und Trimere induzierten Fyn-Phosphorilierung (Lesne S. E. 2013).
Es wird angenommen, dass Aβ*56 das prominenteste Aβ-Oligomer in präklinischen Phasen der AD ist. Die Konzentration der Aβ-Trimere ist in der frühen symptomatischen Phase (*mild cognitive impairment*) erhöht und Aβ-Dimere sind die dominierende oligomere Aβ-Spezies in der späten Phase der AD (Lesne S. E. 2013).

1.3.3 *In vitro* Untersuchungen von Aβ-Oligomeren

Für ein besseres Verständnis von Aβ-Oligomeren sowie Untersuchungen von möglichen Liganden werden die ersteren sehr ausgiebig *in vitro* analysiert. Das vorherige Kapitel beschreibt die Komplexität und Heterogenität der *ex vivo* Befunde auf dem Forschungsfeld der Aβ-Oligomere. Diese Aspekte fließen natürlich auch in die *in vitro* Forschung auf diesem Gebiet mit ein. Zusätzlich entstehen viele andere Probleme, die auf unterschiedlichen Vorbehandlungen des Aβ-Peptids, genutzten Bedingungen fürs Entstehen und Präparationen von Aβ–Oligomeren beruhen.
Allgemein lassen sich all diese Probleme auf eine sehr schnelle und unterschiedliche Aggregation des Aβ-Peptids zurückführen. Es werden z.B. unterschiedliche Aggregationswege für das synthetische und rekombinante Aβ-Peptid beschrieben (Finder et al. 2010). Die meisten Labore nutzen das synthetisch hergestellte Aβ, dessen Aggregationsverhalten auch stark von der Bezugsquelle abhängt.
Das Aβ wird meistens vorbehandelt eingesetzt, damit es möglichst monomerisiert fürs eigentliche Experiment vorliegt, z.B. die Vorbehandlung mit Hexafluorisopropanol (HFIP) (Barrow et al. 1992). Das Aβ aggregiert in Folge einer Inkubation, die je nach Publikation sehr stark variiert, zu unterschiedlichen Spezies. Unter diesen befindet sich ein gewisser Anteil an Aβ-Oligomeren. Dann erfolgt eine analytische oder präparative Trennung der entstandenen Spezies. Die hierzu wahrscheinlich am häufigsten eingesetzte Methode ist die Größenausschluss-Chromatographie (*Size Exclusion Chromatography*: SEC). Dabei wird eine Superdex-Säule mit einem Ausschluss-Volumen von entweder 75 oder 200 kDa verwendet. Dabei ist nicht klar, ab das Säulenmaterial einen Einfluss auf Aβ-Oligomere ausübt. Bei der Auftrennung mit SEC mit 75 kDa Ausschlussvolumen detektiert man meistens nur den Monomeren- und Ausschluss-Volumen-Peak. Der letztere wird auch Aβ-Oligomeren

zugeordnet, obwohl er alle möglichen Moleküle größer als 75 kDa beinhalten kann. Kleinere Aβ-Oligomere wie z.B. Di-, Tri-, Tetra- oder Dodecamere werden bei *in vitro* Präparationen fast nie detektiert. Diese sind aber in SDS-Gelen sehr präsent und entfachen viele Diskussionen über SDS-induzierte Artefakte (siehe vorheriges Kapitel).

Andere Gruppen führen gar keine Auftrennung der oligomeren Spezies durch. Stattdessen nehmen sie die ganze, eine gewisse Zeit inkubierte Aβ-Lösung und gehen davon aus, dass ausschließlich oder im ausreichenden Masse Aβ-Oligomere enthält, z.B. (Fluharty et al. 2013). Diese unterschiedlichen Praktiken könnten vielleicht die im Forschungsgebiet herrschende Heterogenität und eine schlechte Reproduzierbarkeit der Ergebnisse erklären (Lesne S. E. 2013).

Es gelang noch nicht eine hochaufgelöste Struktur von eines Aβ-Oligomers zu bestimmen. Es gibt nur partielle Informationen über die Anordnung bestimmter Aminosäurereste in einem Aβ-Oligomer (Ahmed et al. 2010).

Es gibt aber sehr viele Studien, die die Ultrastruktur dieser Moleküle beschreiben. Dazu zählen EM- und Rasterkraftmikroskopie- (*atomic force microscopy*: AFM) Untersuchungen. Diese zeigen meistens flache runde oder ellipsoide Partikel unterschiedlicher Größen. Die flache Form könnte jedoch durch artifizielle Einflüsse wie Trocknung/Denaturierung an der Oberfläche oder mechanische Kraft des AFMs erklärt werden (E. Ukraintsev 2012).

1.4 Behandlungsversuche und Strategien der Alzheimer-Krankheit

Aus den am Beginn des Kapitels 1.3 beschriebenen Problematiken geht hervor, dass eine wirksame Therapie der Alzheimer-Krankheit von einer sehr großen medizinischen und sozialen Bedeutung wäre. Dabei wäre nicht nur eine vollständige Heilung der Demenz, sondern auch eine Verlangsamung ihres Verlaufs ein großer Erfolg.

Zurzeit kann aber die Alzheimer-Krankheit nicht geheilt werden. Die eingesetzten Therapien behandeln die Symptome aber nicht die Ursachen der Krankheit. Dazu zählen psychotherapeutische Behandlungen, der Einsatz von Acetylcholinesterase- und nicht steroidalen Entzündungshemmern, NMDA-Rezeptor-Antagonisten, Ginkgo biloba Extrakten sowie Aktivierung von ABC-Transportern.

Um die eigentliche Ursache der AD zu bekämpfen, nämlich Aβ-Oligomere, wurden in den letzten Jahren unterschiedliche Strategien und Wirkstoffe entwickelt. Dabei scheint die Verhinderung der Aβ-Oligomer-Bildung oder eine Eliminierung dieser Spezies der beste Therapieansatz zu sein.

Die Wege zu diesem Ziel können aber unterschiedlich sein. Deren Übersicht ist in der Abbildung 12 dargestellt. Der erste Ansatz ist die Produktionsverringerung der löslichen Aβ-Monomere, was auch eine reduzierte Oligomerbildung zu Folge haben sollte. Für diesen Zweck wurden/werden unterschiedliche hochspezifische Inhibitoren der β- und γ-Sekretasen wie Tarenflurbil oder Semagacestat eingesetzt. Obwohl die präklinischen Daten für Tarenflurbil sehr überzeugend gewesen sind (Golde et al. 2010), konnten diese Wirkstoffe nicht in der klinischen Phase III bestehen. Der kognitive Zustand der Patienten hat sich sogar gegenüber der Placebo-Gruppe verschlechtert (Karran et al. 2011).

Dies ist wahrscheinlich darauf zurück zu führen, dass die Inhibition der β- und γ-Sekretasen mit starken Nebenwirkungen verbunden ist, da diese Enzyme nicht nur das APP sondern auch viele anderen Substrate spalten, die für eine normale Funktion des menschlichen Organismus essentiell sind. Des Weiteren gibt es Hinweise, dass die Aβ-Monomere eine natürliche Funktion haben (siehe Kapitel 1.3). Eine drastische Reduktion dieser Peptide hätte demnach negative Auswirkungen. Dieser Ansatz ist also nicht mehr attraktiv.

Eine andere Strategie ist die Entwicklung kleiner Moleküle, die in den Aβ-Katabolismus involvierte Enzyme stimulieren können (Abb. 12 Punkt 2). Das Design dieser Verbindungen basiert auf der Überexpression von Neprilysin oder Cathepsin B, die in APP-transgenen Mäusen die Aβ-Konzentration und Plaqueablagerung reduzieren konnten (Leissring et al. 2003, Mueller-Steiner et al. 2006). Genetische Deletion von NEP erhöht die zerebrale Aβ-Konzentrationen, inklusive die der Oligomere, in APP-transgenen Mäusen (Farris et al. 2007) und führt zur Beeinträchtigung der hypocampalen synaptischen Plastizität und kognitiven Funktion (Huang et al. 2006).

Kleine Moleküle oder biologische Präparate, die an Aβ-Monomere binden und diese stabilisieren, sollten die Aβ-Oligomerisierung verhindern (Abb. 12 Punkt 3). Eine Verbindung dieser Art ist die 3-Amino-1-Propansulfonsäure (Tramiprosate, Homotaurine, ALZHEMED). Sie reduziert die Aggregation synthetischen Aβ *in vitro* und kann in APP-transgenen Mäusen die Plaque-Bildung reduzieren (Gervais et al. 2007). In der klinischen Phase konnte dieser Wirkstoff aber keinen positiven Effekt zeigen (Karran et al. 2011).

Es wurden außerdem mehrere Inhibitoren der Aβ-Aggregation gefunden, die für die Brechung vorgeformter Aβ-Oligomere geeignet sind (Walsh and Selkoe 2007). Nach dem Einsatz von Verbindungen dieser Art konnte bei APP-transgenen Mäusen eine Abschwächung der AD-Symptome gezeigt werden (McLaurin et al. 2006).

Es wurde auch gezeigt, dass Antikörper gegen Aβ Aβ-Oligomere binden und ihre neurotoxische Wirkung neutralisieren (Klyubin et al. 2005).

AD-Patienten, die gegen das aggregierte Aβ immunisiert wurden, zeigt eneinen weniger starken kognitiven Rückgang als die, die nur ein Placebo bekamen (Gilman et al. 2005, Schenk et al. 2005). Unglücklicher Weise musste diese klinische Studie abgebrochen werden, da 18 von 298 Patienten, die immunisiert wurden, Meningoencephalitis entwickelten (Gilman et al. 2005).

Einer der letzten in klinischen Phasen getesteten monoklonalen Antikörper gegen Aβ mit dem Namen Solanezumab zeigte als erste eingesetzte Substanz, die den Amyloid-Kaskaden-Mechanismus angreift, eine geringfügige Verlangsamung der AD (Karran et al. 2011).

Eine relativ neue Strategie, um Aβ-Oligomere zu neutralisieren oder zu eliminieren, ist ein Mimicking von identifizierten und zum Teil charakterisierten Aβ-Oligomere bindenden Rezeptoren oder deren Segmente, z.B. N-terminale Segmente des Prion-Proteins (Fluharty et al. 2013).

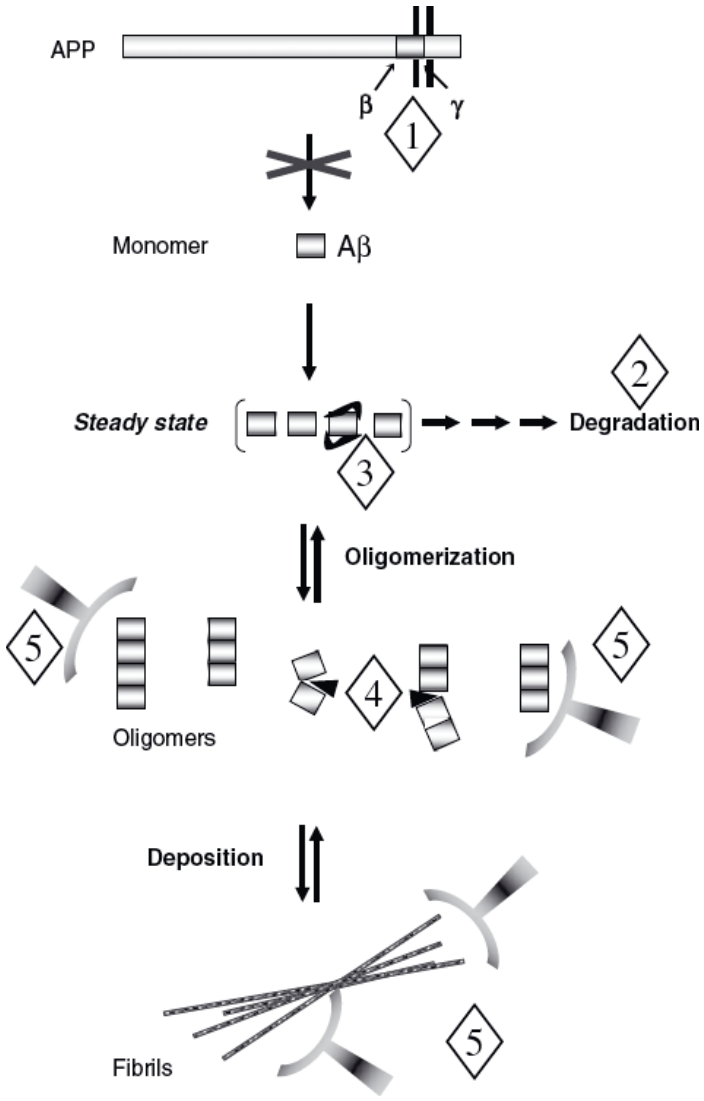

Abbildung 12 – Behandlungsstrategien gegen AD-verursachende Aβ-Oligomere

Die Zahlen markieren unterschiedliche Therapieansätze, um die Aβ-Oligomer-Bildung zu verhindern oder Aβ-Oligomere zu eliminieren. Die Abbildung nach (Walsh and Selkoe 2007).

1.5 Peptide als Medikamente

Da beinahe alle Vorgänge im Körper über Peptide oder Proteine gesteuert werden, sind diese Moleküle mit sehr breiten Bioaktivitäten für die Entwicklung therapeutischer Wirkstoffe sehr interessant. Peptidische Medikamente weisen eine hohe Wirksamkeit und Spezifität; eine niedrige Toxizität und Immunogenität auf (Vlieghe et al. 2010). Sie sind jedoch für die proteolytische Degradation anfällig. Diese Tatsache macht die Verabreichung von peptidischen Wirkstoffen auf oralem Wege nicht möglich, da sie im Magen-Darm-Trakt verdaut werden. Aus diesem Grunde haben sie auch eine kurze Halbwertszeit.

Wegen der geringeren Halbwertszeit akkumuliert wenig Peptid im Gewebe. Dadurch werden die Gefahren verringert, dass es zu Komplikationen durch Abbauprodukte kommt. Dies ist als Vorteil der Peptide zu werten. Die Probleme der geringen Stabilität lassen sich aber mit dem Einsatz nicht natürlicher D-Aminosäuren, Zyklisierung von Peptiden oder modifizieren ihrer Seitengruppen umgehen. L-Peptide, die 12 Aminosäuren lang oder kürzer sind, weisen auch eine höhere Proteasestabilität als längere Peptide auf (Cochran et al. 2001, Skelton et al. 2001). Ein großer Vorteil von Peptiden als therapeutisch wirksame Stoffe ist ihre im Vergleich zu den Antikörpern und anderen Proteinen kleine Größe. Der Größenvorteil erleichtert den Transport dieser Wirkstoffe zum Einsatzort. Zu weiteren Vorteilen der Peptide gegenüber Antikörpern und größeren Proteinen zählen auch geringere Herstellungskosten und höhere Lagerungsstabilität.

Viele Peptide unterschiedlichster Größe und Zusammensetzung finden bereits eine breite Anwendung als Medikamente oder befinden sich in unterschiedlichen klinischen Testphasen.

Z.B. werden Calcitonin, ein Peptidhormon mit 32 Aminosäuren, und Enfuvirtide (T-20), ein aus 36 Aminosäuren bestehender Inhibitor der Fusion von HIV-1 und der Wirtszelle, für die Behandlung von Osteoporose und AIDS entsprechend eingesetzt (Manfredi and Sabbatani 2006, Mehta et al. 2003). Hirudin und seine Analoge werden als Thrombininhibitoren eingesetzt.

Viele therapeutische Peptide stammen von natürlichen Metaboliten ab und weisen eine hohe Interaktion mit Membranproteinen auf. Normalerweise reichen geringe Mengen von einem peptidischen Wirkstoff aus, um die Zielrezeptoren zu aktivieren oder zu deaktivieren. Diese Tatsache macht die Klasse hier beschriebener Therapeutika sehr attraktiv für Behandlungen von Krebserkrankungen.

Heutzutage gibt es eine Fülle vielversprechender Peptide oder Peptidderivate, die durch Modifikationen natürlicher Produkte, Phagen-Display und kombinatorische Chemie

ausgewählt wurden. Die Entwicklung peptidischer Wirkstoffe gegen Krebs, AD und Prion-assoziierte Erkrankungen sowie der Einsatz von Peptiden als anti-mikrobielle Substanzen sind wichtige Gebiete in moderner Forschung (Lien and Lowman 2003).

1.5.1 Einsatz peptidischer Wirkstoffe bei AD

Seit etwa zwei Jahrzehnten werden Peptide auch als potentielle Wirkstoffe für eine AD-Behandlung entwickelt und untersucht. Die meisten von ihnen sind kleine Peptide und zielen auf die Aggregationsinhibition von Aβ. Unterschiedliche Studien beschrieben eine reduzierte Aβ-Toxizität nach Einsatz dieser Peptide (Poduslo et al. 1999, Soto et al. 1998).
Das Pentapeptid LPYFD kann die Blut-Hirn-Schranke passieren und die Synapsen gegen die pathologische Wirkung des fibrillären Aβ schützen (Juhasz et al. 2009).
Mit dem Rücken der Aβ-Oligomere in die zentrale Rolle bei der AD-Pathogenese wurden auch peptidische Wirkstoffe dementsprechend entwickelt. Z.B. wurde von einem β-faltblattbrechenden D-Peptid berichtet, das gezielt die Aβ-Oligomerbildung verhindert. Oral verabreicht reduzierte dieses Peptid die Plaqueablagerung in APP-transgenen Mäusen und verbesserte ihre kognitive Funktionen (Frydman-Marom et al. 2009).

1.6 Selektion Aβ bindender Peptide mit Spiegelbild-Phagen-Display

Eine heutzutage verbreitete Technik, um Peptide mit variablen Aminosäuresequenzen herzustellen und sie auf die Bindung an ein bestimmtes Zielmolekül zu durchsuchen, ist Phagen-Display. Der größte Vorteil dieser Methode basiert auf einer gigantischen Anzahl eingesetzter potenzieller Liganden und, dass man kein Wissen über die Zielmoleküle benötigt (Sun et al. 2012).
Die Peptidbibliothek besteht aus Bakteriophagen, an deren Oberfläche je ein Peptid mit dem Hüllprotein eines Phagen fusioniert ist, und so dem Zielmolekül präsentiert werden kann.
Diese Technik stellt eine Möglichkeit dar, den Phänotyp des Peptids mit seinem Genotyp zu verbinden. Bei den gekauften Bibliotheken gibt es z.B. 10^9 Phagen und jeder von ihnen präsentiert ein anderes Peptid. Dieses kann konstruiert, selektiert und amplifiziert werden (Abbildung 13). Nach einer Inkubation der Zielmoleküle mit Phagen werden nicht oder wenig affine Phagen abgewaschen und verworfen. Die, die binden, werden eluiert. Auf diese Weise selektierte Phagen mit gewünschten Peptiden werden in Bakterien amplifiziert.
Der Prozess der Selektion und Amplifikation kann beliebig oft wiederholt werden, um Peptide mit der höchsten Affinität zu selektieren. Auf diese Weise erhält man eine Peptidpopulation mit einer dominierenden Sequenz, die eine starke Affinität zum Zielmolekül aufweist.

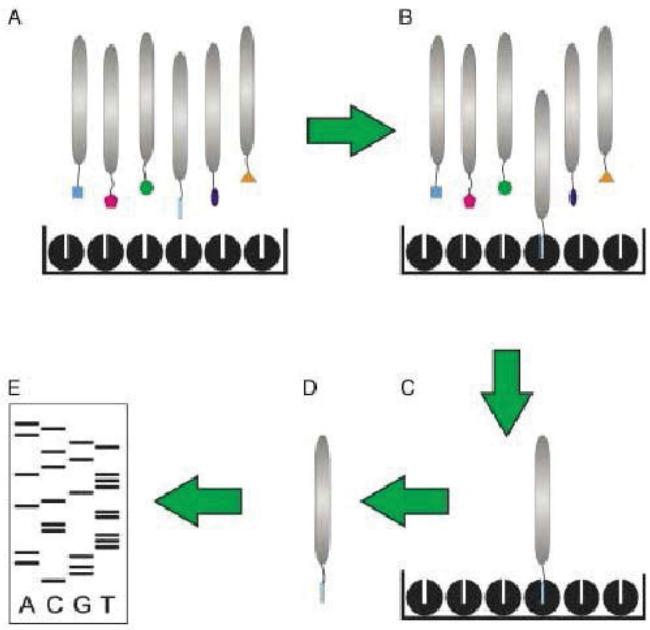

Abbildung 13 – schematische Darstellung der Phagen-Display-Selektion

(A) Unterschiedliche Peptide (symbolisiert durch farbige Figuren) werden an der Oberfläche der Phagen präsentiert. Sie sind mit den Hüllenproteinen fusioniert (lange graue Symbole). Die Peptide werden auf die Zielmoleküle (schwarze runde Symbole) appliziert. Einige der Peptide werden an die Zielmoleküle binden (B). Der Rest wird abgewaschen (C). Affine Peptide werden eluiert (D). Die Sequenz des selektierten Peptids wird durch die DNA-Sequenzierung des Fusionsproteingens bestimmt (E). Die Abbildung nach (Wiesehan and Willbold 2003).

Die Arbeitsgruppe um Peter Kim hat eine elegante kombinatorische Technik entwickelt, die auf der Tatsache basiert, dass die dreidimensionale Struktur eines Proteins aus L-Aminosäuren bestehend exakt dem Spiegelbild dieses Proteins aus D-Aminosäuren entspricht (Schumacher et al. 1996). Diese Methode trägt den Namen Spiegelbild-Phagen-Display.
Wie beim klassischen Phagen-Display werden auch beim Spiegelbild-Phagen-Display L-Peptide auf Phagen-Oberflächen präsentiert, die aber an Zielproteine aus D-Aminosäuren binden. Dies hat auch einen Nachteil, da das Zielprotein synthetisch hergestellt werden muss und somit nach dem heutigen Stand der Technik in der Größe limitiert ist. Auf diese Weise selektierte L-Peptide werden sequenziert und dann werden ihre spiegelbildlichen D-Peptide synthetisiert. Diese D-Peptide werden an das Enantiomer des D-Zielmoleküls, also das natürlich vorkommende L-Protein, binden. D-Peptide weisen eine niedrigere bis gar keine Proteasesensitivität (Sun et al. 2012) und eine höhere Resistenz gegenüber Degradation in Organismen auf (Findeis et al. 1999).

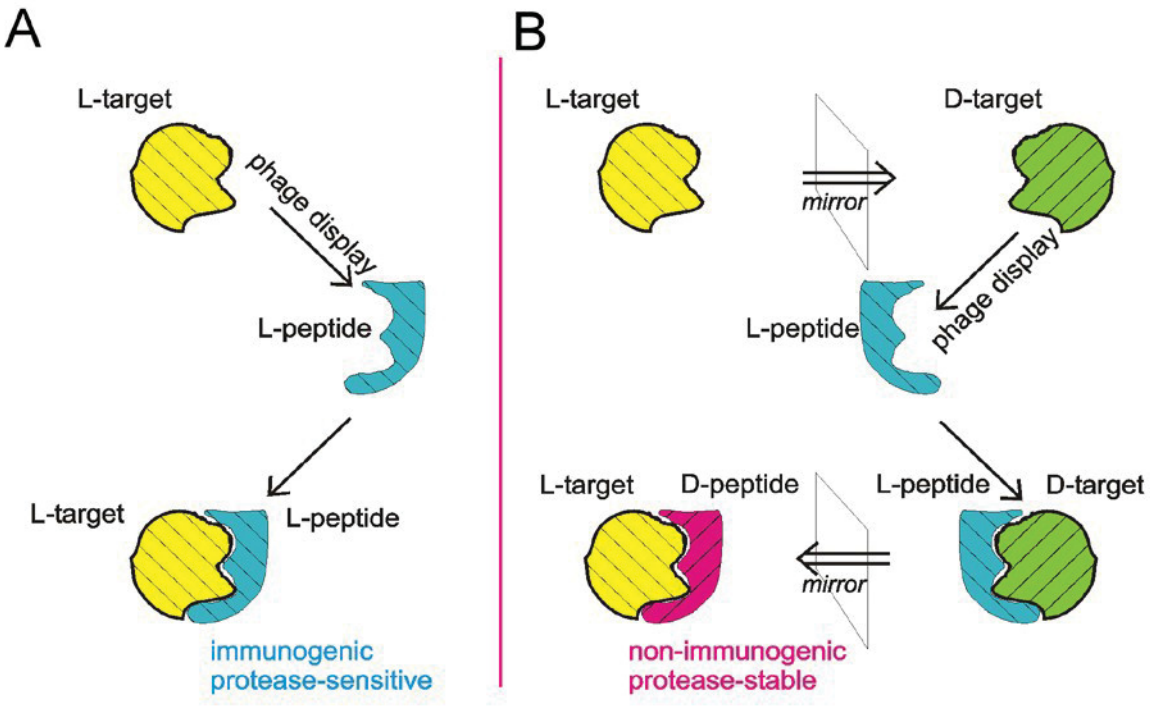

Abbildung 14 – schematische Darstellung des Phagen- und Spiegelbild-Phagen-Displays
(A) L-Peptide werden auf Bindung an ein L-Zielprotein selektiert (L-target). (B) L-Peptide werden auf Bindung an das Spiegelbild des Zielproteins selektiert, das aus D-Aminosäuren besteht (D-target). Das Spiegelbild dieses Komplexes ist ein D-Peptid und ein L-Zielprotein (L-target). Die im Endeffekt selektierten D-Peptide können leicht chemisch synthetisiert werden. Die Abbildung leicht modifiziert nach (Wiesehan and Willbold 2003).

Verwendet man als Zielmolekül das L- oder D-Aβ, selektiert man mit Hilfe vom Phagen-Display oder Spiegelbild-Phagen-Display entsprechend L- oder D-Peptide, die das Aβ spezifisch binden und vielleicht seine Faltung und Aggregation modulieren.
Es besteht die Möglichkeit auf bestimmte Aβ-Spezies und Konformationen zu selektieren, so dass die ausgesuchten Peptide bevorzugt z.B. Aβ-Oligomere binden. Diese Peptide können für die Therapie und Diagnostik eingesetzt werden (Sun et al. 2012).

1.7 Rationales Design von Wirkstoffen

Als rationales Wirkstoffdesign bezeichnet man einen gezielten Entwurf von Wirkstoffen, die z.B. als Medikamente eingesetzt werden können. Das rationale Design basiert auf einem Optimieren und Selektieren von Leitstrukturen (Madsen et al. 2002). Dies sollte zu Folge haben, dass der auf diese Weise optimierte Wirkstoff oder dessen Teil affiner an das Zielmolekül bindet. Diese Optimierung kann aber auch andere Ziele haben, wie die

Veränderung solcher Eigenschaften eines Wirkstoffes wie Toxizität, Pharmakodynamik oder Verstoffwechselung. Beim Wirkstoffdesign werden sowohl Erkenntnisse über die Strukturen von Wirkstoff und Zielmolekül als auch Erkenntnisse über eine herausragende Bedeutung bestimmter Wirkstoff-Fragmente verwendet.

Man unterscheidet beim Wirkstoffdesign folgende Typen.

Beim Liganden-basierten Wirkstoffdesign benutzt man Moleküle, die dem Ausgangsligand, bei dem die Wirkung empirisch bekannt ist, in Form und Ladung ähneln. Durch ein Hochdurchsatz-Screening werden neue affinere Derivate des Ausgangsliganden identifiziert (http://de.wikipedia.org/wiki/Wirkstoffdesign#cite_ref-isbn0-9636817-6-1_7-0).

Beim Struktur-basierten Wirkstoffdesign verwendet man hochaufgelöste Strukturen des Liganden und Zielmoleküls, um durch gezieltes Ändern weniger Elemente des Wirkstoffs eine affinere Bindung an das Zielmolekül zu erreichen. Dafür werden auch verstärkt MD-Simulationen eingesetzt (Leach and Jhoti 2007).

Beim Ligandfragmenten-basierten Wirkstoffdesign (*ligand fragment link*) verwendet man einzelne Bausteine bekannter Liganden. Voraussetzung dafür sind Informationen über die einzelnen funktionalen Gruppen, die Bioaktivität haben. Aus einer relativ geringen Anzahl dieser funktionalen Bausteine kann durch Kombinatorik eine sehr große Vielfalt von Wirkstoffen kreiert werden (http://en.wikipedia.org/wiki/Drug_design).

Zu Methoden des rationalen Wirkstoffdesigns zählen auch eine Di- oder Polymerisierung von Liganden, sowie ihre Zyklisierung. Bei einer Polymerisierung des Liganden geht man davon aus, dass die Anzahl der Bindestellen auch polymerisiert wird. So erhöhen sich die Avidität und somit auch die Affinität des Liganden. Der Nachteil dieser Strategie besteht darin, dass auch die Größe des Wirkstoffes multipliziert wird. Bei der Zyklisierung eines Wirkstoffes (Peptids) geht man davon aus, dass dadurch die Struktur der Bindestelle stabilisiert wird. Einer der größten Vorteile von zyklisierten Peptiden ist ihre höhere Proteaseresistenz, da sie keine freien N- und C-Termini diesen Enzymen präsentieren.

1.8 Fragestellung

Wie oben beschrieben scheint heutzutage die Strategie Aβ-Oligomere zu reduzieren oder besser komplett zu eliminieren die optimale für eine mögliche AD-Therapie zu sein. Entwicklung von einem Wirkstoff, der diesen Anforderungen entspricht, wäre also sehr wünschenswert.

Als Leitstruktur für diese Aufgabe diente ein im Vorfeld in unserer Arbeitsgruppe mit dem Spiegelbild-Phagen-Display selektiertes D-Peptid, das Aβ bindet. Die Untersuchung der Bindung von D3 an Aβ und dessen Einfluss auf die Aβ-Aggregation wäre der erste Schritt.

Um besser diese Zielmoleküle zu verstehen, sollten sie mit biophysikalischen und biochemischen Methoden charakterisiert werden. Da es keine Methode gibt, um die Aβ-Oligomer-Reduktion quantitativ zu messen, musste zwingend auch eine solche Technik im Laufe dieser Arbeit entwickelt werden. Ohne die Möglichkeit eine quantitative Bestimmung der Aβ-Oligomer-Reduktion bestimmter Größen durchzuführen, wäre die Aufgabe des D3-Derivaten-Vergleichs und Selektion neuer Wirkstoffe nur wenigen Fällen lösbar.

Bei der D3-Optimierung sollen unterschiedliche Wege, die auf dem rationalen Wirkstoffdesign basieren, getestet werden: z.B. Dimerisierungen und Zyklisierungen des D3, Herstellung von Hybridverbindungen von diesem Ligand mit anderen, bereits untersuchten Wirkstoffen, sowie Variationen seiner Aminosäuresequenz.

Des Weiteren sollte das D3 auf seine Effektivität der Aβ-Oligomer-Eliminierung optimiert werden, so dass dessen optimierte Derivate in transgenen Tiermodellen und später in der klinischen Phase I eingesetzt und getestet werden könnten.

2 Ergebnisse

2.1 Publizierte Ergebnisse

2.1.1 Oral treatment with the d-enantiomeric peptide D3 improves the pathology and behavior of Alzheimer's Disease transgenic mice.

Publiziert in: ACS Chemical Neuroscience

Impact Factor: 3,871

Eigenanteil an der Publikation: 20 %

Durchführung von Dichtegradientenzentrifugationen, SDS-PAGE und Silberfärbungen. Mitverfassen des Manuskripts.

ACS Chemical Neuroscience pubs.acs.org/acschemicalneuroscience Article

Oral Treatment with the D-Enantiomeric Peptide D3 Improves the Pathology and Behavior of Alzheimer's Disease Transgenic Mice

Susanne Aileen Funke,[†,⊗] Thomas van Groen,[‡,§,⊗] Inga Kadish,[‡,§] Dirk Bartnik,[∥] Luitgard Nagel-Steger,[∥] Oleksandr Brener,[∥] Torsten Sehl,[∥] Renu Batra-Safferling,[⊥] Christine Moriscot,[#,▽,○,♦] Guy Schoehn,[#,▽,○,♦] Anselm H. C. Horn,[¶] Andreas Müller-Schiffmann,[+] Carsten Korth,[+] Heinrich Sticht,[¶] and Dieter Willbold*[,†,∥,#]

[†]Forschungszentrum Jülich, ISB-3, 52425 Jülich, Germany, [‡]Department of Cell Biology, University of Alabama at Birmingham, Birmingham, Alabama 35294, [§]Department of Neurobiology, University of Alabama at Birmingham, Birmingham, Alabama 35294, [∥]Heinrich-Heine-Universität Düsseldorf, Institut für Physikalische Biologie and BMFZ, 40225 Düsseldorf, Germany, [⊥]Forschungszentrum Jülich, ISB-2, 52425 Jülich, Germany, [#]CEA, [▽]CNRS, and [○]Université Joseph Fourier, Institut de Biologie Structurale Jean-Pierre Ebel, UMR5075 Grenoble, France, [♦]Unit for Virus Host Cell Interactions, 6, rue Jules Horowitz BP 181, F38042 Grenoble, France, [¶]Friedrich-Alexander-Universität Erlangen-Nürnberg, Institut für Biochemie, 91054 Erlangen, Germany, and [+]Heinrich-Heine-Universität Düsseldorf, Institut für Neuropathologie, 40225 Düsseldorf, Germany

Abstract

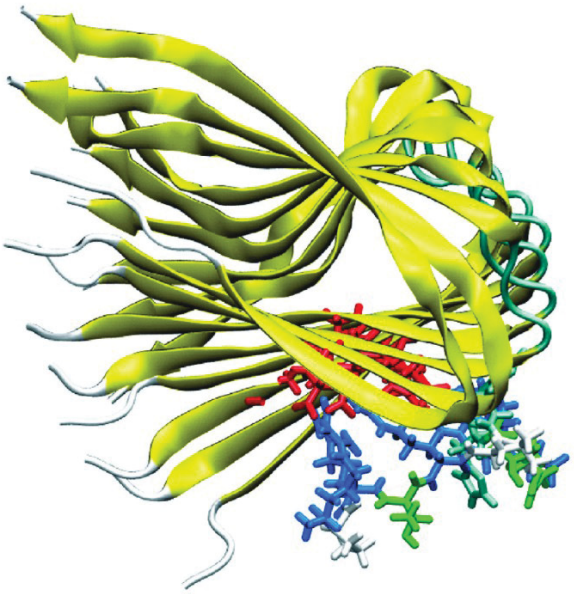

Several lines of evidence suggest that the amyloid-β-peptide (Aβ) plays a central role in the pathogenesis of Alzheimer's disease (AD). Not only Aβ fibrils but also small soluble Aβ oligomers in particular are suspected to be the major toxic species responsible for disease development and progression. The present study reports on in vitro and in vivo properties of the Aβ targeting D-enantiomeric amino acid peptide D3. We show that next to plaque load and inflammation reduction, oral application of the peptide improved the cognitive performance of AD transgenic mice. In addition, we provide in vitro data elucidating the potential mechanism underlying the observed in vivo activity of D3. These data suggest that D3 precipitates toxic Aβ species and converts them into nonamyloidogenic, nonfibrillar, and nontoxic aggregates without increasing the concentration of monomeric Aβ. Thus, D3 exerts an interesting and novel mechanism of action that abolishes toxic Aβ oligomers and thereby supports their decisive role in AD development and progression.

Keywords: Mirror image phage display, D-enantiomeric peptide, Alzheimer's disease, oligomers, drugs

Alzheimer's disease (AD) is a progressive neurodegenerative disorder, affecting more than 27 million people worldwide (*1*). Several lines of research have provided strong evidence of a central role played by amyloid-β-peptide (Aβ) in the pathogenesis of AD. Aβ is produced normally and throughout life as a 39−43 residue peptide from the amyloid precursor protein (APP) by two distinct proteolytic activities, called β- and γ-secretases (*2*−*4*). Histopathological hallmarks of AD are aggregated protein deposits (i.e., senile plaques and neurofibrillary tangles) in the brain. Senile plaques consist mainly of Aβ. According to the amyloid cascade hypothesis, fibrillar forms of Aβ have been thought to be responsible for neuronal dysfunction (*5*, *6*). More recent studies indicate that diffusable Aβ oligomers, including protofibrils, prefibrillar aggregates, and ADDLs, are the major toxic species during disease development and progression (*7*−*10*). Therefore, agents that interfere with early Aβ oligomerization are expected to be especially valuable for use in the therapy or prevention of AD. In turn, if such

Received Date: June 11, 2010
Accepted Date: July 21, 2010
Published on Web Date: August 02, 2010

DOI: 10.1021/cn100057j | ACS Chem. Neurosci. (2010), 1, 639–648

ACS Chemical Neuroscience pubs.acs.org/acschemicalneuroscience Article

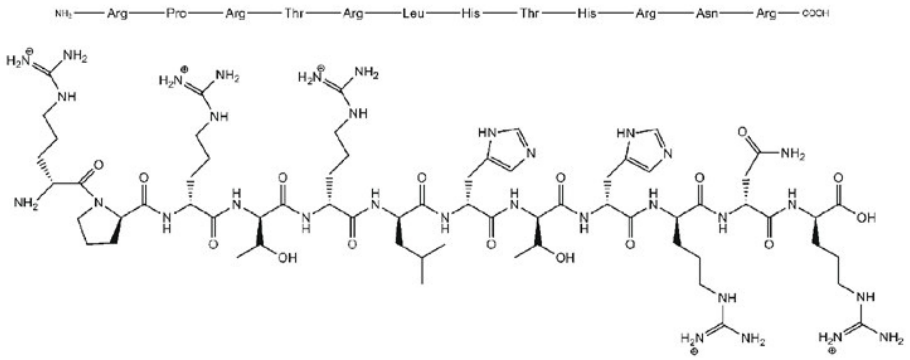

Figure 1. Lewis structure of the D-enantiomeric peptide D3.

agents prove to be effective in therapy or the prevention of AD, they would further strengthen the role of Aβ oligomers for disease development and progression.

So far, only palliative therapies for AD are available. Acetylcholine inhibitors such as Donepezil, Galantamine, and the NMDA receptor antagonist Memantine have been approved for clinical use in the treatment of cognitive symptoms (*11*, *12*). Approaches targeting Aβ include the reduction of Aβ production by inhibitors or modulators of the β- or γ-secretases, Aβ vaccination, and interference of Aβ aggregation by small molecules or peptides (*13*, *14*). A variety of such substances have already been described, e.g., Congo red (*15*), scyllo-Inositol (*16*, *17*), amino-propane sulfonic acid (*18*), Clioquinol (*19*, *20*), methylene blue (*21*), polyphenol (−)-epigallocatechin (EGCG) (*22*, *23*), and oligomeric acylated aminopyrazoles (*24*, *25*).

Small peptides that inhibit the aggregation of Aβ and reduce its toxic effects have also been identified and a fraction of them shown to be effective in AD transgenic mice (*26*−*29*). Recently, a β-sheet breaking D-enantiomeric dipeptide was reported to selectively target Aβ soluble oligomers. The compound was orally bioavailable, reduced the plaque load in AD transgenic mice, and improved their cognitive performance (*30*).

Earlier, we reported the identification of Aβ42 binding D-enantiomeric 12-mer peptides by mirror image phage display selections (*31*−*34*). Such D-peptides are known to be extremely protease resistant, thus being potentially well-suited for in vivo use (*35*, *36*). The D-peptide D3 (amino acid sequence RPRTRLHTHRNR, Figure 1) was identified during a mirror image phage display selection using D-enantiomeric Aβ42 as a target under conditions where monomeric or small oligomeric Aβ42 species can be expected to be the dominating species. In vitro, D3 inhibits the formation of regular Aβ fibrils and reduces Aβ42 cytotoxicty. In vivo, D3 reduces plaque load and cerebral inflammation of transgenic mouse models of AD upon direct application into the brain (*32*). The present study aims to investigate the effect of orally applied D3 on plaque load and on the cognitive behavior of AD transgenic mice. In addition, various in vitro experiments were carried out to elucidate the potential mechanism of D3 action.

Results and Discussion

The APP-PS mouse model expressing human APPswe and PS1-ΔE9 develops elevated levels of Aβ42 at the age of about four months, and at around 5 months of age, it shows typical Aβ plaques (*37*). Young, four-month old female mice were orally treated with D3 by adding D3 to the drinking water for eight weeks. Depending on the water uptake, the mice consumed between 0.5 and 1 mg/day D3. Another group of mice was unilaterally infused in the hippocampus for eight weeks using Alzet minipumps. The amount of D3 totally applied per mouse was 0.5 mg. As a control, the third group was implanted with empty Alzet minipumps. After 7 weeks of D3 treatment, all groups of mice were tested in the Morris water maze. The D3 treated mice showed a significant improvement of learning during the week of testing, but the untreated mice did not (Figure 2A). Interestingly, the orally treated mice performed better in the water maze than the brain infused ones, probably due to the higher amount of applied D3. After the completion of the behavioral testing, the animals were sacrificed and the brains assessed for AD pathology. In the sections that were stained for human Aβ(4−10) immunoreactivity, the total Aβ load in the hippocampus and frontal cortex was measured. Brain tissue sections of D3 treated mice had a significantly lower Aβ load as compared to that of the untreated mice (Figure 2B,C), very similar to those treated with D3 at the age of eight months via direct infusion into the brain (*32*). Analysis of brain sections stained for GFAP or microglia revealed that D3 treatment did not cause any significant inflammation or obvious pathology. A more detailed analysis of the magnitude of inflammation near Aβ deposits even revealed a significant reduction of plaque-related inflammation (measured in both GFAP and CD11b staining) in orally treated mice as compared to that in untreated and brain infused mice (Table 1).

DOI: 10.1021/cn100057j | ACS Chem. Neurosci. (2010), 1, 639–648

ACS Chemical Neuroscience pubs.acs.org/acschemicalneuroscience Article

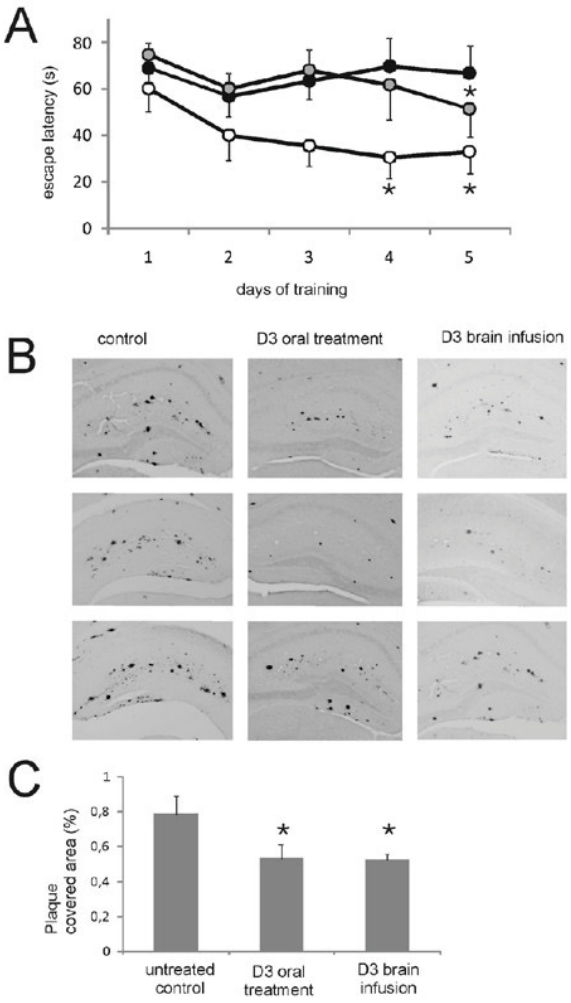

Figure 2. Results of the transgenic animal studies. (A) Time needed to find the hidden platform in the Morris water maze assay by the mice that were treated with D3 added to the drinking water (open circles), by direct brain infusion of D3 (gray filled circles), or not treated (black filled circles). For details see the Methods section. Error bars indicate standard deviations. (B) Photomicrographs of coronal sections of the hippocampus stained for Aβ (W0−2 antibody) from control mice (left column), orally D3 treated mice (middle column), and mice treated by brain infusion (right column). (C) Quantitative evaluation of Aβ plaque load. Bars indicate the Aβ plaque load (area covered by Aβ) in the dorsal hippocampus of D3 treated and untreated mice. * indicates significantly different, $p < 0.05$.

Because of the very different amounts of applied D3, the data of the orally treated mice (up to 1 mg/day) are difficult to compare with the data of the mice that were treated by direct infusion into the brain (9 μg/day). Therefore, the complete oral application assay was repeated, applying smaller amounts of D3. This time, D3 was not added to the drinking water. Instead, implanted Alzet minipumps delivered exact amounts (0.1 mg/day) of saline solved D3 directly into the stomach of the treated group of mice ($n = 8$). A control group ($n = 9$) was treated with saline. The applied amounts of D3 were 5- to 10-fold less than that in the drinking water assay. Nevertheless, the differences between treated and control groups concerning behavior and inflammation were significant (Supporting Information, Table S1 and Figure S1).

Currently, it is critically discussed, whether the reduction of Aβ fibrils in plaques at the cost of augmenting oligomer Aβ assemblies could be harmful. Therefore, it was important to elucidate the potential mechanism of D3 action. To do this, we performed various assays to investigate the effects of D3 on Aβ in vitro.

A method suitable to investigate the effect of D3 on the size distribution of Aβ particles is dynamic light scattering (DLS). Therefore, solutions containing 5 μM Aβ with and without D3 were assayed to estimate the size of Aβ particles and their development over time. In the absence of D3, the Aβ solution revealed a very dominating particle species with an averaged hydrodynamic radius (RH) of 30 nm over a time period of 10 min (Figure 3A), a result that is consistent with other studies (*38*). In the presence of D3, additional particles with sizes of 80 and 700 nm were observed after less than 10 min. This suggests that D3 induces the formation of huge Aβ particles. D3 alone as a control did not develop any detectable particles. D3 induced formation of large Aβ particles was confirmed by size exclusion chromatography (SEC) and turbidity assays (see Supporting Information, Figures S2 and S3).

Aβ species can be separated from each other according to their size using density gradient centrifugation on preformed gradients of iodixanol (*25*). To further investigate the effects of D3 on Aβ particle size, 125 μM Aβ42 samples with and without D3 (1:1) were analyzed by density gradient centrifugation runs. After centrifugation, 14 fractions of 140 μL each were harvested and analyzed for Aβ content by SDS−PAGE analysis and subsequent silver staining (Figure 3B). In the absence of D3, the Aβ42 species are broadly distributed over nearly all fractions, corresponding to all possible Aβ particle sizes with a maximum found in fractions 11 and 12 corresponding to fibrillar aggregates. Samples containing D3 had a drastically reduced Aβ content in fractions 4 to 11. Calibration with proteins of known s-values indicated that these fractions contained Aβ aggregates with s-values in the range of 6.5 to 18 S. Assuming a globular shape as a rough estimation, those species correspond to Aβ 16 to 200-mers. Obviously, the presence of D3 resulted in the loss of oligomers and increased Aβ contents in fractions corresponding to very high molecular weights (Figure 3B, fractions 12 and 14). The large-sized Aβ aggregates in samples containing D3 showed neither a positive ThT signal nor amyloid properties upon staining with Congo red, indicating the absence of regular fibrils.

DOI: 10.1021/cn100057j | ACS Chem. Neurosci. (2010), 1, 639–648

ACS Chemical Neuroscience pubs.acs.org/acschemicalneuroscience Article

Table 1. Summary of Important Quantities: Number of Animals Per Group, Body Weight, the Aβ Load, the Number of Congo Red Positive Plaques, and the Density of Staining for the GFAP and Microglia around Plaques in the Dorsal Hippocampus[a]

group	control	D3 brain infusion	D3 oral treatment
treatment	empty Alzet minipump	D3, brain infused by Alzet minipump	D3 added to drinking water
peptide amount [mg/day]		0.009	0.5−1.0
number	$n = 6$	$n = 6$	$n = 6$
body weight [g]	23.8 ± 0.6	23.4 ± 0.9	23.1 ± 0.6
swim speed [cm/s]	17.04 ± 0.88	16.12 ± 1.72	15.91 ± 1.21
probe trial [s in quadrant]	L 12.68 ± 2.40	L 17.47 ± 3.24	L 13.75 ± 1.84
	C 20.08 ± 2.69	C 20.70 ± 5.14	C 18.99 ± 2.25
	A 9.80 ± 1.79	A 10.13 ± 3.26	A 12.28 ± 2.06
	R 17.60 ± 2.04	R 11.87 ± 2.56	R 14.62 ± 1.77
Aβ plaque load [%]	0.78 ± 0.11	0.53 ± 0.04*	0.53 ± 0.08%*
Congo red	12.9 ± 2.5	11.8 ± 1.5	7.5 ± 2.0*
GFAP	98.6 ± 2.7	96.5 ± 3.1	86.4 ± 3.2*
microglia	136 ± 3.5	132 ± 3.8	112 ± 4.3*

[a] L, left; C, correct; A, across; R, right. * indicates significantly different, $p < 0.05$.

Indeed, electron microscopic (EM) analysis (Figure 4A,B) revealed Aβ typical fibrils (twisted ribbons) and spherical particles in the Aβ42 samples without D3 but huge amorphous structures without any ribbons or elongated fibrillar morphology in the D3 containing Aβ samples.

Recently, Aβ particles have been reported to have infectious properties. Minute amounts of material containing Aβ brought in direct contact with the CNS were shown to induce cerebral β-amyloidosis (*39*). The seeding capabilities of Aβ aggregates are discussed as important toxic and pathogenic properties. To investigate the in vitro seeding potential of D3-induced Aβ aggregates, we carried out seeding experiments (Figure 4C). Aβ only fibrils stimulated fibrillogenesis, whereas Aβ-D3 coaggregates did not, suggesting that Aβ-D3 coaggregates do not have a fibrillar or otherwise amyloidogenic structure. This is in accordance with the observation that Aβ-D3 coaggregates are negative for Congo red absorption and ThT fluorescence.

An additional insight into the mechanism of D3 action can be gleaned from computational studies of an Aβ-nonamer in the presence and absence of D3. The simulations, based on an experimentally determined Aβ structure (*40*), show that D3 is able to form strong interactions with negatively charged groups of Aβ. These interactions, which persist over the entire simulation time (Figure 5E,F), compensate the charge on the Aβ-surface and are therefore expected to reduce solubility and promote the aggregation of Aβ. This is consistent with the experimental observation of large nonfibrillar Aβ-aggregates in the presence of D3.

In addition, D3 binding also has an effect on the topology of the Aβ-oligomer itself. While the twist angle (Figure 5H) of the unliganded oligomer is approximately 5° between adjacent momomers (Figure 5C,D,G), D3 binding induces a twist of more than 12° (Figure 5E,F,G). In this context, it is interesting to note that the twist angle of 5° determined for the unbound oligomer is much larger than the value of 0.45° measured for Aβ42 fibrils (*40*). This observation suggests that Aβ-oligomers represent a much more suitable target for D3 binding than Aβ-fibrils for two reasons: (i) the initial twist of the oligomer is larger, which should facilitate D3 binding; and (ii) the conformational plasticity of the oligomer is higher, which allows it to tolerate the large twist induced by D3 binding. This large twist angle also locks the oligomers in a conformation, less suited to incorporation into fibrils, which are characterized by an extended conformation with a small twist angle. Therefore, also in silico, nonfibrillar aggregates are formed instead.

Our in vitro data clearly show that D3 precipitates toxic Aβ oligomers into large, high-molecular-weight, nontoxic, ThT negative, nonamyloidogenic amorphous aggregates that fail to act as seeds in Aβ fibril formation assays. It is important to stress the fact that in all assays, D3 did not increase the concentration of monomeric Aβ. Therefore, one possible mode of D3 action may be that the D3-induced conversion of Aβ species into amorphous Aβ-D3 aggregates adds an additional equilibrium to the complex network between the various Aβ species. D3 thereby shifts the equilibria among Aβ monomers, oligomers, and fibrils toward Aβ-D3 aggregates that are nonamyloidogenic and may be more amenable to degradation processes. Although D3 does not necessarily need to cross the blood−brain barrier (BBB) in order to do this, a cell culture model revealed D3 to cross the BBB significantly, indicating an adsorptive-mediated

DOI: 10.1021/cn100057j | ACS Chem. Neurosci. (2010), 1, 639-648

ACS Chemical Neuroscience pubs.acs.org/acschemicalneuroscience Article

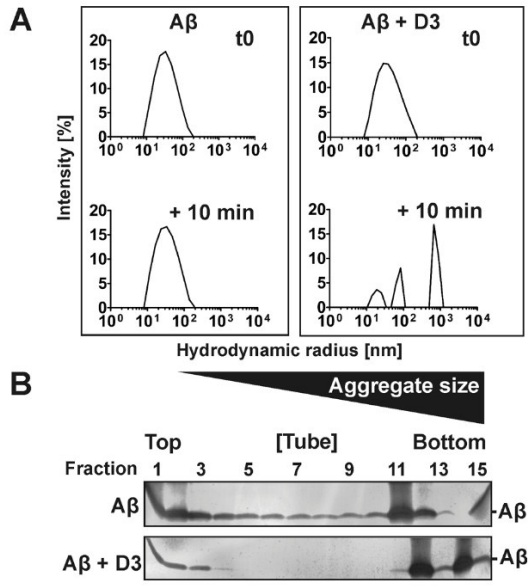

Figure 3. Aβ oligomer modulation by D3. (A) Particle size analysis by dynamic light scattering (DLS). Aβ and D3 as well as mixtures of both were prepared seedless in filtered sodium phosphate/NaCl buffer. DLS measurements were carried out at 20 °C, with a fixed angle (90°) and a cuvette path length of 3 mm. Data acquisition time was 1 s using a 655.6 nm (13 mW) laser. By using calculated autocorrelation functions, a regularization fit was performed in order to obtain size distribution profiles at $t = 0$ min (t0, upper row) and after 10 min (lower row). (B) Analysis of Aβ aggregation by density gradient ultracentrifugation. The size distributions of 125 μM Aβ42 and Aβ42-D3 mixtures (1:1) were determined by sedimentation analysis on a preformed gradient of iodixanol (Optiprep, AXIS-SHIELD, Oslo, Norway). One hundred microliters of aggregation assays containing 125 μM Aβ42 without or with 125 μM D3 was directly overlaid on a step gradient of 5−50% iodixanol. After centrifugation, 14 fractions from top to bottom of the centrifuge tube of 140 μL each were harvested. The 15th fraction represents the pellet. The fractions were analyzed by SDS−PAGE and silver staining.

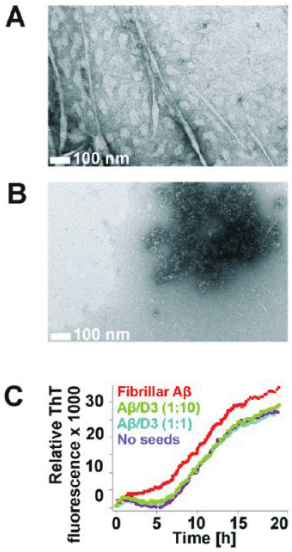

Figure 4. Analysis of amyloid properties of Aβ in the absence and presence of D3. (A and B) Electron micrographs of Aβ samples with and without D3. Twenty-five micromolar Aβ (A) and (1:4) Aβ-D3 (B) were negatively stained by uranyl acetate (1%) and measured as described in the Methods section. Scale bars: 100 nm. (C) Aβ fibril formation with and without seeds monitored by ThT fluorescence. Aβ only fibrils and Aβ-D3 coaggregates were prepared by incubating Aβ42 with and without different concentrations of D3 for 3 days at 37 °C. After washing, the precipitated seeds (20% v/v) were added to the aggregation reactions consisting of freshly prepared Aβ42 solutions. The relative ThT fluorescence of freshly prepared Aβ with fibrillar Aβ seeds (red), Aβ-D3 coaggregates (1:1, light blue), Aβ-D3 coaggregates (1:10, green), and freshly prepared Aβ as a control (purple) is shown as a function of time.

transcytosis mechanism (*41*), very similar to that reported for other arginin-rich proteins such as Tat (*42*).

In summary, we demonstrate that the mirror image phage display derived D-enantiomeric peptide D3 is able to reduce Aβ plaque load and enhance the cognitive state of transgenic AD mice even after oral application. D3 exerts an interesting and novel mechanism of action that abolishes toxic Aβ oligomers and thereby supports their decisive role in AD development and progression.

Methods

Peptides

D3 (RPRTRLHTHRNR, all amino acids are D-enantiomers) and Aβ(1−42) were purchased as reversed phase high performance liquid chromatography purified products (Jerini Biotools, Berlin, Germany).

Seedless Aβ Stock Solutions

Aβ was dissolved in hexafluoroisopropanol (HFIP) to 1 mM and incubated overnight at room temperature. Stock solutions were aliquoted and stored at −20 °C until required. Prior to use, HFIP was evaporated. HFIP pretreated Aβ pellets were incubated in 100 mM NaOH, diluted in seedless buffer (50 mM sodium phosphate buffer, containing 100 mM NaCl, pH 7.5), and the pH value adjusted by the addition of 100 mM HCl.

Thioflavin T (ThT) Assays

ThT assays were performed as described elsewhere (*32*) with minor modifications. Aβ aliquots and D3 were dissolved in PBS (140 mM NaCl, 2.7 mM KCl, 10 mM Na_2HPO_4, and 1.8 mM KH_2PO_4, pH 7.4) and added to a ThT solution (5 μM ThT, 50 mM Glycin, in NaOH−H_2O, pH 8.5). Samples were incubated at 37 °C.

Congo Red Spectral Shift Assay

The amyloidogenic properties of Aβ aggregates were determined by the Congo red spectral shift assay according to Klunk et al. (*43*, *44*). Aggregates were formed as described for density gradient centrifugation either with or without the addition of equimolar (125 μM) amounts of D3 and diluted into PBS buffer, pH 7.4, to a 0.06 mg/mL final concentration of Aβ. A freshly prepared stock solution of Congo red was added to the solution to yield a 10 μM concentration. After 20 min of incubation at ambient temperature, absorption spectra from 700 to 300 nm were recorded using a V-650 UV−vis spectrophotometer (Jasco, Germany). As controls, the spectra of Congo red, ligand, and Aβ alone were recorded.

DOI: 10.1021/cn100057j | ACS Chem. Neurosci. (2010), 1, 639–648

ACS Chemical Neuroscience pubs.acs.org/acschemicalneuroscience Article

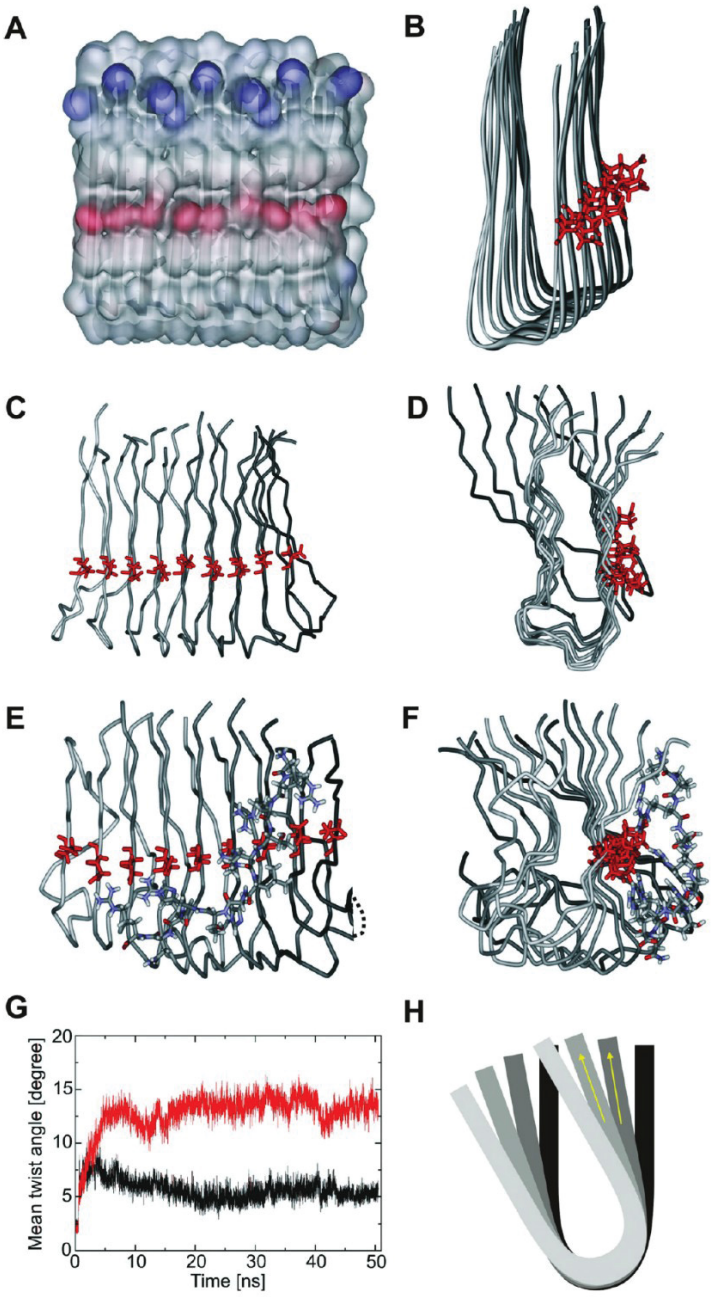

Figure 5. Computational analysis of the Aβ-D3 interaction. The initial structure of the Aβ(15−42) nonamer (A,B) and the structures of the unliganded nonamer (C,D) and the Aβ-D3 complex (E,F) after 50 ns of molecular dynamics simulations are shown as the top and side views, respectively. These two views differ by a rotation of approximately 90° around the vertical axis. The top layers of the oligomer are colored in light gray, and a color gradient is used for the lower layers of the oligomer. The electrostatic surface is shown for the initial structure in Figure 3A, in which the positive and negative surface charges originate from Lys16 and Glu22, respectively. Glu22 is shown as red sticks in panels B to F. D3 is shown in stick representation (colored according to the atom types) in panels E and F. A dotted line represents a disordered region of the terminal Aβ-chain. (G) Changes of the twist angle over the simulation time for the unliganded and D3-bound Aβ-oligomer. (H) Schematic presentation of a twisted Aβ-oligomer. The yellow arrows represents the vector between the Cα-carbons of Val18 and Val24. The angle between two vectors of adjacent chains was used to calculate the twist angle as described in the Methods section. Note the significantly enhanced twist angle in the D3-bound form (F) compared to the starting structure (B), which reflects the properties of the fibril.

DOI: 10.1021/cn100057j | ACS Chem. Neurosci. (2010), 1, 639–648

ACS Chemical Neuroscience pubs.acs.org/acschemicalneuroscience Article

The absorption spectrum of the Aβ in the absence of the dye was used to subtract the scattering contribution of the aggregates from the spectrum of the dye in their presence.

Density Gradient Centrifugation

Density gradient centrifugation was performed according to Rzepecki et al (*25*). Preformed gradients of optiprep (Axis-Shield, Oslo, Norway) of about 2 mL volume were overlaid with 100 μL sample volumes, containing either 125 μM Aβ42 alone or an equimolar mixture of Aβ42 and D3. After centrifugation at 260,000*g* for 3 h at 4 °C in a TL100 ultracentrifuge (Beckman-Coulter, Palo Alto, USA) with aTLS-55 rotor, 14 fractions of 140 μL each were harvested from top to bottom. These fractions and the pellet of each tube were subsequently analyzed with respect to their Aβ42 content by denaturing, discontinuous Tris-Tricine-SDS−PAGE optimized for the separation of small peptides or proteins. Mark12 (Invitrogen, Germany) with molecular weights between 2500 and 200,000 Da was used as a size standard. The protein content was visualized by silver staining.

Dynamic Light Scattering

Seedless Aβ as well as D3 were prepared in a seedless buffer. The buffer was filtered (0.22 μm pore size) prior to use. DLS measurements were carried out with a DynaPro DLS system (Protein Solutions, Lakewood, NJ, USA) at 20 °C, fixed angle (90°), and a cuvette path length of 3 mm. Data acquisition time was 1 s using a 655.6 nm (13 mW) laser. Analysis and averaging of the collected data was performed with the software Dynamic V6 (Protein Solutions). By using calculated autocorrelation functions, a regularization fit was performed in order to obtain the size distribution profile. The data were plotted using GraphPad Prism 5.01.

Electron microscopy

Peptide aggregates were adsorbed on Formvar/carbon coated copper grids (Plano GmbH, Wetzlar), washed, and negatively stained with 1% uranyl acetate (pH 4.0). The grids were observed using a LaB6 CM12 EM (FEI/Philips), operating at 120 kV with a nominal magnification of 40,000×. Images were taken using an Orius 832 SC1000 CCD camera (4008 × 2672 pixels) (Gatan inc.).

Seeding Assays

The assays were performed as already described (*23*) with minor modifications. As Aβ only seeds, lyophilized Aβ was predissolved in DMSO, diluted in PBS (phosphate buffered saline: 140 mM NaCl, 2.7 mM KCl, 10 mM Na_2HPO_4, and 1.8 mM KH_2PO_4, pH 7.4), and incubated (37 °C, 3 d). Aβ-D3-seeds were incubated in the presence of different amounts of D3. After incubation, the respective seeds were washed by centrifugation and redissolved in PBS. In the fresh samples without seeds, Aβ was also predissolved in DMSO. All samples were diluted in PBS to a concentration of 10 μM Aβ containing 100 μM ThT. Mixtures of 80% (v/v) freshly prepared Aβ and 20% (v/v) seeds or control samples were made. The measurements of seed containing samples were corrected by subtracting the ThT signal (fluorescence values) obtained for 20% (v/v) seeds.

Computational Studies

A stack of nine Aβ(15−42)-monomers was generated on the basis of the experimental structural information about the geometry of Aβ42 in the fibrillar state (PDB code 2BEG) (*40*). This nonamer served as a model system for Aβ-oligomers in all subsequent computational studies. A candidate binding site of D3 was determined by inspecting the electrostatic potential of Aβ(15−42). The surface patch with the highest excess of negative charge is formed by the E22 side chains of adjacent Aβ subunits (Figure 5A). The positively charged side chains of D3 were therefore placed in spatial proximity of the E22 ladder. A 50 ns molecular dynamics (MD) simulation was performed to verify, whether this mode of interaction results in a stable complex. In addition, a control MD simulation was performed for the uncomplexed Aβ-nonamer. All simulations and data analysis were performed using standard protocols as described previously (*45*). The calculation of the twist angle followed the work of Zheng et al (*46*). For the calculation of the twist angle, vectors between Cα atoms of Val18 and Val24 were defined. The angle between vector pairs for consecutive Aβ-chains (omitting the first and last chain to account for boundary effects) was computed for all structures obtained from the MD simulation.

Animals

APP and PS1 double transgenic mice (APPswe/PS1ΔE9 mice (*37*), $n = 12/17$) were used in the present study. The mice were acquired from JAX at the age of six weeks, and until the treatments, the animals were housed 4/cage in our facility, in a controlled environment (temperature 22 °C, humidity 50−60%, and light from 07:00−19:00); food and water were available ad libitum. The experiments were conducted in accordance with the local Institutional Animal Care and Use Committee (IACUC) guidelines.

D3 Oral Treatment

The group (6 animals) of four-month old mice was treated for eight weeks with D3 via their drinking water. The peptide concentration was 1 mg/mL. On average, the mice drank ca. 0.5 to 1 mL water per day. The stability of D3 in water containing mouse spit was verified using reversed phase HPLC analysis. Seven weeks after the start of the treatment, the animals were tested in the water maze, and eight weeks after the start of treatment, the animals were sacrificed for histopathological analysis (see below).

Brain Infusion

In parallel to the orally treated mice, 6 mice were treated with D3 via brain infusion. The applied D-peptide amount was 0.5 mg/pump. The Alzet minipump (model #2004; delivery rate: 0.25 μL/h; duration 8 weeks) was soaked in sterile saline for 24 h, and the next day the pump, the connecting tube and cannula (Alzet Brain Infusion Kit 3; Alzet) were filled with the appropriate solution, and they were connected such that no air bubbles were present. Then the cannulae were implanted in the brain (right dorsal hippocampus); in short, mice were anesthetized, placed in a stereotaxic frame, a hole was drilled above the right dorsal hippocampus, and the cannula was lowered into the hippocampus. The implantation of the cannula was in the dorsal hippocampus in all animals. The implantation of the Alzet minipumps did not change any obvious physiological parameters (e.g., growth as measured by body weight or general health) in the implanted mice or cause any noticeable discomfort, and none of the animals lost the brain cannula or developed any other problems. Seven weeks after start of the infusion period, the mice were behaviorally tested in the Morris water maze for one week. During this week, the

DOI: 10.1021/cn100057j | ACS Chem. Neurosci. (2010), 1, 639–648

ACS Chemical Neuroscience pubs.acs.org/acschemicalneuroscience Article

treatment was continued. Subsequently, the animals were sacrificed for histopathological analysis (see below).

Behavior

The animals were tested for one week in an open field water maze (*47*). Our version of the maze consisted of a blue circular tank of clear water (23 ± 1 °C). The mice were placed in the water at the edge of the pool and allowed to swim in order to locate a hidden, but fixed escape platform, using extra-maze cues. On Day 1, the mice were placed in the pool and allowed to swim freely for 90 s to find the hidden platform. If the animal did not locate the platform during that time, it was placed upon it by the experimenter and left there for 10 s. Each animal was tested in four trials per day. The intertrial interval was 60 s. There was no significant difference in the swimming speed between the groups of mice.

Each start position was used equally in a pseudorandom order, and the animals always placed in the water facing the wall. The platform was placed in the middle of one of the quadrants of the pool (i.e., northwest, southwest, northeast, or southeast; approximately 30 cm from the side of the pool). The mouse's task throughout the experiment was to find and escape onto the platform. Once the mouse had learned the task (Day 5, Trial 20), a probe trial was given immediately following the last trial of acquisition on Day 5. In the probe trial (i.e., Trial 21), the platform was removed from the pool and animals allowed to swim for 60 s.

Data were analyzed by Student's paired *t* test (treated versus nontreated) and by ANOVA (Systat 11; between groups), and posthoc tests (Tukey and Scheffe) were carried out to determine the source of a significant main effect or interaction.

Histopathology

In short, the mice were anesthetized, transcardially perfused, and their brains removed. Following postfixation and cryoprotection, six series (1 in 6) of coronal sections were cut through the brain. The first series of sections was mounted unstained, the second, third, and fourth series were stained immunohistochemically according to published protocols (*48*), and the other two series were stored at −20 °C in antifreeze for future analysis. One half of the second series was stained for human Aβ using the W0−2 antibody (mouse antihuman Aβ4−9 (*49*)), and the other half of the second series was stained for mouse Aβ (rabbit antirodent Aβ, Covance (*48*)). The first half of the third series was immunohistochemically stained for Aβ40 (mouse anti-Aβ40, Covance) and the other half for Aβ42 (mouse anti-Aβ42, Covance). One half of the fourth series was stained for GFAP (mouse anti-GFAP; Sigma), whereas the other half was stained for CD11b (rat antimouse CD11b; Serotec), a marker of microglia. Some of these stained sections were double stained with Congo red, thioflavine S, or thiazine red. The sections destined for Aβ staining were pretreated for 30 min with hot (85 °C) citrate buffer. The series of sections were transferred to a solution containing the primary antibody; this solution consists of TBS with 0.5% Triton X-100 added (TBS-T) (*50*). Following incubation in this solution for 18 h on a shaker table at room temperature (20 °C) in the dark, the sections were rinsed three times in TBS-T and transferred to the solution containing the secondary antibody (goat antimouse·biotin; Sigma or sheep antirat Ig·biotin, Serotec). After 2 h, the sections were rinsed three times with TBS-T and transferred to a solution containing mouse ExtrAvidin (Sigma). Following rinsing, the sections were incubated for approximately 3 min with Ni-enhanced DAB (*50*). In a small number of sections, the Aβ deposits were double labeled for Aβ40, Aβ42, GFAP, or CD11b using fluorescent secondary antibodies. All stained sections were mounted on slides and coverslipped.

Quantification

The appropriate areas (dorsal hippocampus and frontal cortex) of the brains were digitized using an Olympus DP70 digital camera, and the images were converted to gray scale using the Paint Shop Pro 7 program (*50*). To avoid changes in lighting, which might affect measurements, all images were acquired in one session. Furthermore, to avoid differences in staining density between sections, the measurements were performed on sections that were stained simultaneously, i.e., in the same staining tray (n = 24). The percentage of area covered by the reaction product to Aβ was measured (*48*) in the ipsi- and contralateral hippocampus and ipsi- and contralateral frontal cortex using the ScionImage (NIH) program (*50*). Employing a similar procedure, using digital images to overlay the defined measurement area, plaques were counted in the same brain area on the adjacent sections that were stained with Congo red. The density of GFAP or CD11b staining was measured by placing a standard sized circle (200 μm diameter) around the plaque core (stained with Congo red) and measuring the optical density of the staining in the circle using the ScionImage (NIH) program. All density measurements were done in triplicate, i.e., measuring the standardized area around three plaques at three different levels of the dorsal hippocampus and the frontal, midline cortex. These measurements were done blind in sections stained by an observer with no knowledge of the treatment of the animal (*50*). Data were analyzed by Student's paired *t* test (ipsi- versus contralateral) and by ANOVA (Systat 11; between groups), and posthoc tests (Tukey and Scheffe) were carried out to determine the source of a significant main effect or interaction.

Supporting Information Available

Details of the stomach infusion experiments, SEC, dot blot analysis, ThT assays, turbidity assays, results of the transgenic animal studies in the Morris water maze assay, summary of important quantities, SEC analysis of 100 μM Aβ without and with FITC-labelled D3, and inhibition of ThT positive Aβ fibril formation. This information is available free of charge via the Internet at http://pubs.acs.org.

Author Information

Corresponding Author

* To whom correspondence should be addressed. ISB-3, Forschungszentrum Jülich, Wilhelm-Johnen Str., 52426 Jülich, Germany. Tel: +49 2461 61 2100. Fax: +49 2461 61 2233. E-mail: d.willbold@fz-juelich.de.

Author Contributions

⊗ These authors contributed equally to this work.

S.A.F. and D.W. did the overal strategic planning and design of the study. S.A.F, D.B., L.N.-S., C.K., T.vG., and I.K.

DOI: 10.1021/cn1000571 | ACS Chem. Neurosci. (2010), 1, 639–648

planned the details of the studies. S.A.F. and D.W. have written major parts of the manuscript. D.B., O.B. L.N.-S., T.S., G.S., C.K., A.M.-S., C.M., and R.B.-S. have designed and performed the in vitro studies. I.K. and T.vG. have designed and performed the in vivo studies. The molecular dynamics simulations were designed and done by A.H. and H.S. All authors have contributed to the manuscript text.

Funding Sources

This work has been supported by a grant from Volkswagen-Stiftung to D.W., C.K., and H.S. (I/82 649). Support from the "Präsidentenfond der Helmholtzgemeinschaft" (HGF, "Virtual Institute of Structural Biology") to D.W. is acknowledged. C.M. was supported by a DGCIS grant (French state). The electron microscopy facility used for this work is part of the Partnership for Structural Biology (PSB). Part of this research was supported by P30 NS47466. I.K. and T.v.G have been supported by 5P50 AG16582-10.

References

1. Brookmeyer, R., Johnson, E., Ziegler-Graham, K., and Arrighi, H. M. (2007) Forecasting the global burden of Alzheimer's disease. *Alzheimer's Dementia 3*, 186–191.

2. Haass, C., and Selkoe, D. J. (1993) Cellular processing of beta-amyloid precursor protein and the genesis of amyloid beta-peptide. *Cell 75*, 1039–1042.

3. Kang, J., Lemaire, H. G., Unterbeck, A., Salbaum, J. M., Masters, C. L., Grzeschik, K. H., Multhaup, G., Beyreuther, K., and Muller-Hill, B. (1987) The precursor of Alzheimer's disease amyloid A4 protein resembles a cell-surface receptor. *Nature 325*, 733–736.

4. Weidemann, A., Konig, G., Bunke, D., Fischer, P., Salbaum, J. M., Masters, C. L., and Beyreuther, K. (1989) Identification, biogenesis, and localization of precursors of Alzheimer's disease A4 amyloid protein. *Cell 57*, 115–126.

5. Hardy, J. A., and Higgins, G. A. (1992) Alzheimer's disease: the amyloid cascade hypothesis. *Science 256*, 184–185.

6. Selkoe, D. J. (1991) The molecular pathology of Alzheimer's disease. *Neuron 6*, 487–498.

7. Haass, C., and Selkoe, D. J. (2007) Soluble protein oligomers in neurodegeneration: lessons from the Alzheimer's amyloid beta-peptide. *Nat. Rev. Mol. Cell Biol. 8*, 101–112.

8. Lambert, M. P., Barlow, A. K., Chromy, B. A., Edwards, C., Freed, R., Liosatos, M., Morgan, T. E., Rozovsky, I., Trommer, B., Viola, K. L., Wals, P., Zhang, C., Finch, C. E., Krafft, G. A., and Klein, W. L. (1998) Diffusible, nonfibrillar ligands derived from Abeta1−42 are potent central nervous system neurotoxins. *Proc. Natl. Acad. Sci. U.S.A. 95*, 6448–6453.

9. Shankar, G. M., Bloodgood, B. L., Townsend, M., Walsh, D. M., Selkoe, D. J., and Sabatini, B. L. (2007) Natural oligomers of the Alzheimer amyloid-beta protein induce reversible synapse loss by modulating an NMDA-type glutamate receptor-dependent signaling pathway. *J. Neurosci. 27*, 2866–2875.

10. Walsh, D. M., and Selkoe, D. J. (2007) A beta oligomers: a decade of discovery. *J. Neurochem. 101*, 1172–1184.

11. Blennow, K., de Leon, M. J., and Zetterberg, H. (2006) Alzheimer's disease. *Lancet 368*, 387–403.

12. Roberson, E. D., and Mucke, L. (2006) 100 years and counting: prospects for defeating Alzheimer's disease. *Science 314*, 781–784.

13. Jakob-Roetne, R., and Jacobsen, H. (2009) Alzheimer's disease: from pathology to therapeutic approaches. *Angew. Chem., Int. Ed. 48*, 3030–3059.

14. Nerelius, C., Johansson, J., and Sandegren, A. (2009) Amyloid beta-peptide aggregation. What does it result in and how can it be prevented? *Front. Biosci. 14*, 1716–1729.

15. Podlisny, M. B., Walsh, D. M., Amarante, P., Ostaszewski, B. L., Stimson, E. R., Maggio, J. E., Teplow, D. B., and Selkoe, D. J. (1998) Oligomerization of endogenous and synthetic amyloid beta-protein at nanomolar levels in cell culture and stabilization of monomer by Congo red. *Biochemistry 37*, 3602–3611.

16. McLaurin, J., Golomb, R., Jurewicz, A., Antel, J. P., and Fraser, P. E. (2000) Inositol stereoisomers stabilize an oligomeric aggregate of Alzheimer amyloid beta peptide and inhibit abeta -induced toxicity. *J. Biol. Chem. 275*, 18495–18502.

17. Townsend, M., Cleary, J. P., Mehta, T., Hofmeister, J., Lesne, S., O'Hare, E., Walsh, D. M., and Selkoe, D. J. (2006) Orally available compound prevents deficits in memory caused by the Alzheimer amyloid-beta oligomers. *Ann. Neurol. 60*, 668–676.

18. Gervais, F., Paquette, J., Morissette, C., Krzywkowski, P., Yu, M., Azzi, M., Lacombe, D., Kong, X., Aman, A., Laurin, J., Szarek, W. A., and Tremblay, P. (2007) Targeting soluble Abeta peptide with Tramiprosate for the treatment of brain amyloidosis. *Neurobiol. Aging 28*, 537–547.

19. Cherny, R. A., Atwood, C. S., Xilinas, M. E., Gray, D. N., Jones, W. D., McLean, C. A., Barnham, K. J., Volitakis, I., Fraser, F. W., Kim, Y., Huang, X., Goldstein, L. E., Moir, R. D., Lim, J. T., Beyreuther, K., Zheng, H., Tanzi, R. E., Masters, C. L., and Bush, A. I. (2001) Treatment with a copper-zinc chelator markedly and rapidly inhibits beta-amyloid accumulation in Alzheimer's disease transgenic mice. *Neuron 30*, 665–676.

20. Price, K. A., Crouch, P. J., and White, A. R. (2007) Therapeutic treatment of Alzheimer's disease using metal complexing agents. *Recent Pat. CNS Drug Discovery 2*, 180–187.

21. Necula, M., Breydo, L., Milton, S., Kayed, R., van der Veer, W. E., Tone, P., and Glabe, C. G. (2007) Methylene blue inhibits amyloid Abeta oligomerization by promoting fibrillization. *Biochemistry 46*, 8850–8860.

22. Bieschke, J., Russ, J., Friedrich, R. P., Ehrnhoefer, D. E., Wobst, H., Neugebauer, K., Wanker, E. E. EGCG remodels mature {alpha}-synuclein and amyloid-{beta} fibrils and reduces cellular toxicity, *Proc. Natl. Acad. Sci. U.S.A.*

23. Ehrnhoefer, D. E., Bieschke, J., Boeddrich, A., Herbst, M., Masino, L., Lurz, R., Engemann, S., Pastore, A., and Wanker, E. E. (2008) EGCG redirects amyloidogenic polypeptides into unstructured, off-pathway oligomers. *Nat. Struct. Mol. Biol. 15*, 558–566.

24. Nagel-Steger, L., Demeler, B., Meyer-Zaika, W., Hochdorffer, K., Schrader, T., and Willbold, D. (2010) Modulation of aggregate size- and shape-distributions of

DOI: 10.1021/cn100057j | *ACS Chem. Neurosci.* (2010), *1*, 639–648

the amyloid-beta peptide by a designed beta-sheet breaker. *Eur. Biophys. J. 39*, 15–22.

25. Rzepecki, P., Nagel-Steger, L., Feuerstein, S., Linne, U., Molt, O., Zadmard, R., Aschermann, K., Wehner, M., Schrader, T., and Riesner, D. (2004) Prevention of Alzheimer's disease-associated Abeta aggregation by rationally designed nonpeptidic beta-sheet ligands. *J. Biol. Chem. 279*, 47497–47505.

26. Juhasz, G., Marki, A., Vass, G., Fulop, L., Budai, D., Penke, B., Falkay, G., and Szegedi, V. (2009) An intraperitoneally administered pentapeptide protects against Abeta (1−42) induced neuronal excitation in vivo. *J. Alzheimer's Dis. 16*, 189–196.

27. Poduslo, J. F., Curran, G. L., Kumar, A., Frangione, B., and Soto, C. (1999) Beta-sheet breaker peptide inhibitor of Alzheimer's amyloidogenesis with increased blood-brain barrier permeability and resistance to proteolytic degradation in plasma. *J. Neurobiol. 39*, 371–382.

28. Soto, C., Sigurdsson, E. M., Morelli, L., Kumar, R. A., Castano, E. M., and Frangione, B. (1998) Beta-sheet breaker peptides inhibit fibrillogenesis in a rat brain model of amyloidosis: implications for Alzheimer's therapy. *Nat. Med. 4*, 822–826.

29. Tjernberg, L. O., Naslund, J., Lindqvist, F., Johansson, J., Karlstrom, A. R., Thyberg, J., Terenius, L., and Nordstedt, C. (1996) Arrest of beta-amyloid fibril formation by a pentapeptide ligand. *J. Biol. Chem. 271*, 8545–8548.

30. Frydman-Marom, A., Rechter, M., Shefler, I., Bram, Y., Shalev, D. E., and Gazit, E. (2009) Cognitive-performance recovery of Alzheimer's disease model mice by modulation of early soluble amyloidal assemblies. *Angew. Chem., Int. Ed. 48*, 1981–1986.

31. van Groen, T., Kadish, I., Wiesehan, K., Funke, S. A., and Willbold, D. (2009) In vitro and in vivo staining characteristics of small, fluorescent, Abeta42-binding D-enantiomeric peptides in transgenic AD mouse models. *ChemMedChem 4*, 276–282.

32. van Groen, T., Wiesehan, K., Funke, S. A., Kadish, I., Nagel-Steger, L., and Willbold, D. (2008) Reduction of Alzheimer's disease amyloid plaque load in transgenic mice by D3, a D-enantiomeric peptide identified by mirror image phage display. *ChemMedChem 3*, 1848–1852.

33. Wiesehan, K., Buder, K., Linke, R. P., Patt, S., Stoldt, M., Unger, E., Schmitt, B., Bucci, E., and Willbold, D. (2003) Selection of D-amino-acid peptides that bind to Alzheimer's disease amyloid peptide abeta1−42 by mirror image phage display. *ChemBioChem 4*, 748–753.

34. Wiesehan, K., Stohr, J., Nagel-Steger, L., van Groen, T., Riesner, D., and Willbold, D. (2008) Inhibition of cytotoxicity and amyloid fibril formation by a D-amino acid peptide that specifically binds to Alzheimer's disease amyloid peptide. *Protein Eng., Des. Sel. 21*, 241–246.

35. Schumacher, T. N., Mayr, L. M., Minor, D. L. Jr., Milhollen, M. A., Burgess, M. W., and Kim, P. S. (1996) Identification of D-peptide ligands through mirror-image phage display. *Science 271*, 1854–1857.

36. Van Regenmortel, M. H., and Muller, S. (1998) D-peptides as immunogens and diagnostic reagents. *Curr. Opin. Biotechnol. 9*, 377–382.

37. Jankowsky, J. L., Slunt, H. H., Ratovitski, T., Jenkins, N. A., Copeland, N. G., and Borchelt, D. R. (2001) Co-expression of multiple transgenes in mouse CNS: a comparison of strategies. *Biomol. Eng. 17*, 157–165.

38. Lafaye, P., Achour, I., England, P., Duyckaerts, C., and Rougeon, F. (2009) Single-domain antibodies recognize selectively small oligomeric forms of amyloid beta, prevent Abeta-induced neurotoxicity and inhibit fibril formation. *Mol. Immunol. 46*, 695–704.

39. Eisele, Y. S., Bolmont, T., Heikenwalder, M., Langer, F., Jacobson, L. H., Yan, Z. X., Roth, K., Aguzzi, A., Staufenbiel, M., Walker, L. C., and Jucker, M. (2009) Induction of cerebral beta-amyloidosis: intracerebral versus systemic Abeta inoculation. *Proc. Natl. Acad. Sci. U.S.A. 106*, 12926–12931.

40. Luhrs, T., Ritter, C., Adrian, M., Riek-Loher, D., Bohrmann, B., Dobeli, H., Schubert, D., and Riek, R. (2005) 3D structure of Alzheimer's amyloid-beta(1−42) fibrils. *Proc. Natl. Acad. Sci. U.S.A. 102*, 17342–17347.

41. Liu, H., Funke, S. A., Willbold, D. (2010) Transport of alzheimer disease amyloid-beta-binding d-amino acid peptides across an in vitro blood-brain barrier model, *Rejuvenation Res. 13*, 210−213.

42. Rapoport, M., and Lorberboum-Galski, H. (2010) TAT-based drug delivery system: new directions in protein delivery for new hopes? *Expert Opin. Drug Delivery 6*, 453–463.

43. Klunk, W. E., Jacob, R. F., and Mason, R. P. (1999) Quantifying amyloid by congo red spectral shift assay. *Methods Enzymol. 309*, 285–305.

44. Klunk, W. E., Jacob, R. F., and Mason, R. P. (1999) Quantifying amyloid beta-peptide (Abeta) aggregation using the Congo red-Abeta (CR-abeta) spectrophotometric assay. *Anal. Biochem. 266*, 66–76.

45. Kassler, K., Horn, A. H., Sticht, H. (2010) Effect of pathogenic mutations on the structure and dynamics of Alzheimer's Abeta(42)-amyloid oligomers, *J. Mol. Model. 16*, 1011−1020.

46. Zheng, J., Jang, H., Ma, B., Tsai, C. J., and Nussinov, R. (2007) Modeling the Alzheimer Abeta17−42 fibril architecture: tight intermolecular sheet-sheet association and intramolecular hydrated cavities. *Biophys. J. 93*, 3046–3057.

47. Handattu, S. P., Garber, D. W., Monroe, C. E., van Groen, T., Kadish, I., Nayyar, G., Cao, D., Palgunachari, M. N., Li, L., and Anantharamaiah, G. M. (2009) Oral apolipoprotein A-I mimetic peptide improves cognitive function and reduces amyloid burden in a mouse model of Alzheimer's disease. *Neurobiol. Dis. 34*, 525–534.

48. van Groen, T., Kiliaan, A. J., and Kadish, I. (2006) Deposition of mouse amyloid beta in human APP/PS1 double and single AD model transgenic mice. *Neurobiol. Dis. 23*, 653–662.

49. Ida, N., Hartmann, T., Pantel, J., Schroder, J., Zerfass, R., Forstl, H., Sandbrink, R., Masters, C. L., and Beyreuther, K. (1996) Analysis of heterogeneous A4 peptides in human cerebrospinal fluid and blood by a newly developed sensitive Western blot assay. *J. Biol. Chem. 271*, 22908–22914.

50. Kadish, I., Pradier, L., and van Groen, T. (2002) Transgenic mice expressing the human presenilin 1 gene demonstrate enhanced hippocampal reorganization following entorhinal cortex lesions. *Brain Res. Bull. 57*, 587–594.

DOI: 10.1021/cn100057j | *ACS Chem. Neurosci.* (2010), *1*, 639–648

Supporting Information

Oral Treatment with the D-Enantiomeric Peptide D3 Improves the Pathology and Behavior of Alzheimer's Disease Transgenic Mice

Susanne Aileen Funke[1,*], Thomas van Groen[2,3,*], Inga Kadish[2], Dirk Bartnik[1,4], Luitgard Nagel-Steger[4], Oleksandr Brener[4], Torsten Sehl[1,4], Renu Batra-Safferling[5], Christine Moriscot[6,7,8,9], Guy Schoehn[6,7,8,9,] Anselm H.C. Horn[10], Andreas Müller-Schiffmann[11], Carsten Korth[11], Heinrich Sticht[10], Dieter Willbold[1,4,6,]

[1]Forschungszentrum Jülich, ISB-3, 52425 Jülich, Germany; [2]Department of Cell Biology, University of Alabama at Birmingham, and [3]Department of Neurobiology, University of Alabama at Birmingham, Birmingham, AL 35294, USA; [4]Heinrich-Heine-Universität Düsseldorf, Institut für Physikalische Biologie and BMFZ, 40225 Düsseldorf, Germany; [5]Forschungszentrum Jülich, ISB-2, 52425 Jülich, Germany; [6]CEA, [7]CNRS, and [8]Université Joseph Fourier, Institut de Biologie Structurale Jean-Pierre Ebel, UMR5075 Grenoble, France; [9]Unit for Virus Host Cell Interactions, 6, rue Jules Horowitz BP 181, F38042 Grenoble, France; [10] Friedrich-Alexander-Universität Erlangen-Nürnberg, Institut für Biochemie, 91054 Erlangen, Germany; [11]Heinrich-Heine-Universität Düsseldorf, Institut für Neuropathologie, 40225 Düsseldorf, Germany.

[*] both authors contributed equally to the paper.

Correspondence to:

Dieter Willbold; ISB-3, Forschungszentrum Jülich; Wilhelm-Johnen Str., 52426 Jülich, Germany; Tel: +49 2461 61 2100; Fax: +49 2461 61 2233; email: d.willbold@fz-juelich.de

Materials and Methods

Stomach infusion

For the stomach infusion experiments, four month old APPswe/PS1ΔE9 mice had an Alzet minipump 1004 implanted under the skin with tubing inserted into stomach. Thus, it was possible to treat the mice with exact amounts of D3 (0.1 mg/day, n=8). The control group (n=9) was treated with saline. Seven weeks after treatment start, the mice were behaviorally tested in the Morris water maze for one week. Subsequently, the animals were sacrificed for histopathological analysis (see methods in the main manuscript).

Size exclusion chromatography (SEC)

For SEC analysis, a Superdex 75 PC3.2/30 column (GE Healthcare) was run with an Äkta Purifier (GE Healthcare) using a protocol as already described (1). Prior to SEC analysis, all samples (250 uM Aβ, Aβ-D3 (1:10) were briefly centrifuged (30 s, at 16.000 x g), and 10 µl of the supernatants were subjected to the SEC runs. SEC was followed by detecting the absorption at 214 nm. Fractions were collected, pooled and precipitated by TCA. The pellets were analyzed for their Aβ content by dot blot analysis.

Dot blot analysis

TCA precipitated pellets were dissolved in a small volume PBS and spotted on a cellulosenitrate membrane (Schleicher & Schluell). After blocking (2 h 10 % Western Blocking reagent, Roche), the membrane was incubated with anti-Aß antibody (6E10, Calbiochem) and anti-mouse horseradishperoxidase (HRP) conjugate (ImmunoPure Antibody, Thermo Scientific). Washing steps were performed using TBS, pH 7.4 (50 mM Tris/HCl, 150 mM NaCl), supplemented with 0.6 % (v/v) Tween 20. HRP activity was detected using a chemiluminescent substrate (SuperSignal West Pico, Pierce).

2

Thioflavin T (ThT) assays

ThT assays were performed as described elsewhere (2) with minor modifications. Aβ aliquots and D3 were dissolved in PBS (140 mM NaCl, 2.7 mM KCl, 10 mM Na_2HPO_4, 1.8 mM KH_2PO_4, pH 7.4) and added to a ThT solution (5 µM ThT, 50 mM Glycin, in NaOH-H_2O, pH 8.5). Samples were incubated at 37 °C.

Turbidity assays

At 355 nm, turbidity of 37 °C incubated samples was measured as described previously (3) using a UV/VIS Spectrometer (Perkin Elmer Lambda 25).

3
Supporting Results and Figures

Supporting Figure 1:

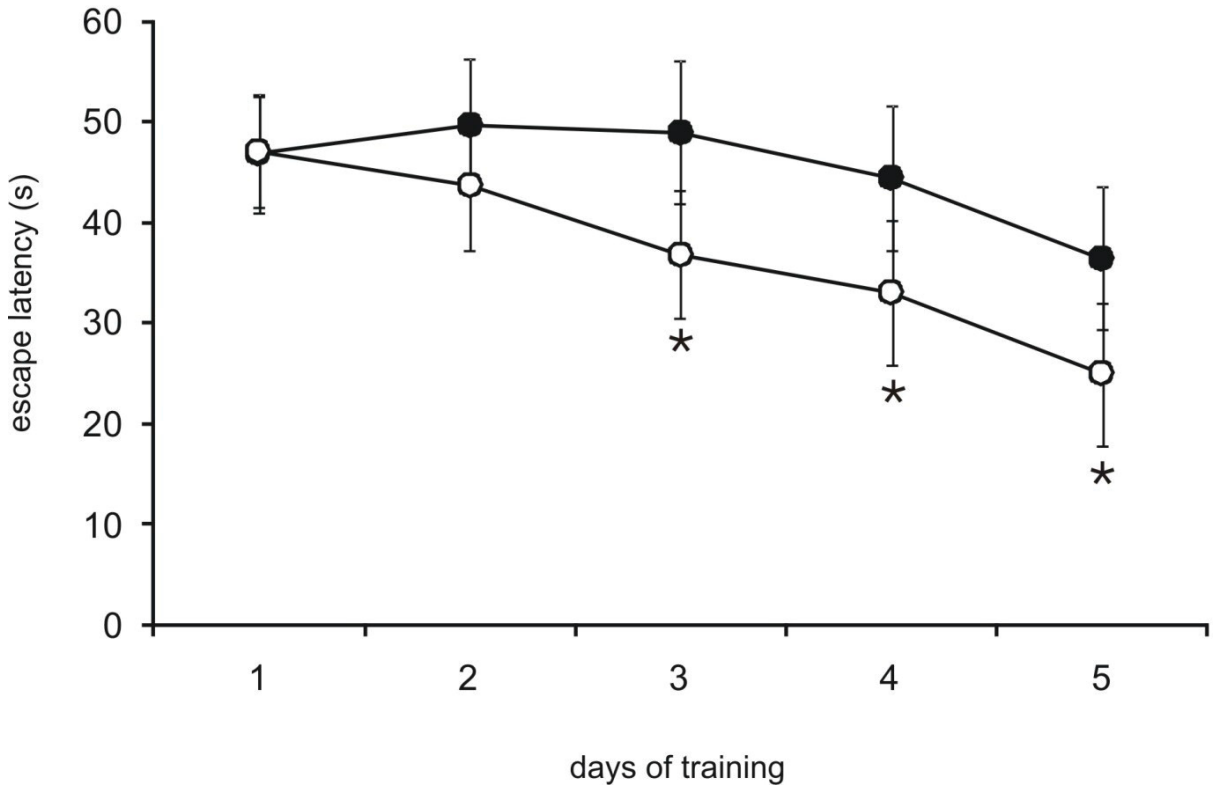

Figure legend S1: A: Results of the transgenic animal studies in the Morris water maze assay. Four months old mice had an Alzet minipump implanted under the skin with tubing inserted into the stomach, delivering the D3 peptide for the treated group (n=8), and delivering saline solution for the control group (n=9). The escape latency is the time, which the D3 treated (open circles) and untreated (filled circles) mice needed to find the hidden platform in the Morris water maze assay (for details see 'Methods' section). Error bars indicate standard deviations, asterisks (*) indicate $p<0.05$.

4

Supporting Table 1:

Summary of important quantities: number of animals per group, body weight, the Aβ load, and the density of staining for GFAP and microglia around plaques in the dorsal hippocampus. L: Left; C: Correct; A: Across; R: Right

Group	Control	D3 oral treatment
treatment	saline	saline solved D3
peptide amount [mg/day]	-	0.1
number	n=9	n=8
body weight [g]	26.16±1.37	24.7±0.03
swim speed [cm/s]	16.35±0.91	16.30±0.82
probe trial [s in quadrant]	L 16.59±4.47 C 17.33±3.91 A 9.61±1.50 R 16.33±3.07	L 14.27±1.48 C 16.69±1.88 A 10.59±1.24 R 15.29±1.60
Aβ plaque load cortex [%]	0.82±0.08	0.61±0.12
Aβ plaque load hippocampus [%]	0.33±0.06	0.23±0.04
GFAP	72.74±1.0	67.79±1.4*
microglia	80.11±1.5	75.25±1.7*

*indicates significantly different, $p < 0.05$

Supporting Figure 2:

Size-exclusion chromatography (SEC) was shown to be useful to separate monomeric Aβ from oligomeric ("protofibrillar") Aβ (1). To elucidate the effect of D3 on the ratio between monomeric and oligomeric Aβ, freshly prepared Aβ42 with or without D3 was briefly centrifuged and loaded onto a Superdex 75 PC3.2/30 column. Untreated Aβ monomers eluted at 1.6 ml, protofibrils at 0.96 ml (Fig. S2A), exactly as expected. Mixtures of Aβ with D3 (ratio 1:10), however, lacked the protofibril fraction, suggestive of a D3 oligomer/protofibril modulating activity. As the Aβ content of the monomer fraction was not increased, D3 clearly did not dissolve protofibrils into monomers. To confirm that the protofibril fraction of the Aβ- D3-mixture was devoid of Aβ, and to locate the missing Aβ, the monomer and the protofibril fractions were precipitated and spotted onto a nitrocellulose membrane. In addition, potentially precipitated material of the samples after pre-SEC centrifugation was treated likewise (Fig. S2B). Interestingly, the result revealed that protofibrillar Aβ was completely precipitated by D3.

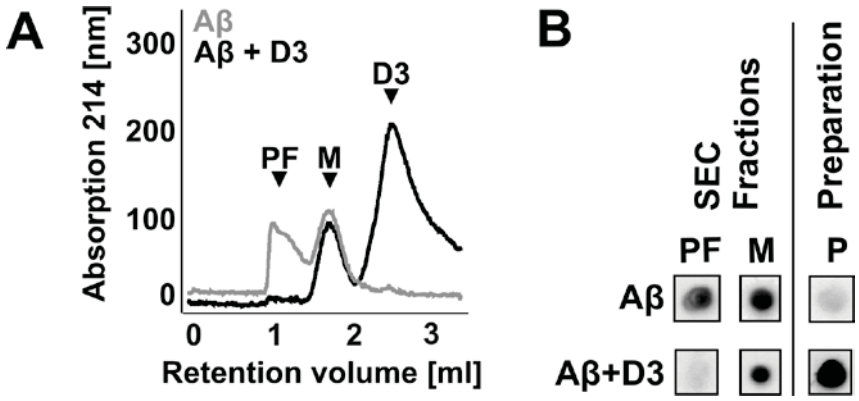

Figure legend S2: A: Size exclusion chromatography (SEC) analysis of 100 µM Aβ without (grey line) and with (black line) FITC-labelled D3. Samples were prepared, briefly centrifuged (30 s, 16.000 x g), and 10 µl of the supernatants were subjected to a Superdex 75 PC3.2/30 size exclusion column with 50 mM sodium phosphate, pH 7.4, 150 mM sodium

6

chloride and 0.6 % Tween-20 as running buffer. Protofibrils (PF) eluted at 1.6 ml and monomers (M) at 0.96 ml, comparable to the results reported by Johansson et al (1).

B: Dot blot analysis of monomer (M) and protofibrillar (PF) SEC fractions as well as pre-SEC centrifugation pellets (P). SEC fractions were precipitated by TCA. The pellets were dissolved in PBS, dotted onto a nitrocellulose membrane and Aβ was detected using 6E10 antibody.

7

Supporting Figure 3:

In order to verify whether D3 is indeed able to decrease ThT fluorescence during Aβ42 aggregation as previously reported (2) and accelerate Aβ42 aggregation at the same time, we determined turbidity as a general measure for aggregate particle formation and ThT fluorescence as a measure for the content of regular fibrils, for the same samples consisting of 25 µM Aβ with and without D3 in different concentrations (Fig. S3A). Measurements were done immediately upon sample preparation and again after a 24-hour incubation period. Indeed, the ThT assays yielded a D3 dose-dependent reduction of the ThT signal. Often, reduction of ThT fluorescence is interpreted as an indication of decreased aggregation, but more exactly, it points to a decrease in regular fibril content. Interestingly, the turbidity measurements performed in parallel (Fig. S3B) revealed an inverse correlation between ThT fluorescence and turbidity, indicating that, compared to Aβ without D3, Aβ-D3 mixtures form larger aggregates which contain less regular fibrils. Again, this suggests that D3 induces the formation of ThT-negative aggregates. Directly after turbidity and ThT measurements, the samples were subjected to electron microscopic (EM) analysis (see Fig. 3 A,B in the main manuscript). The results revealed Aβ typical fibrils (twisted ribbons) and spherical particles in the Aβ42 samples, but huge amorphous structures without any ribbons or long fibrillar morphology in the Aβ-D3 samples.

8

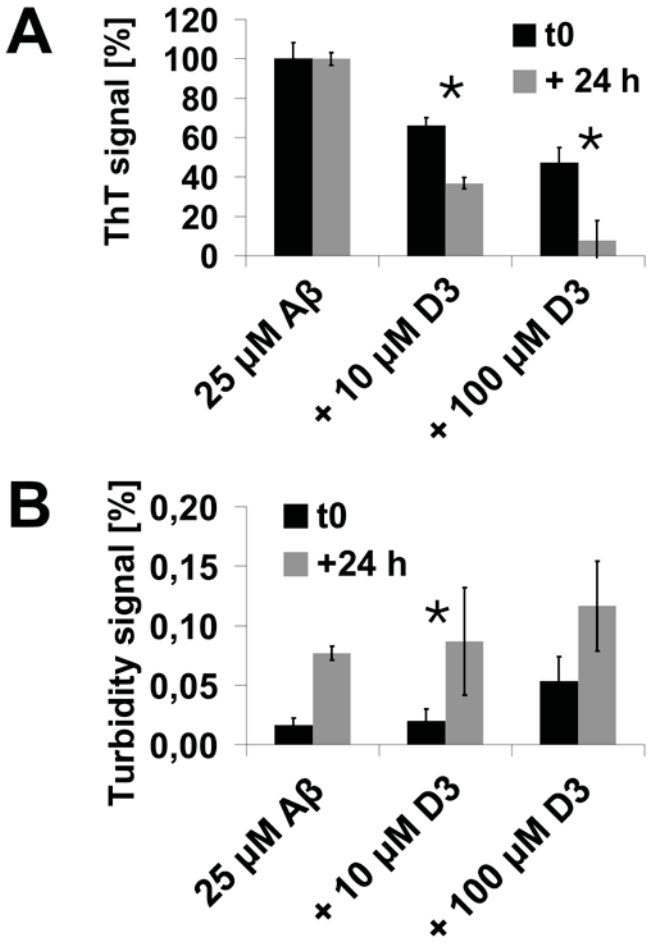

Figure legend S3: A: Inhibition of ThT positive Aβ fibril formation. D3 was added in concentrations of: 0, 10 µM, and 100 µM to 25 µM Aβ42 samples. The Aβ-D3-mixtures were tested immediately (black bars) or after 24 hours incubation (grey bars) at 37°C. Upon addition of ThT, fluorescence was measured at 490 nm in relative units (mean +/- standard deviations of results, four separate runs, three replicates per run) and related to the Aβ signals (100%).

B: Turbidity measurements of the same samples as investigated in A. Turbidity was measured using a UV/VIS spectrometer (Lamda 25, Perkin Elmer) at 355 nm. *indicates significantly different, $p < 0.05$

9

Supplementary References

1. Johansson AS*, et al.* (2006) Physiochemical characterization of the Alzheimer's disease-related peptides A beta 1-42Arctic and A beta 1-42wt. *FEBS J* 273(12):2618- 2630.
2. van Groen T*, et al.* (2008) Reduction of Alzheimer's Disease Amyloid Plaque Load in Transgenic Mice by D3, a D-Enantiomeric Peptide Identified by Mirror Image Phage Display. *ChemMedChem* 3(12):1848-1852.
3. Soderberg L*, et al.* (2005) Collagenous Alzheimer amyloid plaque component assembles amyloid fibrils into protease resistant aggregates. *FEBS J* 272(9):2231- 2236.

2.1.2 Identification and characterization of an Aβ oligomer precipitating peptide that may be useful to explore gene therapeutic approaches to Alzheimer disease.

Publiziert in: Rejuvenation Research

Impact Factor: 2,919

Eigenanteil an der Publikation: 20 %

Durchführung von Dichtegradientenzentrifugationen, SDS-PAGE und Silberfärbungen. Mitverfassen des Manuskripts.

REJUVENATION RESEARCH
Volume 15, Number 2, 2012

DOI: 10.1089/rej.2011.1262

Identification and Characterization of an Aβ Oligomer Precipitating Peptide That May Be Useful to Explore Gene Therapeutic Approaches to Alzheimer Disease

Susanne Aileen Funke,[1,3] Hongmei Liu,[1,3] Torsten Sehl,[1] Dirk Bartnik,[1] Oleksandr Brener,[1,2] Luitgard Nagel-Steger,[1,2] Katja Wiesehan,[1] and Dieter Willbold[1,2]

Abstract

A key feature of Alzheimer disease (AD) is the pathologic self-association of the amyloid-β (Aβ) peptide, leading to the formation of diffusible toxic Aβ oligomers and extracellular amyloid plaques. Next to extracellular Aβ, intraneuronal Aβ has important pathological functions in AD. Agents that specifically interfere with the oligomerization processes either outside or inside of neurons are highly desired for the elucidation of the pathologic mechanisms of AD and might even pave the way for new AD gene therapeutic approaches. Here, we characterize the Aβ binding peptide L3 and its influence on Aβ oligomerization *in vitro*. Preliminary studies in cell culture demonstrate that stably expressed L3 reduces cell toxicity of externally added Aβ in neuroblastoma cells.

Introduction

Fibrillar and especially oligomeric forms of the amyloid-β (Aβ) peptide are currently believed to be responsible for development and progression of Alzheimer disease (AD).[1–3] Increasing evidence is accumulating that intraneuronal Aβ accumulation may precede extracellular Aβ deposition.[4,5] Therefore, in addition to extracellular Aβ, intraneuronal Aβ might represent an alternative and important therapeutic target.

Previously, the D-amino acid peptide D3 (RPRTRLHTHRNR), which specifically binds to Aβ1–42, was identified by mirror image phage display. D3 was found to modulate Aβ oligomerization, to decrease Aβ cytotoxicity in cell culture, and to drastically reduce the Aβ plaque load, cerebral inflammation, and cognitive deficits in transgenic AD mice after oral application.[6–10] Here, we report on a L-enantiomeric peptide, denoted L3, which was selected in parallel to D3. We characterize the influence of L3 on Aβ oligomerization *in vitro*. Subsequently, L3-coding DNA sequences were cloned in eukaryotic expression vectors. In mouse neuroblastoma 2a (N2a) cells, stably expressed L3 reduces cell toxicity of externally added Aβ.

Material and Methods

Peptides

All peptides were obtained commercially (JPT Biotech, Berlin, Germany).

Phage display selection

Phage display selection was done as described earlier for D3[10] with only one modification: L-Aβ42 was used as target instead of D-Aβ42.

Thioflavin T assays

Thioflavin T (ThT) assays were performed as described elsewhere[10] with minor modifications. Aβ aliquots and L3 were dissolved in phosphate-buffered saline (PBS; 140 mM NaCl, 2.7 mM KCl, 10 mM Na_2HPO_4, 1.8 mM KH_2PO_4, pH 7.4) and added to a ThT solution (5 μM ThT, 50 mM glycine, in NaOH–H_2O, pH 8.5).

Turbidity assays

Turbidity assays were carried out as described elsewhere.[11]

Seeding assays

The assays were performed as already described[7] with minor modifications. Lyophilized Aβ was predissolved in dimethylsulfoxide (DMSO), diluted in PBS, and incubated (37°C, 3 days). Aβ–L3 seeds were incubated at equimolar ratios.

Density gradient centrifugation

Density gradient centrifugation was performed as described earlier.[7]

[1]Institut of Complex Systems (ICS-6), Forschungszentrum Jülich, Jülich, Germany.
[2]Institut für Physikalische Biologie, Heinrich-Heine-Universität, Düsseldorf, Germany.
[3]Both authors contributed equally.

Construction of eukaryotic L3 expression vectors

Two oligonucleotides (5′-CCGGTATATATGAATTCATG GTGCTGAGGATGATGCTGCAGATCAAGAGGATCCCCA GGGCCCGGGATATATT-3′ and 3′-ATATATACTTAAGT ACCACGACTCCTACTACGACGTCTAGTTCTCCTAGGGG TCCCGGGCCCTATATAAGTAC-5′; BioTeZ, Berlin Buch GmbH) were annealed to create a double-stranded DNA fragment that was inserted into a *Sma*I *Eco*RI-digested expression plasmid DsRed-N1 (Clontech, USA). The resulting amino acid sequence was VLRMMLQIKRIPR followed by a carboxy-terminal linker sequence and the DsRed-monomer. For construction of the L3 expression and secretion vector, the oligonucleotides 5′-CCGGTATATATGAATTCATGGCCAG CGCCCTGCTGATCCTGGCCCTGGTGGGCGCCGCCGTG GCCGTGCTGAGGATGATGCTGCAGATCAAGAGGATC CCCAGGGCCCGGGATATATT-3′ and 3′-ATATATACTT AAGTACCGGTCGCGGGACGACTAGGACCGGGACCAC CCGCGGCGGCACCGGCACGACTCCTACTACGACGTCT AGTTCTCCTAGGGGTCCCGGGCCCTATATAAGTAC-5′ were treated analogously for the expression with a pre-pro-trypsin leader sequence (PPTLS).[12]

Transfection of L3-expressing vectors into N2a cells and generation of stable cell lines

The constructed DsRed-tagged L3-expressing plasmids were transfected into N2a cells by Polyfect reagent (QIAGEN, Hilden, Germany) according to the manufacturer's protocol. After 24 hr, 900 μg/mL of G418 was added to the medium. G418-resistant colonies were analyzed by confocal laser scanning microscopy and then picked, and cultured. The control cell line was generated by transfection with vectors coding for DsRed.

Cell toxicity assays

To investigate influence of L3 expression on cellular toxicity of L-Aβ(1–42), MTT assays were accomplished as already described.[10]

Results

Selection of peptide L3

Under exactly the same conditions as previously described for the identification of D3 as a therapeutically active D-enantiomeric peptide that has proven to specifically precipitate toxic Aβ42 oligomers into nontoxic Aβ aggregates, another phage display selection was carried out with L-enantiomeric Aβ42 as target instead of D-Aβ42.[7,10] Under the applied conditions for selection, we expected almost exclusively monomeric Aβ to be the dominant Aβ42 species. Due to the high aggregation tendency of Aβ42, the presence of oligomeric Aβ species, however, cannot be excluded. We conducted six rounds of biopanning and determined the peptide sequences of the enriched phage-displayed peptides by DNA sequence analysis of the respective genome region. The amino acid sequence of the dominating peptide from the selection was LRMMLQIKRIPR, referred to as L3. This sequence was found in seven of nine randomly chosen phage clones.

In vitro characterization of L3 influence on Aβ oligomerization

ThT is a benzothiazole dye that exhibits enhanced fluorescence upon binding to amyloid fibrils.[13] To investigate the influence of L3 on Aβ fibrillization, we performed ThT assays as a measure for the content of regular fibrils in 25 μM Aβ with and without 1 mM L3, as well as turbidity as a measure for formation of large particles (Fig. 1A). A reduction of the ThT signal could be observed in Aβ–L3 samples, pointing to a decrease of regular fibril content. Interestingly, the turbidity measurements revealed an inverse correlation between ThT fluorescence and turbidity (Fig. 1B), indicating that Aβ–L3 mixtures contain large aggregates, but less regular fibrils.

To investigate the effects of L3 on Aβ aggregation in more detail, 125 μM Aβ42 samples with and without equimolar amounts of L3 were analyzed by density gradient centrifugation. In the absence of L3, Aβ42 species were broadly distributed over nearly all fractions, indicating the presence of Aβ monomers and oligomers of a broad size range. Samples containing L3, however, had a drastically reduced Aβ content in fractions 3–10, corresponding to Aβ 16- to 200-mers.[7] Obviously, the presence of L3 resulted in complete abolishment of Aβ42 oligomers and an increase of Aβ species with high molecular weight (Fig. 1C, fractions 11–15).

It is well known that Aβ "seeds," *i.e.*, preformed Aβ fibrils, catalyze the fibrillization of soluble Aβ.[14] To investigate the *in vitro* seeding potential of L3-induced Aβ aggregates, we carried out seeding experiments (Fig. 1D). Fibrils consisting of Aβ only stimulated fibrillogenesis, whereas Aβ–L3 co-aggregates did not, suggesting that Aβ–L3 co-aggregates are not amyloidogenic. This is in accordance with the observation that Aβ–L3 co-aggregates are negative for ThT fluorescence.

Characterization of L3 expression and L3 activity in cell culture

To investigate influence of L3 expression on oligomeric L-Aβ42–induced cytotoxicity, two N2a cell lines were produced that stably expressed L3–DsRed (stL3-N2a) and PPT–LS–L3–DsRed (stPLL3-N2a, L3 with a secretion signal peptide). The expression of DsRed-tagged peptides was confirmed by confocal laser scanning microscopy (Fig. 1E). In cells expressing L3–DsRed, the fluorescence was almost evenly distributed throughout the cytoplasm and nucleus, whereas PPT–LS–L3–DsRed was expressed mainly in the cytoplasm. These cell lines maintained stable expression for at least 20 generations, even in the absence of G418 selection pressure. As shown in Fig. 1F, upon incubation with oligomeric L-Aβ42, the mock-transfected cells were clearly susceptible to Aβ treatment, with a reduction of cell viability up to 50%. In contrast, both the two L3-expressing N2a cell lines showed significantly increased cell viability at the three concentrations tested. StPLL3-N2a yielded slightly higher cell viability than stL3-N2a at lower Aβ concentrations (10 μM and 25 μM), but no difference between both cell lines was observed at 50 μM.

Discussion

In conclusion, and as underlined by further *in vitro* studies (data not shown here), L3 modulates Aβ aggregation, eliminating toxic Aβ oligomers and inducing the formation of large, nonamyloidogenic aggregates that do not seed Aβ fibrillization, similarly as already described for the D-enantiomeric peptide D3.[7] Both peptides, D3 and L3, which

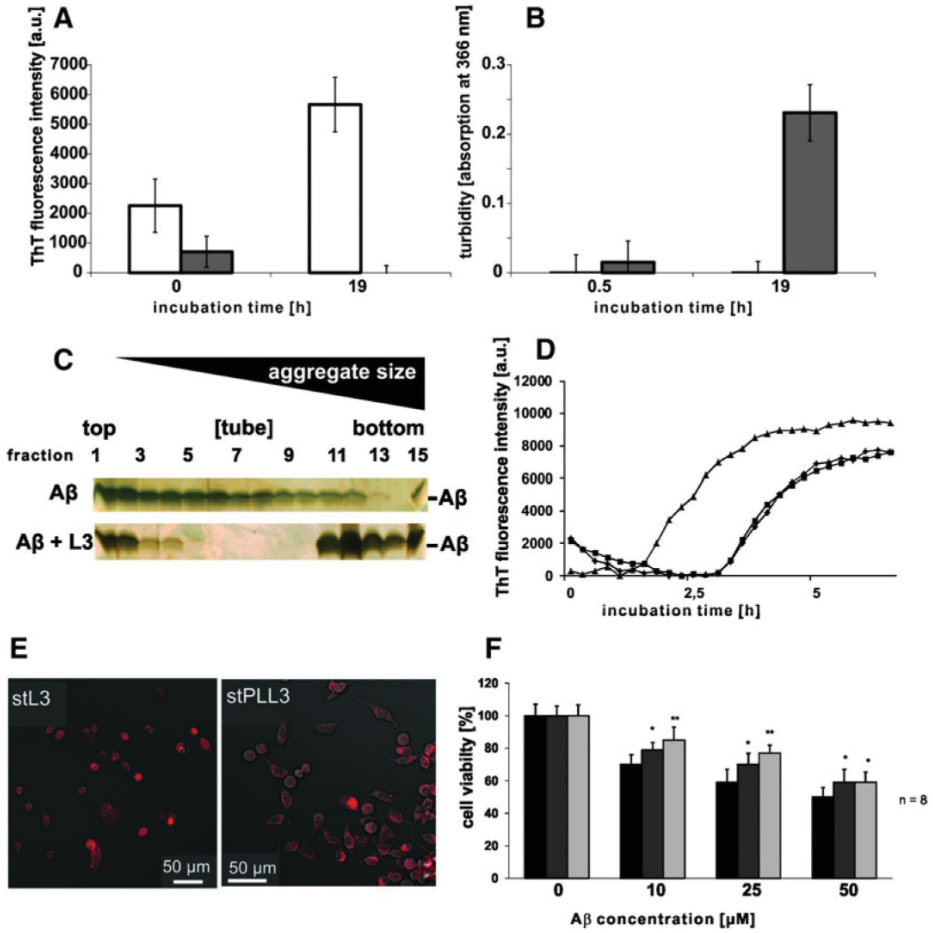

FIG. 1. Impact of L3 on Aβ fibril formation. (**A**) Fibril formation assays have been run with 25 μM Aβ42 in absence (grey bars) or presence (white bars) of 1 mM L3. Thioflavin T (ThT) fluorescence was determined at 490 nm in relative units (mean ± standard deviations of results, three replicates per run) immediately and after 19 hr of incubation at 37°C. (**B**) Turbidity of the same samples as investigated in **A** was determined using an ultraviolet–visible (UV/VIS) spectrometer (Lamda 25, Perkin Elmer) for absorption measurements at 355 nm. (**C**) Analysis of Aβ aggregation ultracentrifugation. The size distributions of 125 μM Aβ42 and Aβ42–L3 mixtures (1:1) were analyzed by density gradient on a preformed step gradient of iodixanol (5%–50%) overlaid by 100 μL of the respective aggregation mixtures. After centrifugation, 14 fractions from top to bottom of the centrifuge tube of 140 μL each were harvested. The 15th fraction represents the pellet. The fractions were analyzed for their Aβ42 content by sodium dodecyl sulfate polyacrylamide gel electrophoresis (SDS-PAGE) and silver staining. (**D**) Aβ fibril formation with and without seeds monitored by ThT fluorescence. Aβ-only fibrils and Aβ–L3 co-aggregates were prepared by incubating Aβ42 with and without L3 for 3 days at 37°C. After washing, the precipitated seeds (20% vol/vol) were added to the aggregation reactions consisting of 10 μM freshly prepared Aβ42 solutions. The relative ThT fluorescence of freshly prepared Aβ with fibrillar Aβ seeds (triangles), Aβ-L3 co-aggregates (1:1, squares), and freshly prepared Aβ as a control (rhombi) is shown as a function of time. (**E**) Live-cell fluorescence imaging of the two established stable N2a cell lines with expression of L3–DsRed (*left*) and PPT–LS–L3–DsRed (*right*). (**F**) Influence of L3 expression on the cytotoxicity of oligomeric P-Aβ42. Cell viability for control N2a cells (mock-transfected with vectors, black bars) and stably L3-expressing N2a cells (stL3-N2a, grey bars; stPLL3-N2a, light grey bars) were assessed by MTT assay following oligomeric P-Aβ42 incubation at the concentrations indicated. Percentages of cell viability were derived as follows: The 100% value was obtained in the absence of oligomeric L-Aβ42 for each cell line. Results are shown as percentage of control (untreated cells). Data represent means of eight independent experiments. Bars, ± standard deviation (SD). (*) $p < 0.05$ or (**) $p < 0.01$ when L3-expressing cells were compared with the DsRed-transfected control cell line at each concentration.

were selected in parallel under identical conditions, are considerably hydrophilic and have similar isoelectric points (L3, 12.3; D3, 12.6). Both contain a considerable number of positively charged amino acids (L3 contains three, D3 contains five arginines), which were already suspected to play an important role in D3 mechanism of action.[7]

In contrast to D-peptides, L-peptides might be susceptible to proteolytic degradation *in vivo*.[15] A potential advantage of L3 is that it can be expressed permanently in cells, as already demonstrated in cell culture. L3 might interfere with early oligomerization processes inside and outside neurons. This could be potentially valuable for the elucidation of the pathologic mechanisms of AD and maybe even for paving the way for a new AD gene therapeutic approach.

In future, we will further investigate the effects of extra- and intracellular overexpression of L3 on Aβ aggregation and toxicity in cell culture. Furthermore, we will investigate L3 expression in different mouse models of AD employing adenovirus expression systems.

Author Disclosure Statement

The authors have no conflict of interest to disclose.

Acknowledgment

The authors gratefully acknowledge support from the "Helmholtz–CSC (China Scholarship Council) Junior Scientists Exchange Program" for Hongmei Liu.

References

1. Haass C, Selkoe DJ. Soluble protein oligomers in neurodegeneration: Lessons from the Alzheimer's amyloid beta-peptide. Nat Rev Mol Cell Biol 2007;8:101–112.
2. Hardy JA, Higgins GA. Alzheimer's disease: The amyloid cascade hypothesis. Science 1992;256:184–185.
3. Selkoe DJ. The molecular pathology of Alzheimer's disease. Neuron 1991;6:487–498.
4. Gouras GK, Tampellini D, Takahashi RH, Capetillo-Zarate E. Intraneuronal beta-amyloid accumulation and synapse pathology in Alzheimer's disease. Acta Neuropatholog 2010;119:523–541.
5. LaFerla FM, Green KN, Oddo S. Intracellular amyloid-beta in Alzheimer's disease. Nat Rev Neurosci 2007;8: 499–509.
6. Bartnik D, Funke SA, Andrei-Selmer LC, Bacher M, Dodel R, Willbold D. Differently selected d-enantiomeric peptides act on different Abeta species. Rejuvenation Res 2010;13: 302–305.
7. Funke SA, van Groen T, Kadish I, Bartnik D, Nagel-Steger L, Brener O, Sehl T, Batra-Safferling R, Moriscot C, Schoehn G, Horn AHC, Müller-Schiffmann A, Korth C, Sticht H, Willbold D. Oral treatment with the D-enantiomeric peptide D3 improves pathology and behavior of Alzheimer's disease transgenic mice. ACS Chem Neurosci 2010;1:639–648.
8. Muller-Schiffmann A, Marz-Berberich J, Andreyeva A, Ronicke R, Bartnik D, Brener O, Kutzsche J, Horn AH, Hellmert M, Polkowska J, Gottmann K, Reymann KG, Funke SA, Nagel-Steger L, Moriscot C, Schoehn G, Sticht H, Willbold D, Schrader T, Korth C. Combining independent drug classes into superior, synergistically acting hybrid molecules. Angew Chem Int Ed Engl 2010;49:8743–8746.
9. van Groen T, Kadish I, Wiesehan K, Funke SA, Willbold D. In vitro and in vivo staining characteristics of small, fluorescent, Abeta42-binding D-enantiomeric peptides in transgenic AD mouse models. ChemMedChem 2009;4:276–282.
10. van Groen T, Wiesehan K, Funke SA, Kadish I, Nagel-Steger L, Willbold D. Reduction of Alzheimer's disease amyloid plaque load in transgenic mice by D3, a D-enantiomeric peptide identified by mirror image phage display. ChemMedChem 2008;3:1848–1852.
11. Soderberg L, Dahlqvist C, Kakuyama H, Thyberg J, Ito A, Winblad B, Naslund J, Tjernberg LO. Collagenous Alzheimer amyloid plaque component assembles amyloid fibrils into protease resistant aggregates. FEBS J 2005;272:2231–2236.
12. Bendtsen JD, Nielsen H, von Heijne G, Brunak S. Improved prediction of signal peptides: SignalP 3.0. J Mol Biol 2004;340:783–795.
13. Khurana R, Coleman C, Ionescu-Zanetti C, Carter SA, Krishna V, Grover RK, Roy R, Singh S. Mechanism of thioflavin T binding to amyloid fibrils. J Struct Biol. 2005;151:229–238.
14. Harper JD, Lansbury PT, Jr. Models of amyloid seeding in Alzheimer's disease and scrapie: mechanistic truths and physiological consequences of the time-dependent solubility of amyloid proteins. Annu Rev Biochem 1997;66:385–407.
15. Fauchere JL, Thurieau, C. Evaluation of the stability of peptides and pseudopeptides as a tool in peptide drug design. Adv Drug Res 1992;23:127–159.

Address correspondence to:
Prof. Dr. Dieter Willbold
Institut of Complex Systems (ICS-6)
Forschungszentrum Jülich
D-52425 Jülich, Germany

E-mail: d.willbold@fz-juelich.de

2.1.3 Combining independent drug classes into superior, synergistically acting hybrid molecules.

Publiziert in: Angewandte Chemie

Impact Factor: 13,734

Eigenanteil an der Publikation: 20 %

Durchführung von Dichtegradientenzentrifugationen, SDS-PAGE und Silberfärbungen. Mitverfassen des Manuskripts.

Angewandte International Edition Chemie

DOI: 10.1002/anie.201004437

Hybrid Drugs

Combining Independent Drug Classes into Superior, Synergistically Acting Hybrid Molecules**

Andreas Müller-Schiffmann, Julia März-Berberich, Aksana Andreyeva, Raik Rönicke, Dirk Bartnik, Oleksandr Brener, Janine Kutzsche, Anselm H. C. Horn, Marco Hellmert, Jolanta Polkowska, Kurt Gottmann, Klaus G. Reymann, S. Aileen Funke, Luitgart Nagel-Steger, Christine Moriscot, Guy Schoehn, Heinrich Sticht, Dieter Willbold, Thomas Schrader, and *Carsten Korth**

Increasing the potency of synthesized drugs has been a stepwise process accomplished by progressively modifying the chemical scaffold of a single parent lead compound. To date, there has been no basis for thinking that the combination of pharmacological effects of independently acting drugs could be achieved beyond mere simultaneous administration. We reasoned that if the target molecule of two independent classes of drugs was the same, chemical synthesis of a hybrid compound where these drugs presented moieties within one molecule might yield synergistic effects; that is, a new quality might emerge that would be more than the sum of the single-moiety compounds. Such multifunctional hybrid compounds that assign different functions to its different moieties to achieve a synergistic pharmacodynamic effect have successful predecessors in nature: for example, bleomycin is a natural compound with three different moieties acting in concert to cleave DNA.[1]

[*] Dr. A. Müller-Schiffmann,[+] Dr. J. Kutzsche, Prof. Dr. C. Korth
Department of Neuropathology
Heinrich Heine University Düsseldorf
40225 Düsseldorf (Germany)
Fax: (+49) 211-811-7804
E-mail: ckorth@uni-duesseldorf.de
Dr. J. März-Berberich,[+] Dipl.-Chem. M. Hellmert, Dr. J. Polkowska, Prof. Dr. T. Schrader
Institute for Organic Chemistry
University Essen-Duisburg (Germany)
Dr. A. Andreyeva, Prof. Dr. K. Gottmann
Institute of Neuro- and Sensory Physiology
Heinrich Heine University Düsseldorf (Germany)
Dr. R. Rönicke, Prof. Dr. K. G. Reymann
German Center for Neurodegenerative Diseases Magdeburg
Magdeburg (Germany)
Dr. D. Bartnik, Dr. S. A. Funke
Institute for Structural Biology and Biophysics
FZ Jülich (Germany)
Dr. O. Brener, Dr. L. Nagel-Steger, Prof. Dr. D. Willbold
Institute for Physical Biology
Heinrich Heine University Düsseldorf (Germany)
Dr. C. Moriscot, Prof. Dr. G. Schoehn
Institute for Structural Biology Jean-Pierre Ebel
Universite Joseph Fourier, Grenoble (France)
Dr. A. H. C. Horn, Prof. Dr. H. Sticht
Institute for Biochemistry
University of Erlangen–Nürnberg (Germany)
[+] These authors contributed equally to this work.

[**] The major support for this work was from a grant of the Volkswagen-Stiftung to C.K., T.S., D.W., and H.S. (I/82 649); further funding was provided by EU-FP6 (cNEUPRO), EU-FP7 (PRIORITY) grants to C.K. and a DFG-GRK1033 grant to J.K. and C.K.

Supporting information for this article is available on the WWW under http://dx.doi.org/10.1002/anie.201004437.

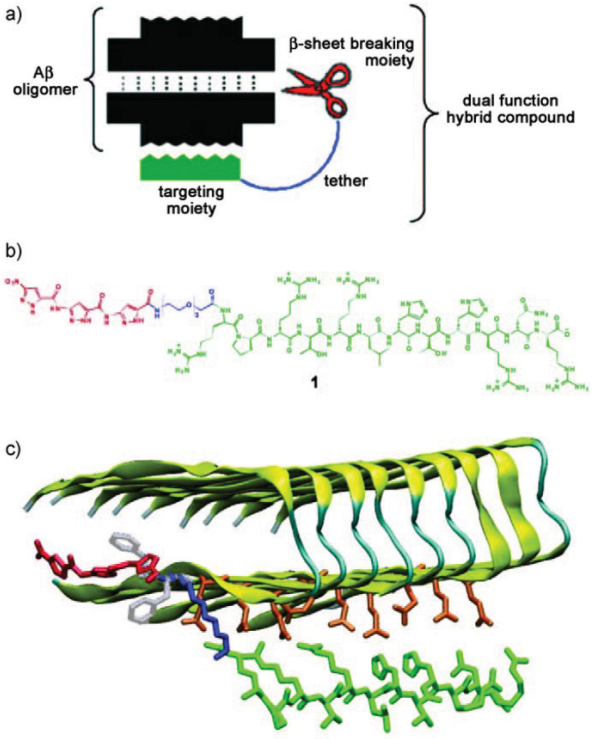

Figure 1. Design, function, and modeling of hybrid compounds. a) Hybrid compound, composed of a recognition moiety docking on the target (here: Aβ oligomers) linked by a flexible tether to the functional moiety, a β-sheet breaker. b) Chemical structure of lead hybrid compound Trimer-TEG-D3 (**1**). c) Model of the Aβ/**1** complex. The side chains of the glutamates (orange) in adjacent Aβ monomers (yellow) are located in close spatial proximity and are contacted by the basic residues of the D3 peptide (green). The aminopyrazole trimer (red) is bound to the Aβ backbone and interacts with the two phenylalanines (F19, F20; gray). The color coding of the individual parts of **1** is according to (a) and (b).

Communications

Herein we describe the design and chemical synthesis of hybrid compounds that target the disassembly of neurotoxic Aβ oligomers. Cross-β-sheeted Aβ oligomers or amyloids are a hallmark of Alzheimer's disease (AD). Misprocessing of an amyloidogenic fragment Aβ derived from proteolytic processing of amyloid precursor protein is critical in a cascade of events that starts with the oligomerization of Aβ and, ultimately, ends in neuronal death in the central nervous system.[2] To date, rationally designed small-molecule β-sheet breakers, although highly efficient in preventing or disassembling β-sheet structures in cell-free in vitro systems, have failed to show convincing effects in vivo owing to their highly unspecific binding.

We reasoned that lack of in vivo efficiency of small β-sheet breakers might be overcome by the addition of a molecular recognition unit that would direct the β-sheet breaking moiety to its target molecule. Molecular recognition is a key property of polypeptides that can be identified in evolutionary algorithms, for example in phage display systems comprising iterative cycles of panning and selection of peptides. We identified D3, a D-enantiomeric dodecapeptide, as a potent Aβ oligomer binder in a mirror-image phage display,[3,4] that is able to modulate Aβ aggregation, plaque load, and neuroinflammation processes in the brains of transgenic (APPswe/PS1ΔE9) mice.[3,5]

In our hybrid compound (Figure 1), we would thus combine two entirely different drug development strategies: evolutionary selection from a peptide library together with rationally designed small molecules. As rationally designed β-sheet breakers, we chose aminopyrazoles (APs) that possess a specific donor–acceptor–donor (DAD) sequence of hydrogen bond donors and acceptors, that are perfectly complementary to that of a β sheet,[6] binding selectively to the backbone of misfolded peptides residing in the β-sheet conformation,[7] and able to disassemble preformed Aβ fibrils in vitro.[8]

Comparative modeling and molecular dynamics simulations were used to investigate the interaction of Aβ[9] of AP linked to D3 with different linkers and to a pentalysine peptide (KKKKKG) as charge control for D3. The AP moiety of **1** was modeled to interact with the diaromatic motif F19/F20, and the D3 part was placed in spatial vicinity of a negatively charged surface patch of the Aβ protofibril to maximize electrostatic complementarity (see the Supporting Information, Figure S1). These simulations revealed that after 10 ns, the multiple interactions formed between D3 peptide and the E22 residues remained stable (Figure 1c; Supporting Information, Figure S2) whilst only one salt bridge was preserved between the pentalysine moiety and the Aβ fibril (Supporting Information, Figure S2D), thus providing an explanation for the enhanced activity of D3 compared to other substances (Figure 2a; Supporting Information, Figure S4B).

When added to cells that continuously secrete Aβ oligomer (7A2 cells[10]), the hybrid compound with the triethylen-

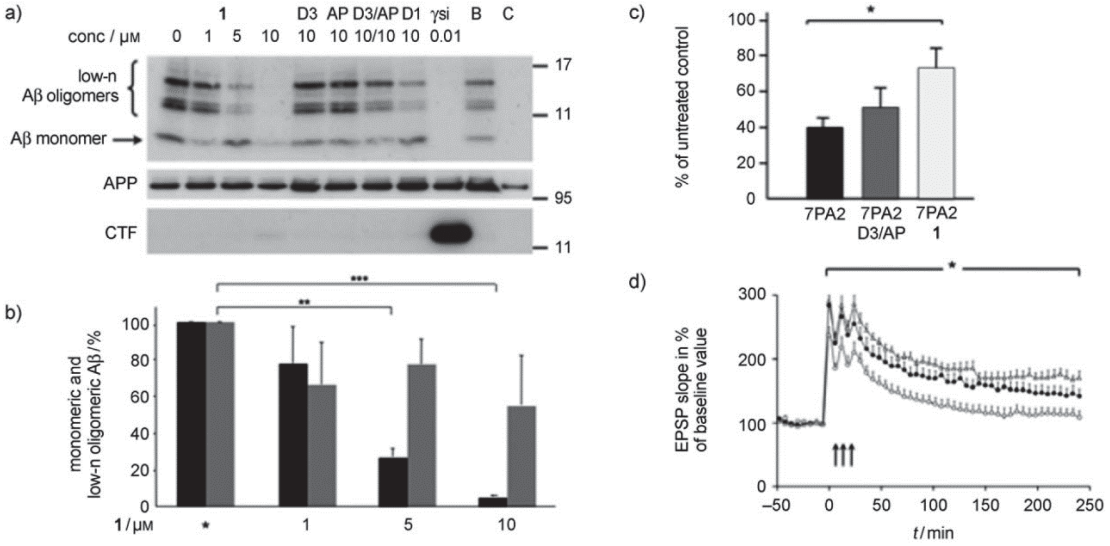

Figure 2. Biochemical and biological effects of hybrid compounds. a) Western blot of immunoprecipitated Aβ oligomers and monomers from 7PA2 cells that were treated with different substances. Addition of **1** led to a dose-dependent reduction of Aβ oligomers. Treatment with the D-peptide D3 or the aminopyrazole (AP) moiety alone, or as simultaneously applied substances (D3/AP) at 10 μM, did not show any Aβ oligomer reducing effects in this assay. Further control experiments included a hybrid compound consisting of another D-peptide (10 μM; D1), as well as γ-secretase inhibitor LY411575 (10 nM), 7PA2 cells treated with AP-dissolving substance DMSO at the same concentrations (B), and untransfected CHO cells not secreting Aβ oligomers (C). Expression of APP and APP-C-terminal fragments (CTF) as a control is shown in the lower panels, as indicated. b) Comparison of 5 independent experiments of 7PA2 cells treated with **1** at 1, 5, and 10 μM, showing clear effects on oligomeric Aβ (*** $p = 0.0007$, ** $p = 0.0082$), whereas monomeric Aβ was not significantly affected (oligomeric Aβ black bars, monomeric Aβ gray bars). c) 10 μM **1**, but not a composition of both single compounds at 10 μM each, reversed the effect of 7PA2 supernatant on mEPSC frequency in cultured cortical mouse neurons. Significant reversal of mEPSC suppression (* $p < 0.025$ by Student's test after Bonferroni correction). Bars represent mean ± SEM (see Supporting Information for details). d) Compound **1** prevented the Aβ-mediated decrease of LTP in acutely isolated hippocampal slices. Compared to control LTP (●), oligomeric Aβ (1–42) significantly reduced LTP (○), which was prevented by co-application of 10 μM **1** (△) * $p < 0.05$ analysis of variance with repeated measures; significance between control and Aβ and between Aβ and **1**/Aβ.

glycol (TEG) linker, termed Trimer-TEG-D3 (**1**), inhibited Aβ oligomerization in a dose-dependent manner (Figure 2a,b). Remarkably, single compounds or the combination of both single-compound moieties administered at same concentrations did not produce any effect in this assay, thus demonstrating the dramatic synergistic action of both moieties within the composite compound that in effect leads to a new function (Figure 2a). Upon administration of **1**, only the decrease of the Aβ oligomer fraction was significant compared to the Aβ monomer fraction, and no increase of C-terminal APP fragments was observed, suggesting that **1** neither decreased Aβ monomer generation nor inhibited γ secretase (Figure 2a). Even very high concentrations of each single compound or their combination did not lead to a reduction in Aβ oligomers (Supporting Information, Figure S3), and **1** revealed cytotoxicty only at concentrations of more than 100 μM (Supporting Information, Figure S4).

To demonstrate the specificity of the D3 moiety in targeting Aβ oligomers, a hybrid with a D-peptide that recognizes a different epitope of Aβ, termed D1, was also tested.[4] With this compound, only an insignificantly weak inhibition of Aβ oligomerization was observed (Figure 2a). Moreover, as predicted from molecular modeling, the AP–pentalysine hybrid had no effect on Aβ oligomer assembly (Supporting Information, Figure S5B).

Our concept of synergistic hybrid compounds predicts a critical importance of linker length between moieties. Structural and energetic considerations suggest that a shorter linker should favor a tight interaction owing to the smaller entropic loss upon binding, whereas longer linkers should be unfavorable. When we synthesized hybrids with no spacer, a shorter γ-aminobutyric acid (GABA) spacer, or a longer $(TEG)_2$ spacer (Supporting Information, Figure S5A), we verified this relation in that only no spacer or a five-atom linker (GABA) showed markedly increased Aβ oligomer inhibition (Supporting Information, Figure S5B,C).

Synaptic pathology is a key biological effect of Aβ oligomers, which should be reversed by **1**. Compound **1** blocked the Aβ-induced decrease in mEPSC frequency (mEPSC = miniature excitatory post-synaptic current) that is mediated by AMPA receptors[11] in cultured cortical neurons (Figure 2c), but it did not affect the mean mEPSC amplitude. The effect was achieved with 10 μM **1** but not with the single compounds or a combination of both single compounds (Figure 2c). Similarly, Aβ-oligomer-induced impairment of long-term potentiation (LTP),[12] a form of synaptic plasticity in acute hippocampal slices, could be reversed by coapplication of 10 μM **1** (Figure 2d). These results demonstrated that **1** prevented Aβ-induced synaptotoxicity in two independent assays.

Multimer growth to amyloid fibrils should be inhibited by increased binding of the two moieties of **1** to Aβ oligomers. Analytical ultracentrifugation of synthetic Aβ in vitro[13] showed an equal distribution across all multimeric fractions (Figure 3a, upper panel). When preincubated with **1**, Aβ partitioned to high-molecular-weight fractions at the expense of oligomeric fractions (Figure 3a, middle panel), as evidence that direct binding of **1** to Aβ oligomers influenced Aβ oligomer assembly. As Aβ thioflavin T (ThT) fluorescence

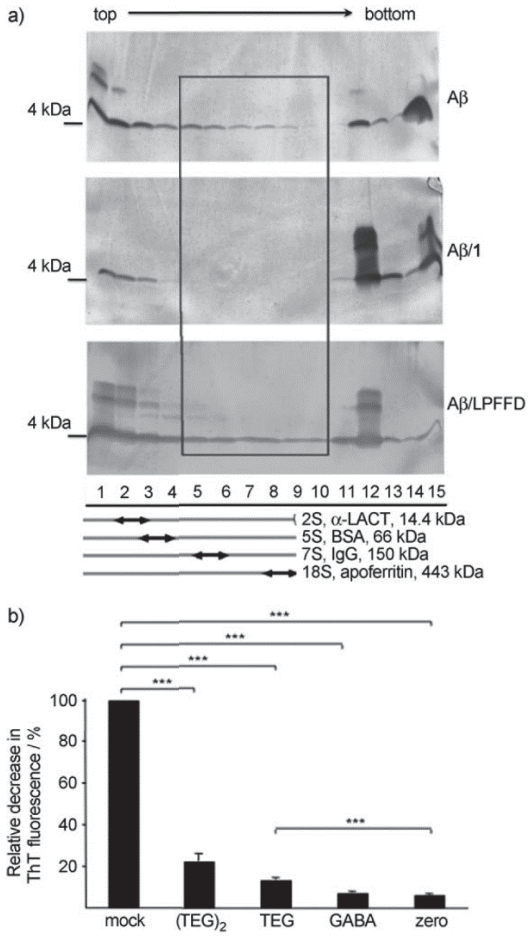

Figure 3. Biophysical characterization of the effect of hybrid compounds on Aβ assembly. a) Analysis of the effect of **1** on Aβ aggregation by analytical density gradient ultracentrifugation analyzed by SDS-PAGE and silver staining. Continuous fractions from light (left) to heavy (right) were loaded: monomeric Aβ in the leftmost fractions (lane 1), oligomeric Aβ in the fractions in the red box (lanes 5–10), and multimeric aggregated Aβ in fractions 12 and higher. Compared to untreated Aβ (125 μM; top panel), or control-treated Aβ (bottom panel), compound **1** (62.5 μM; middle panel) led to a shift of oligomeric fractions to high-molecular-weight, non-amyloid complexes. Calibration of fractions for sedimentation coefficients *S* (black double arrows) with α-lactalbumin (α-LACT), bovine serum albumin (BSA), immunoglobin G (IgG), and apoferritin. b) Inhibition of ThT-positive Aβ fibrillogenesis by **1** (TEG) and hybrid compounds with shorter (GABA) or longer ($(TEG)_2$) linker length or without linker (zero). (mean ± standard deviations of results, four separate runs, three replicates per run; *** $p \leq 0.001$ by Student's t-test). Clear anti-amyloid effects of all hybrid compounds are observed, with the zero linker being strongest.

(an indicator of amyloid fibril content) decreased upon application of **1** (Figure 3b), these higher fractions could not represent Aβ amyloid fibrils but rather irregularly structured high-molecular-weight complexes. Accordingly, transmission electron microscopy revealed the total lack of any remaining fibrillar structures in Aβ/**1** mixtures (Supporting Information, Figure S6), thus demonstrating that **1** inhibited Aβ oligomer assembly by driving Aβ aggregation

to nontoxic, non-amyloid complexes. As for native Aβ oligomer assembly inhibition in 7A2 cells (Supporting Information, Figure S5C), we also observed a structure–activity relationship of hybrid compounds in the cell-free ThT assay (Figure 3b), confirming that the zero-linker compound has strongest activity. Our biophysical analysis by three independent methods (density gradient centrifugation, ThT assay, and transmission electron microscopy), as well as our findings that monomeric Aβ is not elevated when Aβ oligomers are decreased (Figure 2b, 3a), lead us to conclude that rather than inhibiting Aβ oligomer assembly, hybrid compounds lead to incorrect, bioinactive, and non-amyloid Aβ misassembly, which could eventually be degraded more easily.

In conclusion, we demonstrated that chemical synthesis of two entirely different substance classes acting on the same target can be covalently linked to yield dramatic synergistic effects and lead to novel properties. Taking Aβ oligomers as an example, we also showed that two entirely different principles of drug development can be combined: polypeptides developed through mirror image phage display, which takes advantage of evolutionary algorithms to select for molecular recognition, and the rationally designed small-molecule β-sheet breakers. Our investigations may spark similar efforts with different target molecules and thereby greatly accelerate drug development.

Received: July 20, 2010
Published online: October 4, 2010

Keywords: aggregation · amyloid β peptides · drug design · molecular recognition · peptides

[1] B. Meunier, *Acc. Chem. Res.* **2008**, *41*, 69–77.
[2] C. Haass, D. J. Selkoe, *Nat. Rev. Mol. Cell Biol.* **2007**, *8*, 101–112.
[3] T. van Groen, K. Wiesehan, S. A. Funke, I. Kadish, L. Nagel-Steger, D. Willbold, *ChemMedChem* **2008**, *3*, 1848–1852.
[4] K. Wiesehan, K. Buder, R. P. Linke, S. Patt, M. Stoldt, E. Unger, B. Schmitt, E. Bucci, D. Willbold, *ChemBioChem* **2003**, *4*, 748–753.
[5] S. A. Funke, T. van Groen, I. Kadish, D. Bartnik, L. Nagel-Steger, O. Brener, T. Sehl, R. Batra-Safferling, C. Moriscot, G. Schoehn, A. H. C. Horn, A. Müller-Schiffmann, C. Korth, H. Sticht, D. Willbold, *ACS Chem. Neurosci.* **2010**, *1*, 639–648.
[6] T. Schrader, C. Kirsten, *J. Am. Chem. Soc.* **1997**, *119*, 12061–12068.
[7] P. Rzepecki, T. Schrader, *J. Am. Chem. Soc.* **2005**, *127*, 3016–3025.
[8] P. Rzepecki, L. Nagel-Steger, S. Feuerstein, U. Linne, O. Molt, R. Zadmard, K. Aschermann, M. Wehner, T. Schrader, D. Riesner, *J. Biol. Chem.* **2004**, *279*, 47497–47505.
[9] T. Lührs, C. Ritter, M. Adrian, D. Riek-Loher, B. Bohrmann, H. Dobeli, D. Schubert, R. Riek, *Proc. Natl. Acad. Sci. USA* **2005**, *102*, 17342–17347.
[10] M. B. Podlisny, B. L. Ostaszewski, S. L. Squazzo, E. H. Koo, R. E. Rydell, D. B. Teplow, D. J. Selkoe, *J. Biol. Chem.* **1995**, *270*, 9564–9570.
[11] a) G. M. Shankar, B. L. Bloodgood, M. Townsend, D. M. Walsh, D. J. Selkoe, B. L. Sabatini, *J. Neurosci.* **2007**, *27*, 2866–2875; b) G. M. Shankar, S. Li, T. H. Mehta, A. Garcia-Munoz, N. E. et al., *Nat. Med.* **2008**, *14*, 837–842.
[12] M. J. Rowan, I. Klyubin, Q. Wang, N. W. Hu, R. Anwyl, *Biochem. Soc. Trans.* **2007**, *35*, 1219–1223.
[13] R. V. Ward, K. H. Jennings, R. Jepras, W. Neville, D. E. Owen, J. Hawkins, G. Christie, J. B. Davis, A. George, E. H. Karran, D. R. Howlett, *Biochem. J.* **2000**, *348*, 137–144.

Angewandte International Edition Che

Angewandte Chemie
Eine Zeitschrift der Gesellschaft Deutscher Chemiker

Supporting Information

69451 Weinheim, Germany

Combining Independent Drug Classes into Superior, Synergistically Acting Hybrid Molecules**

Andreas Müller-Schiffmann, Julia März-Berberich, Aksana Andreyeva, Raik Rönicke, Dirk Bartnik, Oleksandr Brener, Janine Kutzsche, Anselm H. C. Horn, Marco Hellmert, Jolanta Polkowska, Kurt Gottmann, Klaus G. Reymann, S. Aileen Funke, Luitgart Nagel-Steger, Christine Moriscot, Guy Schoehn, Heinrich Sticht, Dieter Willbold, Thomas Schrader, and *Carsten Korth**

anie_201004437_sm_miscellaneous_information.pdf

Combining independent drug classes (Supplement) *1*

Supplementary Methods:

1. Synthesis of hybrid compounds:

Every hybrid compound consists of three different building blocks: Trimer, linker and D3 peptide. It was synthesized in a convergent semiautomatic manner. Three deferent linkers were introduced: ψ- aminobutyric acid (GABA, short), a triethylenglycol derivative (TEG, medium) and its dimer (TEG_2, long). First the PMB-protected Trimer-OH (10 steps conventional synthesis) was C-terminally elongated with a linker (up to 3 steps conventional synthesis). The whole Trimer-linker-OH unit was then coupled to resin- bound D3 peptide (SPPS, solid phase peptide synthesis), representing the last coupling step of an SPPS protocol. Finally, the hybrid compound was mildly cleaved off the resin at ambient temperature, followed by PMB protective group removal with hot trifluoroacetic acid (TFA).

D3-peptide was synthesized by Fmoc solid-phase peptide synthesis on an automated microwave peptide synthesizer (CEM, Liberty, Kamp-Lintfort, Germany). A Wang-resin was used as the polymer support, preloaded with Fmoc-D-Arg(Pbf) at an average loading of 0.51 mmol/g. Each coupling step was performed with 9-Fluorenyl-methoxycarbonyl-protected D-amino acid (0.20 M in DMF), O-(6- chlorobenzotriazol-1-yl)-*N,N,N´,N´*-tetra-methyluronium hexafluorophosphate, HCTU (0.50 M in DMF), and diisopropylethylamine (2.00 M in 1-methyl-2-pyrrolidinone). Removal of the Fmoc-protecting group was carried out with 20 % piperidine in *N,N*-dimethylformamide (DMF). After D3 SPPS, the free *N*- terminal amino group of the protected D3-peptidyl resin was coupled with para-methoxybenzyl (PMB)- protected Trimer-linker-OH (2.00 equiv), HCTU (2.00 equiv) and diisopropyletylamine (2.00 equiv) in DMF solution for 24 h. The whole PMB-protected aminopyrazoletrimer-linker-peptide hybrid compound was cleaved off the resin concomitant with deprotection of the amino acid side chains by means of an acidic cleavage cocktail (93 % TFA, 5 % triisopropylsilane and 2 % water) for 3.5 h at room temperature. After filtration, the solution was then cooled to 0 °C and the PMB-protected aminopyrazoletrimer-linker- peptide was precipitated and washed with cold diethyl ether. The colorless solid was subsequently dried in vacuo.

To cleave the PMB-protecting groups on the pyrazole nucleus, the colorless solid was heated under

argon in dry TFA for 3 h to 70 °C. The product precipitated after addition of cold Et_2O. The precipitate was filtered, washed with Et_2O and dried in vacuo. The deprotected hybrid compound was analyzed by ESI-TOF and HPLC and stored as lyophilized powder at -18 °C.

Trimer-D3 ("zerolinker")

^{1}H-NMR (500 MHz, H_2O/D_2O (90:10), 298 K): δ[ppm] = 0.79-0.85 (m, 6H), 1.11-1.16 (m, 6H), 1.33-2.02 (m, 21H), 2.73-2.82 (m, 4H), 3.16 (bs, 12H), 4.13-4.26 (m, 5H), 6.94 (bs, 2H), 7.16-7.31 (m, 10H), 7.61-7.67 (m, 2H), 8.20-8.61 (m, 12H). **HRMS (ESI):** $[M + 2H]^{2+}$ = *m/z* calcd for $C_{77}H_{123}N_{41}O_{21}$: 979.4945; found: 979.4913; $[M + 3H]^{3+}$ = *m/z* calcd for $C_{77}H_{124}N_{41}O_{21}$: 652.9960; found: 652.9971; $[M + 4H]^{4+}$ = *m/z* calcd for $C_{77}H_{125}N_{41}O_{21}$: 490.2494; found: 490.2501; $[M + 5H]^{5+}$ = *m/z* calcd for $C_{77}H_{126}N_{41}O_{21}$: 392.2005; found: 392.2033. **Analytical HPLC:** purity: 98.2 %; retention time: 18.5 min; 210 nm, RP-18 column, flow rate: 0.5 mL/min; linear gradient 95-40 % of eluent A in 30 min; (eluent A: 0.1% (v/v) TFA in water, eluent B: acetonitrile).

Trimer-GABA-D3

^{1}H-NMR (500 MHz, H_2O/D_2O (90:10), pH 2.7, 298 K): δ[ppm] = 0.82-0.90 (m, 6H), 1.13-1.19 (m, 4H), 1.30-2.08 (m, 25H), 2.72-2.87 (m, 2H), 3.18-3.28 (m, 12H), 3.53-3.66 (m, 4H), 3.75-3.79 (m, 1H), 4.15-4.36 (m, 4H), 6.72 (bs, 1H), 6.94 (s, 1H), 6.99 (s, 1H), 7.09 (s, 1H), 7.65 (s, 1H), 8.14-8.67 (m, 10H). **HRMS (ESI):** $[M + 2H]^{2+}$= *m/z* calcd for $C_{81}H_{130}N_{42}O_{22}$: 1022.0179; found: 1022.0202; $[M + H,Na]^{2+}$= *m/z* calcd for $C_{81}H_{129}N_{42}NaO_{22}$: 1032.5077; found: 1032.5090; $[M + 3H]^{3+}$ = *m/z* calcd for $C_{81}H_{131}N_{42}O_{27}$: 681.6810; found: 681.6832; $[M + 4H]^{4+}$ = *m/z* calcd for $C_{81}H_{132}N_{42}O_{22}$: 511.2620; found: 511.2630. **Analytical HPLC:** purity: 91.2 %; retention time: 18.7 min; 210 nm, RP-18 column, flow rate: 0.5 mL/min; linear gradient 95-40 % of eluent A in 30 min; (eluent A: 0.1% (v/v) TFA in water, eluent B: acetonitrile).

Trimer-TEG-D3 (JM169)

^{1}H-NMR (500 MHz, DMSO-d_6, 348 K): δ [ppm] = 0.81-0.89 (m, 6H), 1.03-1.06 (m, 4H), 1.19-1.22 (m, 2H), 1.27 (bs, 1H), 1.33 (bs, 1H), 1.56 (bs, 18H), 1.78 (bs, 6H), 1.88 (bs, 2H), 1.98 (bs, 1H), 2.09 (bs, 2H), 3.56-3.62 (m, 12H), 3.95 (s, 2H), 4.02 (bs, 2H), 4.20-4.41 (m, 8H), 4.63 (m, 4H), 7.01 (bs, 18H), 7.21-7.23 (m, 2H), 7.35 (s, 1H), 7.52 (bs, 5H), 7.83-7.86 (m, 4H), 8.06-8.18 (m,4H), 8.57 (bs, 1H), 10.73 (s,1H), 11.19 (s, 1H).

^{1}H-NMR (500 MHz, H_2O/D_2O (90:10), pH 4.50, 363 K): δ [ppm] = 1.46-1.54 (m, 6H), 1.78-1.82 (m, 6H), 2.15-2.54 (m, 24H), 2.88-2.96 (m, 1H), 3.39-3.52 (m, 2H), 3.84-3.97 (m, 13H), 4.21-4.88 (bs, 2H), 5.31-5.44 (m, 4H), 7.56 (s, 1H), 7.70 (s, 1H), 7.90-7.92 (m, 2H), 8.25 (bs, 1H), 8.28 (s, 1H), 8.45 (bs, NH), 9.12-9.14 (m, 2H). **HRMS (ESI):** $[M + 3H]^{3+}$= *m/z* calcd for $C_{85}H_{139}N_{42}O_{25}$: 716.3635; found: 716.3609; $[M + 2H, Na]^{3+}$= *m/z* calcd for $C_{85}H_{138}N_{42}NaO_{25}$: 723.6908; found: 723.6911; $[M + 4H]^{4+}$ = *m/z* calcd for $C_{85}H_{140}N_{42}O_{25}$: 537.2738; found: 537.2719. **Analytical HPLC:** purity: 98.8 %; retention time: 5.41 min; 210 nm, RP-18 column, flow rate: 0.5 mL/min; eluent: water + 0.1 %TFA / acetonitrile (70:30).

Trimer-TEG_2-D3

^{1}H-NMR (500 MHz, H_2O/D_2O (90:10), pH 3.5, 298 K): δ [ppm] = 0.83-0.90 (m, 6H), 1.14-2.03 (m, 27H), 2.75-2.86 (m, 2H), 3.20 (bs, 13H), 3.47-3.78 (m, 19H), 4.08-4.29 (m, 8H), 5.32 (bs, 1H), 6.71 (bs, 1H), 6.95 (s, 1H), 7.09 (s, 1H), 7.20-7.35 (m, 6H), 7.62-7-69 (m, 1H), 8.09-9.04 (m, 10H). **HRMS (ESI):** $[M + 2H]^{2+}$= *m/z* calcd for $C_{93}H_{153}N_{43}O_{29}$: 1168.5917; found: 1168.5978; $[M + 3H]^{3+}$= *m/z* calcd for $C_{93}H_{154}N_{43}O_{29}$: 779.3969; found: 779.4013; $[M + 4H]^{4+}$= *m/z* calcd for $C_{93}H_{155}N_{43}O_{29}$: 584.7995; found: 584.8027. **Analytical HPLC:** purity: 92.5 %; retention time: 19.8 min; 210 nm, RP-18 column, flow rate: 0.5 mL/min; linear gradient 95-40 % of eluent A in 30 min; (eluent A: 0.1% (v/v) TFA in water, eluent B: acetonitrile).

Synthesis of Trimer-TEG-KKKKKG (Poly-K):

Combining independent drug classes (Supplement) *4*

A Wang-resin, preloaded with Fmoc-glycine and an average loading of 0.78 mmol/g was used as a polymeric carrier. The coupling of Fmoc-protected amino acids was accomplished by using HBTU and diisopropylethylamine according to the following method: For each coupling step, Fmoc-Lys(Boc)-OH (8.00 equiv), HBTU (7.62 equiv) and diisopropyletylamine (16.00 equiv) were used in a DMF solution. Removal of the Fmoc-protecting group was carried out with 20 % piperidine in DMF (1 x 3 min, 1 x 7 min). After five cycles, the resin was coupled with the PMB-protected Trimer-TEG-OH (3.00 equiv), HBTU (3.30 equiv) and diisopropyletylamine (6.00 equiv) in DMF solution for 6 h.

The pyrazole-peptide compound was cleaved off the resin concomitant with deprotection of lysine´s ε-amino-Boc groups by means of an acidic cleavage cocktail (93 % TFA, 5 % TIS and 2 % water) during 3 h. The solution was then cooled to 0 °C and the PMB-protected pyrazole-peptide was precipitated and washed with cold diethyl ether. The colorless solid was dried in vacuo.

The cleavage of PMB-protecting groups was performed using the same procedure as the previous (hybrid compounds).

^{1}H-NMR (500 MHz, $CDCl_3$): δ [ppm] = 1.31 (bs, 10H), 1.49-1.65 (m, 20H), 2.76 (bs, 10H), 3.39-3.42 (m, 2H), 3.52-3.61 (m, 10H), 3.69-3.84 (m, 2H), 3.93 (s, 2H), 4.20-4.33 (m, 5H), 7.58 (bs), 7.93-8.01 (m, 4H), 8.11 (d, 1H), 8.26 (t, 1H), 8.68 (bs, 1H), 11.14 (s, 1H), 11.44 (s, 1H), 12.77 (bs, 1H), 13.19 (bs, 1H), 13.50 (bs, 1H), 14.96 (bs, 1H). **^{13}C-NMR** (125.7 MHz, $CDCl_3$): $\mathcal{O}$ [ppm] = 22.0, 22.1, 22.2, 22.3, 26.5, 26.6, 26.7, 31.3, 31.4, 31.5, 38.6, 38.7, 51.8, 52.1, 52.2, 52.3, 68.8, 69.5, 69.6, 69.7, 70.2, 102.4, 116.0, 118.4, 157.8, 158.1, 158.3, 158.6, 169.4, 171.1, 171.2, 171.3, 171.4, 171.5, 171.7. **HRMS (ESI):** $[M + 2H]^{2+}$ = *m/z* calcd for $C_{52}H_{89}N_{21}O_{16}$: 631.8393; found: 631.8493, $[M + 3H]^{3+}$ = *m/z* calcd for $C_{52}H_{90}N_{21}O_{16}$: 421.5619; found: 421.5656.

2. Culture of primary cortical mouse neurons and whole cell recordings

Cultures of cortical neurons were prepared from C57BL/6J mouse fetuses at embryonic day 19 (E19) as described previously [1]. Neurons were grown in Neurobasal A medium (GIBCO) supplemented with 2% NS-21 [2], 100 U/mL penicillin, 100 µg/mL streptomycin, GlutaMAX (GIBCO) on glass coverslips coated

with poly-L-ornithine (1 mg/mL). After 8 days *in vitro* half of the culture medium was exchanged with 7PA2 supernatant (containing 27.7 nM Aβ) and JM169 , D3, and aminopyrazole (AP) were added at a concentration of 10 µM. Neurons incubated with the culture medium used for the production of 7PA2 supernatant (vehicle) served as control. mEPSCs were recorded after 3 days incubation.

mEPSC recordings: Whole-cell voltage-clamp recordings were obtained as described previously [3] at a holding potential of -60 mV. Gabazine (10 µM) and tetrodotoxin (1 µM) were added to the external solution (130 mM NaCl, 5 mM KCl, 2.5 mM $CaCl_2$, 1 mM $MgCl_2$, 20 mM HEPES, pH 7.3) to isolate AMPA receptor mediated miniature EPSCs. All recordings were performed at room temperature. Patch electrodes (3-4 M?) were filled with an internal solution containing the following: 110 mM KCl, 0.25 mM$CaCl_2$, 10 mM EGTA, 20 mM HEPES (adjusted to pH 7.3 with KOH).

mEPSC frequency was reversed compared in cortical neurons incubated with 7PA2 supernatant for 3 days (n = 49 cells, 3 mice) as compared to neurons incubated with vehicle (n=37 cells, 3 mice). For neurons incubated with 7PA2 supernatant and JM169, D3, aminopyrazole trimer (AP) the following numbers of experiments were performed: vehicle + JM169, n=20 cells; 7PA2 supernatant + JM169, n=28 cells, vehicle + D3 + AP, n=26 cells; 7PA2 supernatant + D3 + aminopyrazole trimer (AP) n=29 cells.

3. Thioflavin T (ThT) assays

Aβ(1-42)-peptide (Bachem, Bubendorf, Germany) was prepared in 1,1,1,3,3,3-hexafluoro-2-propanol (HFIP), lyophilized, redissolved in DMSO and stored as (2 µL)-aliquots at -20 °C. The ligand was dissolved in bidestilled H_2O as a 300 µM stock solution and was stored at 4 °C. Thioflavine T (ThT) measurements were carried out after 72 h aggregation under shaking at 37 °C in a 384-well plate (Nunc GmbH, Wiesbaden, Germany) in an InfiniTe 200 plate reader (Tecan GmbH, Crailsheim, Germany). Fluorescence intensity was measured at 37 °C, 446 nm excitation wavelength (bandwidth 9 nm) and 490 nm emission wavelength with a bandwidth of 20 nm. Each data point was averaged over 40 lamp flashes. The 384-well plate was covered with a transparent and DMSO-stable film (Nunc GmbH,

Wiesbaden, Germany). Each single sample was composed of 10 µM Aβ(1-42) in 1 x PBS (phosphate buffered saline), 6.67 % DMSO, 3.03 µM ThT and 60 µM of the hybrid compound. For graph representation emission values of fourfold samples were averaged. The ligand was measured separately, both in 1 x PBS and 1 x PBS with ThT to exclude any potential interactions between ligand and ThT.

ThT displacement experiments were done in PBS similar to the protocol of Hintersteiner et al. [4]. 10µM Aβ were fibrillized with agitation for 5 days at 37°C in the presence of 3.03 µM ThT. Then increasing amounts of the ligand were added, ranging from 7.5 µM to 30 µM, and incubated for another 5 days. The fluorescence emission spectrum was scanned from 476 to 650 nm. A functional EC_{50} of JM169 for releasing 50% of bound ThT from synthetic Aβ fibrils was determined to be 5 µM (ThT replacement assay, see Supplementary Methods). The respective dissociation constant of JM169 was calculated from the displacement assay to be 12 nM. This evaluation was carried out by standard nonlinear regression analysis, under the assumption of a 1:1 binding stochiometry, using the SigmaPlot 10.0 software (Systat).

It may be argued that the established ThT displacement assay only measures the affinity of the test compound towards preformed fibrils and not towards the most neurotoxic oligomer species. However, the latter is problematic, since Aβ oligomers in our assay are only transient species which are effectively eliminated by the hybrid compounds. On the other hand, our proposed mechanistic model does not require direct binding towards these oligomers: independent evidence from CD spectroscopy, ultracentrifugation and electron microscopy suggests, that binding of our hybrid compounds to preformed Aβ fibrils is followed by a redirection of the self-assembly process, leading to amorphous, non-toxic high molecular weight aggregates, but leaving behind no toxic oligomers.

4. Density gradient centrifugation

Density gradient centrifugation was performed according to [5]. Preformed gradients of optiprep (Axis-Shield, Oslo, Norway) of about 2 mL volume were overlaid with 100 µL sample volumes, containing 125 µM of synthetic Aß(1-42), or 125 µM Aß(1-42) and 62.5 µM JM169; and 125 µM Aß(1-42) and 125 µM

LPFFD (a control peptide without aminopyrazole; bottom panel). After centrifugation at 259,000 *x g* for 3 h at 4 °C in a TL100 ultracentrifuge (Beckman-Coulter, Palo Alto, USA) with TLS-55 rotor 14 fractions of 140 µL each were harvested from top to bottom. These fractions and the pellet of each tube were subsequently analyzed with respect to their Aß42 content by denaturing, discontinuous Tris-Tricine SDS-PAGE optimized for separation of small peptides or proteins [6]. Mark12 (Invitrogen, Germany) with molecular weights between 2,500 and 200,000 were used as a size standards. The protein content was visualised by silver staining [7].

5. Long term potentiation in acute hippocampal slices

For Aß oligomer preparation, the lyophilized peptide (Amyloid ß (1–42), MoBiTec) was dissolved in HFIP (Sigma, St. Louis, MO) to 1 mM. The solution was aliquoted, HFIP was evaporated and the peptide stored at -80°C. Twenty-four hours before use, amyloid-ß-peptide was dissolved (100 µM) in dimethylsulfoxide (DMSO; Sigma) and sonicated. Oligomeric amyloid ß peptide was obtained by diluting this stock solution to 20µM in F12/DMEM (without glutamine, Biochrom) and incubating at 4°C for 24 h. JM169 was applied to the Aß (1-42) oligomer preparation at a final concentration of 10 µM. To proof oligomer generation SDS-PAGE and subsequent Coomassie stain with Instant blue Coomassie stain Kit (Expedion) were performed.

The animals used were maintained under constant environmental conditions, with an ambient temperature of 21 ± 2 °C, a relative humidity of 40%, a 12-h light–dark cycle and free access to food and water. All animal procedures have been approved by the Ethics Committee of the German Federal State of Saxony-Anhalt (Sachsen-Anhalt), and are in accordance with the European Communities Council Directive (86/609/EEC).

Hippocampal slices (400 µm thick) were prepared from 4-months-old male C57/Bl6 mice (Institute breeding stock). Briefly, both hippocampi were isolated and transferred into a pre-chamber containing 8 ml permanently carbogen-gasified artificial cerebrospinal fluid (ACSF), to allow substance application. Aß (1-42) oligomers were applied to the slices at a concentration of 500 nM for two hours at room temperature. Slices were then transferred into a submerged-type recording chamber and were allowed

to recover for at least 30 min before the experiment started. The chamber was constantly perfused with artificial cerebrospinal fluid (ACSF) at a rate of 2.5 mL/min at 33±1 °C.

Synaptic responses were elicited by stimulation of the Schaffer collateral–commissural fibers in the stratum radiatum of the CA1 region using lacquer-coated stainless steel stimulating electrodes. Glass electrodes (filled with ACSF, 1–4 MO) were placed in the apical dendritic layer to record field excitatory postsynaptic potentials (fEPSPs). The initial slope of the fEPSP was used as a measure of this potential. The stimulus strength of the test pulses was adjusted to 30% of the EPSP maximum. During baseline recording, single stimuli were applied every minute (0.0166 Hz) and were averaged every 5 min. Once a stable baseline had been established, long-term potentiation was induced by applying a strong tetanic stimulation consisting of three trains at 10 min intervals of 100 pulses each at an interval of 10 ms (single pulses width 0.2 ms). The following number of experiments was performed: control: n= 8; Aß: n=8; Aß+ JM169: n=7.

6. Molecular modeling

Starting point for the calculations was the $Aß_{42}$ fibril structure obtained from NMR spectroscopic data by Lührs et al. [8]. For the Trimer-TEG-D3 simulations, the stack of five $Aß_{17-42}$ chains present in the respective structure (pdb entry 2BEG) was extended by four additional copies of the peptide to provide a sufficiently large surface patch for ligand interaction. In addition, all amyloid peptides were extended *N*-terminally by residue 15 and 16 to ensure ß-sheet complementarity within the U-shaped molecule, following the same strategy as described by Zheng et al. [9]. The *N*-terminus was capped by an acetyl group, whereas the C-terminus was left ionic.

The isolated aminopyrazole trimer was docked to the terminal chain A of the nonamer in such a way that the ligand formed hydrogen bonds to the Aß backbone peptide groups of Gln15 through Ala21. Evidence for this binding site comes from previous NMR spectroscopic studies as well as near UV CD spectroscopy (see Supplementary Figure 1) which indicated interactions of pyrazole ligands with the aromatic side chains of Phe19 and Phe20 [10, 11].

Comparative molecular modelling and molecular dynamics simulations were performed for Trimer-TEG-D3 and Trimer-TEG-KKKKKG. The basic D3 and polylysine peptides were modelled in spatial proximity of the Aß surface patch with the highest excess of negative charge, which is formed by the Glu22 sidechains of adjacent monomers. The basic peptides were modelled in an extended conformation in order to allow multiple electrostatic interactions with Aß. In order to test the conformational stability of the bound ligands, 10-ns molecular dynamics simulations with the Amber9 suite of programs [12] were performed using a standard protocol [13]: the parm99SB parameter set [14] was applied for the peptides, the gaff force field [15] was used to describe the trimer ligand and the TEG spacer. Atomic charges for these two organic compounds were generated based on quantum chemical calculations at the HF/6-31G(d) level, i.e. following the strategy recommended in the Amber manual.

7. Cell culture/ Immunoprecipitation/ Western blot analysis

The anti oligomerization experiments were performed according to the protocol described by [16]. Briefly, 7PA2 cells overexpressing APP751 V717F were cultured in DMEM with 10% fetal bovine serum. $3*10^5$ cells were seeded into 10 cm cell culture dishes und treated as indicated in the figures. After 5 days the medium was replaced with serum free medium and incubated for 72 h. We explain the relatively high effective concentrations of the administered JM169 compared to the low concentrations of Aβ in the supernatant of 7PA2 cells (mid nM range) is due to a lower bioavailability of JM169 in the cell culture buffers used with increased unspecific binding. Cleared supernatants were immunoprecipitated overnight at 4 °C with NHS-sepharose coupled mAB-IC16, recognizing aa 2-8 of Aβ. After washing with PBS samples were electrophoresed on 10-20 % tricine peptide gels (Biorad, Hercules, CA) and transferred to 0.2 µM nitrocellulose membranes at 400 mA for 2 h. Filters were boiled 5 min in PBS [17] and blocked overnight at 4 °C with 5% fat-free milk in PBS containg 0.05 % Tween 20 (PBS-T). After washing in PBS-T the membranes were probed with 1:200 diluted monoclonal 4G8 (Signet, Dedhem, MA). Bound antibody was detected with horseradish peroxidase conjugated goat anti-mouse Ig (at 1:25000) (Thermo Scientific, Bonn, Germany) and the Amersham ECL Western Blotting Detection Reagent (GE, Buckinghamshire, UK). For detection of APP and APP-CTF cells were lysed in 1 ml lysis buffer (50 mM

Tris pH = 8, 150 mM NaCl, 1% NP40, 5 mM EDTA) including the complete protease inhibitor cocktail (Roche, Mannheim, Germany). 15 µg of lysates were separated on a NuPAGE 4-12% Bis-Tris gel (Invitrogen, Carlsbad, CA). After transfer on a 0.2 µm NC-membrane APP and APP-CTF were detected by CT15 polyclonal rabbit antiserum (at 1:3500) and goat-anti rabbit Ig (at 1: 25000) (Thermo Scientific, Bonn, Germany). Quantitation was performed by densitometry using NIH Image.

8. Cell viability assay (MTT)

$1x10^4$ 7PA2 cells were seeded into a 48 well plate. After 48 h the indicated concentrations of JM169 or 5% DMSO as a control were added. After incubation of 48 h 20 µL of a 5 mg/mL MTT solution was mixed into each well and incubated for 5 h at 37°C. The medium was aspirated and the formazan was resuspended into 200 µL DMSO. Optical densities were measured at 560 nm with substraction of background at 670 nm using a Tecan Safire microplate reader (Tecan, Switzerland).

9. Antibodies

Monoclonal antibody IC16 (IgG2a) was raised to human Aβ1-16 and was mapped with deletion mutants to specifically recognize an epitope within residues 2-8 [18]. IC16 stains Aβ-plaques in brain sections of patients with AD and binds with one-digit nanomolar affinity to natural as well as to synthetic monomeric and low-n oligomeric Aβ. Antibodies to the solvent-exposed *N*-termiuns of Aβ have been shown to reliably bind Aβ oligomers [19]. Monoclonal antibody 4G8 (Signet, Dedham, MA) binds to an epitope within human Aβ corresponding to residues 17-24. CT15 is a polyclonal rabbit antiserum, recognizing c-terminal 15 amino acids of APP [20].

9. Statistical analysis

Student's t-test was used for comparison of pairs of parametric variables where indicated. ANOVA was used for comparing multiple measurements where indicated.

Supplementary Figures:

Supplementary Figure 1: Secondary structure changes in A⇓ upon aminopyrazole trimer binding to F19, F20 indicated by near-UV CD spectroscopy

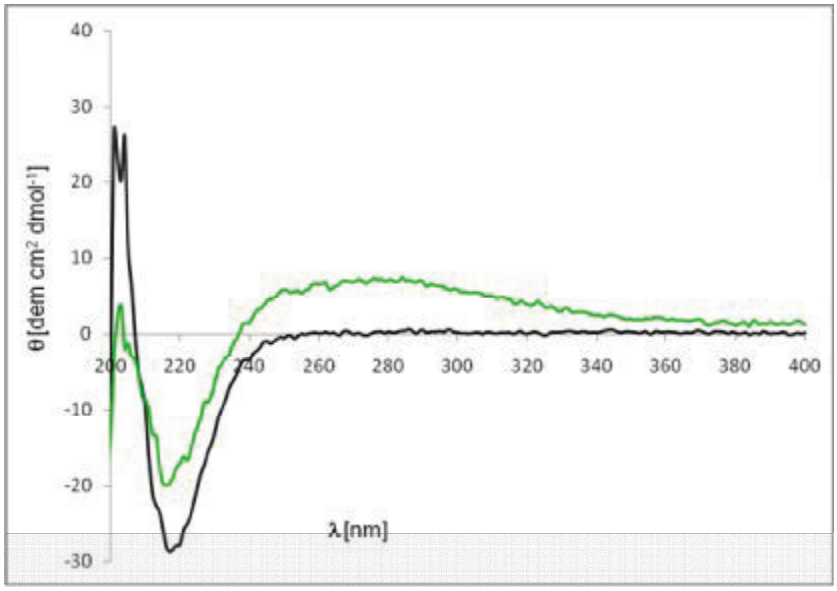

Black line: CD-spectrum of soluble Aβ(1-42) aggregates (10 µM) after 2 days incubation in 5 µM potassium phosphate buffer (pH 7.3) at room temperature. Green line: a complex between Aβ(1-42) and Trimer-TEG- lysine (10 µM) after 2 days incubation in 5 µM potassium phosphate buffer (pH 7.3) at room temperature. A new CD band at 260-320 nm is induced with a positive maximum at 275 nm (induced cotton effect) due to tight complex formation between the two consecutive phenylalanines (F19, F20) and the pyrazole nuclei.

These results complement detailed conformational NMR analyses between aminopyrazole derivatives and the model peptide KLVFF (residues 16-20 in Aβ) that led to the observation of downfield NH-shifts and upfield shifts of aromatic protons in both phenylalanines indicating π-stacking interactions [11]; subsequent Monte-Carlo simulations in water yielded a complex structure with two consecutive phenylalanines sandwiching an aminopyrazole nucleus. Based on these data, it is conceivable that the

aminopyrazole trimer hydrogen-bonded to the solvent-exposed top face of the KLVFF backbone and simultaneously engaged in sandwich-type π-stacking with both phenylalanine residues. Molecular dynamics simulations of this complex in an explicit solvent environment proved that both the backbone hydrogen bonds as well as the π-stacking interactions remained stable.

Supplementary Figure 2: Molecular dynamics simulations of Trimer-TEG-D3 and Trimer-TEG-KKKKKG.

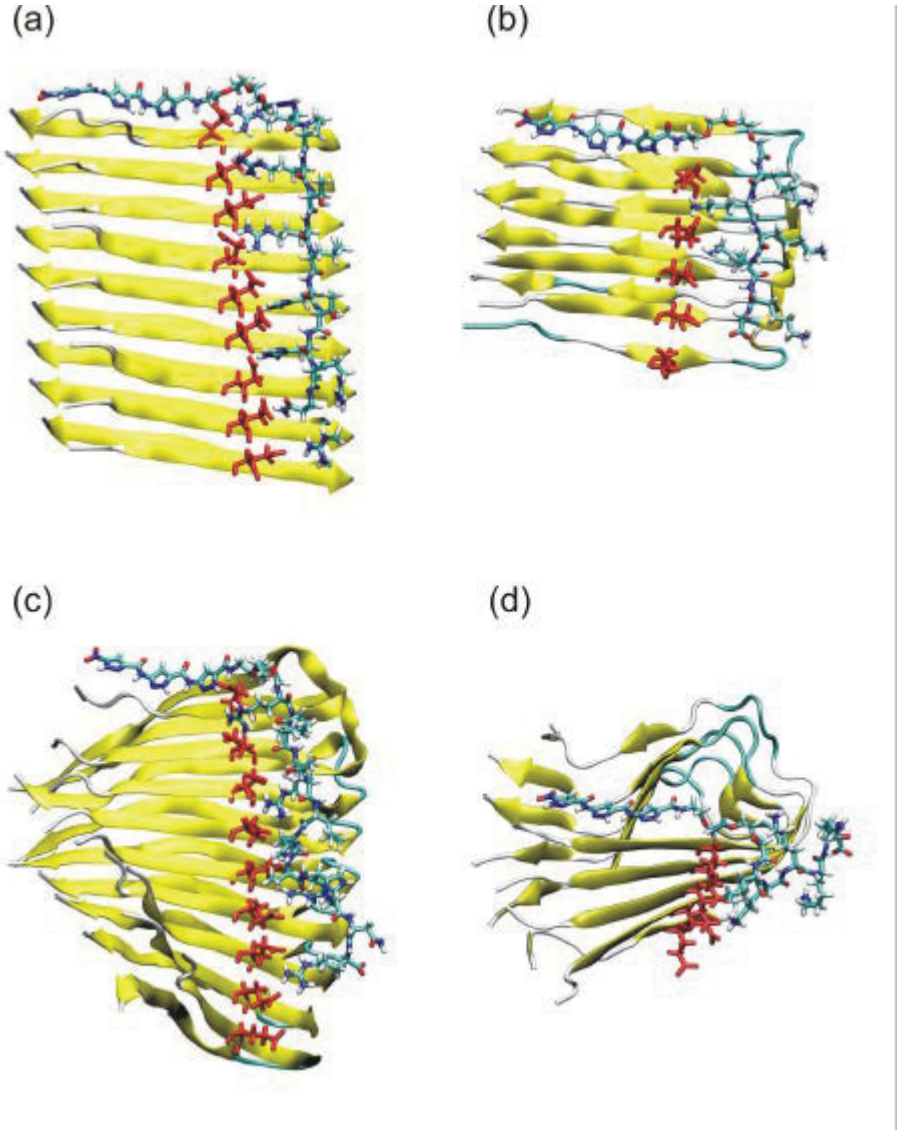

Initial models of Trimer-TEG-D3 (a) and Trimer-TEG-KKKKKG (b) in complex with a segment of the Aβ-protofibril. The ligands are shown in stick presentation and colored according to their atom type. The E22 residues of adjacent Aβ-monomers, which form a negatively charged surface patch, are shown as red sticks.
Structures of Trimer-TEG-D3 (c) and Trimer-TEG-KKKKKG (d) after 10 ns of molecular dynamics simulation. Note that the D3 peptide still tightly interacts with the E22 sidechains, while in Trimer-TEG-KKKKKG only the terminal lysine forms a salt-bridge.

Combining independent drug classes (Supplement) *14*

Supplementary Figure 3: Effect of very high concentrations of single compounds on oligomerization of A⇓

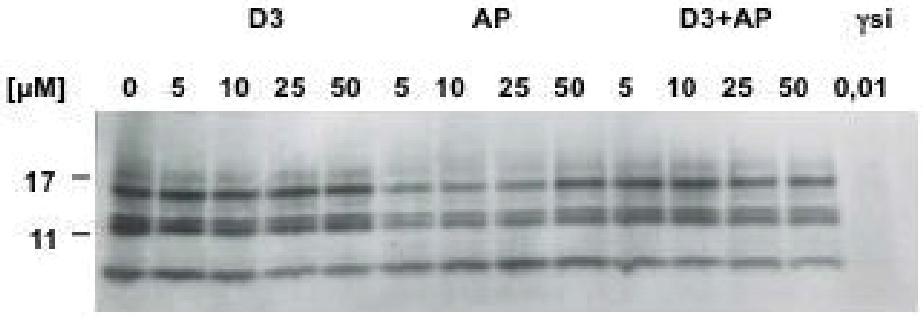

Application of up to 50 µM of D3 or AP separatedly or in combination to 7PA2 cells yielded no dose dependent reduction of oligomeric Aβ. Thus, covalently linkage of D3 to AP clearly leads to a strong synergistic impact on naturally secreted low-n oligomeric Aβ (Figure 2A).

Supplementary Figure 4: Cytotoxicity of hybrid compound JM169

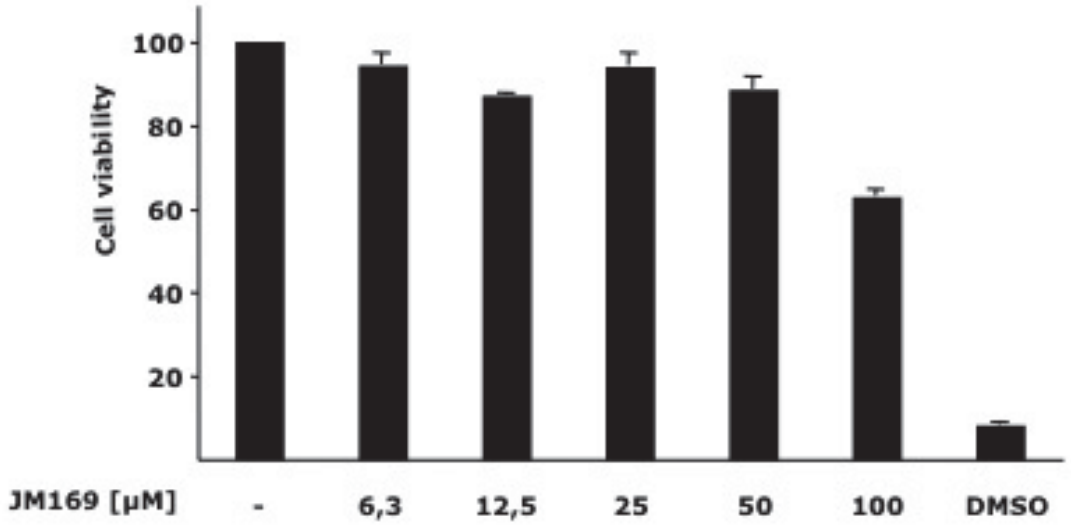

JM169 shows no general cell toxicity in concentrations up to 50 µM. 7PA2 cells were treated for 48 h with increasing concentrations of JM169. Only with 100 µM a significant reduction of cell viability via an MTT assay was observed (LC_{50} >100 µM); 5% DMSO was used as a positive toxic control (see text). These data were confirmed by a second assay based on LDH release (data not shown). Together the results demonstrate the non-toxic nature of the JM169 concentrations used in Figure 2A.

Combining independent drug classes (Supplement) 16

Supplementary Figure 5: Effect of variable linker length on A⇓ oligomerization in 7PA2 cells

A.

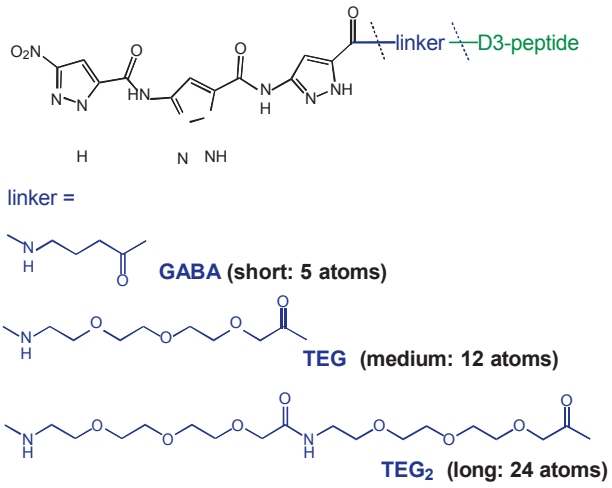

B.

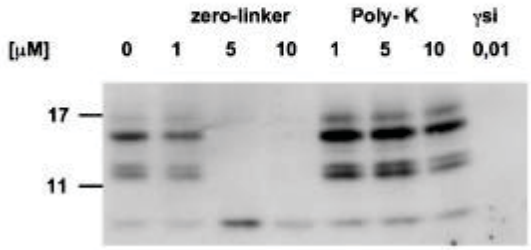

C.

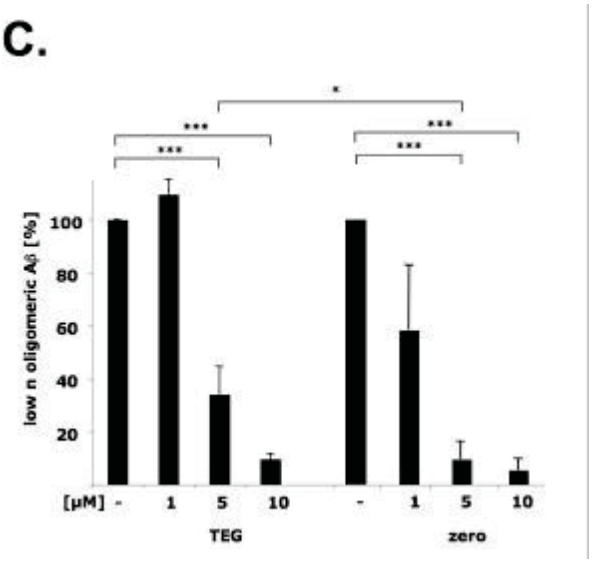

A. Linker structures used. **B.** Western blot of affinity-purified Aβ oligomers after treatment of 7PA2 cells as indicated (similar to Figure 2A). Hybrid compound with no linker ("zero-linker") was more efficient than hybrid compounds with a longer linker (TEG); treatment with a hybrid compound consisting of aminopyrazole (AP) and a pentalysine linked by TEG ("Poly-K") did not prevent Aβ oligomer assembly at concentrations up to 10 μM where the D3 containing hybrid compounds showed efficacy. A γ-secretase inhibitor was used as a positive control (γ-si) **C.** Western blot of affinity-purified Aβ oligomers after treatment of 7PA2 cells as indicated (similar to Figure 2A). The superior effects of treatment by the zero-linker compound compared to JM169 were statistically significant at a dosage of 5 μM among four

independent experiments (Student's t-test; * $p < 0.01$, *** $p < 0.0001$; error bars are standard deviations). Effects of hybrid compounds linked by the short GABA linker were similar to that of no linker and those of the TEG_2 linker similar to those of the TEG linker (data not shown).

Combining independent drug classes (Supplement) *17*

Supplementary Figure 6: Transmission electron microscopy of A⇓ incubated with JM169

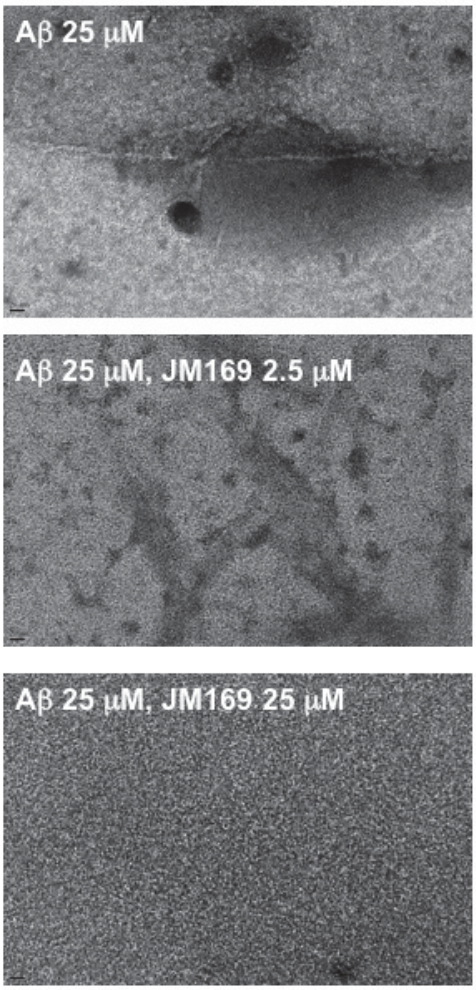

Synthetic Aβ(1-42) was plated at a concentration of 25 μM, together with different concentrations of JM169, as indicated, for 4 hours at room temperature. Peptide aggregates were adsorbed on formvar / carbon coated copper grids (Plano GmbH, Wetzlar), washed and negatively stained with 1% uranyl acetate (pH 4.0). The grids were observed using a LaB6 CM12 EM (FEI/Philips), operating at 120 kV with a nominal magnification of 40,000 x. Images were taken using an Orius 832 SC1000 CCD camera (4008 x 2672 pixels) (Gatan inc.).

References

[1] R. Mohrmann, V. Lessmann, K. Gottmann, *Neuroscience* 2003, *117*, 7-18.
[2] Y. Chen, B. Stevens, J. Chang, J. Milbrandt, B. A. Barres, J. W. Hell, *J. Neurosci. Meth.* 2008, *171*, 239-247.
[3] K. Jungling, V. Eulenburg, R. Moore, R. Kemler, V. Lessmann, K. Gottmann, *J. Neurosci.* 2006, *26*, 6968-6978.
[4] M. Hintersteiner, A. Enz, P. Frey, A. L. Jaton, W. Kinzy, R. Kneuer, U. Neumann, M. Rudin, M. Staufenbiel, M. Stoeckli, K. H. Wiederhold, H. U. Gremlich, *Nat. Biotechnol.* 2005, *23*, 552-554.
[5] R. V. Ward, K. H. Jennings, R. Jepras, W. Neville, D. E. Owen, J. Hawkins, G. Christie, J. B. Davis, A. George, E. H. Karran, D. R. Howlett, *Biochem. J.* 2000, *348 Pt 1*, 137-144; P. Rzepecki, L. Nagel-Steger, S. Feuerstein, U. Linne, O. Molt, R. Zadmard, K. Aschermann, M. Wehner, T. Schrader, D. Riesner, *J. Biol. Chem.* 2004, *279*, 47497-47505.
[6] H. Schagger, G. von Jagow, *Anal. Biochem.* 1987, *166*, 368-379.
[7] J. Heukeshoven, R. Dernick, *Electrophoresis* 1988, *9*, 28-32.
[8] T. Lührs, C. Ritter, M. Adrian, D. Riek-Loher, B. Bohrmann, H. Dobeli, D. Schubert, R. Riek, *Proc. Natl. Acad. Sci. U S A* 2005, *102*, 17342-17347.
[9] J. Zheng, H. Jang, B. Ma, C. J. Tsai, R. Nussinov, *Biophys. J.* 2007, *93*, 3046-3057.
[10] P. Rzepecki, H. Gallmeier, N. Geib, K. Cernovska, B. Konig, T. Schrader, *J. Org. Chem.* 2004, *69*, 5168-5178.
[11] P. Rzepecki, T. Schrader, *J. Am. Chem. Soc.* 2005, *127*, 3016-3025.
[12] D. A. Case, T. A. Darden, T. E. Cheatham, C. L. Simmerling, J. Wang, R. E. Duke, R. Luo, K. M. Merz, D. A. Pearlman, M. Crowley, R. C. Walker, W. Zhang, B. Wang, S. Hayik, A. Roitberg, G. Seabra, K. F. Wong, F. Paesani, X. Wu, S. Brozell, V. Tsui, H. Gohlke, L. Yang, C. Tan, J. Mongan, V. Hornak, G. Cui, P. Beroza, D. H. Mathews, C. Schafmeister, W. S. Ross, P. A. Kollman, University of California Press, San Francisco, 2006.
[13] H. Meiselbach, A. H. Horn, T. Harrer, H. Sticht, *J Mol Model* 2007, *13*, 297-304.
[14] V. Hornak, R. Abel, A. Okur, B. Strockbine, A. Roitberg, C. Simmerling, *Proteins* 2006, *65*, 712-725; J. Wang, P. Cieplak, P. A. Kollman, *J. Comput. Chem.* 2000, *21*, 1049-1074.
[15] J. Wang, R. M. Wolf, J. W. Caldwell, P. A. Kollman, D. A. Case, *J. Comput. Chem.* 2004, *25*, 1157-1174.
[16] D. M. Walsh, I. Klyubin, G. M. Shankar, M. Townsend, J. V. Fadeeva, V. Betts, M. B. Podlisny, J. P. Cleary, K. H. Ashe, M. J. Rowan, D. J. Selkoe, *Biochem. Soc. Trans.* 2005, *33*, 1087-1090; D. M. Walsh, M. Townsend, M. B. Podlisny, G. M. Shankar, J. V. Fadeeva, O. El Agnaf, D. M. Hartley, D. J. Selkoe, *J. Neurosci.* 2005, *25*, 2455-2462.
[17] N. Ida, T. Hartmann, J. Pantel, J. Schroder, R. Zerfass, H. Forstl, R. Sandbrink, C. L. Masters, K. Beyreuther, *J. Bio.l Chem.* 1996, *271*, 22908-22914.
[18] S. Jager, S. Leuchtenberger, A. Martin, E. Czirr, J. Wesselowski, M. Dieckmann, E. Waldron, C. Korth, E. H. Koo, M. Heneka, S. Weggen, C. U. Pietrzik, *J. Neurochem.* 2009, *111*, 1369-1382.
[19] I. Klyubin, V. Betts, A. T. Welzel, K. Blennow, H. Zetterberg, A. Wallin, C. A. Lemere, W. K. Cullen, Y. Peng, T. Wisniewski, D. J. Selkoe, R. Anwyl, D. M. Walsh, M. J. Rowan, *J. Neurosci.* 2008, *28*, 4231-4237.
[20] S. S. Sisodia, E. H. Koo, P. N. Hoffman, G. Perry, D. L. Price, *J. Neurosci.* 1993, *13*, 3136-3142.

2.1.4 QIAD assay for quantitating the efficacy of Aβ oligomer removal

Eingereicht bei: Scientific Reports Nature

Impact Factor: 5,578

Eigenanteil an der Publikation: 35 %

Entwickelung und Durchführung von QIAD; Durchführung und Auswertung von CD-Spektroskopie, AFM, Toxizitätstests, Thioflavin-T-Verfahren; D3D3- Design; Verfassen des Manuskripts.

QIAD assay for quantitating the efficacy of Aβ oligomer removal

Oleksandr Brener[1,2], Tina Dunkelmann[1], Lothar Gremer[1,2], Thomas van Groen[3], Ewa A. Mirecka[2], Inga Kadish[3], Antje Willuweit[4], Janine Kutzsche[1], Dagmar Jürgens[1], Filipp Oesterhelt[2], Karl-Josef Langen[4,5], Hans-Ulrich Demuth[6], Arnold Janssen[8], Wolfgang Hoyer[1,2], Susanne A. Funke[1,7], Luitgard Nagel-Steger[1,2], Dieter Willbold[1,2,*]

[1] Institute of Complex Systems, Structural Biochemistry (ICS-6), Research Centre Jülich, 52425 Jülich, Germany
[2] Institut für Physikalische Biologie, Heinrich-Heine-Universität Düsseldorf, 40225 Düsseldorf, Germany
[3] Department of Cell, Developmental, and Integrative Biology, University of Alabama at Birmingham (UAB), Birmingham, AL, USA
[4] Institute of Neuroscience and Medicine (INM-4), Research Centre Jülich (FZJ), 52425 Jülich, Germany
[5] Department of Nuclear Medicine, RWTH Aachen University Clinic, 52074 Aachen, Germany
[6] Fraunhofer Institute for Cell Therapy and Immunology, Dep. Molecular Drug Biochemistry and Therapy, 04103 Halle, Germany
[7] Bioanalytik, Hochschule für Angewandte Wissenschaften, Coburg, Germany
[8] Institute of Mathematics, Lehrstuhl für Statistik und Wahrscheinlichkeitstheorie, Heinrich-Heine-Universität Düsseldorf, 40225 Düsseldorf, Germany

[*]Correspondence: d.willbold@fz-juelich.de

Strong evidence exists for a central role of amyloid-β oligomers in the pathogenesis of Alzheimer's disease. We have developed a fast, reliable and robust *in vitro* assay, termed QIAD, to quantify the Aβ oligomer eliminating potential of agents. We demonstrate the predictive power of the assay for *in vivo* efficacy by comparing QIAD outcomes of two therapeutically interesting compounds with their treatment effects in animal models of Alzheimer´s disease.

Alzheimer's disease (AD) is a progressive neurodegenerative disorder, which is the most common cause of dementia and is forecasted to affect 1 out of 85 people worldwide in 2050[1,2]. Different species of amyloid-β (Aβ) in various aggregation states are responsible for development and progression of AD. Growing evidence exists that instead of Aβ monomers or fibrils, small and diffusible Aβ oligomers seem to be decisive for disease development and

progression[3]. Although a large number of differently sized and shaped Aβ oligomers and protofibrils have been described[3], the exact nature of the toxic entities remains elusive. Nevertheless, the potency to eliminate Aβ oligomers is, from the current point of view, one of the most desirable criteria for the selection of agents as lead compounds for drug development towards AD treatment[4]. Any screening for oligomer eliminating compounds requires a well characterized target. Therefore, preparation, purification and quantification of specific Aβ oligomers, which are representative for the toxic oligomers involved in AD pathogenesis, are urgently needed in AD drug development. Quantitative assessment of Aβ assembly size-distributions is difficult, because the heterogeneity of *in vitro* obtained Aβ assemblies[5] impedes most of the standard analytical methods.

We have designed an assay for the quantitative determination of interference with Aβ aggregate size distribution (QIAD). It consists of the following steps **(Fig 1a)**: i) preparation of Aβ assemblies containing the target aggregate species by Aβ pre-incubation; ii) incubation with and without the agent of interest; iii) separation of Aβ assemblies by density gradient centrifugation (DGC) and subsequent fractionation; and iv) determination of the total Aβ amount in each fraction by integrating the Aβ absorption signal during reversed-phase high performance liquid chromatography (RP-HPLC) analysis. The principle of the QIAD assay can easily be transferred to measure the quantitative interference on aggregates consisting of aggregation-prone peptides or proteins other than Aβ. Thus, to avoid any confusion with QIAD variants yet to come, we have termed the Aβ-specific QIAD assay "Aβ-QIAD".

DGC allows matrix-free separation and fractionation of different Aβ assemblies according to their sedimentation coefficients, which are dependent on particle size and shape[6,7]. DGC has been used previously to investigate the effect of agent candidates on the size distribution of Aβ aggregates formed *in vitro*[8]. In the Aβ-QIAD assay, the quantitative analysis of the Aβ content

of each fraction is reliably accomplished by UV absorption analysis during analytical RP-HPLC under denaturing conditions (**Fig. 1b**). Concomitantly, the density gradient material iodixanol was separated from Aβ, enabling online UV absorption determination to yield the total Aβ amounts in each DGC fraction (see Methods part for details) independent of the Aβ conformation, the percentage of iodixanol and potential epitope blocking (**Fig. 1b,c**). Importantly, the recovery rate of the complete procedure could be calculated by summing up the Aβ contents of all DGC fractions. Determination of the recovery rates in experiments performed on synthetic Aβ is an important control, because it is known that Aβ is depleted at various application steps by unspecific binding to various surfaces[9] potentially leading to false conclusions. Since Aβ recovery rates are rarely demonstrated[10] in the AD research field, the herein described procedure reliably yielded total Aβ recovery rates close to 100 %, i.e., 95.6 ± 7.9 % for control DGC runs (Aβ without agent) and 89.2 ± 16.1 % for DGC runs in the presence of agents. Moreover, the method described here allows the quantification of yields for any DGC-separated Aβ fraction within the sample. For example, the average amount of the Aβ oligomers (fractions 4 to 6) in eleven independent preparations was 31.7 ± 3.9 % (**Fig. 2a**).

Although we cannot avoid heterogeneity of Aβ assemblies during the pre-incubation step, the potency of any agent to eliminate a specific target Aβ assembly can be quantitatively determined by comparing the Aβ contents of the fractions that contain the target aggregate species obtained from the samples with and without the agent of interest.

Here, we demonstrate the power of the Aβ-QIAD assay by quantitatively comparing the outcome of the assay for two therapeutically interesting agents. The first agent is a mirror image phage display selected D-enantiomeric peptide, termed “D3”, that inhibits the formation of regular Aβ fibrils, removes Aβ oligomers and reduces Aβ cytotoxicity *in vitro*. *In vivo*, D3 is able to reduce plaque load, decrease inflammation and enhance cognition of a transgenic AD

mouse model even after oral application[8,11]. The second agent is a head-to-tail dimer of D3, termed "D3D3", that is expected to have enhanced efficacy due to increased avidity.

As shown in **Figure 2a,** both agents yielded a significant reduction of Aβ oligomers in DGC fractions 4 to 6 in comparison to agent-free controls. D3 (32 µg/ml, 20 µM) and D3D3 (32 µg/ml, 10 µM) reduced Aβ oligomers by 50 and 96%, respectively. D3D3 proved to be significantly more efficient than D3. Notably, monomeric Aβ or small sized oligomers located in DGC fractions 1 and 2 were negligibly affected by D3 and D3D3. The net reduction of Aβ oligomers by D3 and D3D3 was balanced by an increase of high-molecular weight aggregates located in DGC fractions 12 to 15 (**Fig. 2a**). D3-Aβ-co-aggregates were shown previously to be non-toxic, non-amyloidogenic, amorphous and Thioflavin T (ThT) negative[8].

Aβ assemblies located in fractions 4 to 6 were specifically sensitive to D3 and D3D3. Therefore, these species were further characterized in detail. According to the calibration of the density gradient with a set of globular proteins with known *s*-values, the Aβ assemblies in fractions 4 to 6 had *s*-values of about 7 S (**Supplementary Fig. 1a**). Atomic force microscopy (AFM) analysis revealed homogenous assemblies in spherically shaped particles with heights of 4.7 nm and diameters corrected for the tip dimensions of 8.7 nm (**Fig. 1d and Supplementary Fig. 2**). Modeled as oblate spheroids with an axial ratio of ~2, these Aβ oligomers have a molecular weight of about 104 kDa, which corresponds to about 23 monomeric units. This value is in good accordance with the estimated *s*-value of 7 S. Circular dichroism (CD) measurements of the oligomers revealed a spectrum with β-sheet characteristics (**Fig. 1e**), but the particles were negative for ThT fluorescence staining (**Supplementary Fig. 3**). Therefore, we conclude that the secondary structure of the oligomers differs from regular amyloid cross-β fibrils, which typically exhibit strong ThT fluorescence (**Supplementary Fig. 3**). The DGC derived Aβ oligomers exhibited high cytotoxicity to

differentiated human SH-SY5Y neuroblastoma cells[12] (**Fig. 1f**), thus further demonstrating their similarity to toxic Aβ oligomers involved in AD pathogenesis.

To verify the hypothesis that increased efficiency in Aβ oligomer elimination of an agent correlates with the *in vivo* potency of the agent, the therapeutic effects of D3 and D3D3 were investigated in the transgenic mouse model TBA2.1[15]. Three groups of TBA2.1 mice were treated either with saline, D3 or D3D3 (0.1 mg per day per mouse, i.p., for 4 weeks using minipumps). Their phenotypes before and after the treatment were assessed using the rotarod and the SHIRPA tests[14]. Only saline-treated mice showed a significant phenotype progression, i.e. shortening of their latency times (**Fig. 2b**), suggesting that D3 and D3D3 were able to halt phenotype progression during the treatment period. More importantly, D3D3-treated mice did not show significant worsening of their phenotypes in the SHIRPA test, whereas the phenotypes of D3-treated mice and saline-treated mice worsened significantly or very significantly, respectively, during the four weeks duration of the experiment **(Fig 2c)**. Thus, a more significant effect of D3D3 treatment as compared with D3 was visible in this study, exactly as predicted from the Aβ-QIAD assay.

To further verify the *in vivo* efficacy of D3D3, we treated the transgenic mouse model Tg-SwDI[16] with this peptide. Intraperitoneal application of D3D3 (36 µg per day per mouse for 4 weeks, using minipumps) led to significant reduction of plaque load in comparison to the saline treated control group (**Fig. 2d**). Cognitive deficits of Tg-SwDI mice, as measured in the object recognition test, were significantly improved upon D3D3 treatment **(Fig. 2e)**. Side effects caused by the D3D3 treatment as measured by open field and zero maze tests were not detected.

The hereby described Aβ-QIAD assay for analysis of agent-induced Aβ oligomer elimination allows comprehensive and reliable *in vitro* screening of drug candidates for maximum reduction of cytotoxic Aβ oligomers. The quantitative nature of the assay allows comparison

between various drug candidates. The observed relation between Aβ oligomer elimination and *in vivo* results strengthens the role of Aβ oligomers in AD pathology. The assay will help to avoid testing of ineffective compounds in animal and time consuming *in vivo* assays or even in clinical trials. The QIAD assay is adjustable for any aggregation-prone peptide or protein.

METHODS

Methods and any associated references are available in the online version of the paper.

Note: Any Supplementary Information is available in the online version of the paper.

ACKNOWLEDGMENTS

We thank Mario Schneider for assistance in AFM data evaluation.

AUTHOR CONTRIBUTIONS

O.B. and L.G. designed and performed the QIAD and CD experiments, T.D. performed and A.W. designed the TBA2.1 mouse tests, T.v.G. and I.K designed and performed the APPSweDI mouse tests, O.B. and E.M. designed and performed the cell toxicity assays, O.B. performed and F.O. supervised AFM imaging, T.v.G., A.W., J.K. and D.J. evaluated animal assays and did statistics. A.J. supervised statistics. D.W. designed the overall study. D.W., L.N.-S., L.G. O.B., and J.K. wrote large parts of the manuscript. D.J., H.-U.D. S.A.F., W.H. and K.-J.L. contributed to the manuscript.

COMPETING FINANCIAL INTERESTS

The authors declare to have no competing financial interests.

References

1 Brookmeyer, R., Johnson, E., Ziegler-Graham, K. & Arrighi, H. M. *Alzheimers Dement* **3**, 186-191 (2007).
2 International, W. H. O. a. A. s. D. Vol. 2013 (ed World Health Organization and Alzheimer's Disease International) 110 (2012).
3 Haass, C. & Selkoe, D. J. *Nat. Rev. Mol. Cell Biol.* **8**, 101-112 (2007).
4 Gadad, B.S., Britton, G.B. & Rao K.S. *J. Alzheimers Dis.* **24** Suppl 2:223-32 (2011).
5 Finder, V. H. & Glockshuber, R. *Neurodegener Dis.* **4**, 13-27, (2007).
6 Rzepecki, P. *et al. J. Biol. Chem.* **279**, 47497-47505 (2004).
7 Ward, R. V. *et al. Biochem. J.* **348**, 137-144 (2000).
8 Funke, S. A. *et al. ACS Chem. Neurosci.* **1**, 639-648 (2010).
9 Morinaga, A. *et al. Biochim. Biophys. Acta - Prot. Proteom.* **1804**, 986-995 (2010).
10 Johansson, A. S. *et al. FEBS J.* **273**, 2618-2630 (2006).
11 van Groen, T. *et al. ChemMedChem.* **3**, 1848-1852 (2008).
12 Weidner, A. M., Housley, M., Murphy, M. P. & Levine, H. *Neurosci. Lett.* **497**, 1-5 (2011).

13 Sehlin, D. *et al. PLoS ONE* **7**, e32014 (2012).
14 Rogers, D. C. *et al. Mamm. Genome* **8**, 711-713 (1997).
15 Alexandru, A. *et al. J. Neurosci.* **31**, 12790-12801 (2011).
16 Davis J *et al*. *J. Biol. Chem.* **279**, 20296-20306 (2004).
17 van Groen, T., Kiliaan A.J. & Kadish, I. *Neurobiol. Dis.* **23**, 653-662 (2006).

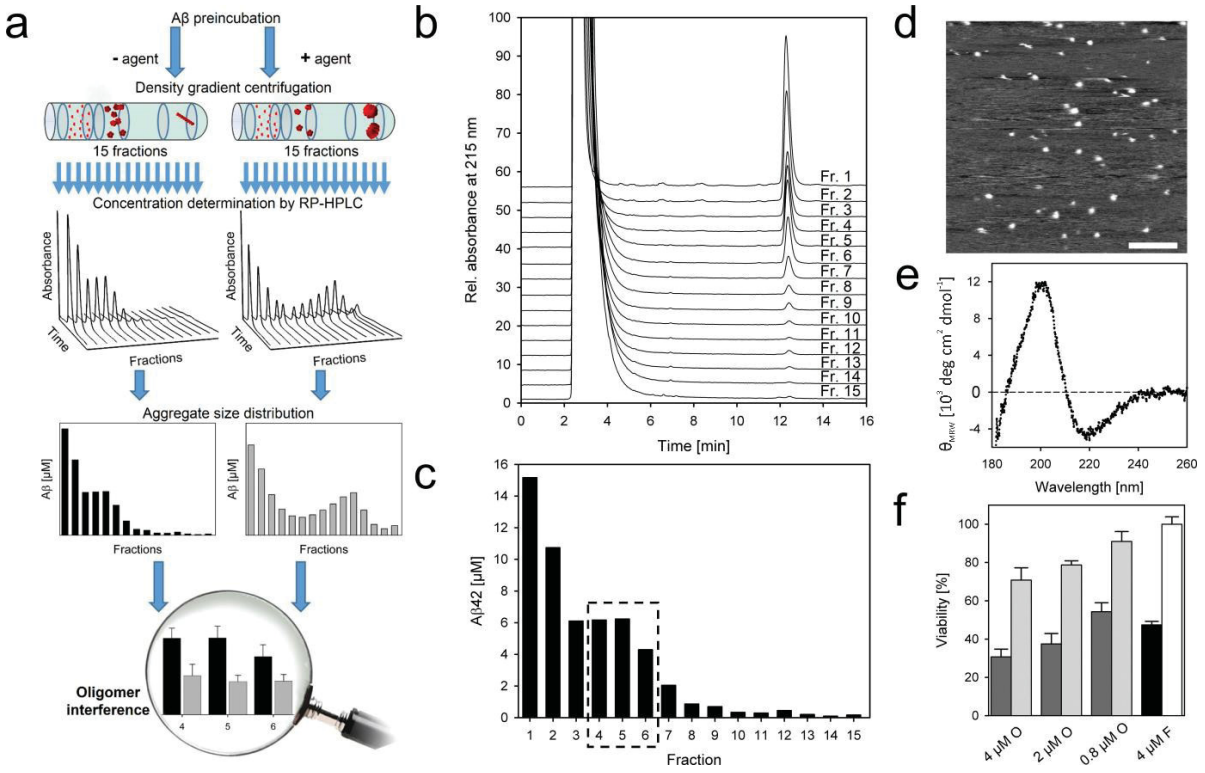

Figure 1 | **(a)** Scheme of the QIAD assay. **(b)** Chromatograms for each fraction obtained from DGC are presented with a constant offset for clarity. Peak 1 at 2 to 4 min corresponds to the density gradient material iodixanol, whereas peak 2 at 12.5 min corresponds to Aβ. **(c)** Bar chart showing the Aβ distribution after DGC of pre-incubated Aβ. Aβ concentrations in each fraction were determined by integration of the Aβ absorption in the RP-HPLC chromatograms shown in b. **(d)** AFM of Aβ oligomers from pooled fractions 5 and 6. Scale bar 200 nm. **(e)** Far-UV CD spectroscopy of Aβ oligomers indicating a predominantly β-strand secondary structure. **(f)** Toxicity of Aβ oligomers tested by a MTT cell viability assay. RA/BDNF differentiated SH-SY5Y cells were treated with Aβ oligomers (dark grey) at concentrations corresponding to 4, 2 and 0.8 µM monomers. Buffer containing 16 % iodixanol (light grey) or buffer without iodixanol (white) were used as controls. All given Aβ assembly concentrations relate to Aβ monomers.

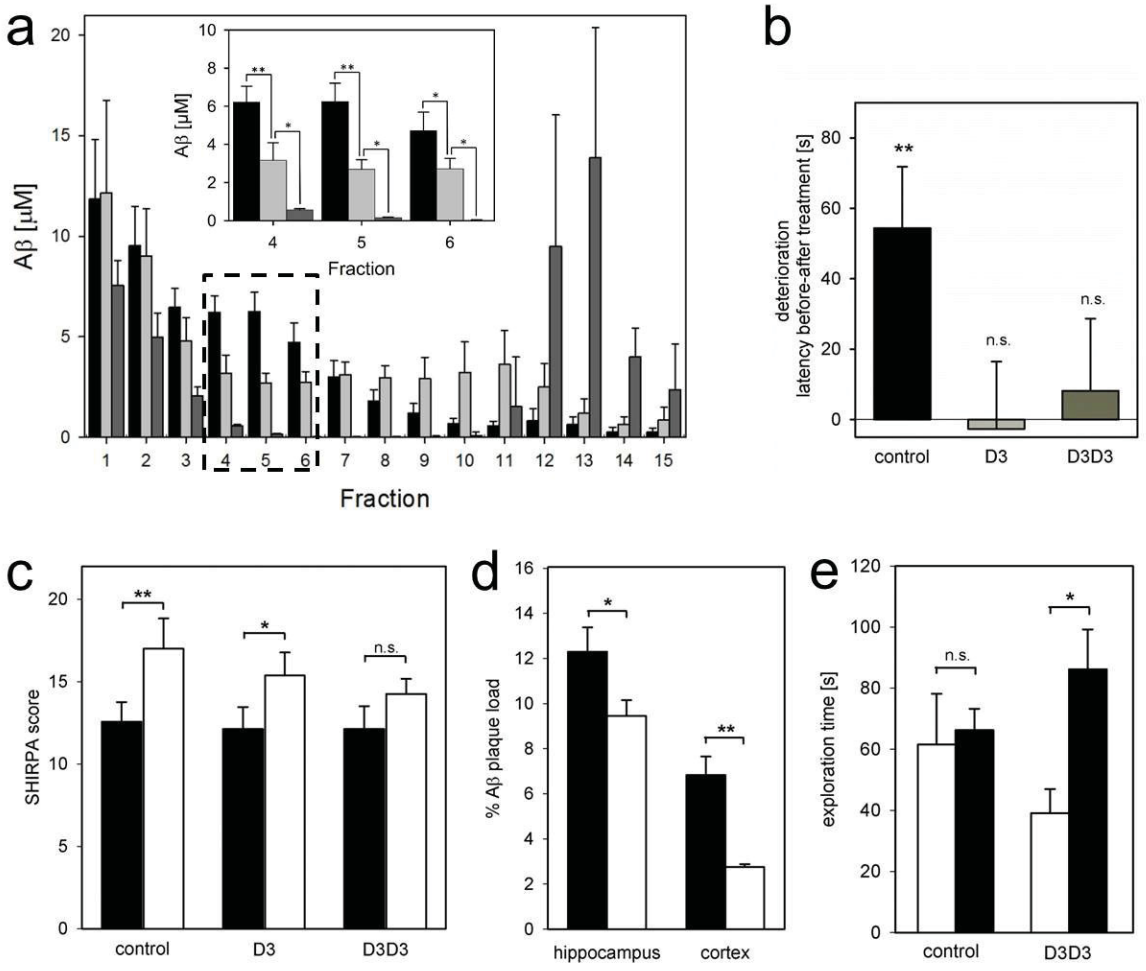

Figure 2 | Effects of D3 and D3D3 *in vitro* and *in vivo*. **(a)** QIAD assay. After preincubation of 80 µM Aβ for 40 min at RT with or without agent, Aβ size distributions in the absence (black) or presence (gray) of either D3 (32 µg/ml, 20 µM) or D3D3 (32 µg/ml, 10 µM) were analyzed by DGC. Aβ concentrations as determined by UV absorption during RP-HPLC are shown with standard deviations. Aβ oligomers of interest (dashed box) are located in fractions 4 to 6. **(Inset)** Magnification of boxed area displaying significant differences of Aβ oligomer contents between untreated (black), D3 treated (light grey) and D3D3 treated Aβ (dark grey). Paired u-test; $*P \leq 0.05$, $**P \leq 0.01$ **(b)** Rotarod assay; shown are the differences in latency times before and after treatment. One-sample t-test (hypothesized difference ≤0), ** $p = 0.0104$. **(c)** Assessment of TBA 2.1 phenotype using part of the SHIRPA test battery before (black) and after i.p. treatment (white) for 4 weeks with saline D3 or D3D3. Repeated measures ANOVA before vs. after $p = 0.0027$, paired t-test (hypothesized difference ≥0) before vs. after, * $p = 0.035$, ** $p = 0.010$. **(d)** Plaque load reduction of D3D3 treated mice as compared to non-treated mice in hippocampus and cortex. Unpaired t-test (hypothesized difference ≥0) D3D3 vs. saline, * $p = 0.020$, ** $p < 0.0001$. **(e)** Object recognition test of Tg-SwDI mice treated either with D3D3 or saline. Preference for the new object (black bar) is expressed as exploration time in comparison with exploration of a familiar object (white bar).

METHODS

Peptides. D3 (rprtrlhthrnr, all amino acids are D-enantiomers) and D3D3 (rprtrlhthrnrrprtrlhthrnr, all amino acids are D-enantiomers) with >95% purity were purchased from JPT (Berlin, Germany) and $A\beta_{1-42}$ with 95.2 % purity from Bachem (Heidelberg, Germany).

Preparation of Aβ peptide solutions. In order to dissolve any pre-existing aggregates of Aβ and to assure the monomeric state of Aβ, the sample was pre-dissolved in 1,1,1,3,3,3-hexafluoro-2-propanol (HFIP; Sigma-Aldrich, Germany) at 1.43 mg/ml and incubated over night at room temperature. HFIP was removed by evaporation for 30 min in the hood followed by a drying step in a centrifugal evaporator (RVC 2-18, Christ, Mainz, Germany) for a further 30 min. The dried Aβ was stored at –20 °C until use.

QIAD assay. The QIAD assay involves four steps: (i) pre-incubation of Aβ; (ii) addition of the agent to oligomer-enriched Aβ samples; (iii) the density gradient centrifugation step; and (iv) the quantification of Aβ assemblies by RP-HPLC (**Fig. 1a**).

i). Pre-incubation of Aβ. Pre-incubation of the Aβ solution leads to an increase of the amount of material with higher *s*-values, penetrating deeper into the gradient during centrifugation. A preincubation of 80 µM Aβ between 4.5 h and 6 h in 10 mM sodium phosphate buffer pH 7.4 at RT and shaking (600 rpm) was found to be the best condition at which the amount of oligomers residing in the middle of the gradient was maximized without the appearance of signals in the bottom fractions, indicating the absence of large or fibrillar aggregates in the sample at the investigated time point. The generated oligomeric species were located in fractions 4 to 6. In this area of the gradient, proteins with *s*-values of about 7 S and molecular weights in the range of 66 to 150 kDa were expected following the centrifugation step. This expectation is based on the analysis of the distribution of standard proteins used for the calibration of the gradient (**Supplementary Fig. 1**). The concentration of iodixanol was about 20 %, giving a density of 1.112 g/cm^3. Based on the proteins used for the calibration of the gradient, the size of oligomers in these fractions was in the range of 50 to 150 kDa.

ii) Our previously described mirror image phage display selected the D-peptide D3 and a derivative thereof were applied as drug candidates. Compounds were added to the pre-incubated Aβ solution 40 min before loading the sample onto the gradient.

iii) Density gradient centrifugation[6,7,13] offers an approach to fractionate aggregates formed by Aβ by their size and shape for further characterization. Analysis of solutions of synthetic Aβ by iodixanol density gradient centrifugation revealed the *s*-value distribution of monomers and assemblies at the time point of analysis.

As a control for each density centrifugation run, a sample without the added agent was used. Statistical evaluation of experimental results from eleven independent control density gradient centrifugation analyses demonstrated the good reproducibility of the procedure (**Fig. 2a**, black bars).

A discontinuous gradient of iodixanol was pre-formed by layering 260 µl of 50 % iodixanol (OptiPrep, AXIS-SHIELD, Oslo, Norway) at the bottom of an 11 × 34 mm polyallomer centrifuge tube, overlaid by 260 µl of 40 %, 260 µl of 30 %, 780 µl of 20 %, 260 µl of 10 %, and 100 µl of 5 % OptiPrep. The total volume of the phosphate-buffered non-linear gradient was 1920 µl. The top of the gradient was overlaid by a 100 µl aliquot of incubated Aβ. The samples were spun at 259,000 × *g* for 3 h at 4 °C in a TL 100 ultracentrifuge with a TLS-55 rotor (both Beckman Instruments, Brea, USA). After the centrifugation, 14 fractions of 140 µl were harvested with a pipette by upward displacement. The pellet of each tube (ca. 60 µl remaining volume) was mixed with 60 µl 6 M guanidinium hydrochloride and boiled for 10 min. The resulting solution represents the 15th fraction. Fraction 1 from the top of the gradient was the least dense, and fraction 15 from the bottom was the densest fraction. All the fractions were analyzed with respect to their Aβ content by RP-HPLC and SDS-PAGE.

3. Analytical RP-HPLC. Quantifications of Aβ present in DGC fractions was performed by RP-HPLC on a Zorbax SB-300 C8 column (5 µ, 4.8 × 250 mm, Agilent, Böblingen, Germany) connected to an Agilent 1260 Infinity system. Denaturation of Aβ assemblies and separation of Aβ from other compounds, especially from the density gradient forming iodixanol, was achieved using 30% (v/v) acetonitrile, 0.1% (v/v) trifluoroacetic acid in H_2O as the mobile phase, an elevated column temperature of 80 °C and a flow rate of 1 ml/min. Applied sample volumes were 20 µl. Eluting substances were detected by their UV absorbance at 215 nm. Data recording and peak area integration was achieved by the program package ChemStation (Agilent, Böblingen, Germany). Calibration of the column was achieved with Aβ solutions of known concentrations (0 to 25 µM Aβ) and the resulting linear equation from a plot of peak area *vs*. Aβ concentration allowed the calculation of molar Aβ concentrations (from corresponding peak areas) (**Supplementary Fig. 4)**.

The quantitative analysis of Aβ amounts in every fraction allows us to determine the recovery rate *R*:

$$R = \frac{c_P V_P + \sum_{n=1}^{14} c_n V_f}{c_0 V_0}$$

with c_P the Aβ concentration in the pellet (15th fraction), c_n the Aβ concentrations in fractions 1 to 14, c_0 the Aβ concentration in the initial sample, V_f the volume of the fractions 1 to 14 (140 µl), V_P the volume of the pellet (15th fraction), and V_0 the volume of the initial sample.

Atomic force microscopy (AFM). AFM was carried out for the Aβ oligomers in solution using a MFP 3D AFM (Asylum Research, Santa Barbara, USA) or for Aβ fibrils under air dried conditions using a NanoWizard II AFM (JPK Instruments AG, Berlin, Germany). Aβ oligomers were prepared by adsorbing 40 µl of undiluted samples (pooled fractions 5 and 6) for 30 to 40 min to freshly cleaved mica followed by thorough washing with 10 mM sodium phosphate buffer, pH 7.4. The samples were imaged in the same buffer after a drifting-equilibration time of ca. 30 min in contact mode using sharp nitride levers (SNL-10) (Bruker, Camarillo, US) with an average tip radius of 7 nm and a scan rate of 1 to 2 lines per second. All images were processed using the Igor Pro 6.22A software. The images were levelled by mean plane subtraction to correct for tilting of the sample stage and servo range errors. The evaluation of the dimensions of Aβ oligomers was done by measuring the cross section of the particles perpendicular to the scanning direction. Every single cross section was fitted by a Gaussian function. The resulting radius at half-height and the fitted height are shown as histograms (**Supplementary Fig. 2**). For statistics, we evaluated 531 particles collected from a surface area of 22 µm^2 from up to four independent Aβ-oligomer preparations. Height and radius histograms were fitted by Gaussian functions.

The particles observed in combined DGC fractions 5 and 6 were of spherical nature. The statistical analysis for 531 particles resulted in a mean height of 4.7 nm and an average radius of 9.9 nm. In contrast to the height, the width had to be corrected for tip broadening to 8.7 nm. The calculation of the oligomer width corrected for tip artefacts was done by a routine written in MATLAB based on a tangent circle as model for the cantilever tip and an ellipse for the Aβ oligomer. Under the assumption of an oblate spheroid with an axial ratio two the particle volume was calculated to be 185 nm^3. This represents the volume sum of the Aβ assembly and hydration water of 0.4 g/g protein. To calculate the volume of the hydration water, a density

15 % higher than bulk water was used. After subtraction of the hydration water the remaining mass corresponds to about 23 monomeric units. Based on the calculated shape and density the oligomeric species would have a sedimentation coefficient of 7.7 S, which agrees with the sedimentation coefficient deduced from the position of the particles within the density gradient.

To test for a possible correlation between radii and heights of Aβ oligomers a plot of height *vs.* radius for the measured particles was drawn (**Supplementary Fig. 2**). In the plot no correlation between the distribution of radii and heights of Aβ oligomers can be detected, which indicates the absence of differently sized particle populations. Consequently the width of the measured distributions is primarily due to measurement errors and tip radius variation.

Samples taken from the higher DGC fractions (**Supplementary Fig. 3**) or from fibril preparations produced for toxicity assays were checked for the presence and nature of Aβ fibrils by AFM. Following adsorption of 40 µl sample volumes for 30–40 min to freshly cleaved mica and thorough washing with ultrapure water, imaging was performed in the intermittent contact mode with silicon tips on a silicon cantilever (OMCL 160TS R3) (Olympus, Muenster, Germany) with a typical tip radius of 7 nm, a spring constant of 26 N/m, a drive frequency of 300 ± 100 kHz and a scan rate of 0.5–1 lines per second.

Cell culture and differentiation. SH-SY5Y cells (Leibniz Institute DSMZ-German Collection of Microorganisms and Cell Cultures) were cultured in DMEM/F-12 medium supplemented with 10% heat-inactivated FBS, penicillin (100 U/ml), streptomycin (100 µg/ml) (all from Invitrogen, Darmstadt, Germany) in a humidified, 5% CO_2, 37 °C incubator and grown for a maximum of 20 passages. For the MTT cell viability assay, the cells were plated in a 96-well tissue culture plate at a density of 20,000 cells/well and 24 h after seeding the cells were treated with all-*trans* retinoic acid (RA) (Sigma-Aldrich, Taufkirchen, Germany) at a final concentration of 10 µM in a culture medium containing 1 % FBS. After 6 days of RA treatment, the cells were grown for a further 2 days in a serum-free medium containing human recombinant BDNF (Sigma-Aldrich, Taufkirchen, Germany) at a final concentration of 2 nM.

MTT cell viability assay. The toxicity of Aβ oligomers was assessed using the MTT assay in differentiated SH-SY5Y cells. Aβ oligomers pooled from DGC fractions 5 and 6 were added to cells at a corresponding monomer concentration of 4, 2 and 0.8 µM, as determined by RP-HPLC. The concentration of iodixanol in the controls without Aβ was adjusted to match that present in oligomer fractions 5 and 6. The data were not normalized to the value of the untreated

control, because the toxic effects of Aβ oligomers and iodixanol might not be additive. Following 24 h, MTT at a final concentration of 0.5 mg/ml was added to the cells for 4 h at 37 °C. Finally, formazan salt crystals were solubilized using 10% SDS and 0.01 M HCl, and the absorbance was measured at 565 nm in an Infinite M1000 plate reader (Tecan, Maennedorf, Switzerland).

We tested the toxicity of our DGC prepared oligomers on RA/BDNF differentiated neuroblastoma cells, which have been shown to be susceptible to Aβ oligomers. These Aβ oligomers were proven to be highly toxic to RA/BDNF differentiated cells and were less toxic to undifferentiated cells. The difference of toxicity between differentiated and undifferentiated cells was not statistically quantified.

Circular dichroism (CD) spectroscopy. The high UV absorbance of the gradient forming iodixanol prohibited a direct CD spectroscopic analysis of oligomeric Aβ preparations derived from DGC. Therefore, immediately before CD measurements iodixanol was removed from freshly prepared Aβ-oligomer preparations by SEC on two 5 ml Sephadex G-25 columns in series equilibrated in 10 mM sodium phosphate (pH 7.4) (HiTrap Desalting, GE Healthcare, Freiburg, Germany) on an ÄKTA purifier system (GE Healthcare, Freiburg, Germany). Typically, 240 to 480 µl of 17.3 µM Aβ oligomers (expressed as molar concentration of Aβ monomers) were applied to SEC. Eluting compounds were monitored by their UV absorbance at 215 nm and collected in 0.4 ml fractions. The Aβ oligomers eluted in the void volume. The concentration was measured by RP-HPLC as described above and is given as molar concentration of Aβ monomers. Typical yields were in the range of 5 to 10 µM and sufficient for CD measurements. Far-UV CD spectra of Aβ oligomers were recorded on a JASCO J-815 instrument at 20 °C using a quartz cuvette with 1 mm path length and instrument settings as follows: 0.2 nm step size, 20 nm min^{-1} scan speed, and 1 nm band width. The signal-to-noise ratio was improved by accumulation of 10 scans per sample. Resulting CD spectra were corrected by subtraction of the corresponding buffer spectra. The mean residue ellipticity $[\theta\theta]_{mmmmmm}$ in $deg \cdot cm^2 \cdot dmol^{-1}$ was calculated from the equation $[\theta\theta]_{mmmm} = (\theta\theta_{obs} \times MRW) / (cc \times dd \times 10)$, where $\theta\theta_{obs}$, observed ellipticity (in degrees); cc, concentration (in g/ml); dd, cell path length (in cm); $MMRRMM$ (mean residue weight), molecular weight divided by number of peptide bonds.

Animals. For study #1 23 four months old female tg/tg TBA2.1 (insertion of precursor of N-terminally modified pyroglutamate-Aβ in C57BL/6 x DBA1 background[15]) and for study #2 19 four months old female Tg-SwDI mice (human APP with Swedish K670N/M671L, Dutch E693Q and Iowa D694N mutations on a C57BL/6 background[16]) were used. Group sizes were decided on the basis of experienced data from previous studies[8]. In advance inclusion and exclusion criteria were determined. Only female mice with an age of 4 months +/- 1 week were included in the study. Exclusion criteria were defined as weight loss of ≥15 %, surgical site infection and very serious general conditions in addition to the normal phenotype of Tg-SwDI or TBA2.1 mice. All animals fulfilled the inclusion criteria and no animal was excluded after enrolment in the study.

The animals were housed 4/cage in a controlled environment (temperature 22 °C, humidity 50–60 %, light from 07:00 to 19:00), food and water were available *ad libitum*. The implantation of the Alzet minipumps was performed intraperitoneal (for study #1, model #1004; delivery rate: 0.11 µl/h duration: 4 weeks; for study #2 model #2004; delivery rate: 0.25 µl/h, duration: 4 weeks). During the treatment the animals were housed individually. The experiments were conducted according to the local Institutional Animal Care and Use Committee (IACUC) guidelines as well as adhering to the Federal German Law on the Protection of Animals.

In study #1, the D3D3 peptide ($n = 8$) was compared with the D3 peptide ($n = 8$) and the control ($n = 7$, phosphate buffered saline). The applied peptide amount was 2.8 mg/pump.

In study #2, treatment took place with the D3D3 peptide ($n = 10$) and control group ($n = 9$, saline). Animals were divided into two groups based on similar average body weight. The applied peptide amount was 1 mg/pump, 0.9 mg of unconjugated peptide and 0.1 mg peptide conjugated with fluorescein.

The Alzet minipumps were filled with the appropriate solutions and implanted into the peritoneal cavity.

Behavior and functional assessment. In study #1, selected tests from the primary screening of the SHIRPA test battery[14] were used to assess levels of spinocerebellar function, muscle and lower motor neuron functions, sensory function, neuropsychiatric function and autonomic function of the TBA2.1 mice. The following tests were used: abnormal body carriage, alertness, abnormal gait, startle response, loss of righting reflex, touch response, pinna reflex, cornea reflex, forelimb placing reflex, hanging behavior and pain response. An arena of 55 cm × 19.5 cm × 33 cm (L × H × W) was used for individual observation and analysis. The scoring

values were from 0 (similar to wild type) to 3 (extremely changed compared to wild type). Before starting the treatment, mice were stratified into treatment groups using the aforementioned tests and two days before the end of the treatment they were tested again. Experimenters were blind to group allocation. Additionally, the motor balance and motor coordination of TBA2.1 mice were determined on the rotarod for 2 days before start and end of treatment using a published protocol[15]. In the morning of the first day mice were trained to stay on the rod for at least 60 s at 10 rpm. The three following test sessions, one in the afternoon and two at the second day, started with habituation for 30 min before the mice need to run three times on the rotarod with an accelerated beam from 4 till 40 rpm in 5 min. After mice falling off the rod latency time was recorded.

During the last week of treatment in study #2, animals were tested in four different behavioral tests to assess cognition and to monitor side effects. Experimenters were not informed about group allocation. First the open field test was conducted. The maze consisted of an arena of 42 × 42 cm with clear Plexiglas sides (20 cm high). The animal was put into the arena and observed for 4 min, with a camera driven tracker system, Ethovision 8.5 (Noldus, The Netherlands). The arena was subdivided into two areas, the "open" center and the area by the wall. The system recorded the position of the animal in the arena at 5 frames/second and the data were analyzed regarding time spent in each area (center *vs.* wall), similarly speed and distance were recorded. For disinfection the apparatus was wiped down with chlorhexidine and 70 % ethanol and allowed to air-dry.

Next, the zero maze test was conducted. The maze consisted of a circular arena with a diameter of 65 cm and four areas of equal size, two without walls, and two with walls of nontransparent material. The animal was put in the arena, and observed for 4 min, with a camera driven tracking system, Ethovision 8.5. The time spent in each area (open *vs*. closed) was recorded, similarly speed and distance were also recorded.

Subsequently the object recognition test (ORT) was carried out in a maze consisting of a rectangular polycarbonate box, with partitions separating the box into three chambers. The partitions have openings that allow the animal to move freely from one chamber to another. The animal was monitored by the Noldus tracking system 8.5. On day one two objects were placed on each side of the box. The mouse was placed in the box and allowed to move freely throughout the apparatus for a 10-minute test session. After 24 h, a new object replaced one of the "old" objects and the mouse was put in the box and allowed to move freely throughout the

box over a 4-minute test session. The time spent with each object and the transitions between the objects were recorded. The apparatus was wiped down with chlorhexidine followed by ethanol and water and dried with paper towels for each mouse tested.

Finally, the mice were tested for 5 days in a Morris water maze (MWM). The maze consisted of a blue circular tank of clear water (23 ± 1°C). The mice were placed in the water at the edge of the pool and allowed to swim in order to locate a hidden, but fixed escape platform, using extra maze cues. On day 1, the mice were placed in the pool and allowed to swim freely for 60 s to find the hidden platform (or until they find the hidden platform); each animal was tested for four trials per day. A maximum swim time per trial of 60 s was allowed; if the animal did not locate the platform in that time, it was placed upon it by the experimenter and left there for 10 s. The inter-trial interval was 120 s. Each start position (east, north, south and west) was used equally in a pseudo random order and the animals were always placed in the water facing the wall. The platform was placed in the middle of one of the quadrants of the pool (approximately 30 cm from the side of the pool). The mouse's task throughout the experiment was to find the platform. The animal was monitored by Ethovision 7.1.

Histopathology. Four weeks after the implantations, the animals were sacrificed for histopathological analysis. Therefore, the mice were anesthetized and transcardially perfused. The brains were then removed and the right hemisphere was fixed overnight in 4% paraformaldehyde and cryoprotected in 30% sucrose for 24 h followed by antifreeze in 15% sucrose and 30 % ethylene glycol in 0.05 M phosphate buffer, pH 7.4. Subsequent six series (1 in 6) of coronal sections (30 μm) were cut through the brain. The first series of sections was mounted unstained; the second and third series were stained immune histochemically, for human Aβ using the W0-2 antibody, for inflammation using mouse anti-GFAP (Sigma) and rabbit anti-mouse Iba1 (WAKO), according to published protocols[17]. The other series were stored in antifreeze at –20 °C.

Statistics. Data were averaged and represented as mean ± standard error of mean (SEM). Statview, Version 5.0.1 served for all calculations, $p > 0.05$ was considered not significant ("n.s.").

Rotarod:

Repeated measures ANOVA before v/s after $p = 0.088$, Paired t-test (hypothesized difference ≤0) before v/s after, * $p = 0.010$.

SHIRPA:

Repeated measures ANOVA before v/s after p=0.0027, Paired t-test (hypothesized difference ≥0) before v/s after, ** $p = 0.010$, * $p = 0.035$.

Object Recognition Test:

Paired t-test (hypothesized difference ≥ 0) before v/s after, * $p = 0.016$.

Plaque Load:

Unpaired t-test (hypothesized difference ≥ 0) D3D3 v/s saline, * $p = 0.020$, ** $p < 0.0001$.

QIAD-Assay:

SigmaPlot, Version 11.0 served for statistical calculations.

Paired Mann-Whitney U-test. Aβ without ligand $n = 11$, Aβ with D3 or D3D3 $n = 4$.

*$P \leq 0.05$, **$P \leq 0.01$ (fraction 4: Aβ vs Aβ+D3, $p = 0.005$; Aβ+D3 vs Aβ+D3D3, $p = 0.029$;

fraction 5: Aβ vs Aβ+D3, $p = 0.005$; Aβ+D3 vs Aβ+D3D3, $p = 0.029$;

fraction 6: Aβ vs Aβ+D3, $p = 0.007$; Aβ+D3 vs Aβ+D3D3, $p = 0.029$).

Supplementary figure 1

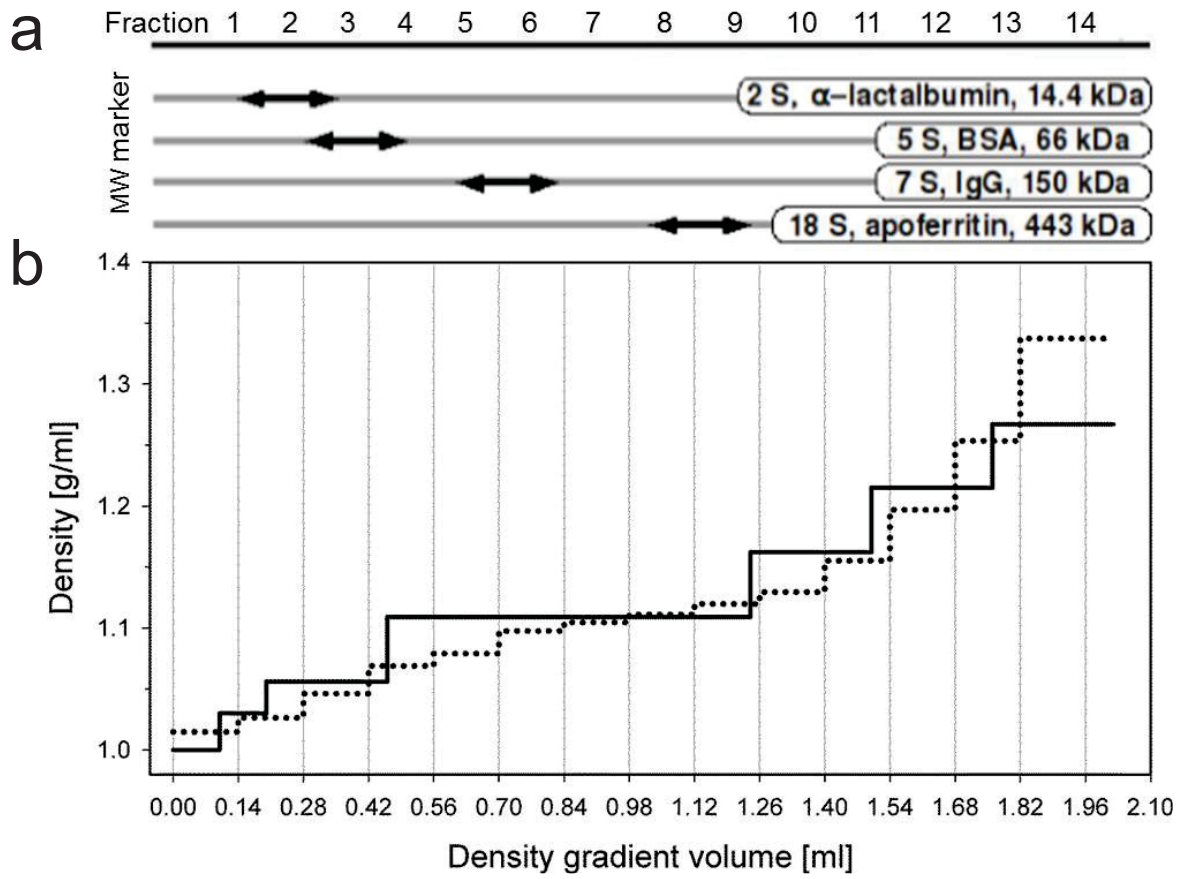

Supplementary figure 1 | Characterization of the density gradient (DG). (**a**) A comparison of the distribution of calibration proteins (α-lactalbumin, BSA, IgG and apoferritin) with different Aβ aggregates in the DG after the centrifugation. Due to known s-values of the calibration proteins one can estimate the size of Aβ aggregates in a certain fraction. (**b**) A comparison of density in the DG before (solid line) and after (dotted line) the centrifugation. Vertical gray lines indicate the final volumes of fractions. The last fraction is the potential pellet with around 60 µl of remaining liquid volume.

Supplementary figure 2

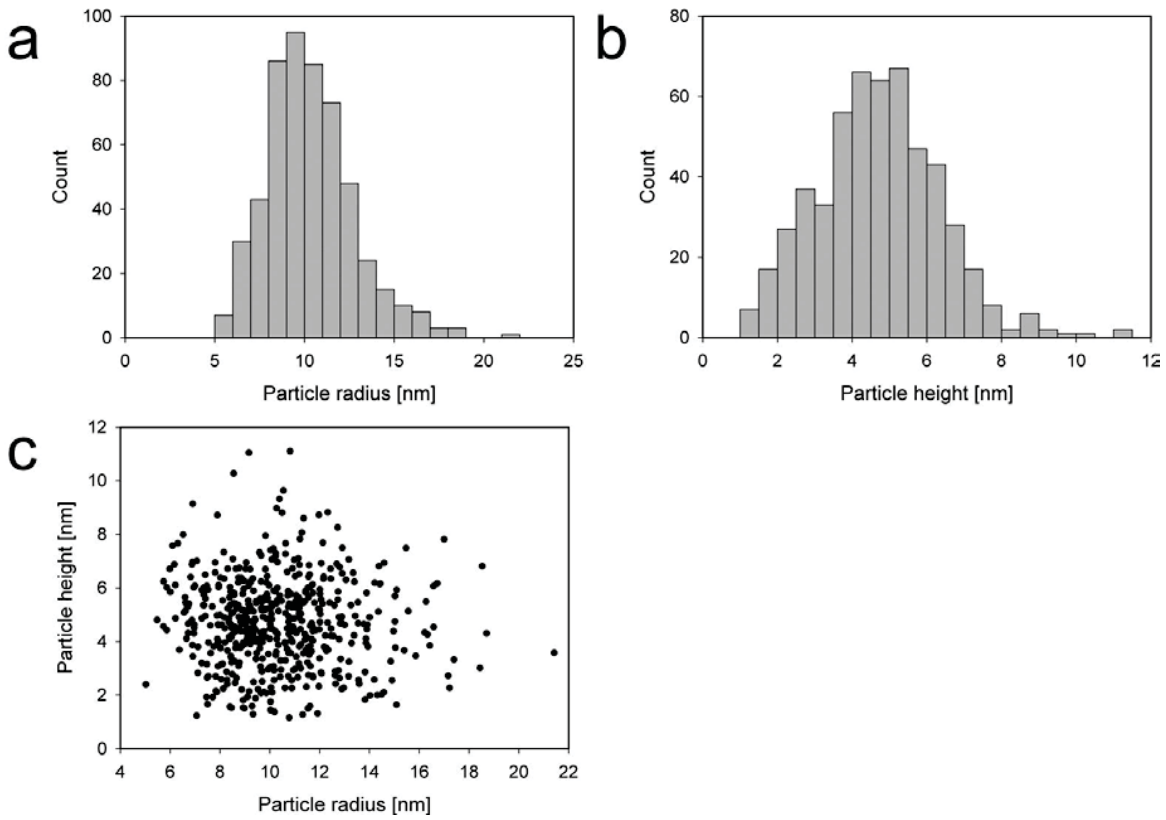

Supplementary figure 2 | Statistical analysis of Aβ oligomer AFM analysis (pooled fractions 5 and 6) dimensions. The AFM measurements were carried out in solvent (10 mM sodium phosphate buffer pH 7.4) in contact mode. Cross sections of Aβ oligomers (531 particles collected from 22 μm^2 surface) perpendicular to the scanning direction were fitted by Gaussian functions. The resulting radius at half-height (**a**) and the fitted height (**b**) are shown as histograms. By global fitting of the histograms with Gaussian functions an average height of 4.7 nm and an average radius of 9.3 nm (not corrected for the tip dimensions) were determined. (**c**) A plot of measured radii vs. heights of Aβ oligomers. No correlation between the distribution of radii and heights of measured particles can be detected indicating that the variance of different measured values is due to measurement inaccuracy and not to differently sized particle populations.

Supplementary figure 3

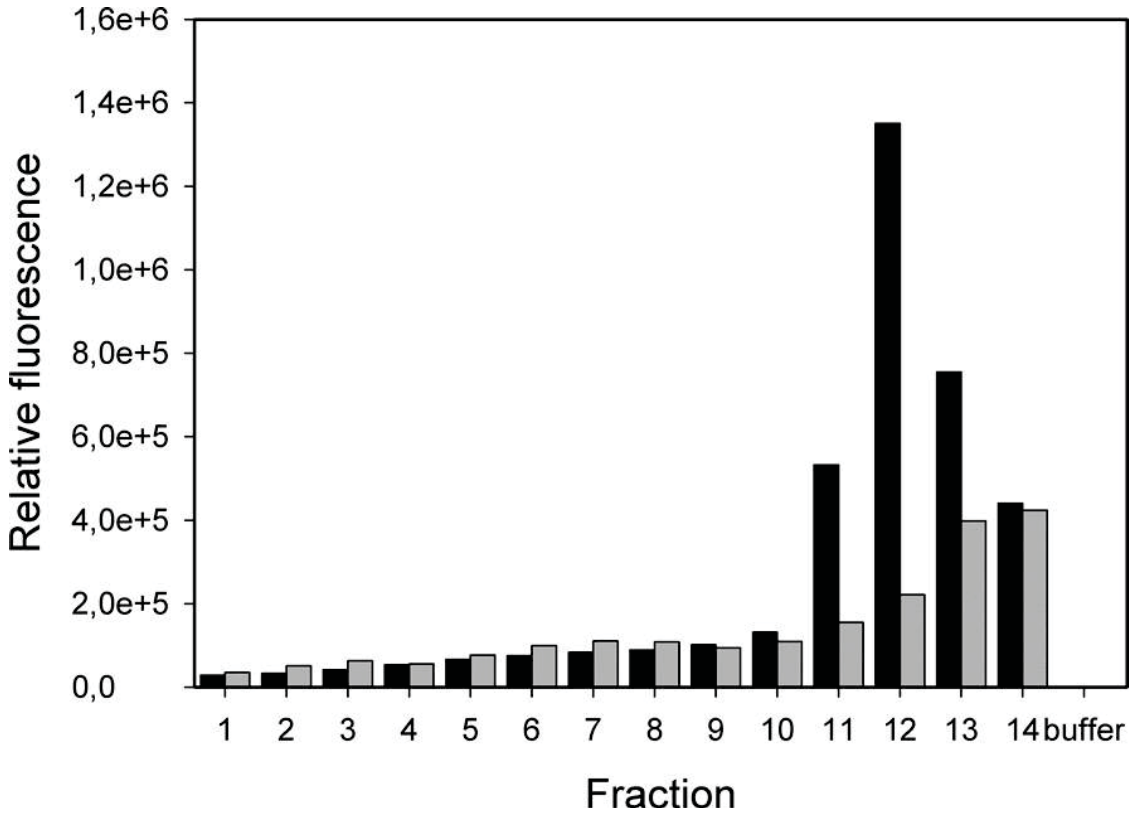

Supplementary figure 3 | Thioflavin T (ThT) test of Aβ species fractionated by DGC. ThT fluorescence was measured in freshly prepared Aβ fractions (black) and in fractions from a density gradient run without Aβ as Iodixanol control (gray) after addition of ThT. Iodixanol alone shows a concentration dependent effect on ThT fluorescence. Only fibrillar Aβ species in fraction 11-13 show amyloid specific ThT fluorescence, while oligomer fractions did not, indicating that the secondary structure of prepared Aβ oligomers differs from the fibril's one

Supplementary figure 4

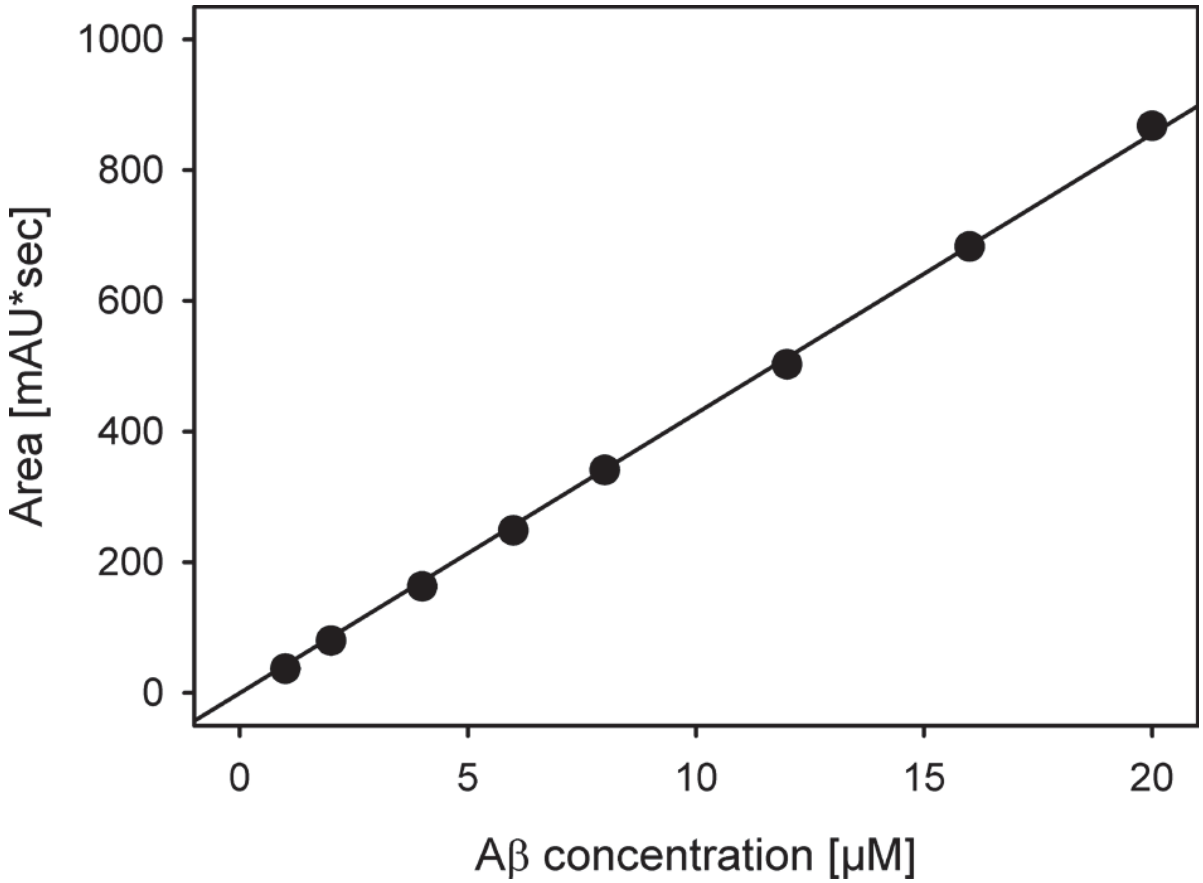

Supplementary figure 4 | Calibration of the analytical RP-HPLC column for quantitative analysis of Aβ content in density gradient fractions. Aβ solutions of known concentrations (0 to 20 µM) were analyzed by RP-HPLC. Absorbance was recorded at 215 nm. Obtained peak areas were plotted against original Aβ concentrations and fitted by a linear equation.

2.1.5 Immobilization of Homogeneous Monomeric, Oligomeric and Fibrillar Aβ Species for Reliable SPR Measurements.

Publiziert in: PLoS ONE

Impact Factor: 3,73

Eigenanteil an der Publikation: 25 %

Entwicklung der Präparation von Aβ-Monomeren, Oligomeren und Fibrillen; Mitverfassen des Manuskripts.

OPEN ACCESS Freely available online

PLOS ONE

Immobilization of Homogeneous Monomeric, Oligomeric and Fibrillar Aβ Species for Reliable SPR Measurements

Daniel Frenzel[1☯], Julian M. Glück[1☯], Oleksandr Brener[1,2], Filipp Oesterhelt[2], Luitgard Nagel-Steger[1,2], Dieter Willbold[1,2]*

1 Forschungszentrum Jülich, ICS-6 Structural Biochemistry, Jülich, Germany, **2** Heinrich-Heine-Universität Düsseldorf, Institut für Physikalische Biologie, Düsseldorf, Germany

Abstract

There is strong evidence that the amyloid-beta peptide (Aβ) plays a central role in the pathogenesis of Alzheimer's disease (AD). In this context, a detailed quantitative description of the interactions with different Aβ species is essential for characterization of physiological and artificial ligands. However, the high aggregation propensity of Aβ in concert with its susceptibility to structural changes due to even slight changes in solution conditions has impeded surface plasmon resonance (SPR) studies with homogeneous Aβ conformer species. Here, we have adapted the experimental procedures to state-of-the-art techniques and established novel approaches to reliably overcome the aforementioned challenges. We show that the application of density gradient centrifugation (DGC) for sample purification and the use of a single chain variable fragment (scFv) of a monoclonal antibody directed against the amino-terminus of Aβ allows reliable SPR measurements and quality control of the immobilized Aβ aggregate species at any step throughout the experiment.

Citation: Frenzel D, Glück JM, Brener O, Oesterhelt F, Nagel-Steger L, et al. (2014) Immobilization of Homogeneous Monomeric, Oligomeric and Fibrillar Aβ Species for Reliable SPR Measurements. PLoS ONE 9(3): e89490. doi:10.1371/journal.pone.0089490

Editor: Karl-Wilhelm Koch, University of Oldenburg, Germany

Received November 15, 2013; **Accepted** January 22, 2014; **Published** March 3, 2014

Funding: The authors have no funding or support to report.

Competing Interests: The authors have declared that no competing interests exist.

* E-mail: D.Willbold@fz-juelich.de

☯ These authors contributed equally to this work.

Introduction

Alzheimer's disease (AD) is the most common form of neurodegenerative disorders. While several genetic risk factors have been identified to be associated with the onset of AD, the major risk factor of AD is age. In 2010 around 35 million people were affected worldwide. With increasing life expectancy, >65 million cases are predicted by 2030 [1]. One of the hallmarks of AD is the appearance of amyloid aggregates [2]. According to the amyloid cascade hypothesis there is evidence that cellular events leading to cell death in AD are initiated by different amyloid beta-peptide (Aβ) assembly states [3]. This is supported by the observation of extracellular amyloid-like aggregates – mainly consisting of Aβ [4] – in the central nervous system of patients suffering from AD. Formation of Aβ is catalyzed by proteolytic cleavage of the amyloid precursor protein (APP) by β-secretase and γ-secretase [5]. The role of the oligomeric and fibrillar assembly states in disease progression is still debatable.

Nevertheless, due to the strong evidence that Aβ plays a central role in the pathogenesis of AD, substantial efforts aim to develop assays that, on the one hand, either allow the detection and quantification of Aβ species in biological matrices as for instance cerebrospinal fluids [6,7] or brain tissue [8–10] or, on the other hand, allow the characterization of compounds that target different Aβ species and/or interfere with their formation. A critical measure describing such compounds is their binding affinities to distinct Aβ species. Thus, reliable assays are urgently needed for quantitative affinity determination between ligands and the various Aβ species.

An optimal assay for binding studies with Aβ-binding molecules should combine minimal consumption of label-free ligands with maximum yield on kinetic and thermodynamic binding data. The surface plasmon resonance (SPR) technology can meet these requirements. In an SPR experiment, one of the interactants is immobilized (ligand) on a sensor chip surface. With regard to the propensity of Aβ(1–42) to aggregate, its use as the ligand is a clear advantage as stable fixation minimizes the risk of structural rearrangements, oligomerization and aggregation throughout the experiment.

However, several challenges exist with respect to the design of an SPR-assay for Aβ: (i) For obtaining robust data it is a prerequisite to use preparation techniques that ensure reliable preparation of homogeneous Aβ species that are free from undesired aggregation states. Aβ readily forms different oligomeric species that vary in size. Hence, samples are frequently heterogeneous, which prevents satisfactory data evaluation and binding curve fitting even when using multi-compound binding models. (ii) It is essential to find a suitable immobilization technique that is compatible with the buffer where formation of the respective Aβ species was performed because this prevents structural rearrangement of the prepared species. Many studies have analyzed the effect of different buffer components, temperature and pH on the formation of different Aβ species [11]. Taken together even slight changes in one of the latter physical parameters can cause structural rearrangements and peptide instability. Unfortunately, the majority of immobilization techniques in SPR are based on chemical reactions that require a change of solution conditions.

Moreover, immobilization of variable amounts of ligand on the surface in a highly reproducible manner is another critical step as this allows adaption of the Rmax (maximum response obtainable when all available ligand binding places are occupied) to the molecular weight of the interaction partner. Since there is a linear dependence of molecular mass to the detected SPR response, analytes with high molecular weights yield higher response signals than smaller analytes [12]. Excessive amounts of ligand eventually lead to heterogeneity in recorded sensorgrams during binding experiments, hampering data evaluation because of mass transport limitations and rebinding events. Generally, the lower the amount of immobilized ligand that yields a sufficient response during interaction with an analyte the lower the risk of heterogeneity. (iii) In addition to preparation and immobilization, special requirements for the measurement procedure are also present. A standard SPR assay includes regeneration steps between multiple analyte injections. This introduces the risk of critical structural rearrangements in the immobilized Aβ aggregates. It would therefore be beneficial to circumvent this step to yield reproducible interaction data. (iv) A reference molecule for quality control purposes of the surface activity during every single step of an experiment would greatly facilitate experimental design. Accordingly, selection of a proper analyte for assay development and surface characterization is crucial. It should be available in sufficient amounts, possess an on- and off-rate within SPR instrument specifications without introducing avidity effects.

Methods

Expression of the single chain variable fragment IC16

For recombinant production of scFv-IC16, *E. coli* BL21 DE3 pRARE2 was transformed with the expression vector pET22b-scFv-IC16-5His. Each 1 l 2YT (10 g l-1 yeast extract, 20 g l-1 tryptone, 10 g l-1 NaCl, 10 ml l-1 20% dextrose, 5 ml l-1 2 M $MgCl_2$, chloramphenicol and ampicillin, pH 7.4) expression culture was inoculated with an aliquot of a 50 ml overnight LB (5 g l-1 yeast extract, 10 g l-1 tryptone, 10 g l-1 NaCl) culture (grown at 37°C, 150 rpm) to a final OD_{600} of ~0.1. Cells were grown at 37°C (150 rpm) to an OD_{600} of 1.6–1.8. Subsequently, cultures were chilled for 1 hour at 4°C until IPTG was added to a final concentration of 0.2 mM for induction of scFv-IC16 protein expression. Expression was carried out for 24 hours at 18°C under gentle agitation (150 rpm). Cells were harvested by centrifugation (30 min, 4°C, 3750 rpm), pellets washed with PBS (10 mM sodium phosphate buffer pH 7.4, 137 mM NaCl, 2.7 mM KCl) and stored at −20°C until further use.

Purification of scFv-IC16

Pellets were resuspended in 20 ml lysis buffer I (50 mM Tris-HCl pH 8.0, 1 mM EDTA, 1 mg/ml lysozyme), supplemented with protease inhibitors (Complete EDTA-free Protease Inhibitor Cocktail Tablets, Roche). For cell lysis 20% Triton X-100 was added to a final concentration of 1%. $MgCl_2$ was added to a final concentration of 20 mM together with 500 U DNAse I. After an incubation at RT for ~15 minutes the volume was adjusted to 50 ml with lysis buffer II (8.33 mM imidazole, 833 mM NaCl, 16.6 mM $CaCl_2$, 1% Triton X-100) followed by centrifugation for 30 min at 20,000 g. Pellets containing scFv-IC16 in inclusion bodies were resuspended in 30 ml binding buffer (50 mM Tris-HCl pH 7.8, 500 mM NaCl, 8 M urea) followed by overnight incubation at 4°C in an orbital shaker. Suspensions were centrifuged (45 min, 20,000 g) and supernatants containing scFv-IC16 were purified by denaturing Ni^{2+}-NTA-chromatography. Affinity chromatography was performed with Ni^{2+}-loaded nitrilotriacetic acid (NTA) agarose from Qiagen (column volume, CV, of 3 ml) that was equilibrated with binding buffer. Supernatant was loaded onto the column by gravity flow, followed by washing steps with two CVs of wash buffer I (50 mM Tris-HCl pH 6.0, 500 mM NaCl, 8 M urea) and two CVs of wash buffer II (50 mM Tris-HCl pH 5.3, 500 mM NaCl, 8 M urea). scFv-IC16 was eluted with elution buffer (50 mM Tris-HCl pH 4.0, 500 mM NaCl, 8 M urea). All fractions were analyzed by SDS-PAGE with subsequent Coomassie staining and scFv-IC16-containing fractions were pooled. For refolding, renaturation buffer (50 mM Tris-HCl, 500 mM NaCl, 1% Triton X100, pH 7.2) was added to elution fractions in a 10:1 ratio (v/v). Afterwards, a second affinity chromatography purification was performed with Aβ(1–16) coupled NHS-sepharose (Pierce). After equilibration with a 10:1 mixture of refolding and elution buffer fractions containing scFv-IC16 were loaded onto the column. A washing step with 10 CVs TBS (50 mM Tris-HCl, 150 mM NaCl, pH 7.4) removed non-bound material. Elution was achieved with 50 mM glycine, pH 2.5. Each elution fraction was immediately neutralized by addition of 50 µl 2 M Tris-HCl, pH 8.0 per ml fraction volume and checked by SDS-PAGE. Fractions containing scFv-IC16 were pooled, dialyzed against PBS, and concentrated to a final concentration of 5 µM with Vivaspin 20 columns from Sartorius Stedim (3000 MWCO PES).

Preparation of Aβ(1–42) monomers and oligomers by size exclusion chromatography (SEC)

The protocol used by Johansson, Berglind-Dehlin, Karlsson, Edwards, Gellerfors and Lannfelt [13] was adapted for Aβ(1–42) monomer and oligomer preparation by SEC with minor modifications. Lyophilized stocks of Aβ(1–42) (Bachem), carboxy-terminally biotinylated Aβ(1–42) (Eurogentec) and amino-terminally biotinylated Aβ(1–42) (Anaspec) were separately dissolved in 100% hexafluoroisopropanol (HFIP) and incubated overnight at RT. In the case of oligomer preparations, amino-terminally biotinylated Aβ(1–42) and non-biotinylated Aβ(1–42) were mixed in a 1:10 ratio. After incubation, solutions were divided into 125 µg aliquots. HFIP was removed by evaporation in a Concentrator 5301 (Eppendorf). Aβ(1–42) was resolubilized in 100 µl SEC-buffer (50 mM sodium phosphate buffer, 150 mM NaCl, 0.6% Tween 20, pH 7.4) and briefly centrifuged (30 s) at 15,000 *g* to sediment insoluble material immediately prior to separation by SEC. Separation was performed with a Superdex 75 10/300 GL column operated at RT by an Äkta purifier system at a flow rate of 0.8 ml min^{-1}. For each single run ~100 µl of solubilized Aβ(1–42) was loaded onto the column. Monomers eluted at ~14 ml, whereas oligomers eluted close to the void volume (at ~8 ml). Samples were immediately used for immobilization on sensor chip surfaces. Initially, for establishment of the immobilization assay a BCA-assay was used to correlate the absorbance at 214 nm of the SEC fractions to the overall Aβ concentration. We observed, that an A_{214} = 250 mAU (oligomers) or A_{214} = 150 mAU (monomers) in the size exclusion chromatogram correlates with ~1 µM total Aβ concentration derived from a BCA-assay. Omitting the BCA-assay step dramatically reduces the time between elution and immobilization. For immobilization of monomers and oligomers (10% amino-terminally biotinylated) Aβ(1–42) concentrations of ~10 nM and ~100 nM, respectively, were used.

Preparation of Aβ(1–42) fibrils

The protocols used by Wood, Maleeff, Hart and Wetzel [14] and Nagel-Steger, Demeler, Meyer-Zaika, Hochdorffer, Schrader and Willbold [15] were adapted for Aβ(1–42) fibril preparation

with minor modifications. Lyophilized aliquots of Aβ(1–42) and amino-terminally biotinylated Aβ(1–42) were dissolved separately in 100% HFIP and incubated at RT overnight. Biotinylated Aβ(1–42) and non-biotinylated Aβ(1–42) in HFIP were mixed in a 1:10 ratio and subsequently divided into 72 µg aliquots. HFIP was removed by evaporation in a Concentrator 5301 (Eppendorf). Then, Aβ pellets were solubilized in 200 µl sodium phosphate buffer pH 7.4 (10 mM; yielding an 80 µM Aβ solution) and incubated for 24 hours at 25°C (600 rpm). To separate the hereby obtained fibrils from smaller aggregates and from monomers, they were subjected to a density gradient centrifugation (DGC) step. The gradient was prepared in thin-walled ultracentrifugation tubes (Ultra-Clear 11×34 mm, 2.2 ml from Beckman) by successively overlaying the following volumes of density gradient solutions: 260 µl 50%, 260 µl 40%, 260 µl 30%, 780 µl 20%, 260 µl 10% and 100 µl 5% (v/v) Iodixanol in 10 mM sodium phosphate buffer pH 7.4. After addition of 100 µl sample, the gradient was centrifuged (3 h, 4°C, 259,000 *g*) using a TLS-55 rotor in a benchtop ultracentrifuge Optima TL-100 (Beckman-Coulter). From each gradient 14 fractions of 140 µl were harvested from top to bottom. Fibrils were typically located in fractions 11 to 13.

Surface Plasmon Resonance (SPR)

For SPR experiments Series S Sensor Chips SA (GE Healthcare Life Sciences) in combination with a Biacore T200 system were used. Series S Sensor Chips SA are coated with streptavidin and allow ligand immobilization based on the biotin-streptavidin interaction. For our experiments PBS (filtered with 0.2 µm, PVDF) was used as running buffer. After docking a new sensor chip, the system was initiated with a "Prime" command and the detector normalized with 70% glycerol (GE Healthcare Life Sciences). All flow cells were activated with three consecutive one minute injections of 1 M NaCl in 50 mM NaOH. For ligand immobilization the flow rate was adjusted to 5 µl min^{-1} in order to minimize sample consumption. After immobilization we let the flow cells stabilize overnight to remove unspecifically bound material and detergence. To do so, we set the flow speed and temperature to 30 µl min^{-1} and 25°C respectively.

For interaction studies the flow speed and temperature were adjusted to 30 µl min^{-1} and 25°C respectively. All interaction studies were performed in the single-cycle kinetic mode [16]. Here, five different analyte concentrations were injected within a single cycle (contact time: 90 s, final dissociation time after the highest concentration: 1800 s) in order of increasing concentration. The applied analyte concentrations for scFv-IC16 were 312.5, 625, 1250, 2500 and 5000 nM. Binding studies with monoclonal antibody 6E10 were performed with concentrations of 0.32, 1.6, 8, 40 and 200 nM. All binding data were double referenced by collecting data in dual-channel mode with an untreated and therefore not Aβ(1–42) containing reference flow cell connected upstream of the flow cell with the respective Aβ(1–42) assembly state and by the subsequent subtraction of a blank buffer injection (1× PBS) from the obtained binding responses.

Double referenced SPR data were evaluated with Biacore T200 Evaluation Software (version 1.0) using the available binding models. Aβ monomer data was fit to a 1:1 binding model, whereas sensorgrams of Aβ oligomers and fibrils were analyzed with a heterogeneous ligand binding model accounting for two separate ligand sites for analyte binding. Values for bulk refractive index (R_I) and mass transfer (k_t) correction were manually set to zero, because double-referencing was applied and low amounts of ligand were immobilized.

Results

For immobilization of different Aβ(1–42) species we have chosen a streptavidin-biotin-coupling procedure as this avoids change in buffer conditions during Aβ(1–42) immobilization [17] concomitant with many alternative protocols. In addition, due to the strong interaction of streptavidin and biotin with a dissociation constant K_D of around 10^{-15} M [18] there is virtually no loss of ligand during the experiment. Moreover, streptavidin-biotin-coupling can be used effectively to control the amount of bound ligand simply by varying the concentration of the ligand or the duration of the injection. Fig. 1 shows the experimental setup scheme for the preparation of different Aβ(1–42) species and their immobilization.

Because any harsh regeneration steps between measurements will very likely do harm to the immobilized Aβ(1–42) species, they need to be avoided completely. Instead, very long washing steps have been introduced between separate measurements. To save time, so called kinetic titration [13], where the analyte is injected in increasing concentrations without regeneration steps in-between, is the method of choice. In comparison with classical multi-cycle kinetics, sample consumption and analysis time is reduced and, most importantly, the need for regeneration is eliminated [16,19]. For analysis of the kinetic titration obtained sensorgrams the tool "single-cycle kinetics" of the Biacore evaluation software package has been used.

For assay development and for quality check of surface characterization of immobilized Aβ species, the single-chain variable fragment (scFv-IC16) of the antibody IC16 that was initially selected to target the first 16 amino-acid residues of Aβ was selected [20,21]. scFvs are easy to produce and purify, stable at high concentrations for at least weeks, and possess only a single binding site with high specificity for their epitope, thereby avoiding any avidity effects.

Characterization of Aβ monomers

To test the specificity of scFv-IC16 to the amino-terminal part of Aβ, the chosen biotin-streptavidin immobilization procedure should be well-suited. The orientation of Aβ on the surface can be modulated easily by changing the location of the biotin tag. In theory it should therefore be possible to hide the epitope of scFv-IC16 by fusion of a biotin tag in close proximity. To do so we have immobilized the amino-terminally biotinylated Aβ(1–42) monomers (Fig. S1 A) that have been purified by size exclusion chromatography (SEC) prior to immobilization (Fig. S2 A) [13]. SEC purification ensures monodispersity of Aβ monomers. Binding of an anti-Aβ(1–42) antibody (6E10) demonstrated that Aβ was successfully immobilized (Fig. S3). In contrast, binding of scFv-IC16 to the N-terminally biotinylated Aβ(1–42) monomer loaded surface could not be detected (for details see Fig. S4). Conversely, C-terminally biotinylated Aβ(1–42) monomers that were immobilized to the surface was bound by both, 6E10 and scFv-IC16 (Fig. 2 and Fig. S5). We conclude that both, N- and C-terminally biotinylated Aβ monomers were successfully immobilized, but immobilization of N-terminally biotinylated Aβ(1–42) on the streptavidin-coated sensor chip restricts binding of scFv-IC16. To extract quantitative information from the experimental data of scFv-IC16 and C-terminally biotinylated Aβ(1–42) we fitted the obtained sensorgrams to a Langmuir 1:1 binding model. Refractive index correction (R_I) was not required because all binding data were double referenced prior to analysis. As can be seen in Fig. 2 and Tab. 1, the resulting fit represents the experimental data very well and yields a dissociation constant (K_D) of 0.77 µM. A low χ^2-value of 4.1 supports this finding. A

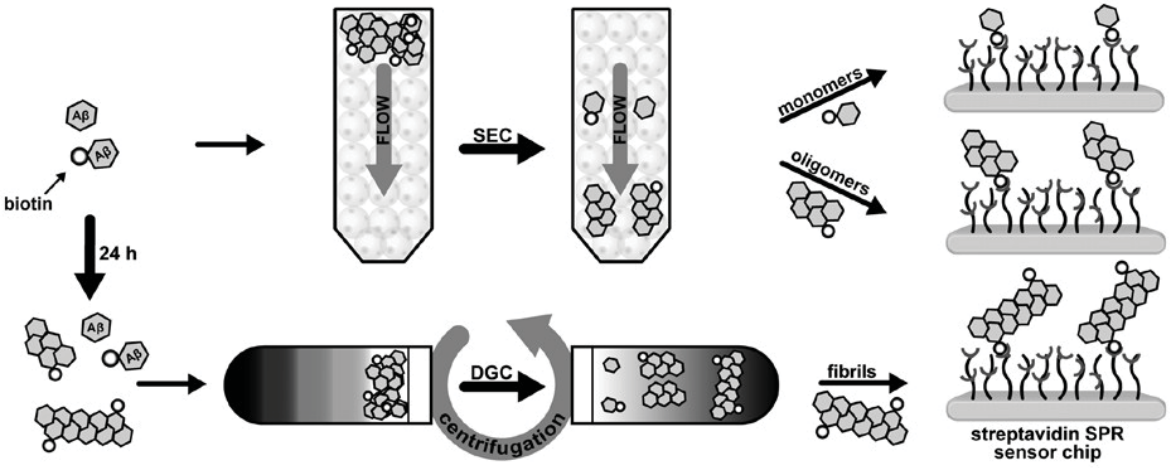

Figure 1. Surface preparation with different Aβ(1–42) assembly states for surface plasmon resonance (SPR) analysis. Size exclusion chromatography (monomers and oligomers) and density gradient centrifugation (fibrils) ensure highly pure samples for immobilization on sensor surfaces and subsequent SPR measurements.
doi:10.1371/journal.pone.0089490.g001

comparison with steady state affinity analysis (a linear fitting approach, see Fig. S7) revealed an excellent match. With this approach the K_D determined was equal to 0.97 µM (χ^2: 0.38).

Characterization of an example for Aβ oligomers

Next we immobilized Aβ(1–42) oligomers containing 10% amino-terminally biotinylated Aβ(1–42) and checked for successful immobilization of Aβ with 6E10 and scFv-IC16. To reduce the risk of sample heterogeneity we removed species different than oligomers by SEC [13] and immediately immobilized these oligomers (Fig. S1 A). 6E10 and scFv-IC16 were both able to bind to the Aβ oligomers on the surface (see Fig. 2 and Fig. S6). Importantly, since amino-terminally biotinylated monomers are not recognized by scFv-IC16 we can conclude that the obtained responses rely on scFv-IC16 binding to oligomers. Therefore, scFv-IC16 proves to be a powerful tool for surface characterization and quality control of immobilized Aβ and application as a molecular tool for SPR studies with Aβ in higher aggregation states is conceivable. Antibodies and their respective Fab fragments are often known to recognize both, linear and conformational epitopes. Binding curves were therefore fit with a heterogeneous ligand binding model. Again, owing to double referencing, a refractive index (RI) correction was not required. We obtained two separate K_D values (0.37 µM and 5.60 µM; χ^2: 3.0) with affinities differing by one order of magnitude. Use of simpler models increased χ^2 by at least a factor of ten and supports the initial assumption of a second epitope of Aβ(1–42) oligomers for scFv-IC16. This effect is very likely not being caused by rebinding effects of the analyte. The total mass of immobilized Aβ(1–42) oligomers is very comparable with the amount of immobilized Aβ(1–42) monomers, in which clearly no rebinding could be observed (Fig. S1 A).

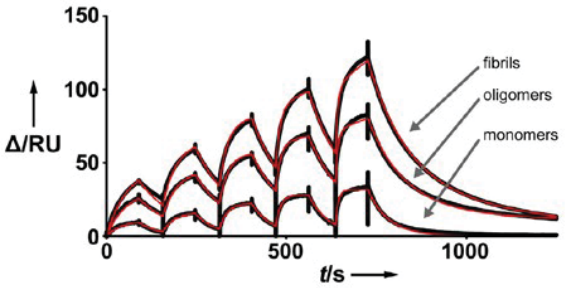

Figure 2. Interaction of scFv-IC16 with different immobilized Aβ(1–42) assembly states. SPR sensorgrams were recorded separately with single-cycle kinetics. Experimentally obtained, double-referenced binding data (black traces) were superimposed with the corresponding fit (red traces). Monomer data was fit to a 1:1 Langmuir binding model, and oligomer and fibril data were fit to a heterogeneous ligand binding model. ΔRU: delta of the response units. t/s: time in seconds.
doi:10.1371/journal.pone.0089490.g002

Characterization of Aβ fibrils

For immobilization of fibrils, an Aβ(1–42) mixture with 10% amino-terminally biotinylated Aβ(1–42) was used. To ensure the absence of lower molecular weight species we applied density gradient centrifugation (DGC) for separation of fibrils from other oligomeric states and monomers. Iodixanol was used as gradient media because this reagent has several advantages over other potential agents: it is non-ionic, forms self-generated gradients in comparatively short centrifugation times and, most importantly, it is iso-osmotic [22]. This ensures a low influence on protein stability and structure. Nevertheless, to analyze the potential influence of Iodixanol on the structural assembly of the prepared fibrils AFM studies were performed (Fig. S8). The obtained AFM results indicate that fibril formation is not altered by Iodixanol, that the fibrils are virtually identical to Aβ fibrils previously studied by AFM [23] and that no background signal by lower molecular weight species such as oligomers can be observed. As observed for SEC-purified Aβ-oligomers, it was possible to immobilize reproducible amounts of the DGC separated Aβ-fibrils on the surface (Fig. S1 B). To the best of our knowledge, this is the first report on the immobilization of Iodixanol DGC-separated Aβ(1–42) fibrils via a biotin-streptavidin technique and acts as a proof-of-principle

Table 1. Overview of kinetic rates for scFv-IC16 binding to different Aβ(1–42) assembly states obtained within the single-cycle kinetic SPR experiments.

	monomers	monomers#	oligomers#	fibrils#
k_{a1} [a]	$2.27*10^4$	$2.16*10^4$	$2.66*10^4$ ($4.9*10^3$; n = 4)	$2.96*10^4$ ($3.9*10^3$; n = 3)
k_{d1} [b]	$1.74*10^{-2}$	$2.03*10^{-2}$	$0.98*10^{-2}$ ($1.8*10^{-3}$; n = 4)	$0.92*10^{-2}$ ($1.5*10^{-3}$; n = 3)
K_{D1} [c]	$7.69*10^{-7}$	$9.36*10^{-7}$	$3.70*10^{-7}$ ($1.4*10^{-7}$; n = 4)	$3.12*10^{-7}$ ($7.5*10^{-8}$; n = 3)
k_{a2} [a]	-	$4.80*10^4$	$1.03*10^2$ ($9.2*10^1$; n = 4)	$4.54*10^2$ ($3.7*10^2$; n = 3)
k_{d2} [b]	-	$4.78*10^{-9}$	$5.76*10^{-4}$ ($2.9*10^{-3}$; n = 4)	$1.93*10^{-3}$ ($1.0*10^{-3}$; n = 3)
K_{D2} [c]	-	$9.90*10^{-14}$	$5.60*10^{-6}$ ($7.9*10^{-6}$; n = 4)	$4.26*10^{-6}$ ($2.2*10^{-6}$; n = 3)
χ^2	4.1	2.4	3.0	1.2
R_{max1} [d]	36.6	36.2	69.1	89.3
R_{max2} [d]	-	1.6	206.1	143.1

The hash (#) denotes that kinetic rates were determined with a heterogeneous binding model. Standard deviation with number of experiments is given in brackets. #fit to a heterogeneous binding model. Units are: [a] Ms^{-1}, [b] s^{-1}, [c] M, and [d] RU.
doi:10.1371/journal.pone.0089490.t001

experiment that demonstrates this combination of methods as a powerful tool for future sample preparation of ligands for SPR studies. However, the refractive index shows a dramatic jump following sample injection because of the presence of Iodixanol (Fig. S1 B). Incubation of the flow cell in a continuous flow mode revealed a linear decay of 4 RU (RU: response units) per hour after 8 h. We assumed this decay is caused by a small amount of the fibrils dissociating, because similar decays have been observed previously for immobilized fibrils [24]. scFv-IC16 was able to bind to the fibril surface. The binding curves were fit with the identical model used for Aβ(1–42) oligomers. The resulting dissociation constants for scFv-IC16 binding to Aβ(1–42) fibrils were determined to be 0.31 μM and 4.26 μM (χ^2: 1.2, Tab. 1), which are very similar to those obtained for Aβ oligomers.

Discussion

A direct comparison of the obtained kinetic rates and overall affinities for scFv-IC16 and Aβ species reveals that for each Aβ assembly state (C-terminally biotinylated monomers, as well as 10% N-terminally biotinylated oligomers and fibrils), there is one interaction component present with nearly identical properties among all three assembly states (Fig. 3. and Tab. 1). The attained association and dissociation rates for the high affinity site of scFv-IC16 binding to Aβ monomers, oligomers and fibrils are 2.3×10^4 Ms^{-1} and 1.7×10^{-2} s^{-1}, 2.7×10^4 Ms^{-1} and 1.0×10^{-2} s^{-1}, 3.0×10^4 Ms^{-1} and 0.9×10^{-2} s^{-1}, respectively. Based on these rate constants, it is tempting to speculate that the same binding epitope for scFv-IC16 is present in each of the studied Aβ assembly states. Because this epitope is obviously missing in purely N-terminally biotinylated monomers, we can conclude that this epitope contains the very N-terminal residues of Aβ. Moreover, the affinity of the slower binding reaction of scFv-IC16 binding oligomers and fibrils was nearly one order of magnitude weaker (K_{D2}-values in Tab. 1). Based on this observation we conclude that Aβ generates a secondary binding site for scFv-IC16 when forming higher assembly states like oligomer and fibril structures. Remarkably, fitting of sensorgram data obtained with scFv-IC16 binding monomeric Aβ(1–42) to the heterogeneous ligand binding model, as used for oligomers and fibrils, did not yield a second binding component similar to the oligomer and fibril data. Instead, an unlikely apparent K_D of 9.9×10^{-14} M in concert with an R_{max} value of 1.6 supports the notion that scFv-IC16 binding data for monomers follows a 1:1 Langmuir interaction, which confirms that the Aβ monomer preparation was extremely homogeneous, and that the secondary binding epitope existing in oligomers and fibrils is clearly not a fitting artefact.

In addition to the specific findings concerning the properties of scFv-IC16, we hereby describe a general approach to immobilize any Aβ assembly that contains a fraction of n-terminally biotinylated Aβ molecules to streptavidin-coated SPR chips while having the possibility to confirm integrity of the immobilized Aβ species via binding of scFv-IC16 at any time of the experiment. IC16 was chosen, because it recognizes the amino-terminus of Aβ only, when it is not biotinylated and bound to streptavidin. The scFv fragment of IC16 has been chosen because it binds in a 1:1 ratio to the target and is eluting more rapidly than the full-length IC16 antibody. The setup allows immobilization of either C-

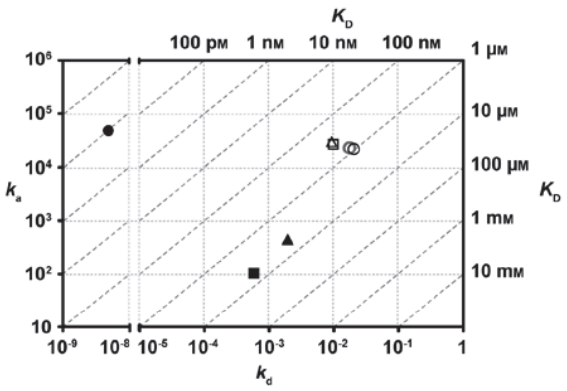

Figure 3. Kinetic rates obtained for scFv-IC16 binding to different immobilized Aβ(1–42) assembly states. Association rate constants (k_a) were plotted against dissociation rate constants (k_d). The dissociation constant (K_D) can be extracted from the diagonal lines. Circles, squares and triangles correspond to data from interactions with monomers, oligomers and fibrils, respectively, whereas filled symbols represent data for the second binding site. All data was determined with the heterogeneous fitting model. The grey circle represents monomer data obtained with a 1:1 binding model.
doi:10.1371/journal.pone.0089490.g003

terminally Aβ monomers or any kind of higher order Aβ forms that were artificially prepared employing a fraction of N-terminally biotinylated Aβ. We have given one example each of a monomer, oligomer and fibril preparation, as were published previously by others.

Conclusions

Taken together, we have established a novel approach allowing reproducible interaction studies with different homogeneous Aβ(1–42) assembly states by SPR. SEC and DGC purification of Aβ species prior to streptavidin-biotin coupling ensures sample homogeneity and minimal surface alterations, which are major limitations of SPR experiments involving Aβ. In addition, we have employed a monoclonal antibody-derived scFv for direct verification of successfully immobilized higher Aβ assembly states. Although, the hereby described approach is straightforward only for in vitro-generated Aβ assemblies, it may prove to be an essential step toward future screening and in-depth characterization of potential drug candidates and thereby has the capability to greatly simplify and accelerate drug development for AD.

Supporting Information

Figure S1 Overlay of sensorgrams obtained during immobilization of three different Aβ(1–42) assembly states on a streptavidin sensor chip. Oligomers and fibrils were prepared in a 1:10 molar ratio of amino-terminally biotinylated and non-biotinylated Aβ(1–42), whereas monomers were completely biotinylated at the carboxy-termini. Final immobilized amounts are given in brackets. Shown are examples of sensorgrams obtained during immobilization of Aβ(1–42) monomers and oligomers (A) as well as fibrils (B). Because the procedure involves changes in buffer, these sensorgrams don't allow conclusions about association and dissociation rates of the immobilized Aβ(1–42) assembly states. After a few hours a stable baseline decay dependent on the immobilized assembly state was reached. RU: response units.
(PNG)

Figure S2 Size exclusion chromatography profile at 214 nm of A) 100% C-terminal biotinylated Aβ(1–42), B) 100% N-terminal biotinylated Aβ(1–42), C) 10% N-biotinylated Aβ(1–42)/90% Aβ(1–42), D) Molecular weight standard with Aprotinin (6.5 kDa), Lysozyme (14.4 kDa) and Conalbumin, Catalase, Aldolase, Ferritin in the void volume with Superdex 75 10/300 GL. Oligomers elute partly within the void volume and the monomers at ~9 kDa. AU: absorption units at 214 nm.
(PNG)

Figure S3 SPR sensorgram depicting binding of monoclonal IgG antibody 6E10 to N-terminally biotinylated Aβ(1–42) monomers immobilized on a streptavidin-coated SPR sensor chip.
(PNG)

Figure S4 SPR sensorgrams depicting binding pattern of scFv IC16 to ~1200 RU N-terminally biotinylated Aβ(1–42) monomers, immobilized on a streptavidin-coated SPR sensor chip.
(PNG)

Figure S5 SPR sensorgram depicting binding of monoclonal IgG antibody 6E10 to C-terminally biotinylated Aβ(1–42) monomers immobilized on a streptavidin-coated SPR sensor chip.
(PNG)

Figure S6 SPR sensorgram depicting binding of monoclonal IgG antibody 6E10 to Aβ(1–42) oligomers immobilized on a streptavidin-coated SPR sensor chip. Aβ oligomers were composed of a 1:10 ratio of amino-terminally biotinylated Aβ(1–42) and non-biotinylated Aβ(1–42).
(PNG)

Figure S7 Steady-state analysis of scFv-IC16 binding to immobilized C-terminally biotinylated Aβ(1–42) monomers. The dissociation constant K_D for a 1:1 interaction is calculated from equation $R_{eq} = (C*R_{max})/(K_D+C)$, where C refers to the analyte concentration, R_{eq} to the obtained equilibrium binding levels and R_{max} to the maximum analyte binding capacity of the surface. Values for K_D and R_{max} were determined to 0.97 µM and 39.7 RU with a corresponding χ^2 value of 0.38.
(PNG)

Figure S8 Analysis of Aβ(1–42) fibrils after density gradient centrifugation (DGC) by atomic force microscopy. The fibrils were created in 10 mM sodium phosphate buffer (pH 7.4) and separated by density gradient centrifugation to remove smaller Aβ(1–42) assembly states. Fibrils are illustrated in (A) and shows the height image of the surface. Image (A) was used to determine a height profile (B) of the surface indicated by the black bar in (A).
(PNG)

Figure S9 Development of the baseline after immobilization of: A) ~150 RU N-terminally biotinylated Aβ(1–42) monomers, B) ~200 RU Aβ(1–42) oligomers, C) ~400 RU Aβ(1–42) fibrils. Aβ(1–42) oligomers and fibrils were composed of a 1:10 ratio of amino-terminally biotinylated Aβ(1–42) and non-biotinylated Aβ(1–42).
(PNG)

Acknowledgments

Carsten Korth, Andreas Müller-Schiffmann and Silke Dornieden are gratefully acknowledged for providing the vector coding for scFv-IC16. We would like to thank Max Michel for his help with the purification of scFv-IC16 and Andrew Dingley for proofreading of the manuscript.

Author Contributions

Conceived and designed the experiments: JMG DW. Performed the experiments: DF OB FO. Analyzed the data: DF JMG OB DW FO LNS. Wrote the paper: JMG DF DW. Prepared Aβ species and scFv-IC16, performed size exclusion chromatography and surface plasmon resonance experiments: DF. Carried out density gradient centrifugation: DF OB. Executed the atomic force experiments: DF OB FO.

References

1. Gulland A (2012) Number of people with dementia will reach 65.7 million by 2030, says report. Bmj 344: e2604.
2. Ross CA, Poirier MA (2004) Protein aggregation and neurodegenerative disease. Nature medicine 10 Suppl: S10–17.
3. Tanzi RE, Bertram L (2005) Twenty years of the Alzheimer's disease amyloid hypothesis: a genetic perspective. Cell 120: 545–555.
4. Schmidt ML, DiDario AG, Otvos L Jr, Hoshi N, Kant JA, et al. (1994) Plaque-associated neuronal proteins: a recurrent motif in neuritic amyloid deposits throughout diverse cortical areas of the Alzheimer's disease brain. Experimental neurology 130: 311–322.
5. Milligan CE (2000) Caspase cleavage of APP results in a cytotoxic proteolytic peptide. Nature medicine 6: 385–386.

6. Xia N, Liu L, Harrington MG, Wang J, Zhou F (2010) Regenerable and simultaneous surface plasmon resonance detection of abeta(1–40) and abeta(1–42) peptides in cerebrospinal fluids with signal amplification by streptavidin conjugated to an N-terminus-specific antibody. Analytical chemistry 82: 10151–10157.
7. Wang-Dietrich L, Funke SA, Kühbach K, Wang K, Besmehn A, et al. (2013) The amyloid-beta oligomer count in cerebrospinal fluid is a biomarker for Alzheimer's disease. Journal of Alzheimer's disease: JAD 34: 985–994.
8. Stravalaci M, Bastone A, Beeg M, Cagnotto A, Colombo L, et al. (2012) Specific recognition of biologically active amyloid-beta oligomers by a new surface plasmon resonance-based immunoassay and an in vivo assay in Caenorhabditis elegans. The Journal of biological chemistry 287: 27796–27805.
9. Bruggink KA, Jongbloed W, Biemans EA, Veerhuis R, Claassen JA, et al. (2013) Amyloid-beta oligomer detection by ELISA in cerebrospinal fluid and brain tissue. Analytical biochemistry 433: 112–120.
10. Esparza TJ, Zhao H, Cirrito JR, Cairns NJ, Bateman RJ, et al. (2013) Amyloid-beta oligomerization in Alzheimer dementia versus high-pathology controls. Annals of neurology 73: 104–119.
11. Finder VH, Glockshuber R (2007) Amyloid-beta aggregation. Neuro-degenerative diseases 4: 13–27.
12. Stenberg E, Persson B, Roos H, Urbaniczky C (1991) Quantitative-Determination of Surface Concentration of Protein with Surface-Plasmon Resonance Using Radiolabeled Proteins. J Colloid Interf Sci 143: 513–526.
13. Johansson AS, Berglind-Dehlin F, Karlsson G, Edwards K, Gellerfors P, et al. (2006) Physiochemical characterization of the Alzheimer's disease-related peptides A beta 1–42Arctic and A beta 1–42wt. The FEBS journal 273: 2618–2630.
14. Wood SJ, Maleeff B, Hart T, Wetzel R (1996) Physical, morphological and functional differences between ph 5.8 and 7.4 aggregates of the Alzheimer's amyloid peptide Abeta. Journal of molecular biology 256: 870–877.
15. Nagel-Steger L, Demeler B, Meyer-Zaika W, Hochdorffer K, Schrader T, et al. (2010) Modulation of aggregate size- and shape-distributions of the amyloid-beta peptide by a designed beta-sheet breaker. European biophysics journal: EBJ 39: 415–422.
16. Karlsson R, Katsamba PS, Nordin H, Pol E, Myszka DG (2006) Analyzing a kinetic titration series using affinity biosensors. Analytical biochemistry 349: 136–147.
17. Amijee H, Bate C, Williams A, Virdee J, Jeggo R, et al. (2012) The N-methylated peptide SEN304 powerfully inhibits Abeta(1–42) toxicity by perturbing oligomer formation. Biochemistry 51: 8338–8352.
18. Green NM (1963) Avidin. 1. The Use of (14-C)Biotin for Kinetic Studies and for Assay. The Biochemical journal 89: 585–591.
19. Glück JM, Koenig BW, Willbold D (2011) Nanodiscs allow the use of integral membrane proteins as analytes in surface plasmon resonance studies. Analytical biochemistry 408: 46–52.
20. Dornieden S, Müller-Schiffmann A, Sticht H, Jiang N, Cinar Y, et al. (2013) Characterization of a single-chain variable fragment recognizing a linear epitope of abeta: a biotechnical tool for studies on Alzheimer's disease? PloS one 8: e59820.
21. Müller-Schiffmann A, Marz-Berberich J, Andreyeva A, Ronicke R, Bartnik D, et al. (2010) Combining independent drug classes into superior, synergistically acting hybrid molecules. Angewandte Chemie 49: 8743–8746.
22. Ford T, Graham J, Rickwood D (1994) Iodixanol: a nonionic iso-osmotic centrifugation medium for the formation of self-generated gradients. Analytical biochemistry 220: 360–366.
23. Stine WB Jr, Snyder SW, Ladror US, Wade WS, Miller MF, et al. (1996) The nanometer-scale structure of amyloid-beta visualized by atomic force microscopy. Journal of protein chemistry 15: 193–203.
24. Cannon MJ, Williams AD, Wetzel R, Myszka DG (2004) Kinetic analysis of beta-amyloid fibril elongation. Analytical biochemistry 328: 67–75.

2.1.6 Amyloid Aggregation Inhibitory Mechanism of Arginine-rich D-peptides.

Publiziert in: Current Medicinal Chemistry

Impact Factor: 4,07

Eigenanteil an der Publikation: 15 %

Kreatives Design von RD2

Send Orders for Reprints to reprints@benthamscience.net

1448 *Current Medicinal Chemistry*, 2014, *21*, 1448-1457

Amyloid Aggregation Inhibitory Mechanism of Arginine-rich D-peptides

O.O. Olubiyi[1,2], D. Frenzel[1], D. Bartnik[1], J.M. Glück[1], O. Brener[1,3], L. Nagel-Steger[1,3], S.A. Funke[1,4], D. Willbold*[,1,3,a] and B. Strodel*[,1,5,a]

[1]*Forschungszentrum Jülich, Institute of Complex Systems: Structural Biochemistry (ICS-6), 52425 Jülich, Germany;* [2]*German Research School for Simulation Sciences GmbH, 52425 Jülich, Germany;* [3]*Institut für Physikalische Biologie, Heinrich-Heine-Universität Düsseldorf, 40225 Düsseldorf, Germany;* [4]*Bioanalytik, Hochschule für Angewandte Wissenschaften, 96450 Coburg, Germany;* [5]*Institut für Theoretische und Computerchemie, Heinrich-Heine-Universität Düsseldorf, 40225 Düsseldorf, Germany*

Abstract: It is widely believed that Alzheimer's disease pathogenesis is driven by the production and deposition of the amyloid-β peptide (Aβ) in the brain. In this study, we employ a combination of *in silico* and *in vitro* approaches to investigate the inhibitory properties of selected arginine-rich D-enantiomeric peptides (D-peptides) against amyloid aggregation. The D-peptides include D3, a 12-residue peptide with anti-amyloid potencies demonstrated *in vitro* and *in vivo*, RD2, a scrambled sequence of D3, as well as truncated RD2 variants. Using a global optimization method together with binding free energy calculations followed by molecular dynamics simulations, we perform a detailed analysis of D-peptide binding to Aβ monomer and a fibrillar Aβ structure. Results obtained from both molecular simulations and surface plasmon resonance experiments reveal a strong binding of D3 and RD2 to Aβ, leading to a significant reduction in the amount of β structures in both monomer and fibril, which was also demonstrated in Thioflavin T assays. The binding of the D-peptides to Aβ is driven by electrostatic interactions, mostly involving the D-arginine residues and Glu11, Glu22 and Asp23 of Aβ. Furthermore, we show that the anti-amyloid activities of the D-peptides depend on the length and sequence of the D-peptide, its ability to form multiple weak hydrophobic interactions with Aβ, as well as the Aβ oligomer size.

Keywords: Amyloid beta, amyloid inhibition, D-peptides, *in silico*, surface plasmon resonance, ThT assay.

INTRODUCTION

Alzheimer's disease (AD), the most common form of dementia in the elderly, is characterised by progressive brain neural dysfunction associated with the toxic aggregation of misfolded amyloid β-peptides (Aβ). Aβ, the soluble Aβ oligomers in particular, occupy the central role in AD pathogenesis [1-3]. At the moment, however, there are no drugs capable of modifying the progression of AD. This, in part, results from Aβ's peculiar features as a drug target, such as its high conformational flexibility and strong aggregation propensity. The latter, in particular, has been a challenge for the rational design of Aβ aggregation inhibitors, which has yet to be overcome [4]. Progress in the *in vitro* screening of compound libraries for small molecules that inhibit Aβ aggregation has been hampered by the poor binding specificity demonstrated by the candidate compounds [1]. Immunotherapeutic techniques can be used to overcome this size limitation and has been extensively explored [5, 6]. In this approach, the use of antibodies that are highly specific for certain regions of the Aβ molecule, coupled with the relatively large molecular size of the antibodies, facilitate specific binding to the Aβ peptide. Due to the high cost and severe side effects associated with the therapeutic use of antibodies, alternative mechanisms for the treatment of Alzheimer's disease are still being sought. The development of drug design methods that selectively target Aβ requires an understanding of Aβ's structural and aggregation dynamics. For example, knowledge of the self-recognition sequence $A\beta_{16-22}$, which is believed to be decisive for toxic β-sheet formation, has been shown to be an important target for the design of inhibitors of Aβ aggregation.

A number of *β-sheet breakers* that target the $A\beta_{16-22}$ sequence have been identified and demonstrated to be effective at suppressing the formation of β-sheets as well as Aβ-associated neurotoxicity. Aminopyrazoles are a prominent example of rationally designed β-sheet breakers with a specific sequence of hydrogen-bond donors and acceptors thatare complementary to those in the β-sheet structure [7]. In numerous experiments, aminopyrazoles have been shown to bind selectively to the backbone of peptides in which the predominant structural element is the cross-β-sheet [8, 9]. This binding facilitates the disassembly of preformed Aβ fibrils in a dose- and time-dependent manner [10, 11]. The design of other molecules that target β-sheet formation include the approach by Tjernberg *et al.*, which utilizes the ability of the $A\beta_{16-22}$ fragment to inhibit Aβ fibrillization when added to a solution containing the full-length Aβ peptide [12]. Other approaches include the polylysine-based peptide inhibitors of Ghanta *et al.* [13] and Pallitto *et al.* [14], and the hybrid peptide inhibitors incorporating bulky

*Address correspondence to these authors at the Forschungszentrum Jülich, Institute of Complex Systems: Structural Biochemistry (ICS-6), 52425 Jülich, Germany; Tel: +49-2461-613670; Fax: +49-2461-619497;
E-mails: d.willbold@fz-juelich.de and b.strodel@fz-juelich.de

This work is a part of proceedings of "DDTWC".

1875-533X/14 $58.00+.00

hydrogen bond-disrupting functionalities reported by Findeis *et al.* [15, 16], Hughes *et al.* [17] and Gordon *et al.* [18].

These (or similar) methods have led to the development of D-peptide inhibitors with protease resistance and low immunogenic properties. One such D-peptide is D3 [19-21], a 12-residue arginine-rich aggregation inhibitor discovered using mirror image phage display [22]. *In vitro* and *in vivo* assays revealed a significant dose-dependent reduction in Aβ's toxicity in the presence of D3 [19, 20]. Following administration in transgenic mice, D3 also improved cognitive function and reduced amyloid plaque burden [21]. Furthermore, dynamic light scattering measurements of D3-treated Aβ solutions showed the formation of large amorphous aggregates devoid of amyloid fibrils. In a recent publication we rationalized the reported effects of D3 by analyzing its binding to full-length $A\beta_{1-42}$ monomer (Aβm) using molecular simulations [23]. D3 binding to Aβm was observed to be mainly driven by electrostatic attraction between the arginine residues of D3 and the negatively charged aspartyl and glutamyl residues in the N-terminal region of Aβm, and resulted in the disruption of secondary structure in Aβm. The β-sheets, in particular, were converted to random coil structure. This is in agreement with the experimental observation in which the binding of D3 converted β-sheet-rich Aβ into predominantly ThT (Thioflavin T)-negative amorphous aggregates [21]. The electrostatically driven association causes the D3 peptide to bind to the N-terminal half of Aβm, which includes the central hydrophobic core, LVFFA. This suggests that D3 prevents the aggregation of Aβ into toxic β-sheets by shielding the amyloid-aggregation nucleating sequence $A\beta_{16-22}$ [22].

In this study, we investigate the interaction of D3 with a β-sheet oligomer representing the fibrillar $A\beta_{1-42}$ (Aβf). Furthermore, we examine the interaction of both Aβm and Aβf with three analogues of the D3 peptide. To this end, we employ the basin-hopping (BH) approach to global optimization [24] for the generation and optimization of D-peptide-Aβ complexes. We then use the MM/GB formalism [25] for calculating binding free energies, which are used to rank the strength of the complexes. Finally, explicit solvent molecular dynamics (MD) simulations of selected complexes are performed in order to better describe the peptide-inhibitor interactions. Our simulation results are compared to experimental results obtained from ThT and surface plasmon resonance assays.

MATERIALS AND METHODS

Structural Models

D3, RD2, HN5 and R5 denote D-enantiomeric peptides with the sequences RPRTRLHTHRNR-Am, PTLHTH NRRRRR-Am, HNRRRRR-Am and RRRRR-Am, respectively, where "-Am" represents C-terminal amide capping while the N-terminus was modelled as an amine with a positive charge. The GROMOS53a6 [26] and CHARMM22 [27] force field models were generated for the D-amino acid residues present in these peptides. A 100 ns MD simulation was performed for each peptide starting from the fully extended configuration using GROMOS53a6 (henceforth ffG53a6) and the MD software GROMACS [28]. Each peptide was centered in a cubic box with at least 10 Å from any peptide atom and the box edges. Then a sufficient number of water molecules, represented by the simple point charge (SPC) model [29] were added in order to fill the box. Thereafter, Na^+ and Cl^- ions were added to both neutralize the net peptide charge and to achieve a 150 mM NaCl concentration. After energy minimization (steepest descent followed by conjugate gradient), we performed 1 ns position restrained dynamics for each peptide system under NPT conditions (Berendsen barostat, 1 bar; Berendsen thermostat, 300 K) using a 239 kcal/mol restraining force applied to the peptide's non-hydrogen atoms. After turning off the restraints, a 100 ns MD run was conducted in the NPT ensemble (Parrinello-Rahman barostat, 1 bar; Nosé-Hoover thermostat, 300 K). Periodic boundary conditions (PBC) were applied for boundary treatment and a 14 Å cutoff was used for non-bonded interactions. We employed the particle mesh Ewald method to compute long-range electrostatic interactions [30]. The resulting MD trajectories were subjected to cluster analysis using the Daura method [31] and the centroid of the largest cluster, representing the dominant conformation, was identified for each D-peptide.

For Aβm, five starting conformations, obtained from previously reported 1.5 μs MD sampling of $A\beta_{1-42}$ monomer [23], were employed to study the Aβm-D-peptide interactions. The use of multiple Aβm starting structures allows us to account for Aβ's structural flexibility in aqueous solution. In case of Aβf, we employed the full-length structure shown in (Fig. **1**). To obtain this structure, the coordinate file of an $A\beta_{18-42}$ pentamer determined by solid-state NMR (PDB code 2BEG) of $A\beta_{1-42}$ fibrils was used [32]. In this structure, Aβ adopts a strand-turn-strand conformation with residues 18–26 and 31–42 forming an in-register β-sheet arrangement. However, since the N-terminal residues 1–17 are disordered, the corresponding PDB file does not contain coordinates for the atoms of these residues. Therefore, starting from 2BEG, residues 1-17 sampling coil conformation were taken from previous MD simulations of the $A\beta_{1-42}$ monomer [23], and *ligated* to each of the five chains of the fibrillar structure. The resulting construct was subjected to BH optimization [24] (see below for a description of the BH procedure) using the program GMIN [33]. During the procedure, the positions of residues 18-42 were fixed while those of the newly attached residues 1-17 were optimized to resolve atomic clashes and lower inter-peptide interaction energies. Several cycles of BH optimization were performed, during which the coordinates of residues 1-17 of the five chains were sequentially *frozen* and optimized. This way we were able to achieve the desired level of random coil in the N-terminal segments. After optimization, the lowest energy configuration, hereafter referred to as Aβf or Aβ fibril fragment (shown in Fig. **1**), was employed in the subsequent Aβf-D3/RD2 interaction studies reported herein.

Generation and Optimization of Aβ-D-peptide Complexes

We employed the BH approach to global optimization [24] as implemented in GMIN [33] to produce low-energy structures for the Aβ-D-peptide complexes. The BH method is analogous in principle to the Monte Carlo-minimization approach with minimization [34]. Moves are proposed by perturbing the current geometry and are accepted or rejected

based on the energy difference between the local minimum obtained by minimization from the instantaneous configuration and the previous minimum in the Markov chain. We used the oligomer-generation procedure [23, 35, 36] in GMIN to generate the Aβ-D-peptide complexes. These complexes were subsequently optimized within 400 BH steps, which allowed dihedral angle moves [37] and limited rigid-body rotations and translations [34] for the D-peptides. For the GMIN runs, parameters from the CHARMM22 potential [27] and the Fast Analytic Continuum Treatment of Solvent (FACTS) implicit solvent model [38] were employed. The choice of force field employed in our MD and GMIN simulations are based on the following facts: (i) The GROMOS force fields are not compatible with GMIN as they lack an implicit solvent description. (ii) The CHARMM potential was not yet implemented in GROMACS when this study was started. (iii) In our previous MD simulations of $A\beta_{1-40}$ and $A\beta_{1-42}$ ffG53a6 produced a very good agreement with experimental results; this gave us enough justification to continue to use this particular force field in our MD studies [23]. 5000 complexes involving Aβm (1000 per Aβm starting structure) were produced for each of D3, RD2, HN5 and R5 in a 1:1 ratio, and 4000 complexes were produced for each of D3 and RD2 interacting with Aβf in a 1:5 ratio.

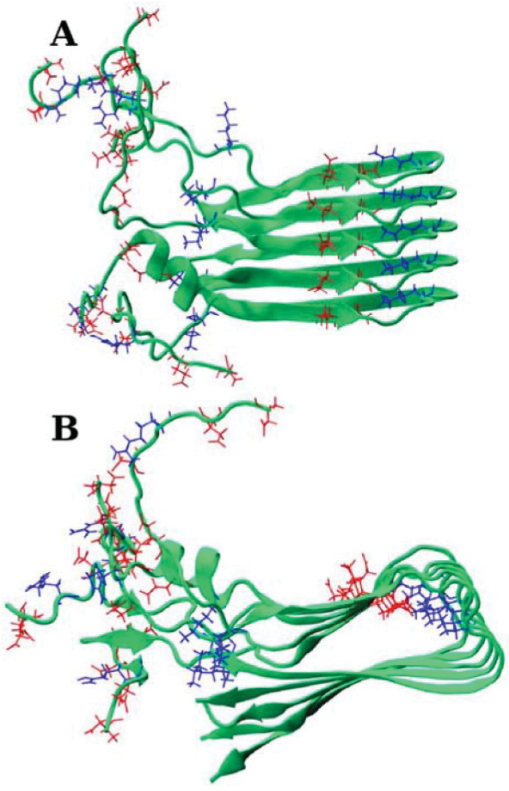

Fig. (1). Full-length $A\beta_{1-42}$ fibril structure in VMD [46] green New Cartoon representation showing the top view (**A**) and the side view (**B**). The side chains of the charged amino acid residues are represented with liquorice with red and blue representing acidic and basic amino acids, respectively.

Binding Free Energy Calculations

We employed the MM/GB formalism [25] to compute binding free energies (ΔG_{bind}), with MM and GB parameters taken from the CHARMM22 [27] force field and the FACTS solvent model [38], respectively:

$$\Delta G_{bind} = E_{int} + \Delta G_{sol} \quad (1)$$

ΔG_{bind} was calculated from the intermolecular interaction energies (E_{int}) and the solvation energy terms (ΔG_{sol}). E_{int} contains van der Waals (E_{int}^{vdW}) and electrostatic (E_{int}^{ele}) interactions, which can be directly computed using the CHARMM software [39], whereas the solvation term is composed of the polar (ΔG_{sol}^{pol}) and nonpolar (ΔG_{sol}^{npol}) solvation terms. The solvation energy values were obtained by subtracting the values for Aβ and the D-peptide from that of the complex:

$$\Delta G_{sol} = G_{sol}^{A\beta/Dpep} - G_{sol}^{A\beta} - G_{sol}^{Dpep} \quad (2)$$

ΔG_{bind} was computed for all Aβm-D-peptide and Aβf-D-peptide complexes, which helped in identifying the binding poses with the best interaction strength, i.e., with the lowest ΔG_{bind}. The ΔG_{bind} values obtained for each of the Aβm-D-peptide and Aβf-D-peptide systems are presented in (Table **1**). It should be noted that the binding energies ΔG_{bind} computed here are relative energies, which cannot be directly compared to the experimental binding energy given by

$$\Delta G_{bind}^{exp} = -RT \ln K_D \quad (3)$$

where R is the molar gas constant and T the temperature. In order to obtain estimates of the absolute binding free energy from simulations, the interaction energy E_{int} has to be broken down into electrostatic and van der Waals contributions, and the contributions to ΔG_{bind} linearly fitted to experimental binding affinities using a training set of ligands [40, 41]:

$$\Delta G_{bind}^{abs} = \alpha E_{int}^{vdW} + \beta E_{int}^{ele} + \gamma \Delta G_{sol} \quad (4)$$

Depending on the system under study, the force field and fitting procedure used, different values—generally smaller than one—have been reported for the scaling factors α, β and γ [41]. While the ΔG_{bind} values we obtain from our simulations are relative and not absolute energies, the conclusions drawn from this analysis remain valid. The reason is that our focus is on the difference in the binding of the various D-peptides to Aβ and the contributions of individual residues to ΔG_{bind}, i.e., we compare relative and not absolute energies. In a future study we will derive the parameters α, β and γ in Eq. (**4**) in order to obtain absolute binding free energies, which can be compared to experiment.

Explicit Solvent MD Simulations

The top 100 complexes, in terms of ΔG_{bind}, for each of the four Aβm-D-peptide systems were each subjected to 10 ns explicit solvent MD simulations. In case of the Aβf systems, the top 100 complexes were first clustered into 15 clus-

Table 1. Binding Free Energies and Interaction Energies for D-peptide in Aβm-D-peptide and Aβf-D-peptide Systems. All Values are in kcal/mol

	Complex	$\overline{\Delta G}_{bind}$	$\overline{\Delta G}_{res}$	$\overline{E}_{int}^{Arg}$	$\overline{E}_{int}^{non-Arg}$
Aβm	D3	-133.9	-11.2	-16.5	-11.1
	RD2	-128.0	-10.7	-18.8	-9.6
	HN5	-103.9	-14.8	-16.8	-11.6
	R5	-93.1	-18.6	-18.1	-
Aβf	D3	-175.3	-14.6	-	-
	RD2	-182.2	-15.2	-	-

ters based on D3 and RD2's distribution around Aβf. Six unique poses were then selected, each of which was subjected to 50 ns MD. To obtain good control systems, we also performed MD sampling of Aβm and Aβf alone (i.e., each complex stripped off its D-peptide) under the same simulation conditions as the complex structures.To this end, 10 ns MD simulations of the 100 Aβm structures and a 50 ns simulation of the single Aβf structure were conducted.

Thioflavin T (ThT) Assay

ThT is a benzothiazole dye which exhibits a shift and an increase in quantum yield while binding to β-sheet rich fibrils [42]. During Aβ fibrillization, an increase in ThT fluorescence can be observed until a saturation level is reached. Synthetic human $A\beta_{1-42}$ was purchased from Bachem (Bubendorf, Switzerland). Aβ was dissolved in hexafluoroisopropanol (HFIP) to 1 mM and incubated over night at room temperature. Stock solutions were aliquoted and stored at -20°C until required. Prior to use, HFIP was evaporated. ThT assays were performed as described previously [19, 21] with minor modifications. Aβ aliquots and D3 or its derivatives were dissolved in PBS (137mM NaCl, 2.7 mM KCl, 10 mM Na_2HPO_4, 1.8 mM KH_2PO_4, pH 7.4) and added to a ThT solution (5 μM ThT in PBS). Samples were incubated at 37 °C and measured in a 384-well plate (384-well polypropylene, Greiner Bio-One GmbH, Frickenhausen, Germany). The plate was covered by an adhesive film preventing the evaporation of the sample buffer. Fluorescence recordings were performed at an excitation wavelength of 440 nm and an emission wavelength of 490 nm (Polarstar Optima, BMG, Ortenberg, Germany). The experiments have been performedat least two times and the standard deviation was less than 10%.

Surface Plasmon Resonance Assay

All surface plasmon resonance experiments were performed on a Biacore T200 instrument (GE Healthcare, Freiburg, Germany) operated with Control Software version 1.0 [43]. To immobilize the N-terminally biotinylated Aβm, a sensor chip coated with streptavidin (Series S Sensor Chip SA, GE Healthcare, Freiburg, Germany) was utilized as this allows the immobilization to occur via a biotin-streptavidin interaction. Prior to the immobilization of Aβm, a lyophilized stock of N-terminally biotinylated $A\beta_{1-42}$ (Eurogentec) was dissolved in 100% HFIP, followed by an overnight incubation at room temperature. Subsequently, HFIP was evaporated in a SpeedVac, Aβ resolubilized in 100 μl size-exclusion chromatography (SEC) buffer (50 mM sodium phosphate buffer, 150 mM sodium chloride, 0.6% Tween 20, pH 7.4), centrifuged for 30 seconds at 20000 g and the supernatant loaded onto a Superdex 75 10/300 GL column (GE Healthcare, Freiburg, Germany) operated with a flow rate of 0.8 ml min^{-1} with SEC buffer. Monomeric Aβ samples eluting at ~14 ml were directly immobilized at a ligand density of 2150 RU on flow cell 2 of a SA Sensor Chip. Flow cell 1 was unaltered and used as a reference surface. Immobilization was performed in accordance with the manufacturer's recommendations. The binding behavior of D3, RD2 and D3Δhth (residues 7-9 were removed in D3) to Aβm were compared at 25 °C in a single-cycle kinetic mode, which is based on a kinetic titration series. Within a single cycle, five different analyte concentrations were injected in order of increasing concentration intoa running buffer (PBS, 10 mM sodium phosphate buffer, 137 mM NaCl, 2.7 mM KCl, pH7.4) at a flow rate of 60 μl min^{-1} for 90 seconds, with a final dissociation time of 1800 s after the highest concentration. Prior to data evaluation, sensorgrams were double-referenced. This was achieved by monitoring interactions in dual-channel mode with the reference flow cell connected upstream of the flow cell containing immobilized Aβm and by the subtraction of the blank PBS buffer injection from the peptide binding data. Results were evaluated by steady-state affinity analysis [44].

RESULTS AND DISCUSSION

Aβm Systems

The average binding free energies $\overline{\Delta G}_{bind}$ (Table **1**) calculated for the top 100 complexes are -133.9 (D3), -128.0 (RD2), -103.9 (HN5) and -93.1 kcal/mol (R5). This suggests an important role for inhibitor size, as demonstrated by stronger interaction between Aβ and the 12-residue D3 and RD2, than with Aβm and either of the 7-residue HN5 or the 5-residue R5. With the binding strength differing by no more than 5.9 kcal/mol, the interaction configuration of D3 and RD2 with Aβm is likely to be similar, especially since the two peptides share 100% residue similarity. The only difference between D3 and RD2 is the amino acid sequence, which as the $\overline{\Delta G}_{bind}$ values suggest, does not significantly

affect the electrostatic attraction previously identified as the dominant force driving D3's interaction with Aβm [23]. Indeed, a semi-quantitative evaluation of surface plasmon resonance (SPR) sensorgrams obtained with Aβm shows nearly equal binding responses for D3 and RD2 (Fig. **2**). Interestingly, however, HN5 and R5 with the higher arginine-per-sequence proportions demonstrate significantly higher (i.e., less favorable) $\overline{\Delta G}_{bind}$ values, suggesting a contribution from the non-arginine residues to Aβm-D-peptide binding. This also explains the trend RD2 << HN5 < R5 obtained for the RD2-derived peptides in terms of $\overline{\Delta G}_{bind}$.

Normalizing $\overline{\Delta G}_{bind}$ to the number of D-peptide residues (N_{res}),

$$\overline{\Delta G}_{res} = \frac{\overline{\Delta G}_{bind}}{N_{res}} \quad (5)$$

we find that $\overline{\Delta G}_{res}$ for HN5 (-14.8 kcal/mol) and R5 (-18.6 kcal/mol) are more favourable than those for RD2 (-10.7 kcal/mol) and D3 (-11.2 kcal/mol). This trend results from the increasing proportion of D-arginine residues going from the 12-residue RD2 and D3 (41.7%) to the penta-D-arginine R5 (100%). This also highlights the importance of arginine residues in driving the interaction. The $\overline{\Delta G}_{res}$ for R5 is markedly different from the other three systems mostly because, unlike the other systems, it contains only arginine residues. To properly describe the differences between the binding of the four D-peptide systems, we calculated the contributions from the D-arginine as well as the non-arginine residues to interaction energies $\overline{E}_{int}$. To this end, we averaged the interaction energies over the 10 ns MD simulations for Aβm and the 50 ns simulations for Aβf. The resulting energies are denoted as $\overline{E}_{int}^{Arg}$ and $\overline{E}_{int}^{non-Arg}$, respectively.

The time-averaged interaction energies were subsequently decomposed into inter-residue contributions, which were then averaged over the 100 complexes to generate the interaction energy maps in (Fig. **3**). A similar pattern of electrostatic interaction was obtained for each of the four D-peptides, which is characterized by the five D-arginine residues interacting with Aβm's acidic residues (Glu22 and Asp23 in particular). However, the D-peptides bearing the penta-D-arginine groups (RD2, HN5, R5) exhibit a higher selectivity for Aβm's acidic residues than D3. For instance, compared with D3, the interaction of RD2 and Aβm features more contacts involving favorable interaction energies between -3.0 and -2.0 kcal/mol. Interaction with Aβm's N-terminus is observed to increase in the order D3, RD2, HN5, R5. As can be observed in the interaction energy plots in (Fig. **3**), for the latter two peptides the interaction is nearly exclusively confined to residues Asp1 to Glu11 of Aβm. This can be attributed to repulsive interactions of R5 and HN5 with the Lys28 of Aβm. Compared with the immediately neighboring Aβm residues, the interaction of the D-peptides with Glu22 and Asp23 increases with the number of non-arginine residues present in the respective D-peptide (Fig. **3**). RD2 interacts with Aβm's hydrophobic C-terminal residues to a slightly lower extent than D3 does, but to a higher extent with the Glu11 and Asp23 residues than D3 does. This is a result of the arrangement of the D-arginine residues in RD2, which allows the inhibitor to interact more locally but also more strongly with Aβm. The $\overline{E}_{int}^{Arg}$ and $\overline{E}_{int}^{non-Arg}$ values in (Table **1**) provide an explanation for this. With the five D-arginine residues concentrated in the C-terminal, RD2 demonstrates a more favorable $\overline{E}_{int}^{Arg}$ of -18.79 kcal/mol compared with that of D3 (-16.49 kcal/mol). This leads to stronger interaction between RD2 and the Glu11 and Asp23 residues of Aβm. However, there is a trade-off in $\overline{E}_{int}^{non-Arg}$ values of RD2 (-9.60 kcal/mol), which are higher than those in the case of D3. This also explains why RD2 features a decrease in the hydrophobic interaction with Aβm's hydrophobic residues compared with D3 ($\overline{E}_{int}^{non-Arg}$ of -11.06 kcal/mol).

As the number of non-arginine residues increases in R5, HN5 and RD2, so does the hydrophobic interaction with Aβm's uncharged residues. R5 exhibits the fewest number of hydrophobic contacts with Aβm, followed by HN5. Interestingly, the D-arginine residues remain the principal players even in hydrophobic interaction with Aβm's C-terminal residues, roughly centered on Met35 (Fig. **3**). For all four D-peptides, the hydrophobic interaction also includes Aβm's Val12-His-His-Gln15 and Leu17-Val-Phe-Phe-Ala21 residues of the central hydrophobic core region. Apart from the D-arginine residues, the D-histidine residues were also involved in the interaction with Aβm (Fig. **3**). And in fact, the D-histidine residue in HN5 can be used to explain the higher number of hydrophobic contacts formed with Aβm compared with R5. As can be seen in the interaction involving the 12-residue D-peptides, RD2 in particular, the strength of the interaction involving D-histidine residue appears to increase the closer it is to D-arginine residues. This effect is generally absent in the other non-D-arginine residues as can be seen in the D3 interaction map, but also to some extent in RD2. Interestingly, a variant of D3 lacking both histidine residues and the adjacent threonine (D3Δhth) showed a strongly reduced binding response in the SPR (Fig. **2**). This effect is nicely confirmed by the experimental results of the fibril formation assay, where D3 and RD2 yielded strong inhibition of fibril formation, but D3Δhth yielded only weak inhibition of fibril formation (Fig. **4**). Residues at position 1 in the four D-peptides interact strongly with Aβm's acidic residues, an effect that can be explained by the presence of an extra positive charge at the N-terminus of each D-peptide. Interestingly however, this effect is much more pronounced in RD2 where D-proline occupies the first position. The secondary structural changes induced by the binding of the D-peptides to Aβm are shown in (Table **2**). Using the DSSP program [45] the time-dependent evolution of Aβm secondary structure was calculated in both the bound and unbound states. The obtained values were then averaged over the simulation length and over the 100 complexes in each of the Aβm-D-peptide systems. Finally, the changes in the Aβm

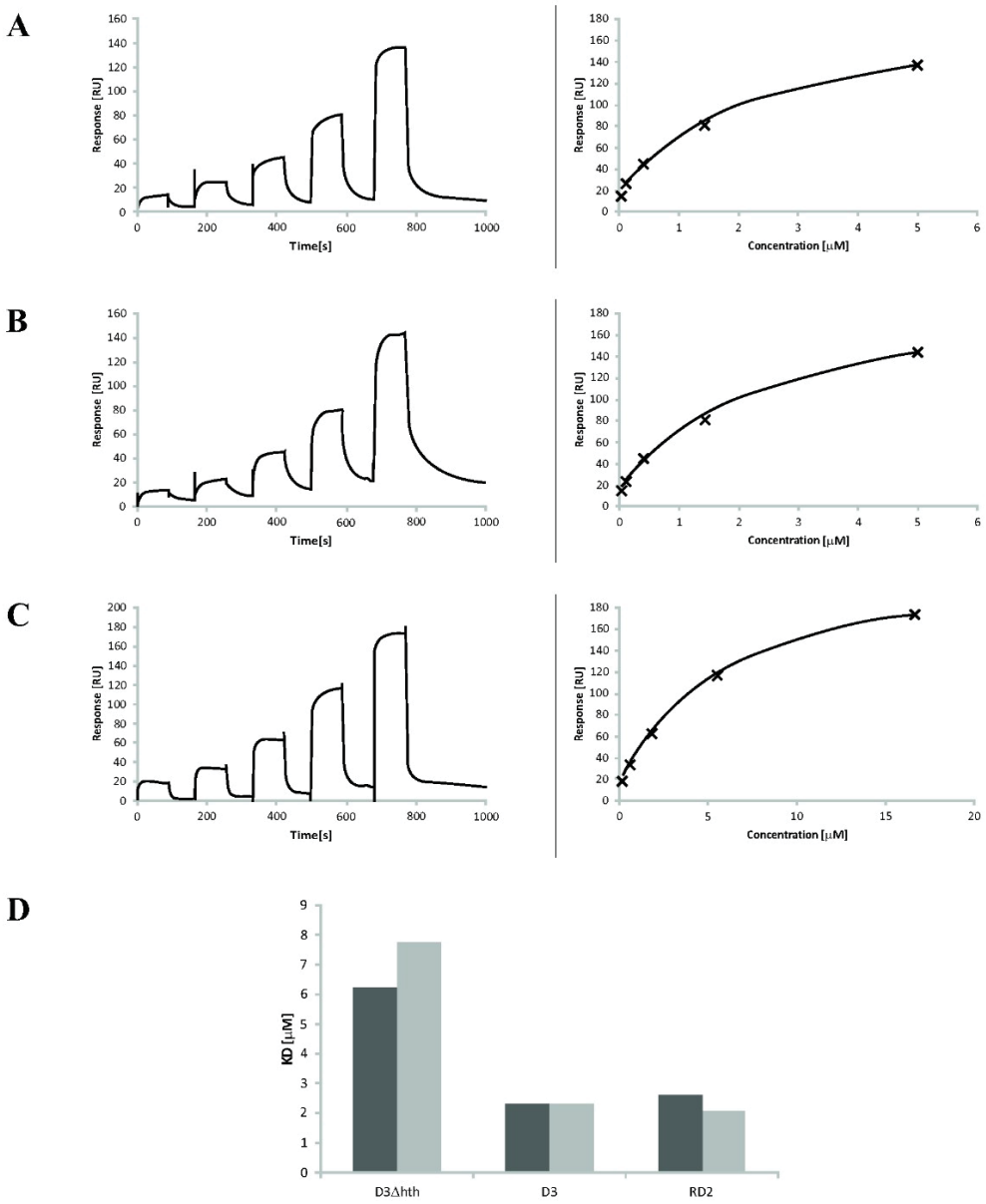

Fig. (2). Single-cycle kinetic surface plasmon resonance measurements for the characterization of the interaction of D3 (**A**), RD2 (**B**), and D3Δhth (**C**) to Aβm. (**A**) to (**C**) show one representative single cycle kinetic measurement per tested peptide (left column) with the corresponding steady-state analysis (right column). (**D**) The equilibrium dissociation constants K_D obtained from two independent measurements are plotted as a bar chart. For D3 and RD2 the highest concentration and dilution factor were 5 μM and 3.5, respectively. For D3Δhth the highest concentration and dilution factor were 16.6 μM and 3 because of its lower affinity.

secondary structure induced by the D-peptide binding were calculated from the values for the bound and unbound Aβm. Of the four D-peptides, D3 followed by RD2 produced the most marked reduction in β-sheet and increase in coil contents. Compared to RD2, D3 more significantly destroys Aβm's β-sheets because it is able to more efficiently interact with the hydrophobic residues of Aβm. This is indicated by average per-residue interaction energies of ≈ -0.72 kcal/mol formed between D3 and Aβm's Lys17→Ala21 and Ala30→Ala42 residues, compared with > -0.24 kcal/mol for RD2, HN5 and R5. With Aβm's structure only minimally affected, the binding of HN5 and R5 fail to translate into desirable anti-amyloid activity.

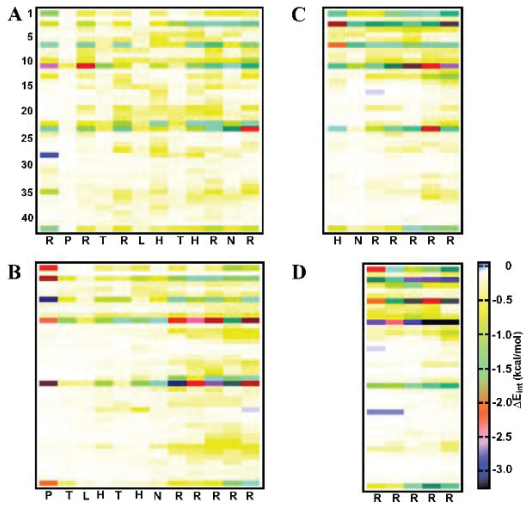

Fig. (3). Interaction energy maps for $A\beta_{1-42}$ monomer residues interacting with the residues of (**A**) D3, (**B**) RD2, (**C**) HN5, and (**D**) R5.

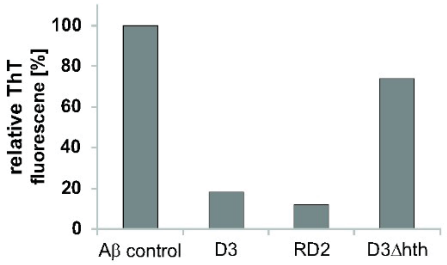

Fig. (4). Inhibition of ThT positive Aβ fibril formation in presence of different D3 derived peptides. The peptides (or buffer for the Aβ control) were added in a concentration of 100 μM to 10 μM $A\beta_{1-42}$ samples. Upon addition of ThT, fluorescence was measured at 490 nm in relative units. All values are corrected by background fluorescence of ThT in PBS. The value for the Aβ control was set at 100 %.

Aβf Systems

The binding of D3 and RD2 to Aβf produced $\overline{\Delta G}_{bind}$ values of -175.3 kcal/mol and -182.2 kcal/mol, respectively (Table **1**). Compared to Aβm, this represents a gain in binding energy of ≈ -50 kcal/mol. This suggests a stronger interaction with Aβf, resulting from Aβf's bigger size that allows for more contacts with D3 and RD2. Also, contrary to the pattern obtained for Aβm, RD2 shows a slightly stronger interaction with Aβf than D3 does. It is likely that the differences between RD2 and D3's binding to Aβf results from the ordered arrangement of Aβf's five Asp23 residues within Aβf's fibril core (Fig. **1**) which provides a good binding surface for RD2's penta-D-arginine moiety.

To further examine this, the centers-of-mass of D3 and RD2 were calculated for the top 100 complexes obtained from docking using GMIN, and were displayed around the Aβf structure (Fig. **5**). The regular scaffold formed by Aβf strongly influences the way the two D-peptides interact with Aβf. D3 largely binds to Aβf's disordered N-terminus, while in 16% of the cases it binds within Aβf's fibril core to interact with the Asp23-Lys28 salt-bridge. The distribution around Aβf suggests the absence of a unique binding pose for D3. RD2 on the other hand, generally adopts one of two binding poses involving a slightly favored binding to Aβf's disordered region, whereas it interacted within the hydrophobic fibril core 41% of the time. In other words, RD2's penta-D-arginine motif renders it ≈ 2.6 times more capable of interacting within Aβf's fibril core than D3.

Following explicit solvent MD simulations of the top 6 Aβf-D-peptide complexes, the changes in Aβf secondary structure obtained from D3 and RD2 binding were calculated. For the D3-Aβf system, the central structure of clusters 1, 4, 5, 6, 11 and 12 were selected for further analysis using MD simulations (Fig. **6**). For RD2, the central structure of clusters 1, 2, 7, 8, 9 and 13 were considered for MD (Fig. **7**). The smallest perturbation to the Aβf structures by D3 was observed in cluster 6 (Fig. **8A**), where D3 exclusively interacts with Aβf's N-terminus (Fig. **6D**). The largest change to the structure of Aβf was recorded in cluster 12 (Fig. **8A**) in which D3 inserts between adjacent chains within Aβf's fibril core (Fig. **6F**), thus destroying Aβf's backbone hydrogen bonds and the Asp23-Lys28 salt-bridge. Compared with D3, and in most clusters, RD2 induced a larger disruption of Aβf's β-sheet structure (Fig. **8B**). The highest β-sheet disruption was obtained with RD2 binding along Aβf's fibril axis (clusters 8 and 9) as shown in (Fig. **7D** and **E**). Analysis of the backbone hydrogen bonds (H-bonds) indicates the β-sheet breaking effect to mainly result from H-bond destruction (data not shown). In addition, a higher number of H-bonds were destroyed by RD2 than by D3, and this number correlates with the degree of β-sheet disruption and the adopted binding pose. These results differ from the pattern observed in Aβm where D3's ability to form more diverse interactions caused a higher β-sheet destruction compared to RD2 (Table **2**). With RD2 being the better interaction partner for Aβf and D3 for Aβm,

Table 2. Effects of D3, RD2, HN5 and R5 on $A\beta_{1-42}$ Monomer's Secondary Structure

D-peptide	Beta (%Δ)	Coil (%Δ)	Bend (%Δ)	Turn (%Δ)
D3	-22.84	11.36	-1.63	-32.43
RD2	-15.09	5.53	1.95	-20.00
HN5	-3.66	0.60	1.68	-8.33
R5	-4.07	1.00	2.03	-15.38

our analyses suggest that, under experimental conditions, the effects of the two peptides may likely depend on the relative abundance of different Aβ species. These results also suggest that the experimentally observed transformation of Aβ's β-sheet-rich structure to non-β-sheet-rich amorphous aggregates does not involve a single unique binding arrangement.

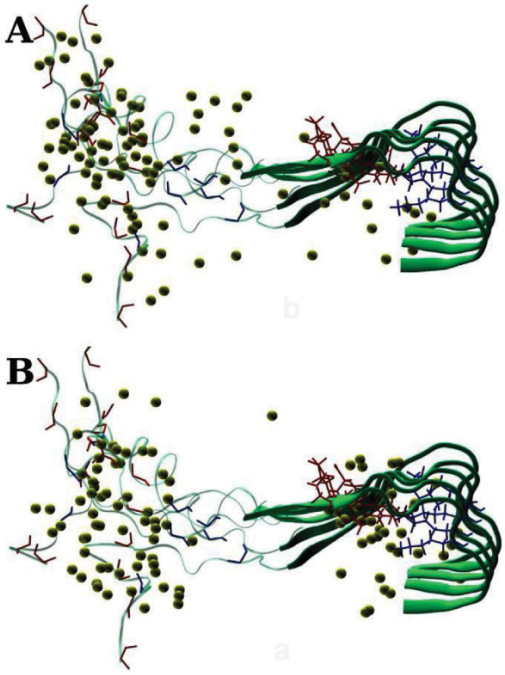

Fig. (5). Binding of (**A**) D3 and (**B**) RD2 to the $A\beta_{1-42}$ fibril fragment. The yellow spheres are the centres of mass of D3 and RD2, while residues 1→20 and 21→33 of $A\beta_{1-42}$are shown as transparent and green ribbons, respectively, and residues 34→42 have been omitted for clarity. The side chains of Glu22 (red), Asp23 (red), and Lys28 (blue) are represented with liquorice.

CONCLUSION

Using a combination of global optimization, binding free energy calculation and MD simulation, we investigated the interaction of D-peptide aggregation inhibitors with the $A\beta_{1-42}$ monomer and pentamer. The interactions in all four D-peptides are principally driven by interaction between their D-arginine residues and $A\beta_{1-42}$'s Glu11, Glu22 and Asp23 residues. While RD2, a reshuffled form of D3 with a C-terminal penta-D-arginine sequence, demonstrates a similar binding pattern as D3 did to the $A\beta_{1-42}$ monomer, it is not as efficient at disrupting β-sheet structures present in the Aβ monomer in aqueous solution. Binding energy calculations show that this effect results from D3's greater ability to also interact with Aβ's hydrophobic residues. In spite of their strongly electrostatic interaction with the $A\beta_{1-42}$ monomer, HN5 and R5, which are truncated forms of RD2, failed to significantly disrupt the β-sheets in the Aβ monomer. The binding study of D3 and RD2 to pentameric $A\beta_{1-42}$ revealed that the D-peptides are able to disrupt the H-bonds between β-strands and thus the β-sheet structure. This mode of action explains why D3 is able to remodel Aβ fibrils into predominantly ThT-negative amorphous aggregates [21]. Interestingly, in binding to the $A\beta_{1-42}$ fibril fragment, RD2 destroys the amyloid β-sheet more efficiently than D3 does. Our observations suggest that this results from RD2's higher tendency to bind inside the $A\beta_{1-42}$ pentamer's fibril core. This is an indication of a difference in the binding specificities of D3 and RD2 for the different Aβ species. D3 possesses a higher binding specificity for the $A\beta_{1-42}$ monomer and elicits more structural perturbations on it, while RD2's specificity and effect are higher against $A\beta_{1-42}$ pentamer. We believe this mechanism of modulating Aβ binding specificity by intramolecular rearrangement of D-peptide residues presents a possible means of achieving a synergistic advantage via co-administration of both D-peptides.

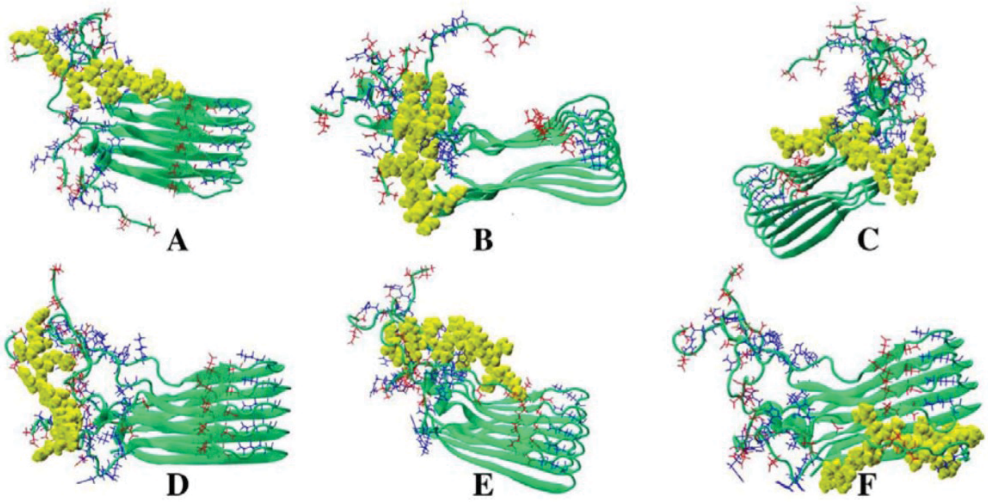

Fig. (6). Clusters (**A**) 1 (**B**) 4 (**C**) 5 (**D**) 6 (**E**) 11 and (**F**) 12 showing the six unique Aβf-D3 binding poses. D3 is shown with yellow vdW spheres, while $A\beta_{1-42}$ is represented with green New Cartoon with acidic and basic residues shown in red and blue liquorice.

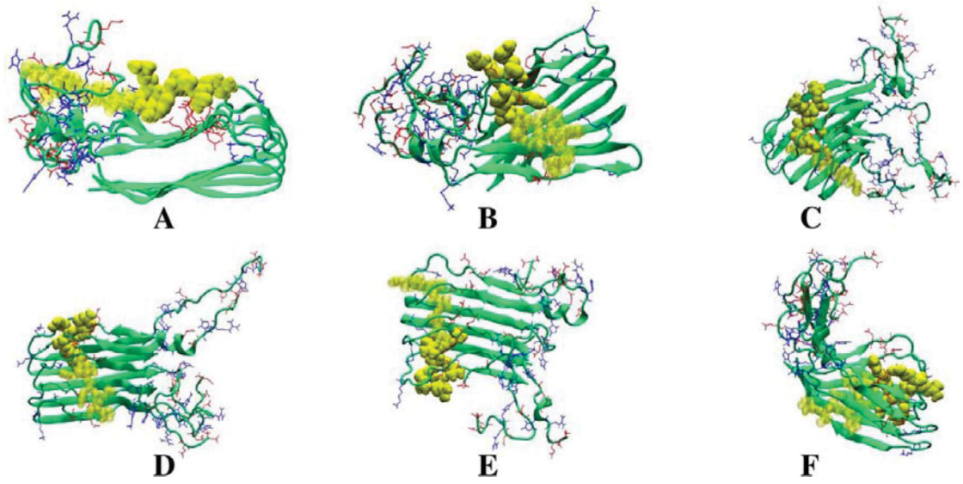

Fig. (7). Clusters (**A**) 1 (**B**) 2 (**C**) 7 (**D**) 8 (**E**) 9 and (**F**) 13 showing the six unique Aβf-RD2 binding poses. RD2 is shown with yellow vdW spheres, while the $A\beta_{1-42}$ pentamer is represented with green New Cartoon with acidic and basic residues shown in red and blue liquorice.

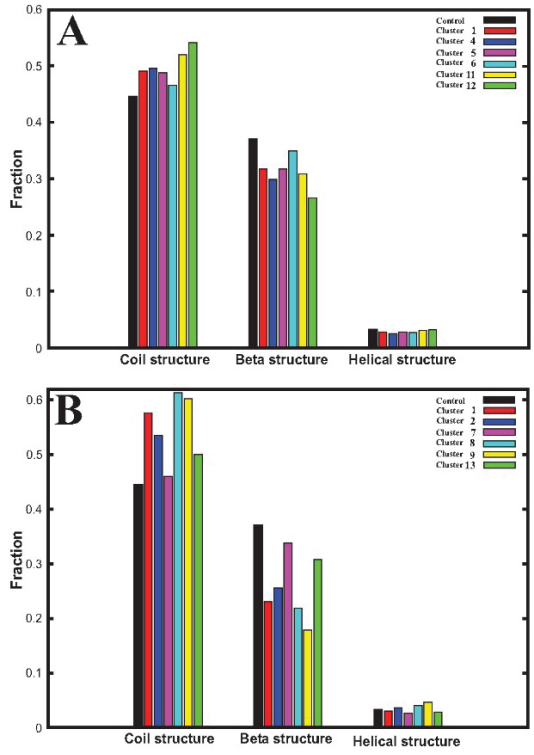

Fig. (8). Effect of the binding of (**A**) D3 and (**B**) RD2on the secondary structure of $A\beta_{1-42}$ in the fibril fragment (Aβf).

CONFLICT OF INTEREST

The author(s) confirm that this article content has no conflicts of interest.

ACKNOWLEDGEMENTS

O. Olubiyi and B. Strodel acknowledge supercomputer time at the Jülich Supercomputing Centre (computing time grant JICS61). We thank Dr. Michael C. Owen for proofreading the manuscript.

REFERENCES

[1] Walsh, D. M.; Klyubin, I.; Fadeeva, J. V.; Cullen, W. K.; Anwyl, R.; Wolfe, M. S.; Rowan, M.J.; Selkoe, D.J.Naturally secreted oligomers of amyloid beta protein potently inhibit hippocampal long-term potentiation *in vivo*. *Nature*,**2002**, *416*, 535-539.

[2] Walsh, D. M.; Klyubin, I.; Shankar, G. M.; Townsend, M.; Fadeeva, J. V.; Betts, V.;Podlisny, M.B.; Cleary, J.P.; Ashe, K.H.; Rowan, M.J.; Selkoe, D.J. The Role of Cell-Derived Oligomers of Abeta in Alzheimer's Disease and Avenues for Therapeutic Intervention. *Biochem. Soc. Trans.*,**2005**, *33*, 1087-1090.

[3] Walsh, D. M.; Klyubin, I.; Fadeeva, J. V.; Rowan, M. J.; Selkoe, D. J. Amyloid-beta Oligomers: Their Production, Toxicity and Therapeutic Inhibition. *Biochem. Soc. Trans.*,**2002**, *30*, 552-557.

[4] Estrada, L.D.; Lasagna, C.; Soto, C. In: *Design of Inhibitors of Amyloid-β Misfolding and Aggregation Alzheimer's Therapy*. Cuello, A.C. Ed.; Springer Science+Business Media LLC: New York, **2008**, pp. 238-254.

[5] Schenk, D.; Barbour, R.; Dunn, W.; Gordon, G.; Grajeda, H;Guido, T.; Hu, K.; Huang, J.; Johnson-Wood, K.; Khan, K.; Kholodenko, D.; Lee, M.; Liao, Z.; Lieberburg, I.; Motter, R.; Mutter, L.; Soriano, F.; Shopp, G.; Vasquez, N.; Vandevert, C.; Walker, S.; Wogulis, M.; Yednock, T.; Games, D.; Seubert, P. Immunization with Amyloid-PeptideAttenuates Alzheimer-Disease-Like Pathology in PDAPP Mouse. *Nature*, **1999**, *400*, 173-177.

[6] Bard, F.; Cannon, C.; Barbour, R.; Burke, R. L.; Games, D.; Grajeda, H.; Guido, T.; Hu, K.; Huang, J.; Johnson-Wood, K.; Khan, K.; Kholodenko, D.; Lee, M.; Lieberburg, I.; Motter, R.; Nguyen, M.; Soriano, F.; Vasquez, N.; Weiss, K.; Welch, B.; Seubert, P.; Schenk, D.; Yednock, T. Peripherally Administered Antibodies Against Amyloid Beta-peptide Enter the Central Nervous System and Reduce Pathology in a Mouse Model of Alzheimer's Disease. *Nat. Med.*, **2000**, *6*, 916-919.

[7] Kirsten, C. N.; Schrader, T. H. Intermolecular β-Sheet Stabilization with Aminopyrazoles. *J. Am. Chem. Soc.*,**1997**, *119*, 12061-12068.

[8] Rzepecki, P.; Nagel-Steger, L.; Feuerstein, S.;Linne, U.; Molt, O.; Zadmard, R.; Aschermann, K.; Wehner, M.; Schrader, T.; Riesner, D.Prevention of Alzheimer's Disease-associated Aβ Aggregation by Rationally Designed Nonpeptidicβ-Sheet Ligands. *J. Biol. Chem.*, **2004**, *279*, 47497-47505.

[9] Rzepecki, P.; Schrader, T. β-Sheet Ligands in Action: KLVFF Recognition by Aminopyrazole Hybrid Receptors in Water. *J. Am. Chem. Soc.*, **2005**, *127*, 3016-3025.

[10] Hochdörffer, K.;März-Berberich, J.; Nagel-Steger, L.;Epple, M.; Meyer-Zaika, W.;Horn, A.H.C.; Sticht, H.; Sinha, S.; Bitan, G.; Schrader, T. Rational design of beta-sheet ligands against $A\beta_{42}$-induced toxicity. *J. Am. Chem. Soc.*, **2011**, *133*, 4348-4358.

[11] Kroth, H.; Ansaloni, A.; Varisco, Y.; Jan, A.; Sreenivasachary, N.; Rezaei-Ghaleh, N.; Giriens, V.; Lohmann, S.; López-Deber, M.P.; Adolfsson, O.; Pihlgren, M.; Paganetti, P.; Froestl, W.; Nagel-Steger, L.; Willbold, D.; Schrader, T.; Zweckstetter, M.;Pfeifer, A.;Lashuel, H.A.;Muhs, A. Discovery and Structure Activity Relationship of Small Molecule Inhibitors of Toxic β-Amyloid-42 Fibril Formation. *J. Biol. Chem.*, **2012**, *287*, 34786-34800.

[12] Tjernberg, L.O.; Näslund, J.; Lindqvist, F.; Johansson, J.; Karlstrom, A.R.;Thyberg, J.; Terenius, L.; Nordstedt, C.Arrest of β-amyloid Fibril Formation by a Pentapeptide Ligand. *J. Biol. Chem.*,**1996**, *271*, 8545-8548.

[13] Ghanta, J.; Shen, C.L.; Kiessling, L.L.; Murphy, R.M. A Strategy for Designing Inhibitors of Beta-amyloid Toxicity. *J. Biol. Chem.*, **1996**, *271*, 29525-29528.

[14] Pallitto, M.M.;Ghanta, J.;Heinzelman, P.;Kiessling, L.L.; Murphy, R.M. Recognition Sequence Design for Peptidyl Modulators of Beta-amyloid Aggregation and Toxicity. *Biochemistry*, **1999**, *38*, 3570-3578.

[15] Findeis, M.A.; Musso, G.M.; Arico-Muendel, C.C.; Benjamin, H.W.; Hundal, A.M.;Lee, J.J.; Chin, J.; Kelley, M.; Wakefield, J.; Hayward, N.J.; Molineaux, S.M. Modified Peptide Inhibitors of Amyloid Beta-peptide Polymerization. *Biochemistry*, **1999**, *38*, 6791-6800.

[16] Findeis, M.A.; Lee, J.J.; Kelly, M.; Wakefield, J.D.; Zhang, M.H.;Chin, J.; Kubasek, W.; Molineaux, S.M. Characterization of Choly-Leu-Val-Phe-Phe-Ala-OH as an Inhibitor of Amyloid Beta-peptide Polymerization. *Amyloid*, **2001**, *8*, 231-241.

[17] Hughes, E.; Burke, R.M.; Doig, A.J. A General Strategy to Prevent Amyloid Formation. *J. Biol. Chem.*, **2000**, *275*, 25109-25115.

[18] Gordon, D.J.; Sciarretta, K.L.; Meredith, S.C. Inhibition of Beta-amyloid(40) Fibrillogenesis and Disassembly of Beta-amyloid(40) Fibrils by Short Beta-amyloid Congeners Containing N-Methyl Amino Acids at Alternate Residues. *Biochemistry*, **2001**, *40*, 8237-8245.

[19] van Groen, T.; Wiesehan, K.; Funke, S.A.; Kadish, I.; Nagel-Steger, L.; Willbold, D. Reduction of Alzheimer's Disease Amyloid Plaque Load in Transgenic Mice by D3, a D-Enantiomeric Peptide Identified by Mirror Image Phage Display. *ChemMedChem*, **2008**, *3*, 1848-1852.

[20] Wiesehan, K.; Buder, K.; Linke, R.P.; Patt, S.; Stoldt, M.;Unger, E.; Schmitt, B.; Bucci, E.; Willbold, D.Selection of D-amino Acid Peptides that Bind to Alzheimer's Disease Amyloid Peptide Abeta1-42 by Mirror Image Phage Display. *ChemBioChem*, **2003**, *4*, 748-753.

[21] Funke, S.A.; van Groen, T.; Kadish, I.; Bartnik, D.; Nagel-Steger, L.; Brener, O.; Sehl, T.; Batra-Safferling, R.; Moriscot, C.; Schoehn, G.; Horn, A.H.C.; Müller-SchiffmannA.; Korth, C.; Sticht, H.; Willbold, D.Oral Treatment with the D-Enantiomeric Peptide D3 Improves the Pathology and Behavior of Alzheimer's Disease Transgenic Mice. *ACS Chem. Neurosci.*, **2010**, *1*, 639-648.

[22] Schumacher, T.N.M.; Mayr, L.M.; Minor, D.L.; Jr., Milhollen, M.A.; Burgess, M.W.; Kim, P.S. Identification of D-Peptide Ligands through Mirror Image Phage Display. *Science*, **1996**, *271*, 1854-1857.

[23] Olubiyi, O.O.; Strodel, B. Structures of the Amyloid Beta-Peptides Abeta1-40 and Abeta1-42 as Influenced by pH and a D-Peptide. *J. Phys. Chem. B*, **2012**, *116*, 3280-3291.

[24] Wales, J. D.; Doye, J. P. K. Global Optimization by Basin-Hopping and the Lowest Energy Structures of Lennard-Jones Clusters Containing up to 110 Atoms. *J. Phys. Chem. A*, **1997**, *101*, 5111-5116.

[25] Kollman, P.A.; Massova, I.; Reyes, C.; Kuhn, B.; Huo, S.; Chong, http://pubs.acs.org/doi/abs/10.1021/ar000033j - ar000033jAF2 L.; Lee, http://pubs.acs.org/doi/abs/10.1021/ar000033j - ar000033jAF2 M.; Lee, T.; Duan, Y.; Wang, http://pubs.acs.org/doi/abs/10.1021/ar000033j - ar000033jAF2 W.; Donini, O.; Cieplak, P.; Srinivasan, J.; Case, http://pubs.acs.org/doi/abs/10.1021/ar000033j - ar000033j AF3 D.A.; Cheatham III, T.E. Calculating Structures and Free Energies of Complex Molecules: Combining Molecular Mechanics and Continuum Models. *Acc. Chem. Res.*, **2000**, *33*, 889-897.

[26] Oostenbrink, C.; Villa, A.; Mark, A.E.; van Gunsteren, W.F. A Biomolecular Force Field Based on the Free Enthalpy of Hydration and Solvation: The GROMOS Force-Field Parameter Sets 53A5 And 53A6. *J. Comput. Chem.*, **2004**, *25*, 1656-1676.

[27] MacKerell, A.D.; Jr. Bashford, D.; Bellott, M.; Dunbrack, R.L.; Jr. Evanseck, J.D.; Field, M.J.; Fischer, S.; Gao, J.; Guo, H.; Ha, S.; Joseph-McCarthy, D.; Kuchnir, L.; Kuczera, K.; Lau, F.T.K.; Mattos, C.; Michnick, S.; Ngo, T.; Nguyen, D.T.; Prodhom, B.; Reiher III, W.E.; Roux, B.; Schlenkrich, M.; Smith, J.C.; Stote, R.; Straub, J.; Watanabe, M.; Wiórkiewicz-Kuczera, J.; Yin, D.; Karplus, M. All-atom Empirical Potential for Molecular Modeling and Dynamics Study of Protein. *J. Phys. Chem. B.*, **1998**, *102*, 3586-3616.

[28] Hess, B.; Kutzner, C.; van der Spoel, C.; Lindahl, E. GROMACS 4: Algorithms for Highly Efficient, Load-Balanced, and Scalable Molecular Simulation. *J. Chem. Theory Comput.*, **2008**, *4*, 435-447.

[29] Berendsen, H.J.C.; Postman, J.P.M.; van Gunsteren, W.F.; Hermans, J. In: *Intermolecular Forces*; Pullman, B. Ed.; *Reidel*, Dordrecht, **1981**, pp. 331-342

[30] Darden, T.; York, D.; Pedersen, L. Particle Mesh Ewald: An N.log(N) Method for Ewald Sums in Large Systems. *J. Chem. Phys.*, **1993**, *98*, 10089-10092.

[31] Daura, X.; Gademann, K.; Jaun, B.; Seebach, D.; van Gunsteren, W.F.; Mark, A.E. Peptide Folding: When Simulation Meets Experiment. *Angew. Chem. Int. Ed.*, **1999**, *38*, 236-240.

[32] Luhrs, T.; Ritter, C.; Adrian, M.; Riek-Loher, D.; Bohrmann, B.;Döbeli, H.; Schubert, D.; Riek, 3D Structure of Alzheimer's Amyloid-Beta(1-42) Fibrils. *Proc. Natl. Acad. Sci. U.S.A.*, **2005**, *102*, 17342-17347.

[33] GMIN: A Program for Basin-Hopping Global Optimization. http://www-wales.ch.cam.ac.uk/GMIN (Accessed July 20, **2013**).

[34] Li, Z.; Scheraga, H.A. Monte Carlo-minimization Approach to the Multiple-Minima Problem in Protein Folding. *Proc. Natl. Acad. Sci. U.S.A.*, **1987**, *84*, 6611-6615.

[35] Strodel, B.; Wales, D.J. Implicit Solvent Models and the Energy Landscape for Aggregation of the Amyloidogenic KFFE Peptide. *J. Chem. Theory Comput.*, **2008**, *4*, 657-672.

[36] Strodel, B.; Lee, J.W.; Whittleston, C.S., Wales, D.J. TransmembraneStructures for Alzheimer's Abeta(1-42) Oligomers. *J. Am. Chem. Soc.*, **2010**, *132*, 13300-13312.

[37] Mortenson, P.N.; Wales, D.J. Energy Landscapes, Global Optimization and Dynamics of the Polyalanine Ac(ala)8NHMe. *J. Chem. Phys.*, **2001**, *114*, 6443-6454.

[38] Haberthur, U.; Caflisch, A. FACTS: Fast Analytical Continuum Treatment of Solvation. *J. Comput. Chem.*, **2008**, *29*, 701-715.

[39] Brooks, B.R.; Bruccoleri, R.E.; Olafson, B.D.; States, D.J.; Swaminathan, S.; Karplus, M. CHARMM: A Program for Macromolecular Energy Minimization, and Dynamics Calculations. *J. Comput. Chem.*, **1983**, *4*, 187-217.

[40] Åqvist, J.; Mowbray, S.M. Sugar Recognition by a Glucose/Galactose Receptor. *J. Biol. Chem.*, **1995**, *270*, 9978-9981.

[41] Jones-Hertzog, D.K.; Jorgensen, W.L. Binding Affinities for Sulfonamide Inhibitors with Human Thrombin Using Monte Carlo Simulations with a Linear Response Method. *J. Med. Chem.*, **1997**, *40*, 1539-1549

[42] LeVine, H. Thioflavine T interaction with synthetic Alzheimer's disease beta-amyloid peptides: detection of amyloid aggregation in solution. *Protein Sci.*,**1993**, *2*, 404-410.

[43] Rich, R.L.; Myszka, D.G. BIACORE J: a new platform for routine biomolecular interaction analysis. *J. Mol.Recognit.*, **2001**, *14*, 223-228.

[44] Hahnefeld, C.; Drewianka, S.; Herberg, F.W. Determination of kinetic data using surface plasmon resonance biosensors. *Methods Mol. Med.*, **2004**, *94*, 299-320.

[45] Kabsch, W.; Sander, C. Dictionary of Protein Secondary Structure: Pattern Recognition of Hydrogen-bonded and Geometrical Features. *Biopolymers*, **1983**, *22*, 2577-2537.

[46] Humphrey, W.; Dalke, A.; Schulten, K.VMD-Visual Molecular Dynamics. *J. Mol. Graphics*, **1996**, *14*, 33-38.

Received: July 02, 2013 **Revised: November 11, 2013** **Accepted: November 20, 2013**

2.1.7 Insights into infectious sheep prions by solid-state NMR spectroscopy.

Eingereicht bei: Prion

Impact Factor: 2,241

Eigenanteil an der Publikation: 25 %

Durchführung und Auswertung von AFM, Mitverfassen des Manuskripts.

Insights into infectious sheep prions by solid-state NMR spectroscopy

Henrik Müller[a,b], Oleksandr Brener[a,b], Olivier Andreoletti[c], Timo Piechatzek[a,b], Dieter Willbold[a,b], Giuseppe Legname[d], and Henrike Heise[a,b]

[a] Institute of Complex Systems, ICS-6: Structural Biochemistry, Forschungszentrum Jülich (FZJ), 52425 Jülich, Germany

[b] Institut für Physikalische Biologie, Heinrich-Heine-Universität Düsseldorf, 40225 Düsseldorf, Germany

[c] UMR 1225 INRA-ENVT Interactions Hôtes Agents Pathogènes, Ecole Nationale Vétérinaire, 31076 Toulouse, France

[d] Department of Neuroscience, Laboratory of Prion Biology, Scuola Internazionale Superiore di Studi Avanzati (SISSA), 34136 Trieste, Italy

To whom correspondence should be addressed: Henrik Müller & Henrike Heise

Henrik Müller, Chemical Research Laboratory (CRL), University of Oxford, 12 Mansfield Road, Oxford, OX1 3TA, UK, Tel.: +44(0)1865-285159; Fax: +44(0)1865-285002;

Email: henrik.muller@chem.ox.ac.uk

Henrike Heise, Institute of Complex Systems (ICS-6), Research Centre Jülich GmbH (FZJ), 52425 Jülich, Germany, Tel.: +49(0)2461-61-4658; Fax: +49(0)2461-61-8766;

Email: h.heise@fz-juelich.de

ABSTRACT

The still elusive structure of the infectious form of the mammalian prion protein (PrP^{Sc}) is a major pending milestone in understanding mammalian prions. Prion preparations proven to be infectious have never been investigated with a high resolution technique. All available models to date have been based on low-resolution data. Here, we have established protocols for the preparation of infectious samples of full-length recombinant (rec) PrP^{Sc} in NMR-sufficient amounts by seeded fibril growth from brain extract. We link biological and structural data of $recPrP^{Sc}$, derived from bioassays, atomic force microscopy, and solid-state NMR spectroscopy. Our data indicate a semi-mobile N-terminus, some residues with secondary chemical shifts typical for α-helical secondary structure in the middle part between ~115 to ~155, and a distinct β-sheet core C-terminal of residue ~155. These findings enable distinction between current PrP^{Sc}-models. We also provide evidence that samples with different infectivity may not differ in the overall arrangement of secondary structure elements but rather in the flexibility of protein segments outside of the β-core region. This may have relevance for all transmissible amyloid fibrils in general.

Keywords: protein structure, amyloid fibril, infectious diseases, neurodegenerative diseases, atomic force microscopy

INTRODUCTION

Prion diseases are fatal neurodegenerative disorders including Creutzfeldt-Jakob disease (CJD) in humans, bovine spongiform encephalopathy (BSE) in cattle, and scrapie in sheep. These disorders are associated with the conformational conversion of the cellular prion protein (PrP^{C}) into a misfolded isoform (PrP^{Sc}), the pathological and infectious prion agent [1]. Prions are formed via nucleation-dependent polymerisation, in which pre-formed fibrils of PrP^{Sc} act as template for PrP^{C}-conversion. Infectious PrP^{Sc} have also been formed spontaneously solely from recombinant (rec) PrP [2]. Whereas solution-state NMR spectroscopy was used to determine the structure of soluble PrP^{C} [3] and to identify segments involved in oligomerisation [4], the structure of PrP^{Sc} is still elusive. Studies have so far been limited to relatively low resolution techniques[5; 6; 7; 8; 9]. From such studies, a superpleated β-sandwich model was suggested for recPrP-fibrils characterised by a parallel, in-register alignment of β-strands within a core domain comprising residues 160-220 [5]. Alternatively, a left-handed parallel β-helix with the β-sheet core between residues 89-175 has been suggested based on EM studies on 2D-crystals of fibrillar PrP(89-227) [10]. Further, an alternative "spiral" model comprising parallel and anti-parallel β-strands in the region 116-164 in which all three C-terminal α-helices are retained was proposed earlier on, based on MD-simulations [11]. Recent high-resolution solid-state NMR-studies of recPrP(23-144)-fibrils suggested a β-strand-turn-β-strand motif for the ~30 C-terminal amino acid residues, whereas no distinct NMR resonances were observed for the highly dynamic and disordered N-terminus [12]. A lack of β-strands N-terminal of position 145 in full-length recPrP-fibrils as demonstrated by H/D exchange [13], how- ever, indicates that data on truncated PrP-constructs or PrP-fragments cannot be extrapolated to infer the full-length PrP-structure. For full-length recPrP(23-231)-fibrils, solid-state NMR studies on selectively ^{13}CO-labelled samples confirmed an in-register parallel arrangement of β-strands [14].

Due to severely broadened lines in spectra of uniformly ^{13}C,^{15}N-labeled fibrils, however, only residue types could be partially assigned to cross peak clusters. Assignment probabilities predicted by a Monte Carlo/simulated annealing algorithm suggested a fibril core comprising the 173-224 segment but could not rule out involvement of the 95-161 segment [14].

Taken together, there is a need for additional experimental data to discriminate between the different PrP^{Sc}-models and to understand which structural features can render proteins infectious. The lack of high resolution data is not only due to the general challenge posed to structure analysis by insoluble, non-crystalline, and heterogeneous samples, but also to the impossibility to prepare NMR-sufficient amounts of homogeneous brain-purified samples. However, it is known that fibrils grown from seeds, i.e. short fibril fragments produced by sonication of brain-purified fibrils, retain the molecular structures of the seeds [15; 16; 17]. Consequently, seeded fibril growth can be exploited to amplify and label structures present in brain tissue [18; 19]. In a similar manner, different strains of the yeast prion Sup35p were faithfully passed on to recombinantly expressed Sup35p monomers by seeding with yeast cell lysates.[20]

In contrast to all other amyloid fibrils, *in vitro*-generated PrP-fibrils carry the crucial advantage that their physiological relevance to neurodegenerative diseases in mammals can be assessed directly. Only when *in vitro*-generated PrP-fibrils prove to be infectious in animals, they are relevant *in vivo*. Up to now, PrP-fibrils, which were proven to be infectious, have never been investigated with a high-resolution technique. Moreover, data of infectious samples are restricted to PrP^{Sc} from laboratory animals such as mouse and hamster. Species that are important from a veterinary point of view, such as cattle or sheep, have never been investigated.

Here, we demonstrate methodologies for reproducibly preparing infectious samples containing sheep full-length recPrP(25-233)-fibrils formed by spontaneous conversion and by seeding

with PrP^{Sc} purified from scrapie brain in high yield and purity. For the first time, we have investigated the biologically authentic system of full-length PrP^{Sc}-like recPrP-fibrils ($recPrP^{Sc}$) by a multidisciplinary combination of bioassays and biophysical characterisation with high-resolution solid-state NMR spectroscopy. Our data are consistent with a β-sheet core C-terminal of residues ~155 and a partially α-helical middle segment between residues ~115-155. Since NMR spectroscopy of our $recPrP^{Sc}$ samples investigates not only single molecules within the sample but the complete ensemble of all conformations present in oligomeric and fibrillar states, our data allow us to verify structural models for the dominating PrP^{Sc}-conformation. In addition, our data indicate that recPrP-fibrils in differently infectious samples may differ in the flexibility of the partially α-helical middle segment.

RESULTS

Concept of the study. We investigated infectious samples of scrapie prion-like fibrils from ovine (ov) ARQ full-length recombinant (rec) PrP(25-233) for several reasons: (i) Only full-length recPrP (see **Fig. S1**) encompasses the entire brain PrP^{Sc} sequence containing all prion disease-related polymorphism sites. Only fibrils from full-length PrP closely resemble structures formed *in vivo* [13]. (ii) Scrapie is the biochemically most investigated as well as the most widespread prion disease. (iii) The well-defined set of sheep PrP-polymorphisms at positions 136 (A/V), 154 (R/H), and 171 (Q/R/H) governs scrapie susceptibility and allows further study of structure-infectivity relationships. The homozygous combination $A_{136}R_{154}Q_{171}$ is associated with highest scrapie susceptibility and frequency [21]. (iv) RecPrP-fibrils can be generated either under partially denaturing conditions [2] or by protein misfolding cyclic amplification (PMCA) [22]. Although PMCA generates

highly infectious recPrP-samples, if only in some batches, its usefulness for NMR studies is limited because PMCA sonication introduces a high well-to-well variability in PrP^{Sc}-yield, and a gravely polymorphic mixture is the undesirable PMCA outcome [23; 24; 25]. In contrast, uniform protein denaturation by guanidinhydrochloride (GdnHCl) and urea results in homogeneous and infectious recPrP-samples ($recPrP^{Sc}$).

Generation of NMR-sufficient amounts of ovrecPrP-fibrils. Reproducible fibrillation conditions were established in 96-well plates for spontaneous conversion of ovrecPrP(25-233). In a second approach, ovrecPrP(25-233) was seeded with sequence-identical full-length PrP^{Sc} purified from scrapie sheep brain by PTA-precipitation (see **Materials and Methods**). PrP^{Sc}-seeded growth took place days before spontaneous conversion (**Fig. 1a**). Due to this considerable difference in lag phases, PrP^{Sc}-seeded and spontaneous samples could be produced and analysed independently of each other. Furthermore, this confirms that the fibrillation kinetics is dominated by propagation of seeds and not by spontaneous conversion. PTA-precipitation is not specific for PrP^{Sc} though. Therefore, normal sheep brain was subjected to the identical purification protocol and PTA-precipitated material (lacking PrP^{Sc}) was used as seed. A lack of any ThT-fluorescence increase, even after prolonged incubation times, confirmed that recPrP-fibrillation kinetics is dominated by propagation of specific seeds, namely PrP^{Sc} (**Fig. 1a**). To further reduce the risk of generating polymorphic fibril mixtures by pooling 96-well plates, optimal conditions were scaled up to volumes of up to 10 ml (**Fig. 1b**). Differential ultracentrifugation of samples from the fibrillation end point followed by densitometric quantification of Western blots indicated that about 95 % of ovrecPrP was always converted to a fibrillar form. In summary, NMR-sufficient fibrillar yields of 10 mg of both spontaneously generated and PrP^{Sc}-seeded ovrecPrP-fibrils could be prepared in 10 ml volumes each.

Infectivity. Aliquots of $^{13}C,^{15}N$-ARQ-ovrecPrP(25-233)-samples were inoculated in transgenic mice, homozygously overexpressing ovine VRQ- or ARQ PrP(25-233), respectively. Non-fibrillated ovrecPrP(25-233) failed to induce noticeable prion disease symptoms in any mouse even 630 days after inoculation (**Tab. 1**), disproving a prion disease-inducing effect of the stress during sample injection. In contrast, 3 out of 12 mice inoculated with spontaneously fibrillated ovrecPrP (in the absence of seeding with infectious prions) succumbed to a prion disease. Because less than 100 % of mice developed a prion disease, the infectious titre can be considered to be lower than 10^2 ID_{50}/ml [26]. The range of incubation periods in diseased mice also indicates the presence of low infectivity titres[27; 28; 29]. After inoculation of the brain homogenates of these diseased mice into the same mouse line, 100 % of mice developed a prion disease with incubation periods characteristic for high prion infectivity. The incubation periods in transgenic ARQ mice even indicate prion infectivity as high as in brain-derived PrP^{Sc} (see below). Small standard deviations in incubation periods also indicate a highly efficient transmission. Taken together, this confirms the infectious character of our non-seeded samples. It is also noteworthy that the incubation periods observed in these second passages differ from incubation periods of PrP^{Sc}-seeds and PrP^{Sc}-seeded ovrecPrP-fibrils (see below). This makes a contamination of spontaneously generated ovrecPrP-fibrils with PrP^{Sc}-seeds highly unlikely.

In order to confirm the presence of PrP^{Sc} in mice, brain extracts were analysed for partial proteinase K (PK)-resistance which is the biochemical marker in routine prion tests [30]. A partial PK-resistance is evident from a molecular weight shift of the di-, mono-, and glycosylated PrP-forms caused by the digestion of about 70 N-terminal residues. All mice inoculated with non-fibrillated ovrecPrP(25-233) failed to show any PK-resistant PrP^{Sc} (**Fig. 2a**). Although samples of spontaneously fibrillated ovrecPrP(25-233) used for inoculation did not show any PK-resistance

either (**Fig. 2b**), the three partially PK-resistant PrP^{Sc}-forms were present in brain extracts of all symptomatical mice (**Fig. 2a**), confirming prion diseases. In summary, these data confirm that our samples after spontaneous conversion of ovrecPrP(25-233) are characterised by at least a small fraction of infectious PrP^{Sc}-like conformations.

This is different for PrP^{Sc}-seeded conversion of ovrecPrP(25-233). In contrast to spontaneously generated fibrils, PrP^{Sc}-seeded samples induced prion diseases in 100 % of the inoculated mice in the first passage. Since bioassays are the ultimate functional test, our PrP^{Sc}-seeded samples can be regarded as *in vivo*–like as possible to date (**Tab. 1**). It is well known that animals inoculated with *in vitro*-propagated PrP^{Sc} exhibit an altered relationship between incubation period and infectivity titre [23]. A comparison with the incubation periods of animals inoculated with brain-derived PrP^{Sc} is thus not valid. It cannot be decided yet whether shorter incubation periods indicate higher infectivity. It was also beyond the scope of this manuscript to determine whether infectivity is associated with ovrecPrP-fibrils or pre-fibrillar aggregates. Solid-state NMR spectroscopy, however, allowed us to investigate the complete ensemble of conformations present after ovrecPrP-conversion. Measured line widths indicate structurally very similar conformations (see below).

Secondary and ultrastructural properties. A circular dichroism (CD) spectrum of the fibrillation starting point, i.e. monomeric ovrecPrP(25-233), is indicative of low β-sheet content as known for both PrP^{C} and natively refolded recPrP [30]. Satisfactory CD spectra of recPrP-fibrils were only obtained after gentle sonication in presence of small concentrations of SDS. This mild treatment does not influence the secondary structure of amyloids fibrils (see **Materials and Methods** for details) but allow for CD-analysis. OvrecPrP-conformations after spontaneous conversion or PrP^{Sc}-seeding combine a β-sheet-structure with additional α-helical/random coil segments and are thus completely different from natively folded monomeric ovrecPrP(25-233) (**Fig. 3**). Although

CD spectra after spontaneous conversion or PrP^{Sc}-seeding are characterised by identical minima, zero crossings, and maxima, the measured mean residue molar ellipticities of both sample types differed considerably. The higher mean residue molar ellipticity intensities (which are values normalised by the respective protein concentration) after PrP^{Sc}-seeding indicate an increased proportion of ovrecPrP-fibrils amenable to CD analysis.

AFM analysis demonstrated that spontaneously generated and PrP^{Sc}-seeded ovrecPrP-fibrils substantially differ in morphology, but each fibril type is morphologically homogeneous. After spontaneous fibrillation (**Fig. 4a**), we observed short amyloid fibrils similar to so-called prion rods. Prion rods are purified from infectious brain material using detergents and limited proteolytic digestion [31]. Our short fibrils are in agreement with literature[8; 32] in terms of a straight appearance, lengths of up to 400 nm, heights between 5 and 20 nm, and a strong tendency to associate into higher order aggregates. OvrecPrP-fibrils longer than 400 nm or twisted fibrils were never observed, even when pre-formed fibrils were used for seeded fibrillation. Pre-fibrillar aggregates were never observed either. The histogram in **Figure 4c** showing the fibril widths distribution illustrates that the fibril species have an average width of 30±11 nm, which is identical to literature values [8]. In contrast, ovine PrP^{Sc}-fibrils (**Fig. 4e**) are characterised by lengths of several µm and a far wider width distribution resulting in an average width of 56±31 nm. The appearance of PrP^{Sc}-fibrils in AFM images, however, was obscured by co-purified brain matter in the form of extraneous non-fibrillar material. Also the natural presence of GPI-anchor and un-, mono- and diglycosylated PrP^{Sc} forms obscured the underlying proteinaceous parts of PrP^{Sc}-fibrils causing high width standard deviations. When ovrecPrP-fibrils were grown in presence of 0.5 % (vol/vol) PrP^{Sc}-seeds, the resulting amyloid fibrils combined the PrP^{Sc}-like curvature and the length of several µm with an average fibrillar width of 25±13 nm (**Fig. 4b** and **d**). In contrast to spontaneous preparations,

short fibrils were never observed. As is evident from **Figure 4c** and **d**, spontaneously generated and PrP^{Sc}-seeded ovrecPrP-fibrils have indiscernible average fibrillar widths. The narrowest fibrillar structures were observed to be 6 to 8 nm in width, which is in agreement with diameters for single PrP-filaments as determined by negative stain EM (4.8 to 5.7 nm for PrP27-30, 7.6 to 7.9 nm for recPrP(90-231)-fibrils) [33]. Taken together, spontaneously generated ovrecPrP-fibrils differ morphologically from brain-purified PrP^{Sc}. No ultrastructural difference between PrP^{Sc} and PrP^{Sc}-seeded fibrils was observed.

Absence of strongly mobile segments. NMR spectroscopy is sensitive to molecular motions on the µs to ms time scale. It is well-known that solid-state NMR spectra, which employ dipolar couplings for CP-excitation and magnetisation transfer, often display only peaks from a minor fraction of all residues in amyloid fibrils. Only residues in rigid segments, i.e. in the rigid amyloid core, are characterised by strong dipolar couplings resulting in observable solid-state NMR signals. Highly flexible protein segments on the other hand, undergoing motions in the sub-microsecond range, may be discriminated easily from the rigid core by INEPT-based excitation[20; 34; 35; 36; 37] In contrast to rigid and highly flexible residues though, signals from semi-flexible regions, such as the fuzzy coat of amyloid fibrils, may be completely missing due to intermediate range molecular motion resulting in severe line broadening and/or disappearance of signals.[12; 20; 34; 38] In order to compare the amounts of rigid and highly mobile protein segments, we recorded 1D-^{13}C-CP- and 1D-^{13}C-INEPT-NMR spectra. CP-spectra, which selectively detect rigid protein segments, revealed identically strong and appropriately resolved resonances in samples after spontaneous conversion or PrP^{Sc}-seeding of ovrecPrP(25-233). An absence of any protein signal in all INEPT-spectra, even after rehydration with 10 µl of H_2O and measurement at 20 °C, indicated a lack of sub-microsecond dynamics in any protein segment. When CP-excitation was combined with a

transverse spin echo delay, leading to dipolar dephasing of magnetisation in rigid protein segments, all signals disappeared already after delays as short as 300 µs. Thus, all segments in ovrecPrP-conformers after spontaneous conversion or PrP^{Sc}-seeding are rigid on a sub-microsecond time scale. In 2D-spectra obtained by direct ^{13}C-excitation followed by 100 ms PDSD-mixing, no additional cross peaks were visible, thus confirming that all NMR-visible residues had been observed in the spectra obtained with CP-excitation.

Homogeneity of samples. In order to identify spin systems visible in solid-state NMR spectra, we recorded sets of 2D-(^{13}C-^{13}C)- and (^{15}N-^{13}C)-correlation experiments (see **Materials and Methods**) at 0 °C. Essentially identical spectra were obtained for two independently prepared samples indicating reproducibility of the experiments. In **Figure 5**, 2D-(^{13}C-^{13}C)- and (^{15}N-^{13}C)-spectra are depicted exemplarily. Solid-state NMR spectroscopy investigates the complete ensemble of conformations present in pre-fibrillar and fibrillar states. ^{13}C-line widths of isolated cross peaks of about 120 Hz thus indicate that all conformations present in our samples, whether they be infectious or non-infectious, need to be structurally very similar. A conformational ensemble comprising a distinctive number or a continuous distribution of slightly varying conformations cannot be completely excluded though. Since we could assign nearly every cross peak residue type-specifically (see below), we can rule out the presence of a minor fraction giving rise to resonance sets with intensities > 5 % of those of the main peak set.

Despite careful control of sophisticated fibrillation conditions in one tube per sample and ^{13}C and ^{15}N line widths for resolved peaks of about 120 Hz and 450 Hz, respectively, average line widths could not be reduced further. Neither did hydration by addition of 10 µl H_2O nor measurements at higher temperatures up to 20 °C increase the spectral resolution. Also, two times seeding

with seeds prepared from spontaneously generated ovrecPrP-fibrils did not render the conformational ensemble more homogeneous. Seeding with PrP^{Sc}, however, did result in samples whose 2D-correlation spectra exhibit both reduced intensities and absence of some cross peaks (see below).

Assignment process. In light of the spectral overlap, particularly in highly populated chemical shift regions (e.g. at 55 ppm x 35 ppm or 30 ppm x 25 ppm in **Fig. 5a**), the challenge of obtaining residue type-specific assignments could only be met by comparing peak maxima in a given spectrum with the complete set of all other homonuclear and heteronuclear 2D-spectra. A cross peak was only regarded to be genuine and residue type-specific, when (i) it was visible using different apodisation functions, (ii) a clear peak was visible in the corresponding 1D-traces, and most importantly (iii) cross peaks at corresponding chemical shifts were observed in all other correlation spectra. **Tables S1** and **S2** summarise average chemical shifts. In light of the cross peak overlap, the numbers of identified residues (59 out of 209 after PrP^{Sc}-seeded conversion and 73 out of 209 after spontaneous conversion, respectively) have to be regarded as a lower estimate of visible residues. We cannot exclude that more residues contribute to the observed signals, particularly in highly populated chemical shift regions. To provide a measure for the accuracy of our chemical shifts, standard deviations and numbers of assignments are given in addition. We could differentiate between distinct spin systems of nearly every amino acid type. In **Figures S2, S3, and S4**, the identification of alanine, leucine, and glycine spin systems is depicted exemplarily.

Sequence position-specific assignments can in principle be obtained by linking NCACX-cross peaks of individual residues via backbone ^{15}N chemical shifts with NCOCX-cross peaks of the preceding residue in the amino acid sequence. Our heteronuclear spectra (see e.g. **Figure 5b**),

however, suffer from severe spectral overlap in the ^{15}N-dimension. Since several residue-type assignments are conceivable for nearly every cross peak in (^{15}N-^{13}C)-correlation spectra (except alanine and threonine N-Cβ- and glycine N-Cα-cross peaks), no unambiguous sequential assignments could be obtained. All possibilities for residue type–specific ^{15}N-assignments are summarised in **Table S3.** To improve resolution and thereby allow for sequential assignments, heteronuclear 3D-spectra of selectively labelled samples are necessary. This analysis is currently underway in our laboratory but is beyond the scope of this manuscript.

Secondary structure distribution, comparison of fibril types, and flexibility. In contrast to earlier studies of recPrP-samples, all of which were not tested for infectivity, our solid-state NMR-data of infectious samples containing recPrP^{Sc}-fibrils allow us to draw the following conclusions:

(i) The secondary chemical shifts of ovrecPrP(25-233) after spontaneous conversion or PrP^{Sc}-seeding are similar though not identical (**Fig. 6**), indicating similar underlying conformational motifs. An overlay of solid-state NMR spectra of both preparations, however, visualises slightly different cross peak patterns and intensities suggesting the presence of deviating structural features. Since site-specific information is missing, however, it cannot be decided whether slightly different cross peak positions indicate local structural differences only.

(ii) The number of identified residues in solid-state NMR spectra is apparently smaller than the number of amino acid residues in the ovrecPrP(25-233)-sequence. However, this is owed to severe spectral overlap, particularly in highly populated chemical shift regions. The numbers given in **Tables S1** and **S2** are a lower limit of visible residues because it is highly probable that more residues contribute to overlapping cross peaks. In addition, the N-terminus before sequence position ~ 100 is consistently known for its unstructured and flexible character [30]. Since it is highly

likely that such an N-terminus does not form part of the rigid fibril core, it may not contribute to solid-state NMR spectra[12].

The complete lack of INEPT-signals (see above), however, also excludes mobility on a sub-microsecond scale. This apparent lack of NMR signals may either be due to exchange broadening by molecular motions on the NMR-time scale or due to extensive inhomogeneous line broadening beyond detectability as a result of a high degree of disorder in completely rigid segments. A recent study of two yeast prion strains demonstrated that in one strain a larger rigid core is accompanied by a larger fraction of highly dynamic residues. The other strain combined a reduced rigid core with a smaller number of highly flexible residues. Consequently, a reduced number of signals in CP-based spectra is not necessarily linked to an increased number of residues of high flexibility.[20]

The segment C-terminal of sequence position 100 contains only 10 out of 43 glycine residues. We observed, however, up to two times more glycine cross peaks (see **Fig. S4**). A number of 10 glycine residues represent only 7.5 % of all 133 residues C-terminal of sequence position 100. The integrals of the glycine-specific N-Cα-region in 2D-(^{15}N-^{13}Cα)-spectra (without any following mixing) and the glycine-specific CO-Cα-region in 2D-(^{13}C-^{13}C)-correlation spectra, however, constitute on average 14.6 ± 1.5 % of the entire Cα-region in the respective spectrum. This indicates that either a small fraction of the N-terminus does contribute to solid-state NMR-spectra or that glycine-containing regions C-terminal of sequence position 100 are disordered to some extent.

(iii) The secondary chemical shifts (**Fig. 6**) are in agreement with our CD measurements confirming a dominance of residues in a β-sheet conformation. PrP^{Sc} comprises 30 % α-helices and 43 % β-sheets, whereas PrP27-30, obtained by proteolytic removal of the flexible N-terminal

PrP^{Sc}-segment, is characterised by 21 % α-helical and 54 % β-sheet contents [39]. When we differentiate our secondary chemical shifts into the categories > 1 ppm α-helical, < 1 ppm/ > -1 ppm random coil, and < -1 ppm β-sheet content, then α-helical/β-sheet contents of 28 %/60 % (PrP^{Sc}-seeded conversion) and 24 %/53 % (spontaneous conversion) matches best with the values for PrP27-30. This supports the view that mainly signals from a rigid C-terminal fibril segment contribute to our solid-state NMR spectra.

(iv) A sequentially assigned minimum of three consecutive β-sheet residues or four consecutive α-helical residues are required to define a β-strand or an α-helix, respectively, at a distinct sequence position [40]. Although we lack site-specific assignments, we found some hints for the position of secondary structure elements. The three ovrecPrP(25-233)-leucine residues are at positions 128, 133, and 141, i.e. clustered in the middle region. All of them are characterised by α-helical chemical shift signatures. Seven out of nine alanine residues in ovrecPrP(25-233) are clustered at positions 116, 118, 119, 120, 121, 123, and 136. At least four alanine residues identified in our spectra have chemical shifts indicative of α-helical secondary structure. Eight out of eleven arginine residues in ovrecPrP(25-233) are N-terminal of position 168. All signals assigned to arginine residues have chemical shifts indicative of α-helical secondary structure. These observations suggest that this middle region of fibrillated ovrecPrP(25-233) contains either several closely adjacent β-turns and/or an α-helical secondary structure. All resonances with an α-helical chemical shift signature can be assigned to this region, either unambiguously (Leu128, Leu133, Leu141) or tentatively (Ala116, Ala118, Ala119, Ala120, Ala121, Ala123, Ala136, Asp147, Asp150, Arg139, Arg151, Arg154, His114, His143, Gln101, Ser135, Ser138, and Val124, Val125).

(v) A semi-mobile N-terminus and partially α-helical segments between residues ~115 and ~155 imply that the majority of β-strand residues are confined to the segment C-terminal of residue ~155.

(vi) Higher mean residue molar ellipticity intensities after PrP^{Sc}-seeding indicated an increased proportion of ovrecPrP-conformers amenable to CD analysis which implies higher flexibility of at least some segments of PrP^{Sc}-seeded conformations (**Fig. 3**). In 2D-(^{13}C-^{13}C)-solid-state NMR spectra using homonuclear transfer based on dipolar recoupling, cross peak intensities of specific amino acid residues, e.g. of proline and leucine residues, are weakened when samples were generated by PrP^{Sc}-seeding. To account for possibly deviating hydration states, samples were rehydrated by addition of 10 µl of H_2O each. No change in the respective intensities or line widths of cross peaks was observed. A comparison of identically recorded and processed 2D-(^{13}C-^{13}C)-DREAM spectra of identically prepared (except for the presence or absence of PrP^{Sc}-seeds during fibrillation) 10-mg samples of both fibril types confirmed an increased flexibility after PrP^{Sc}-seeding. An overlay of the aliphatic regions of these spectra is depicted in **Figure 7a**, whereas **Figures 7c - e** display some regions of interest in higher magnification. DREAM spectra display cross peaks only for correlations between directly bound ^{13}C atoms and thus allowed for quantitative intensity analysis. Since only some cross peaks of lysine, glutamine, glutamate, aspartate, histidine, isoleucine, asparagine, serine, and tyrosine residues differed in intensity, a quantitative conclusion could hardly be drawn for them without heteronuclear 3D-spectra reducing the number of overlapping cross peaks. For the spectrally separated proline, valine, arginine, leucine, alanine, and threonine residues, however, the volumes of the complete Cα-Cβ-/Cβ-Cα-cross peaks with α-helical or β-sheet chemical shift signatures, respectively, could be determined (**Fig. 7b**). For threonine residues (not present between positions 115-155; nine of eleven threonine residues are

C-terminal of position 185), no difference in the normalised cross peak intensities was observed comparing spontaneously generated and PrP^{Sc}-seeded samples. Cross peak intensities of β-sheet alanine and β-sheet valine residues also did not differ within an error margin of 10 %. In contrast, all proline cross peaks almost completely vanished in spectra of PrP^{Sc}-seeded samples. The most C-terminal of 15 ovrecPrP(25-233) proline residues is located at sequence position 168. The substantially reduced proline intensities therefore suggest that PrP^{Sc}-seeding results in enhanced flexibility of the N-terminal fibril segment. The cross peaks of α-helical alanine, α-helical leucine, α-helical arginine, and α-helical valine residues are also considerably weakened after PrP^{Sc}-seeding (**Fig. 7**). Seven of nine alanine residues are clustered between positions 116 and 136. All three leucine residues are at positions 128, 133, and 141. Eight of eleven arginine residues are located N-terminal of position 168. Valine residues with α-helical chemical shift signatures are believed to be located between residues 115 to 155 (see above). Taken together, only cross peak intensities of residues N-terminal of Pro168 seem to be affected indicating again that PrP^{Sc}-seeding induces a more flexible fibril region N-terminal of Pro168.

DISCUSSION

Several structural models of amyloid fibrils have been published[41; 42]. Recent data indicate that aberrantly folded proteins in other neurodegenerative diseases share self-propagating infectious properties similar to those in spongiform encephalopathies caused by misfolded PrP [43; 44]. This emphasises the importance of investigating physiologically relevant conformations. Proving that *in vitro*-fibrillated structures are physiologically relevant is still a challenge though. Since no

functional test is available, only infectious samples or brain-seeded fibrils have so far been regarded to reflect *in vivo*-structures[18]. Earlier high-resolution studies have never investigated samples that have been proven to be infectious. Here, for the first time we have linked structural and biological data by applying a high-resolution technique to infectious and thus physiologically authentic samples of recPrP^{Sc} from sheep, an important species from the veterinary point of view. Our use of solid-state NMR spectroscopy allows for direct probing of subunit structure and dynamics of the complete ensemble of conformations present after conversion of ovrecPrP(25-233).

As both samples prepared in absence or presence of brain-purified PrP^{Sc}-seeds display similar, although not identical, cross peak positions in solid-state NMR spectra, they are likely to have some structural features in common. This is reflected by the fact that both samples are infectious. However, they differ in crucial aspects. Only after seeding of ovrecPrP(25-233) with brain-purified PrP^{Sc} we observed a PrP^{Sc}-like morphological appearance of recPrP^{Sc}-fibrils (**Fig. 4**) and PrP^{Sc}-like incubation periods in transgenic mice (**Tab. 1**) suggesting an amplification of the prion conformation. In contrast, for spontaneously generated ovrecPrP-fibrils an *in vivo* - maturation during a second passage into transgenic mice was necessary to derive highly infectious recPrP^{Sc}. Considerably shortened lag phases during seeded ThT assays and the specificity of our seeded ThT assay for the presence of fibrillar structures such as in PrP^{Sc} (**Fig. 1**) are also in agreement with a specific propagation of PrP^{Sc}. The increased flexibility in PrP^{Sc}-seeded samples as suggested by solid-state NMR spectra (**Fig. 7**) is in agreement with an increased proportion of recPrP^{Sc}-conformers amenable to CD analysis (**Fig. 3**) as well as the finding that high prion infectivity requires an increased degree of disorder [33; 45]. Taken together, the prion conformation is only amplified by means of PrP^{Sc}-seeding resulting in physiologically authentic recPrP^{Sc}, which is as *in vivo*-like as possible to date.

Natively folded ovine PrP^C comprises a flexible unstructured N-terminus, three α-helices Asn146-Tyr158, Asn174-Thr196, and Glu203-Tyr228, and a small β-sheet formed by Gly129-Gly134 and Gln163-Arg167 [46]. According to our solid-state NMR-data, PrP^{Sc}-seeded con- version results in (i) a semi-mobile N-terminus, (ii) a partially α-helical/β-turn middle segment approximately between residues ~115 to ~155, and (iii) a β-sheet-core C-terminal of residue ~155. No hints were found for an α-helical region in the C-terminus.

(i) An unstructured semi-mobile N-terminus agrees with biochemical literature [30] and earlier solid-state NMR studies [12] of non-infectious recPrP-fibrils [47] concluding that the N-terminus up to position 131 is not as mobile as a fully disordered polypeptide in solution.

(ii) An α-helical/β-turn middle segment would be divided by the α-helix-breaking Pro140. An α-helical segment C-terminal of Pro140 may correspond to the remainder of the PrP^C α-helix Asn146-Tyr158. An α-helical segment N-terminal of Pro140, however, would imply a rearrange- ment of the β-strand Gly129-Gly134 to an α-helix upon fibrillation. Since such a conversion has never been observed, it is doubtful whether all α-helical chemical shift signatures N-terminal of Pro140 do indicate an α-helical segment. They can also indicate β-turn motifs [48] which might ad- join to a more or less preserved PrP^C β-strand Gly129-Gly134. Additional β-turn motifs within the C-terminal β-sheet core cannot be excluded.

(iii) A β-sheet-core C-terminal of ~155 is consistent with the finding that Tyr152-Arg154 remains flexible during fibrillation, whereas Tyr165-Arg167 is part of the rigid core [49]. Although we cannot determine the precise location of β-strands, a β-sheet-core C-terminal of residue ~155 implies a refolding of the two C-terminal PrP^C α-helices. This location of β-strands is in agreement with that proposed for the β-sandwich model[5] but not with that suggested for the spiral model [11]

or the published β-helix model [10]. An alternative β-helix model [50] comprising the C-terminal segment would be consistent with our solid-state NMR-data though. **Figure 8** summarises our data and the findings of earlier studies.

In addition to morphological influences, PrP^{Sc}-seeding increases flexibility of some protein regions. Although we cannot completely exclude an increased flexibility of C-terminal β-strands, our data suggest that PrP^{Sc}-seeding induces an enhanced flexibility of the α-helical/β-turn-rich segments between residues ~115 to ~155 (**Fig. 7**). This is in agreement with the observations that high prion infectivity requires an unusually high degree of disorder [33; 45] and that PrP^{Sc}-seeded recPrP(90-231)-fibrils consist of subpopulations with highly accessible disordered as well as protected ordered segments in the regions 117-133 and 145-168 [51]. The presence of the segments N-terminal of position 165 is mandatory for fibrillation[49], though it is not necessarily incorporated in the β-sheet core [5] but rather at the fibril surface. We hypothesise that the flexibility of this segment might act as a sort of "gatekeeper" subtly influencing the β-interface between monomeric units within fibrils and in turn stability and length of recPrP-fibrils (see **Fig. 4**) as well as infectivity characteristics (see **Tab. 1**).

In summary, we have established protocols for the preparation of infectious full-length ovine $recPrP^{Sc}$ in solid-state NMR-sufficient amounts uniformly labelled with ^{13}C and ^{15}N. Our biophysical and solid-state NMR characterisation of several samples is consistent with $recPrP^{Sc}$ in a single conformation. This demonstrates promise for full assignment in the near future. Such an analysis will allow structural information to be obtained at atomic resolution of the complete conformational ensemble present in mammalian prions. Our previous data indicate (1) a unique structure characteristic in line with a distinct C-terminal β-sheet core and a partially α-helical middle part as the common motif of prions; and (2) deviating flexibility of non-β-core segments in different

PrP-fibril types. Key questions remain unanswered: Are fibrils or pre-fibrillar aggregates the source of infectivity? In which detailed segment do lowly infectious conformations undergo adaption *in vivo* to become highly infectious? Do unique β-interfaces or characteristics of non-β-sheet but aggregation-promoting segments account for the infectious exceptionalism of prions?

MATERIALS AND METHODS

Biological safety. Prion material was handled in biosafety hoods in a BSL-3**-laboratory. For NMR-experiments, samples were transferred into deformable, unbreakable, and hermetically sealable polyformaldehyde rotor inserts that were custom-built and are NMR-silent in the chemical shift range typical for proteins (^{13}C signals are at 89.1 ppm and 1.0 ppm).

Fibrillation. PrP expression in *Escherichia coli* and purification was performed as described [52] and adapted to full-length ovine ARQ recPrP (25–233). Typical yields of uniformly ^{13}C,^{15}N isotope labelled ovrecPrP(25-233) of 10-15 mg per litre M9 minimal medium were achieved. *In vitro*-conversion was carried out in presence of 1 M GdnHCl, 2.4 M urea, and 167 mM NaCl in 20 mM sodium acetate pH 5.0 with continuous shaking at 600 r.p.m. and 37 °C with 100 ng μl^{-1} ovrecPrP(25-233) (150 µl in 96-well plates) or 1000 ng μl^{-1} ovrecPrP(25-233) (1 ml in 1.5 ml microcentrifuge tubes or 10 ml in 15 ml conical tubes), respectively. For seeded fibrillation, PrP^{Sc}-seeds were prepared by precipitation of 700 µl of 10 % (vol/vol) scrapie-infected homozygous ARQ sheep brain homogenate with sodium phosphotungstic acid (NaPTA) adapted to ovine PrP^{Sc} [53] resulting in sequence-identical 30 µg-ARQ PrP^{Sc}-seeds and sonicated for 10 sec with a Misonix sonicator 3000 at 200 W and <25 °C. As control, brain homogenate of non-infected ARQ sheep was treated identically. At the conversion endpoint, the fibrillation buffer including residual non-

fibrillar material was removed by differential ultracentrifugation in a TL-100 ultracentrifuge (Beckman Instruments) with a TLA-45 rotor for 1 h at 100,000 × g and 4 °C. Each pellet was washed with sterile bidest. water, centrifuged for 1 h at 100,000 x g and 4 °C, washed and centrifuged again. NMR samples were dried until any solution was evaporated and immediately packed in 3.2-mm rotors and stored at 4 °C.

Thioflavin T–assay. Fibrillation kinetics were monitored by thioflavin T (ThT)-fluorescence assays in 96-well, black-bottom Nunc plates in a microplate reader Infinite M200 Pro (Tecan Trading AG) at 37 °C in 150 µl fibrillation buffer and 5 µM ThT. The recording parameters were: 442 nm excitation wavelength, 475 nm-555 nm spectral range, 2 nm step resolution, 10 nm excitation bandwidth, 20 nm emission bandwidth, gain of 80, z-position of 18300±500 µm. For analysis, intensity integrals from 475 nm to 555 nm were calculated.

Mouse bioassay. Fibril preparations were inoculated in ovine PrP(25-233) transgenic mice tgshpXI and tg338 homozygously overexpressing the ARQ- or VRQ-allele, respectively, which are both associated with highest scrapie susceptibility and frequency [21]. Before inoculation, each sample was suspended in sterile PBS pH 7.4, quick-frozen in liquid nitrogen, and stored at -80 °C. For each determination of mean incubation periods, six tgshpXI mice and six tg338 mice aged 6 to 8 weeks were inoculated intracerebrally with 50 µl of a given sample, examined for clinical signs of mouse prion disease at least twice a week, and euthanised at the point of neurologic dysfunction. Only coded information was displayed on mice boxes to avoid observer bias. Bioassays were terminated 630 days after inoculation. Incubation periods were measured as the time from inoculation to onset of clinical symptoms. Crude brain homogenates [10 % (w/v)] were prepared from diseased mice inoculated with spontaneously generated ovrecPrP(25-233)-fibrils and used for a second passage into the same mouse line.[54] PrP^{Sc} in the brains of animals was detected by digestion of 10 % brain homogenates with 50 µg/ml PK (recombinant grade; Roche Applied Sci-

ence) for 2 h at 37 °C followed by Western blot analysis.

Circular dichroism (*CD*) *spectroscopy.* Ten CD spectra per sample were collected with a Jasco J-815 spectropolarimeter at room temperature in 10 mM sodium phosphate pH 7.4 over the spectral range of 185 nm-260 nm at a scan speed of 50 nm/min and a step resolution of 1 nm. Only CD signals with a HT-value below 600 were regarded to be reliable. Below a wavelength of 185 nm, excessive buffer absorption impeded further readings. A blank spectrum for cuvette and buffer was subtracted from each spectrum. Satisfactory CD ellipticities of recPrP-fibrils were only obtained after increasing fibril solubility by gentle sonication of 1 µg µl^{-1} PrP in presence of 0.12 % (vol/vol) SDS with a Misonix sonicator 3000 at 240 W for 1 min at < 25 °C [55]. Neither sonication only nor SDS-treatment only did result in measurable ellipticity. An influence of sonication or SDS-treatment on the secondary structure of amyloid fibrils is assumed to be negligible. A SDS-concentration as high as 0.2 % (vol/vol) only solubilises prion fibrils [56]. Prion infectivity, which depends crucially on structural features, remains even after boiling in 5 % SDS [57]. Sonication of monomeric ovrecPrP(25-233) for 45 min at 240 W neither changes ellipticity intensity nor spectral features. Sonication for 1 min at 240 W in 0.12 % (vol/vol) SDS resulted in an increase in ellipticity intensity, only accompanied by slight shifts in spectral features of ± 1nm. PTA-precipitated PrP^{Sc} was not measured because brain homogenate impurities, glycosylations, and GPI-anchor prevent a valid quantitative analysis.

Atomic force microscopy (*AFM*) *and image processing.* All AFM measurements were carried out with the sample dried on the mica surface. Liquid cell AFM could not be performed because of prion safety limitations, to avoid interference of the cantilever movement with the solvent, and because a soft coat formed in the presence of water by the disordered N-terminal segment of PrP-

fibrils may hide fibrillar topology details [8]. Immediately before AFM measurement, samples were briefly sonicated for 10 sec with a Misonix sonicator 3000 at 200 W and < 25 °C. Sample volumes of 40 µl containing 0.44 – 4.4 µM ovrecPrP from the fibrillation end point or PrP^{Sc}-seeds purified from brain homogenate by precipitation with sodium phosphotungstic acid (NaPTA) were adhered for 30 min onto a freshly cleaved mica crystal, washed thirty times with 40 µl water drops, and dried at room temperature for 45 min. Samples were imaged with a NanoWizard II AFM (JPK Instruments AG) using Olympus silicon tips on a silicon cantilever (OMCL-160TS-R3) with a typical tip size of 7 nm, a spring constant of 26 N m^{-1}, a drive frequency of 300±100 kHz, and a scan rate of 0.5 - 1 lines sec^{-1}. Data were collected using intermittent current AFM-mode from up to four different samples and up to three different scanning sessions as 512 x 512 or 1024 x 1024 pixel images and processed using Gwyddion software 2.22. All images were levelled by mean plane subtraction to correct for tilting of the sample stage and servo range errors. Each scan line was corrected for streaks, scratches, and noise related to the mica surface. Fibrillar heights were measured perpendicular to the fibrillar axis using Gwyddion's extract profile tool, but not quantified in detail. In contrast to widths, the heights of soft objects are usually underestimated with AFM[58; 59] due to the mechanical force applied, which results in elastic deformation of polymers such as nucleic acids and proteins fibrils. Mean fibril widths and lengths were quantified at half of the maximal heights. Width distribution histograms were obtained by classifying the cross section widths of > 700 ovrecPrP-fibrils into groups of 5 nm size. To avoid measurement errors from stacked fibrils, only isolated fibrils were considered. To account for tip convolution, all measured widths and lengths were corrected for the tip size.

Solid-state NMR spectroscopy. All NMR-experiments were conducted using 3.2 mm triple-resonance (^{1}H, ^{13}C, ^{15}N) probe heads at static magnetic fields of 14.1 and 18.8 T (Agilent Technologies) and MAS frequencies of 11 kHz±3 Hz or 12.5 kHz±3 Hz, respectively, for (^{13}C, ^{13}C) PDSD- [60] and NCACX-/NCOCX-type spectra [61] or 23.0 kHz±5 Hz for DREAM mixing [62], respectively. Temperature was calibrated for each probe head and each spinning speed using nickelocene [63]. The cooling gas was set to a temperature that resulted in an actual sample temperature of 0 °C ± 2.5 °C. ^{13}C and ^{15}N chemical shifts were referenced externally to adamantane. Typical ^{1}H, ^{13}C, and ^{15}N 90° pulse lengths were 3.0 µs, 5.5 µs, and 6 µs, respectively. For heteronuclear through-bond transfer, the INEPT scheme [64] was applied. For heteronuclear through-space transfer, chemical-shift selective (^{15}N, ^{13}C) and broad-band (^{1}H, ^{13}C)/(^{1}H, ^{15}N) SPECIFIC-CP [61] schemes were applied. (^{13}C, ^{13}C) mixing was performed using PDSD-mixing times of 5, 10, 20, and 80 ms for intraresidue correlations or 80, 150, and 500 ms for sequential correlations. (^{15}N, ^{13}C) spectra were recorded using SPECIFIC-CP contact times between 1500 and 3500 ms followed by homonuclear PDSD-mixing of 50 to 100 ms or DREAM mixing. During indirect chemical shift evolution periods and FID acquisition, 83 kHz SPINAL decoupling [65] was applied. All spectra were recorded in form of successive one day data sets, which were recorded and added until no further improvement of signal-to-noise ratios was visible. Data sets were processed with NMRPipe [66] by routinely using different apodisation functions, primarily shifted sine-bell squared functions, with or without linear prediction in the indirect dimension and analysed with Sparky version 3.114 (T. D. Goddard and D. G. Kneller, University of California, San Francisco). For peak intensity analysis, square chemical shift areas were integrated manually using Sparky's sum over box integration method. For every amino acid type, the identical chemical shift areas were integrated ten times, to ensure that peak volumes were not biased by slight variations in the areas selected for integration.

Standard deviations were calculated according to $[\sum(x-\bar{x})^2/(n-1)]^{1/2}$ with $\bar{x}$ the sample mean and n the sample size.

Acknowledgements

We thank Bernd Esters for recPrP(25-233) expression and the precision engineering workshop of Waldemar Seidel for MAS-rotor inserts. We are deeply indebted to Detlev Riesner, Filipp Oesterhelt, Eva Birkmann, and Christian Dumpitak for fruitful discussions.

REFERENCES

1. Prusiner, S. (1998). Prions. *Proc Natl Acad Sci U S A* **95**, 13363-83.
2. Legname, G., Baskakov, I., Nguyen, H., Riesner, D., Cohen, F., DeArmond, S. & Prusiner, S. (2004). Synthetic mammalian prions. *Science* **305**, 673-6.
3. Wuthrich, K. & Riek, R. (2001). Three-dimensional structures of prion proteins. *Adv Protein Chem* **57**, 55-82.
4. Schlepckow, K. & Schwalbe, H. (2013). Molecular Mechanism of Prion Protein Oligomerization at Atomic Resolution. *Angew Chem Int Ed Engl* **52**, 10002-10005.
5. Cobb, N., Sonnichsen, F., McHaourab, H. & Surewicz, W. (2007). Molecular architecture of human prion protein amyloid: a parallel, in-register beta-structure. *Proc Natl Acad Sci U S A* **104**, 18946-51.
6. Bocharova, O., Breydo, L., Parfenov, A., Salnikov, V. & Baskakov, I. (2005). In vitro conversion of full-length mammalian prion protein produces amyloid form with physical properties of PrP(Sc). *J Mol Biol* **346**, 645-59.
7. Smirnovas, V., Baron, G., Offerdahl, D., Raymond, G., Caughey, B. & Surewicz, W. (2011). Structural organization of brain-derived mammalian prions examined by hydrogen-deuterium exchange. *Nat Struct Mol Biol* **18**, 504-6.
8. Anderson, M., Bocharova, O., Makarava, N., Breydo, L., Salnikov, V. & Baskakov, I. (2006). Polymorphism and ultrastructural organization of prion protein amyloid fibrils: an insight from high resolution atomic force microscopy. *J Mol Biol* **358**, 580-96.
9. Vazquez-Fernandez, E., Alonso, J., Pastrana, M. A., Ramos, A., Stitz, L., Vidal, E., Dynin, I., Petsch, B., Silva, C. J. & Requena, J. R. (2012). Structural organization of mammalian prions as probed by limited proteolysis. *PLoS One* **7**, e50111.
10. Govaerts, C., Wille, H., Prusiner, S. & Cohen, F. (2004). Evidence for assembly of prions with left-handed beta-helices into trimers. *Proc Natl Acad Sci U S A* **101**, 8342-7.
11. DeMarco, M. & Daggett, V. (2005). Local environmental effects on the structure of the prion protein. *C R Biol* **328**, 847-62.
12. Helmus, J., Surewicz, K., Nadaud, P., Surewicz, W. & Jaroniec, C. (2008). Molecular conformation and dynamics of the Y145Stop variant of human prion protein in amyloid fibrils. *Proc Natl Acad Sci U S A* **105**, 6284-9.
13. Lu, X., Wintrode, P. & Surewicz, W. (2007). Beta-sheet core of human prion protein amyloid fibrils as determined by hydrogen/deuterium exchange. *Proc Natl Acad Sci U S A* **104**, 1510-5.
14. Tycko, R., Savtchenko, R., Ostapchenko, V., Makarava, N. & Baskakov, I. (2010). The alpha-helical C-terminal domain of full-length recombinant PrP converts to an in-register parallel beta-sheet structure in PrP fibrils: evidence from solid state nuclear magnetic resonance. *Biochemistry* **49**, 9488-97.
15. Kodali, R., Williams, A. D., Chemuru, S. & Wetzel, R. (2010). Abeta(1-40) forms five distinct amyloid structures whose beta-sheet contents and fibril stabilities are correlated. *J Mol Biol* **401**, 503-17.
16. Paravastu, A. K., Leapman, R. D., Yau, W. M. & Tycko, R. (2008). Molecular structural basis for polymorphism in Alzheimer's beta-amyloid fibrils. *Proc Natl Acad Sci U S A* **105**, 18349-54.

17. Petkova, A. T., Leapman, R. D., Guo, Z., Yau, W. M., Mattson, M. P. & Tycko, R. (2005). Self-propagating, molecular-level polymorphism in Alzheimer's beta-amyloid fibrils. *Science* **307**, 262-5.
18. Paravastu, A., Qahwash, I., Leapman, R., Meredith, S. & Tycko, R. (2009). Seeded growth of beta-amyloid fibrils from Alzheimer's brain-derived fibrils produces a distinct fibril structure. *Proc Natl Acad Sci U S A* **106**, 7443-8.
19. Lu, J. X., Qiang, W., Yau, W. M., Schwieters, C. D., Meredith, S. C. & Tycko, R. (2013). Molecular structure of beta-amyloid fibrils in Alzheimer's disease brain tissue. *Cell* **154**, 1257-68.
20. Frederick, K. K., Debelouchina, G. T., Kayatekin, C., Dorminy, T., Jacavone, A. C., Griffin, R. G. & Lindquist, S. (2014). Distinct prion strains are defined by amyloid core structure and chaperone binding site dynamics. *Chem Biol* **21**, 295-305.
21. Baylis, M. & Goldmann, W. (2004). The genetics of scrapie in sheep and goats. *Curr Mol Med* **4**, 385-96.
22. Castilla, J., Saa, P., Hetz, C. & Soto, C. (2005). In vitro generation of infectious scrapie prions. *Cell* **121**, 195-206.
23. Deleault, N., Harris, B., Rees, J. & Supattapone, S. (2007). Formation of native prions from minimal components in vitro. *Proc Natl Acad Sci U S A* **104**, 9741-6.
24. Kim, J., Cali, I., Surewicz, K., Kong, Q., Raymond, G., Atarashi, R., Race, B., Qing, L., Gambetti, P., Caughey, B. & Surewicz, W. (2010). Mammalian prions generated from bacterially expressed prion protein in the absence of any mammalian cofactors. *J Biol Chem* **285**, 14083-7.
25. Cosseddu, G., Nonno, R., Vaccari, G., Bucalossi, C., Fernandez-Borges, N., Di Bari, M., Castilla, J. & Agrimi, U. (2011). Ultra-efficient PrP(Sc) amplification highlights potentialities and pitfalls of PMCA technology. *PLoS Pathog* **7**, e1002370.
26. Prusiner, S., Safar, J. & DeArmond, S. (2004). Bioassays of prions. *In: Prion biology and diseases. Eds. Prusiner, S.B. 2nd ed. Cold Spring Harbor Laboratory Press, Cold Spring Harbor, N.Y.* , 143-186.
27. Colby, D., Wain, R., Baskakov, I., Legname, G., Palmer, C., Nguyen, H., Lemus, A., Cohen, F., DeArmond, S. & Prusiner, S. (2010). Protease-sensitive synthetic prions. *PLoS Pathog* **6**, e1000736.
28. Colby, D., Giles, K., Legname, G., Wille, H., Baskakov, I., DeArmond, S. & Prusiner, S. (2009). Design and construction of diverse mammalian prion strains. *Proc Natl Acad Sci U S A* **106**, 20417-22.
29. Makarava, N., Kovacs, G., Bocharova, O., Savtchenko, R., Alexeeva, I., Budka, H., Rohwer, R. & Baskakov, I. (2010). Recombinant prion protein induces a new transmissible prion disease in wild-type animals. *Acta Neuropathol* **119**, 177-87.
30. Riesner, D. (2006). The Scrapie Isoform of the Prion Protein PrPSc Compared to the Cellular Isoform PrPC. *In: Prions and prion diseases. Eds. Hörnlimann, B., Riesner, D., Kretzschmar, H. Berlin New York: Walter de Gruyter.*, 505-15.
31. McKinley, M., Meyer, R., Kenaga, L., Rahbar, F., Cotter, R., Serban, A. & Prusiner, S. (1991). Scrapie prion rod formation in vitro requires both detergent extraction and limited proteolysis. *Journal of Virology* **65**, 1340-51.
32. Piro, J., Wang, F., Walsh, D., Rees, J., Ma, J. & Supattapone, S. (2011). Seeding specificity and ultrastructural characteristics of infectious recombinant prions. *Biochemistry* **50**, 7111-6.
33. Wille, H., Bian, W., McDonald, M., Kendall, A., Colby, D., Bloch, L., Ollesch, J., Borovinskiy, A., Cohen, F., Prusiner, S. & Stubbs, G. (2009). Natural and synthetic prion structure from X-ray fiber diffraction. *Proc Natl Acad Sci U S A* **106**, 16990-5.
34. Heise, H., Hoyer, W., Becker, S., Andronesi, O., Riedel, D. & Baldus, M. (2005). Molecular-level secondary structure, polymorphism, and dynamics of full-length alpha-synuclein fibrils studied by solid-state NMR. *Proc Natl Acad Sci U S A* **102**, 15871-6.
35. Andronesi, O. C., Becker, S., Seidel, K., Heise, H., Young, H. S. & Baldus, M. (2005). Determination of membrane protein structure and dynamics by magic-angle-spinning solid-state NMR spectroscopy. *J Am Chem Soc* **127**, 12965-74.
36. Siemer, A. B., Arnold, A. A., Ritter, C., Westfeld, T., Ernst, M., Riek, R. & Meier, B. H. (2006). Observation of highly flexible residues in amyloid fibrils of the HET-s prion. *J Am Chem Soc* **128**, 13224-8.
37. Helmus, J. J., Surewicz, K., Surewicz, W. K. & Jaroniec, C. P. (2010). Conformational flexibility of Y145Stop human prion protein amyloid fibrils probed by solid-state nuclear magnetic resonance spectroscopy. *J Am Chem Soc* **132**, 2393-403.
38. Daebel, V., Chinnathambi, S., Biernat, J., Schwalbe, M., Habenstein, B., Loquet, A., Akoury, E., Tepper, K., Muller, H., Baldus, M., Griesinger, C., Zweckstetter, M., Mandelkow, E., Vijayan, V. & Lange, A. (2012). beta-Sheet core of tau paired helical filaments revealed by solid-state NMR. *J Am Chem Soc* **134**, 13982-9.
39. Pan, K. M., Baldwin, M., Nguyen, J., Gasset, M., Serban, A., Groth, D., Mehlhorn, I., Huang, Z., Fletterick, R., Cohen, F. & et al. (1993). Conversion of alpha-helices into beta-sheets features in the formation of the scrapie prion proteins. *Proc Natl Acad Sci U S A* **90**, 10962-6.
40. Wishart, D. & Sykes, B. (1994). The 13C chemical-shift index: a simple method for the identification of protein secondary structure using 13C chemical-shift data. *J Biomol NMR* **4**, 171-80.
41. Tycko, R. & Wickner, R. B. (2013). Molecular Structures of Amyloid and Prion Fibrils: Consensus versus Controversy. *Acc Chem Res*.
42. Heise, H. (2008). Solid-state NMR spectroscopy of amyloid proteins. *Chembiochem* **9**, 179-89.
43. Stohr, J., Watts, J., Mensinger, Z., Oehler, A., Grillo, S., DeArmond, S., Prusiner, S. & Giles, K. (2012). Purified and synthetic Alzheimer's amyloid beta (Abeta) prions. *Proc Natl Acad Sci U S A* **109**, 11025-30.
44. Prusiner, S. B. (2012). Cell biology. A unifying role for prions in neurodegenerative diseases. *Science* **336**, 1511-3.
45. Legname, G., Nguyen, H., Peretz, D., Cohen, F., DeArmond, S. & Prusiner, S. (2006). Continuum of prion protein structures enciphers a multitude of prion isolate-specified phenotypes. *Proc Natl Acad Sci U S A* **103**, 19105-10.
46. Eghiaian, F., Grosclaude, J., Lesceu, S., Debey, P., Doublet, B., Treguer, E., Rezaei, H. & Knossow, M. (2004). Insight into the PrPC-->PrPSc conversion from the structures of antibody-bound ovine prion scrapie-susceptibility variants. *Proc Natl Acad Sci U S A* **101**, 10254-9.

47. Tateishi, J. & Kitamoto, T. (1995). Inherited prion diseases and transmission to rodents. *Brain Pathol* **5**, 53-9.
48. Shen, Y. & Bax, A. (2012). Identification of helix capping and b-turn motifs from NMR chemical shifts. *J Biomol NMR* **52**, 211-32.
49. Kumar, J., Sreeramulu, S., Schmidt, T., Richter, C., Vonck, J., Heckel, A., Glaubitz, C. & Schwalbe, H. (2010). Prion protein amyloid formation involves structural rearrangements in the C-terminal domain. *Chembiochem* **11**, 1208-13.
50. Kunes, K. C., Clark, S. C., Cox, D. L. & Singh, R. R. P. (2008). Left handed beta helix models for mammalian prion fibrils. *Prion* **2**, 81-90.
51. Smirnovas, V., Kim, J., Lu, X., Atarashi, R., Caughey, B. & Surewicz, W. (2009). Distinct structures of scrapie prion protein (PrPSc)-seeded versus spontaneous recombinant prion protein fibrils revealed by hydrogen/deuterium exchange. *J Biol Chem* **284**, 24233-41.
52. Jansen, K., Schafer, O., Birkmann, E., Post, K., Serban, H., Prusiner, S. & Riesner, D. (2001). Structural intermediates in the putative pathway from the cellular prion protein to the pathogenic form. *Biol Chem* **382**, 683-91.
53. Panza, G., Stohr, J., Dumpitak, C., Papathanassiou, D., Weiss, J., Riesner, D., Willbold, D. & Birkmann, E. (2008). Spontaneous and BSE-prion-seeded amyloid formation of full length recombinant bovine prion protein. *Biochem Biophys Res Commun* **373**, 493-7.
54. Torres, J. M., Espinosa, J. C., Aguilar-Calvo, P., Herva, M. E., Relano-Gines, A., Villa-Diaz, A., Morales, M., Parra, B., Alamillo, E., Brun, A., Castilla, J., Molina, S., Hawkins, S. A. & Andreoletti, O. (2014). Elements modulating the prion species barrier and its passage consequences. *PLoS One* **9**, e89722.
55. Muller, H., Stitz, L., Wille, H., Prusiner, S. & Riesner, D. (2007). Influence of water, fat, and glycerol on the mechanism of thermal prion inactivation. *J Biol Chem* **282**, 35855-67.
56. Leffers, K. W., Schell, J., Jansen, K., Lucassen, R., Kaimann, T., Nagel-Steger, L., Tatzelt, J. & Riesner, D. (2004). The structural transition of the prion protein into its pathogenic conformation is induced by unmasking hydrophobic sites. *J Mol Biol* **344**, 839-53.
57. Taylor, D. M., Fernie, K., McConnell, I. & Steele, P. J. (1999). Survival of scrapie agent after exposure to sodium dodecyl sulphate and heat. *Vet Microbiol* **67**, 13-6.
58. Ukraintsev, E., Kromka, A., Kozak, H., Remeš, Z. & Rezek , B. (2012). Artifacts in Atomic Force Microscopy of Biological Samples. *In: Force Microscopy Investigations into Biology - From Cell to Protein, Ed. Christopher Frewin, InTech*, 29-54.
59. Rezek, B., Shin, D. & Nebel, C. (2007). Properties of hybridized DNA arrays on single-crystalline undoped and boron-doped (100) diamonds studied by atomic force microscopy in electrolytes. *Langmuir* **23**, 7626-33.
60. Szeverenyi, N., Sullivan, M. & Maciel, G. (1982). Observation of Spin Exchange by Two-Dimensional Fourier-Transform C-13 Cross Polarization-Magic-Angle Spinning. *J Magn Reson* **47**, 462-475.
61. Baldus, M., Petkova, A., Herzfeld, J. & Griffin, R. (1998). Cross polarization in the tilted frame: assignment and spectral simplification in heteronuclear spin systems. *Molecular Physics* **95**, 1197-1207.
62. Verel, R., Ernst, M. & Meier, B. (2001). Adiabatic dipolar recoupling in solid-state NMR: The DREAM scheme. *J Magn Reson* **150**, 81-99.
63. Heise, H., Kohler, F. & Xie, X. (2001). Solid-state NMR spectroscopy of paramagnetic metallocenes. *J Magn Reson* **150**, 198-206.
64. Morris, G. & Freeman, A. (1979). Enhancement of nuclear magnetic resonance signals by polarization transfer. *J. Am. Chem. Soc.* **101**, 760-762.
65. Bennett, A., Rienstra, C., Griffiths, J., Zhen, W., Lansbury, P. & Griffin, R. (1998). Homonuclear radio frequency-driven recoupling in rotating solids. *J Chem Phys* **108**, 9463-9479.
66. Delaglio, F., Grzesiek, S., Vuister, G., Zhu, G., Pfeifer, J. & Bax, A. (1995). Nmrpipe - a Multidimensional Spectral Processing System Based on Unix Pipes. *J Biomol NMR* **6**, 277-293.

FIGURE LEGENDS

FIGURE 1. ThT fluorescence detection of amyloid formation during spontaneous and PrP^{Sc}-seeded fibrillation. In (**a**), amyloid formation of 100 ng μl^{-1} ovrecPrP(25-233) in volumes of 150 µl was analysed in 96-well plates in absence or presence of PrP^{Sc}-seeds obtained by PTA-precipitation of scrapie sheep brain homogenate. As controls for PrP^{Sc}-seeded fibrillation, PTA-precipitated scrapie sheep brain homogenate in absence of ovrecPrP(25-233) (PrP^{Sc} seed only) and PTA-precipitated normal sheep brain homogenate in presence of ovrecPrP(25-233) (neg. seed + recPrP) demonstrate the specificity of the fibrillation assay. In (**b**), amyloid formation of 1000 ng μl^{-1} ovrecPrP(25-233) in NMR-sufficient volumes of 10 ml was analysed. Note that seeded fibril growth (PrP^{Sc} seed + recPrP) is completed before spontaneous conversion (recPrP only) starts. The decrease in ThT-fluorescence intensity after long times is attributed to lateral fibril association and blockage of ThT-binding sites. Values shown are means ± standard errors for up to ten distinct experiments. The gradually increasing error bars reflect the fibril size distribution in a heterogeneous system.

FIGURE 2. **Immunoblots of samples inoculated in transgenic mice and of brain material from transgenic mice**. (**a**) PrP^{Sc} in brains of tgshpXI (ARQ) and tg338 (VRQ) mice, inoculated with scrapie fibrils, after spontaneous fibrillation of ovrecPrP(25-233) (SP), or with non-fibrillated ovrecPrP(25-233) (NON), respectively, with (+) or without (-) digestion with 50 µg/ml PK for 2 h at 37 °C. Only mice inoculated with fibrillated ovrecPrP(25-233) show PK-resistant PrP27-30 identical to scrapie fibrils. (**b**) Spontaneously fibrillated ovrecPrP(25-233) after digestion with increasing concentrations of PK for 1 h at 37 °C does not show any PK-resistance. (**c**) For comparison, PrP^{Sc}-seeds are depicted characterised by a partial PK-resistance even at high PK-

concentrations. An immunoblot of a PrP^{Sc}-seeded ovrecPrP-sample after PK-treatment is not shown because potentially PK-resistant recPrP cannot be unambiguously distinguished from unglycosylated PrP^{Sc}. Apparent molecular masses based on migration of protein standards are indicated in kDa.

FIGURE 3. Secondary structural properties. As revealed by CD-spectroscopy, the secondary structural transition of monomeric ovrecPrP(25 233) due to spontaneous and PrP^{Sc}-seeded fibrillation results in spectral minima at 218 nm typical for β sheets. Zero crossings at 204 nm and spectral maxima at 193 nm are probable to indicate additional α helical/random coil elements. For comparison, a spectrum of α-helical monomeric ovrecPrP(25 233) is also presented. All given values are mean residue molar ellipticities ([θ]MRW).

FIGURE 4. Ultrastructural properties. Low magnification amplitude AFM-images (**a, b**) and corresponding fibril width distributions (**c, d**) obtained after (**a, c**) spontaneous or (**b, d**) PrP^{Sc}-seeded fibrillation of ovrecPrP(25-233) display variability in fibrillar topology. The black curves in (**c, d**), are fits with a Gaussian function illustrating that spontaneous and PrP^{Sc}-seeded ovrecPrP-fibrils have identical average widths within the margin of error. However, spontaneously generated ovrecPrP-fibrils have only a length of up 400 nm (**a**), whereas PrP^{Sc}-fibrils in scrapie-infected sheep brain homogenate (**e**) and PrP^{Sc}-seeded fibrils (**b**) are several μm long. In (**a**), an inset of higher magnification shows the morphology of spontaneously generated ovrecPrP-fibrils to higher details. Immediately before AFM-measurement, all samples were subjected to mild sonication for 10 sec. Thus, (**e**) depicts PrP^{Sc}-fibrils as they were used for seeding of ovrecPrP(25-233).

FIGURE 5. 2D-(^{13}C-^{13}C)- and (^{15}N-^{13}C)-solid-state NMR-correlation spectra. For identification of spin systems, homo- and heteronuclear correlation spectra were analysed jointly. The aliphatic regions of (**a**) (^{13}C-^{13}C)- and (**b**) (^{15}N-^{13}C)-correlation spectra after spontaneous fibrillation of ovrecPrP(25-233) are depicted, acquired with (**a**) PDSD-mixing for 20 ms at 11 kHz MAS and (b) DREAM-mixing at 23 kHz MAS, to obtain intraresidue correlations. All cross peaks are labelled according to **Tables S1, S2,** and **S3**. Note that in (**b**) several tentative assignments are present more than one time, reflecting the ambiguity as summarised in **Tab. S3.**

FIGURE 6. Secondary chemical shifts. A comparison of secondary chemical shifts of ovrecPrP(25-233) after spontaneous (black) or PrP^{Sc}-seeded (red) conversion suggests that both fibril types share a similar overall arrangement of secondary structure elements. All amino acid residues are listed in alphabetic order.

FIGURE 7. Structure and dynamics details. Solid-state NMR comparison of ovrecPrP(25-233) after spontaneous (black) or PrP^{Sc}-seeded (red) conversion reveals an increased flexibility after PrP^{Sc}-seeding. (**a**) Overlay of 2D-(^{13}C-^{13}C)-correlation spectra which were acquired with the identical number of transients and increments and processed identically. DREAM-mixing at 23 kHz was performed to obtain only direct correlations. Spin systems after PrP^{Sc}-seeded conversion for which cross peaks are weakened up to almost completely vanished on both sides of the diagonal are indicated by arrows. (**b**) For intensity analysis, Cα-Cβ/Cβ-Cα-peak volumes in α-helical and β-sheet chemical shift ranges of 2D-(^{13}C-^{13}C)-DREAM spectra were calculated. Peak volumes were normalised two-fold: (1) To account for deviating protein amounts in the samples, all values were standardised to the peak volume of the corresponding spectrum diagonal. (2) The highest

peak volume of each amino acid type (α-helical black or β-sheet black or α-helical red or β-sheet red) was set to 100 %. Note that α-helical and β-sheet spin systems are not present for all amino acid types. Whereas all threonines are located in β-strands, all arginines and leucines are characterised by α-helical secondary structure signatures. Prolines are not known to be present in any secondary structure. Valines are located in α-helices as well as β-strands. (**c - e**) High magnification overlays of some exemplary regions of (**c**) leucine, (**d**) proline and valine, and (**e**) alanine residues show that cross peak intensities for prolines (all N-terminal of position 168), α-helical valines, α-helical leucines (at positions 128, 133, and 141), and α-helical alanines (clustered between positions 116 and 136) are reduced or even completely vanished, whereas β-strand alanines and β-strand valines do not display a decrease in cross peak intensities.

FIGURE 8. Schematic representation of secondary structures. Compared are the cellular isoform PrP^{C} [3] (above), several literature models of the misfolded isoform PrP^{Sc} (middle: β-sandwich model[5], spiral model[11], β-helix model 1[10], and β-helix model 2[50]), and our solid-state NMR data for infectious full-length ovrecPrP(25-233)-fibrils (below). So far, we have only indications for the position of secondary structure elements but not for their 3D-arrangement. As not all of our α-helical chemical shift signatures N-terminal of Pro140 may indicate an α-helical segment (see text for details), an α-helical segment and a preserved PrP^{C} β-strand Gly129-Gly134 are drawn on top of each other. Pro140 is indicated by a gap in the α-helical segment. Red ribbons, blue arrows, and black lines represent α-helices, β-strands, and loops/unordered segments, respectively.

SUPPLEMENTAL FIGURE 1. The amino acid sequence of full-length ovine PrP(25-233). The 24 N-terminal and 23 C-terminal signal sequence residues are cut off during posttranslational modification.

SUPPLEMENTAL FIGURE 2. Identification of alanine spin systems. Excerpts of several 800 MHz 2D-correlation spectra after spontaneous fibrillation of ovrecPrP(25-233) demonstrate how alanine spin systems were identified: (**a**) and (**c**) CO-regions, (**b**) and (**e**) Cα-regions, and (**d**) and (**f**) Cβ-regions using (**a**), (**b**), and (**c**) (^{13}C-^{13}C) PDSD with a mixing time of 80 ms, (**d**) (^{13}C-^{13}C) DREAM-mixing, (**e**) and (**f**) (^{15}N-^{13}C) CP followed by (^{13}C-^{13}C) DREAM-mixing. For comparison purposes, all alanine cross peaks are labelled according to **Tables S1, S2,** and **S3**. Cross peaks could only be distinguished using the N-Cβ-correlations nicely resolved in (**f**) and comparing peak maxima in regions of overlapping signals with all other correlation spectra. The cross peak at 125 ppm x 21 ppm in (**f**) (indicated as 'A8?') cannot be explained yet. No other cross peaks with corresponding chemical shift signatures were observed in any other homo- or hetero-nuclear correlation spectrum.

SUPPLEMENTAL FIGURE 3. Identification of leucine spin systems. Excerpts of two 800 MHz 2D-correlation spectra after spontaneous fibrillation of ovrecPrP(25-233) demonstrate how leucine spin systems were identified. For the half above the diagonal, (^{13}C-^{13}C) PDSD with a mixing time of 20 ms was used, whereas the half below the diagonal was obtained by using the DREAM scheme for mixing. For comparison purposes, all leucine cross peaks are labelled according to **Table S1, S2,** and **S3**.

SUPPLEMENTAL FIGURE 4. Identification of glycine spin systems. Excerpts of two 800 MHz 2D-correlation spectra after spontaneous fibrillation of ovrecPrP(25-233) demonstrate how glycine spin systems were identified. (**a**) N-Cα-region of a (^{15}N-^{13}C) correlation spectrum using (^{15}N-^{13}C) CP followed by (^{13}C-^{13}C) DREAM-mixing and (**b**) CO-Cα-region of a (^{13}C-^{13}C) correlation spectrum with a PDSD mixing time of 5 ms. For comparison purposes, all glycine cross peaks are labelled according to **Tables S1, S2,** and **S3**. Cross peaks could only be distinguished focusing stringently on peak maxima in regions of overlapping signals.

TABLES

Table 1. Incubation periods of *in vitro*-fibrillated ovrecPrP(25-233) and PrP^{Sc} purified from scrapie-infected sheep brains.

Inoculum	Host mice	No. infected/ No. inoculated	Mean incubation period ± SD[days]
ovrecPrP(25-233) after spontaneous fibrillation (in absence of any PrP^{Sc}seeds)			
1. passage	tg338 (VRQ)	1/6	507
	tgshpXI (ARQ)	2/6	388 ± 84
2. passage	tg338 (VRQ)	6/6	253 ± 4
	tgshpXI (ARQ)	6/6	193 ± 3
ovrecPrP(25-233) after PrP^{Sc}-seeded fibrillation	tg338 (VRQ)	6/6	249 ± 51
	tgshpXI (ARQ)	6/6	267 ± 9
purified PrP^{Sc}-seeds	tg338 (VRQ)	6/6	177 ± 16
	tgshpXI (ARQ)	6/6	211 ± 23
monomeric ovrecPrP(25-233)	tg338 (VRQ)	0/6	-
	tgshpXI (ARQ)	0/6[a]	-

[a] Two mice were found dead after 297 and 384 days, respectively, but lacked clinical signs and PK-resistant PrP27-30.

FIGURES

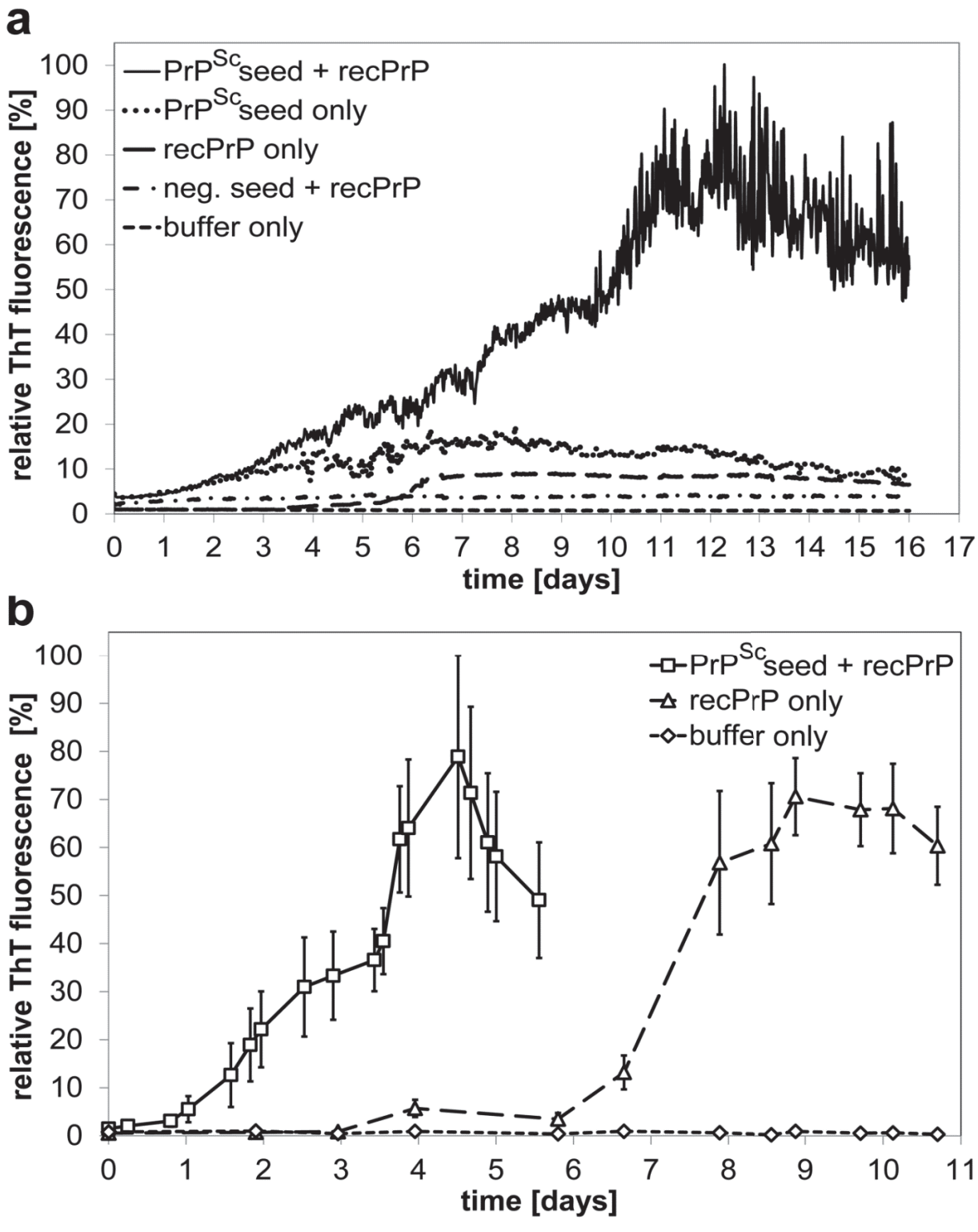

Figure 1

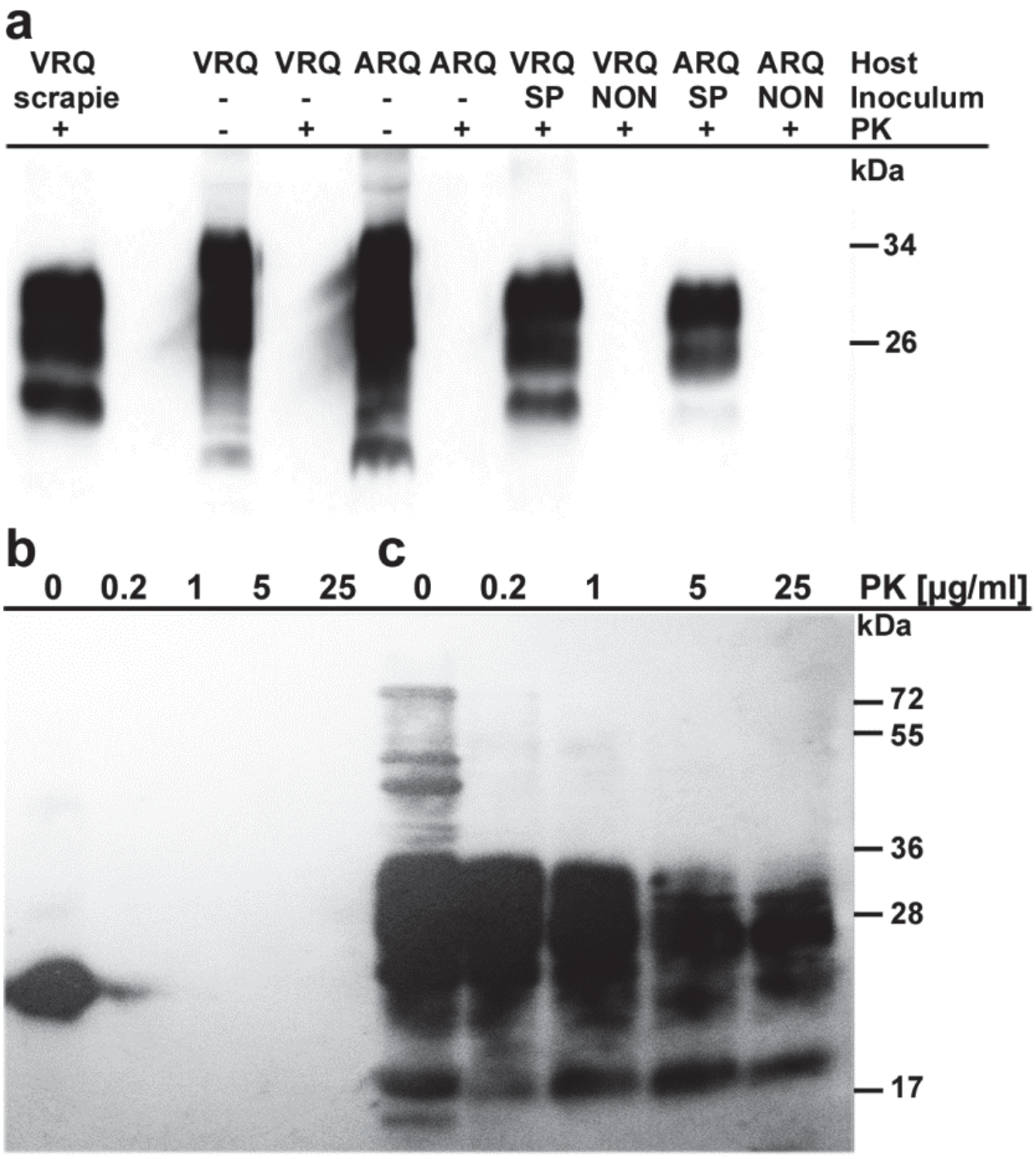
a
VRQ scrapie + | VRQ - - | VRQ - + | ARQ - - | ARQ - + | VRQ SP + | VRQ NON + | ARQ SP + | ARQ NON + | Host Inoculum PK
kDa
34
26
b
0 0.2 1 5 25
c
0 0.2 1 5 25
PK [µg/ml]
kDa
72
55
36
28
17

Figure 2

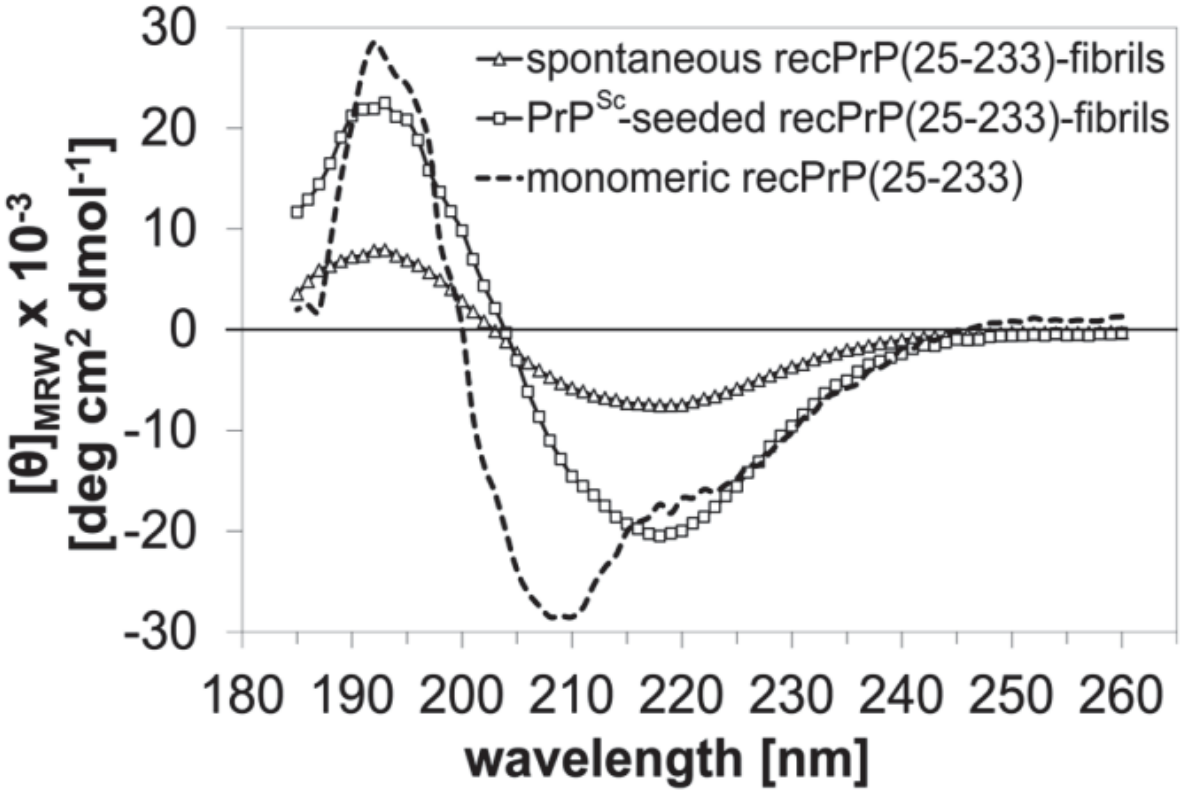
30
20
10
0
-10
-20
-30
180 190 200 210 220 230 240 250 260
wavelength [nm]
[θ]MRW x 10-3
[deg cm2 dmol-1]
spontaneous recPrP(25-233)-fibrils
PrPSc-seeded recPrP(25-233)-fibrils
monomeric recPrP(25-233)

Figure 3

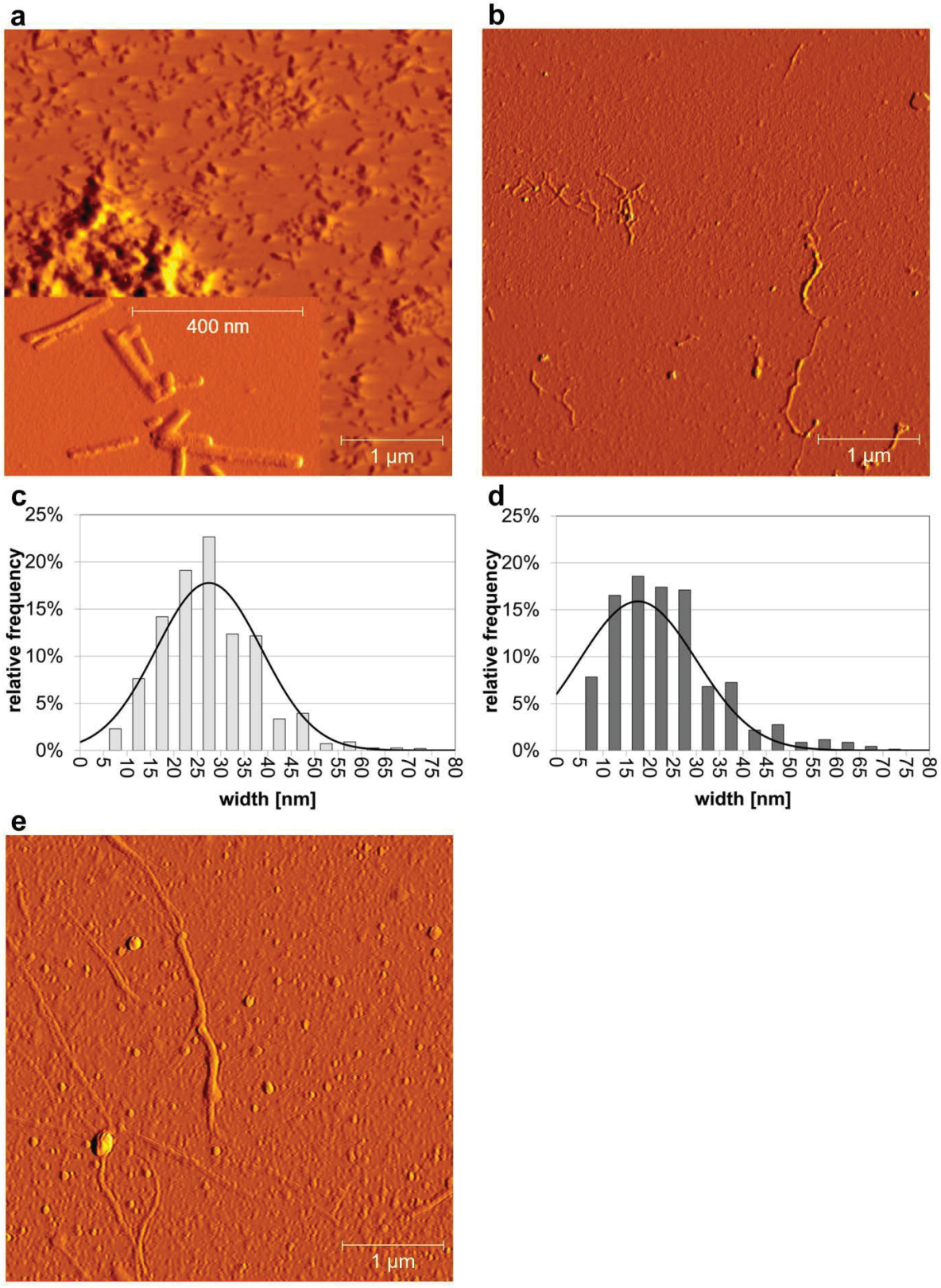
a
400 nm
1 µm
b
1 µm
c
relative frequency
25%
20%
15%
10%
5%
0%
0 5 10 15 20 25 30 35 40 45 50 55 60 65 70 75 80
width [nm]
d
relative frequency
25%
20%
15%
10%
5%
0%
0 5 10 15 20 25 30 35 40 45 50 55 60 65 70 75 80
width [nm]
e
1 µm

Figure 4

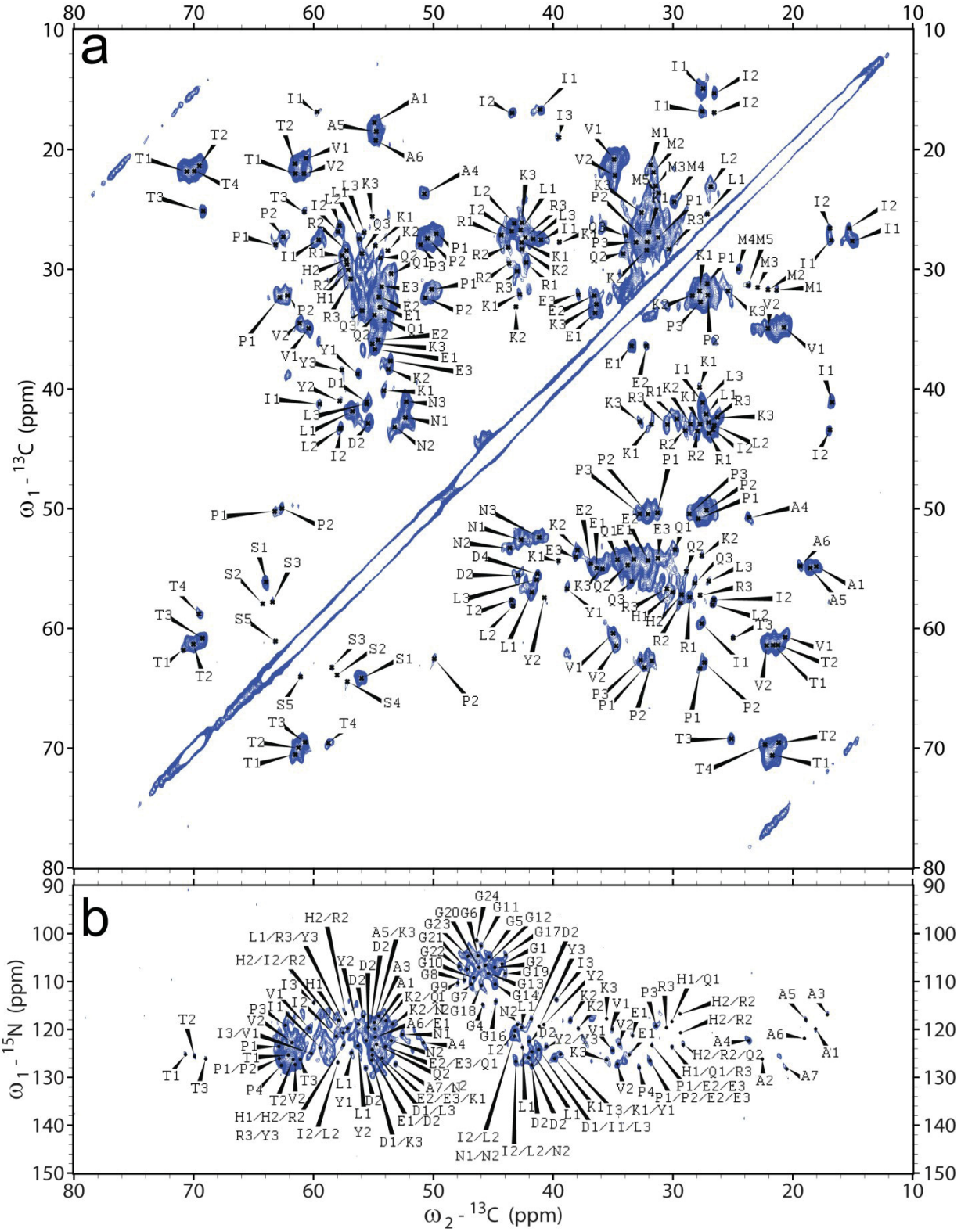

Figure 5

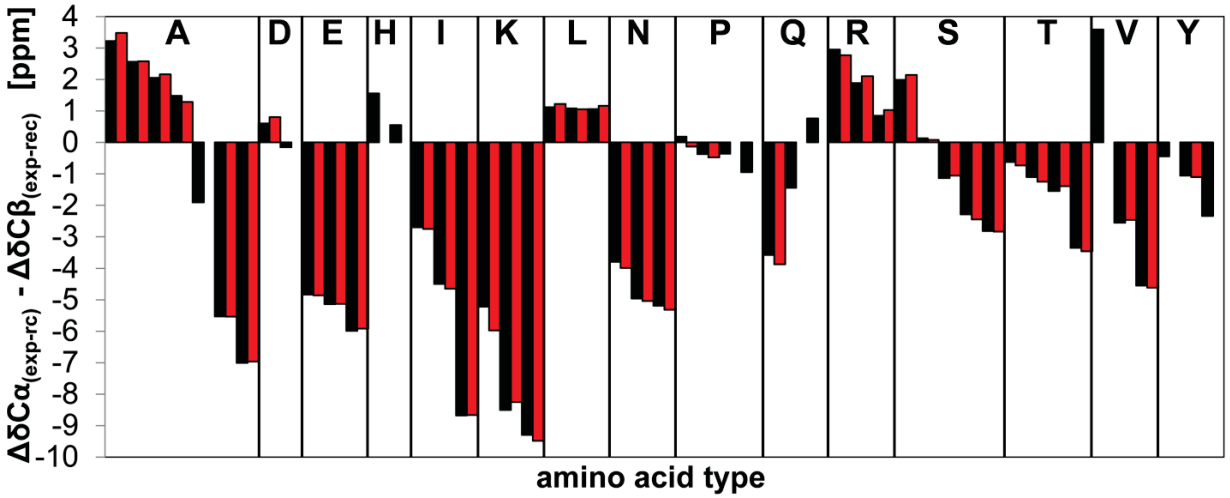
A
D
E
H
I
K
L
N
P
Q
R
S
T
V
Y
4
3
2
1
0
-1
-2
-3
-4
-5
-6
-7
-8
-9
-10
ΔδCα(exp-rc) - ΔδCβ(exp-rec) [ppm]
amino acid type

Figure 6

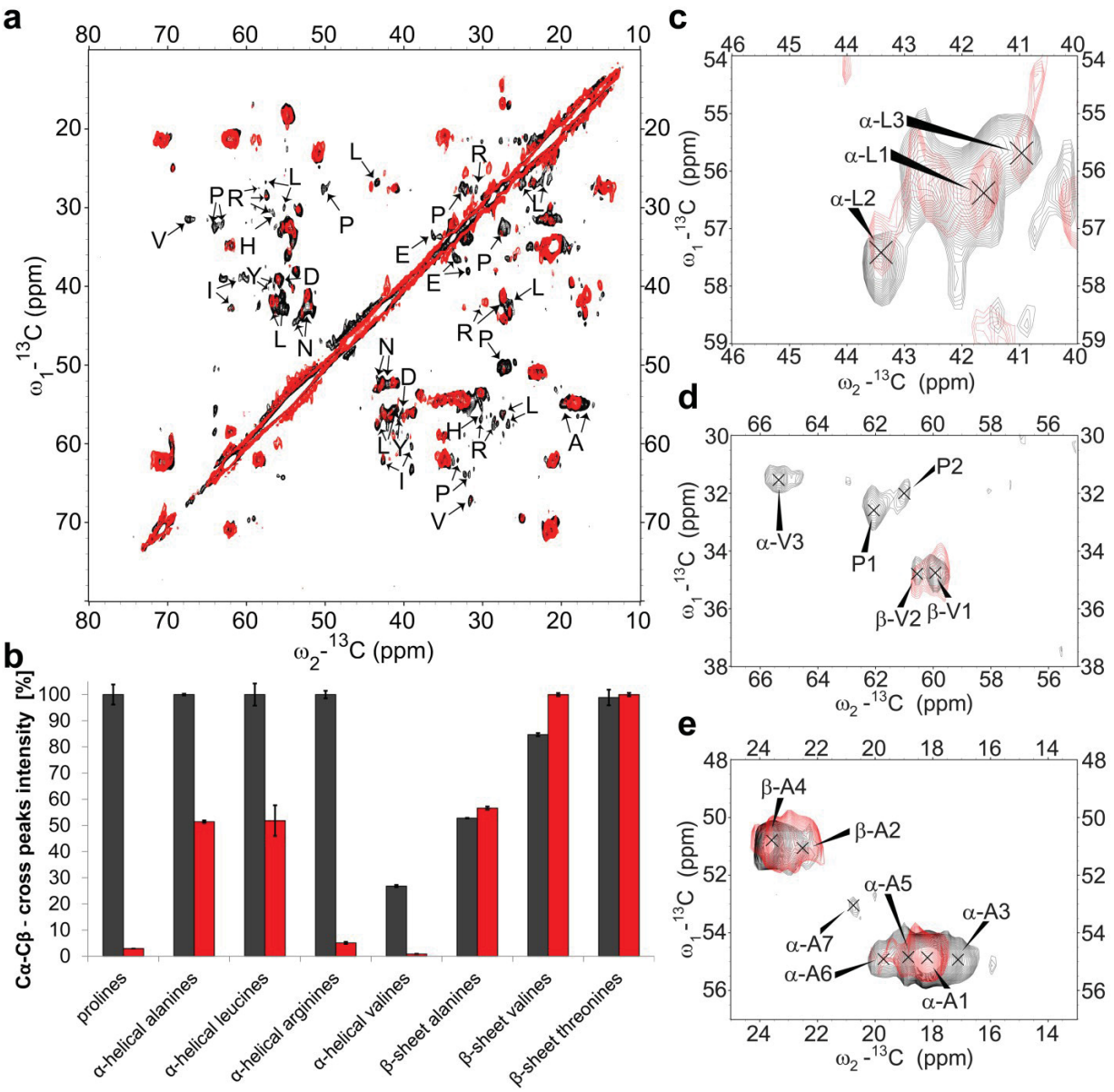
a
b
c
d
e
ω1-13C (ppm)
ω2-13C (ppm)
Cα-Cβ - cross peaks intensity [%]
prolines
α-helical alanines
α-helical leucines
α-helical arginines
α-helical valines
β-sheet alanines
β-sheet valines
β-sheet threonines
α-L3
α-L1
α-L2
α-V3
P2
P1
β-V2
β-V1
β-A4
β-A2
α-A5
α-A3
α-A7
α-A6
α-A1

Figure 7

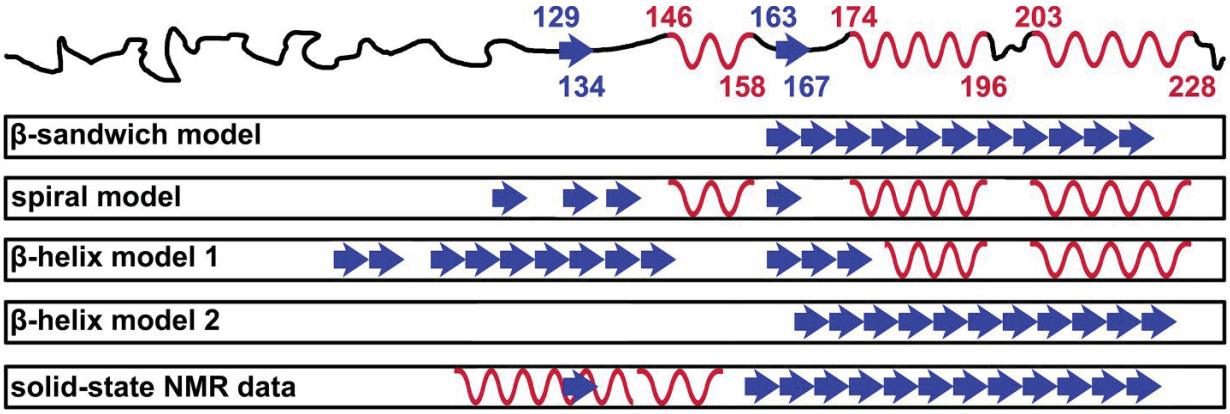
129
146
163
174
203
134
158
167
196
228
β-sandwich model
spiral model
β-helix model 1
β-helix model 2
solid-state NMR data

Figure 8

1 MVKSHIGSWILVLFVAMWSDVGLC
25 KKRPKPGGGWNTGGSRYPGQGSPGGNRYPPQGGGGWGQPHGGGWGQPHGG
75 GWGQPHGGGWGQPHGGGGWGQGGSHSQWNKPSKPKTNMKHVAGAAAAGAV
125 VGGLGGYMLGSAMSRPLIHFGNDYEDRYYRENMYRYPNQVYYRPVDQYSN
175 QNNFVHDCVNITVKQHTVTTTTKGENFTETDIKIMERVVEQMCITQYQRE
225 SQAYYQRGA
234 SVILFSSPPVILLISFLIFLIVG

Figure S1

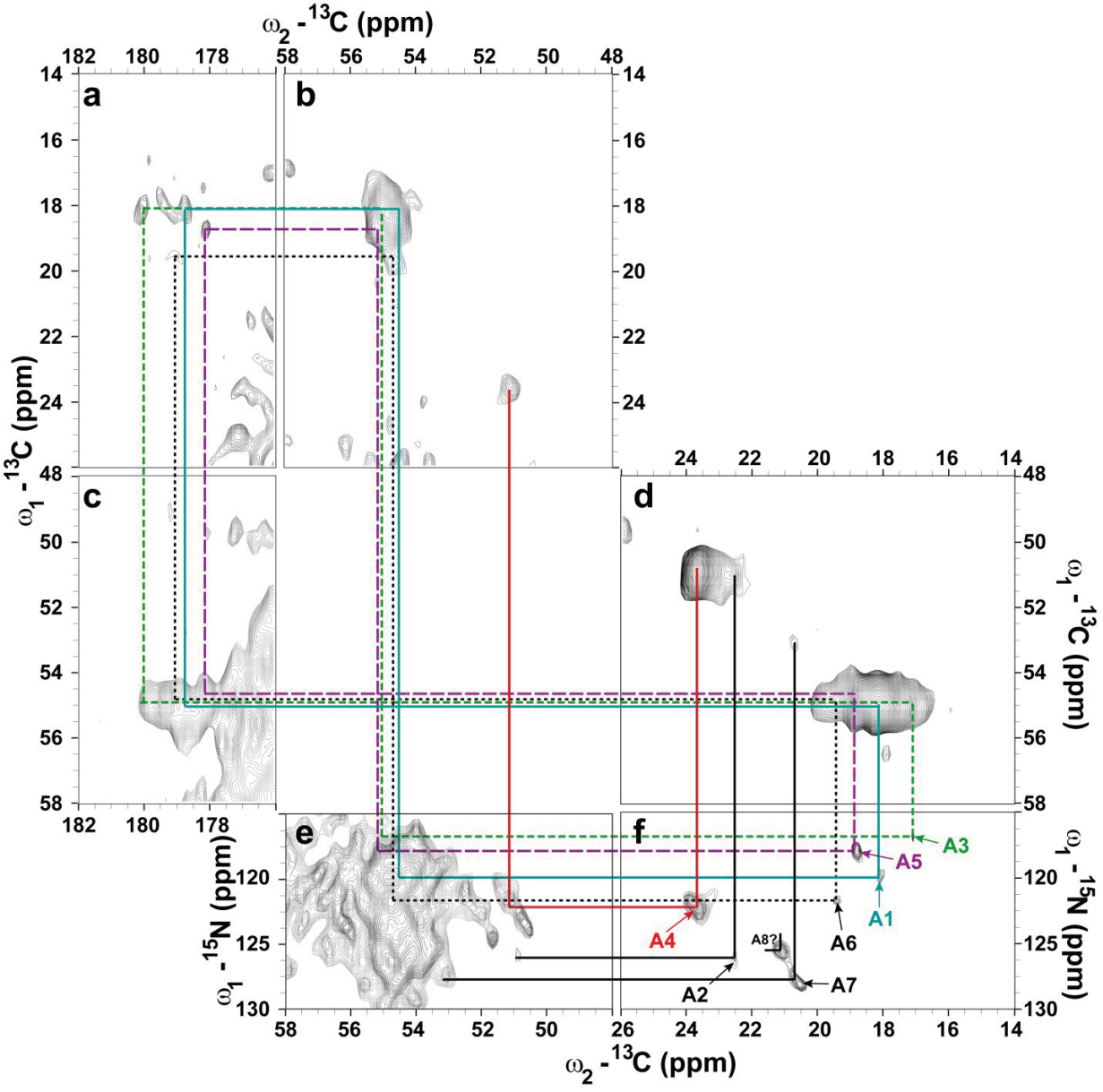

Figure S2

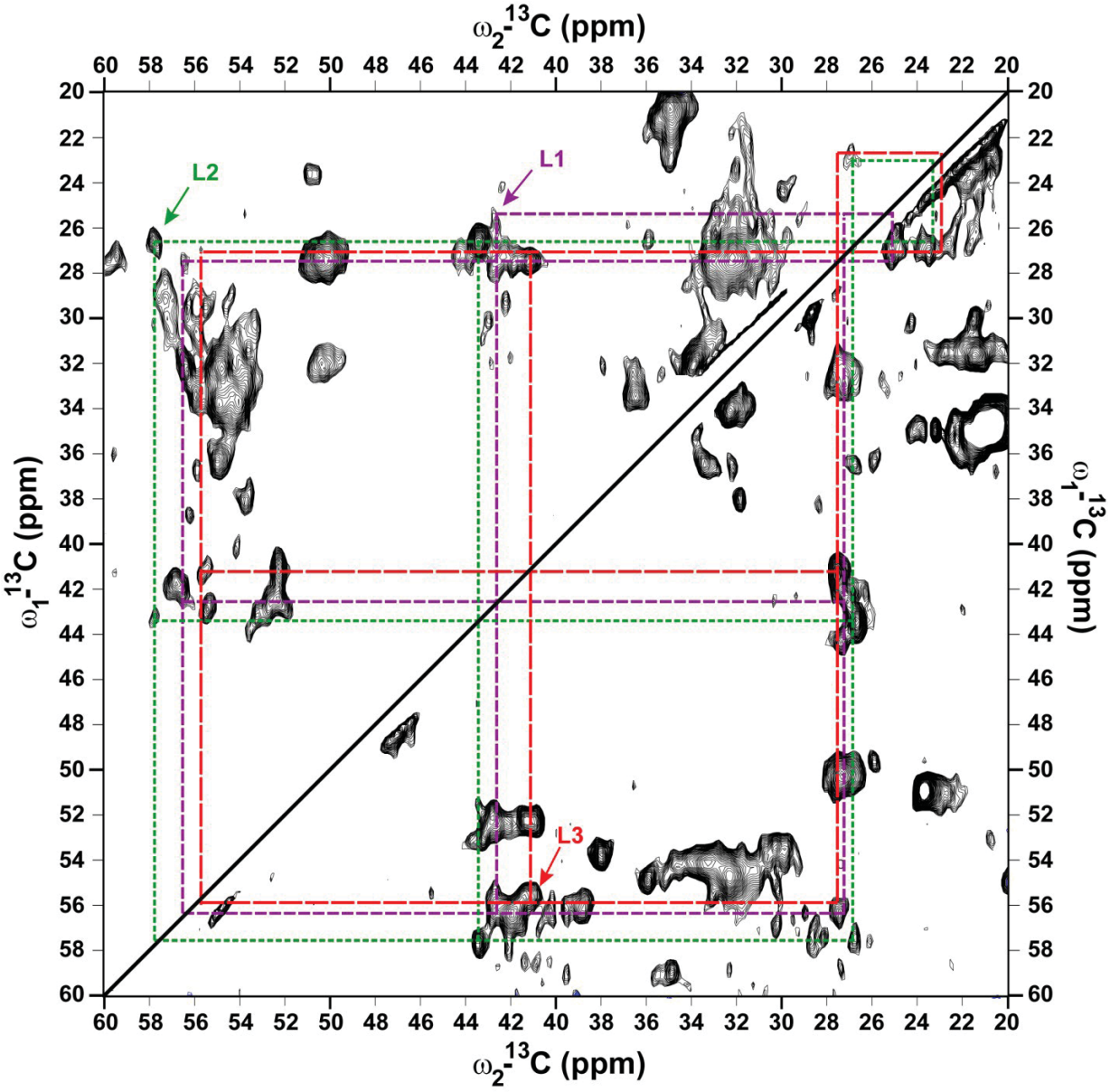

Figure S3

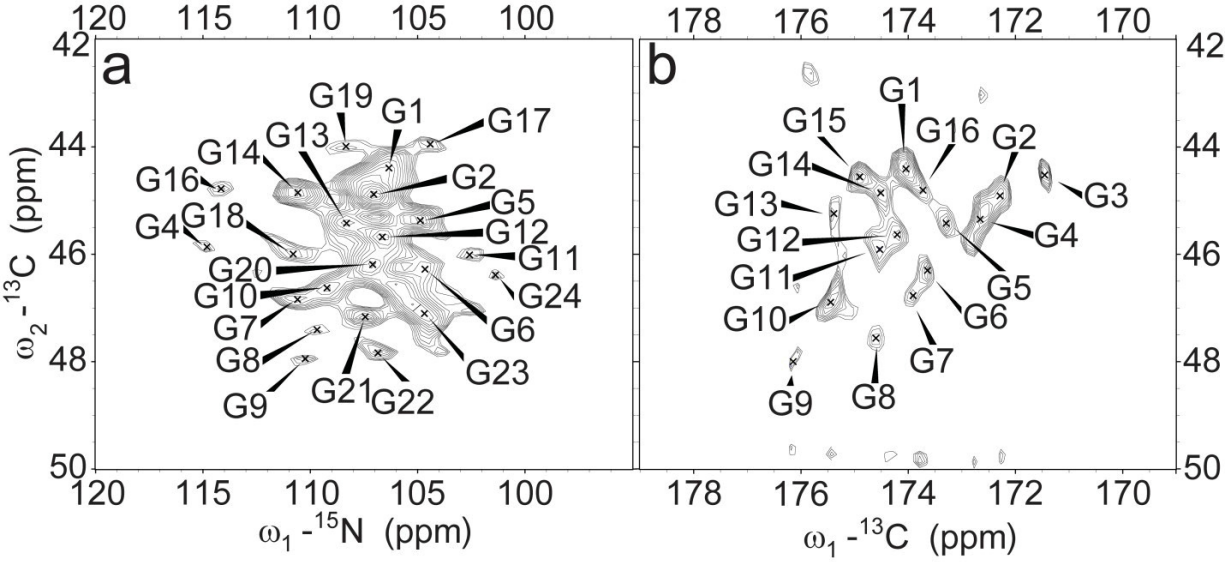
a
b
G19
G1
G17
G13
G14
G16
G2
G5
G4
G18
G12
G11
G20
G10
G24
G7
G6
G8
G23
G9
G21
G22
G15
G16
G2
G3
G14
G13
G4
G12
G11
G5
G10
G6
G7
G9
G8
120 115 110 105 100
178 176 174 172 170
42 44 46 48 50
ω2 -13C (ppm)
ω1 -15N (ppm)
ω1 -13C (ppm)

Figure S4

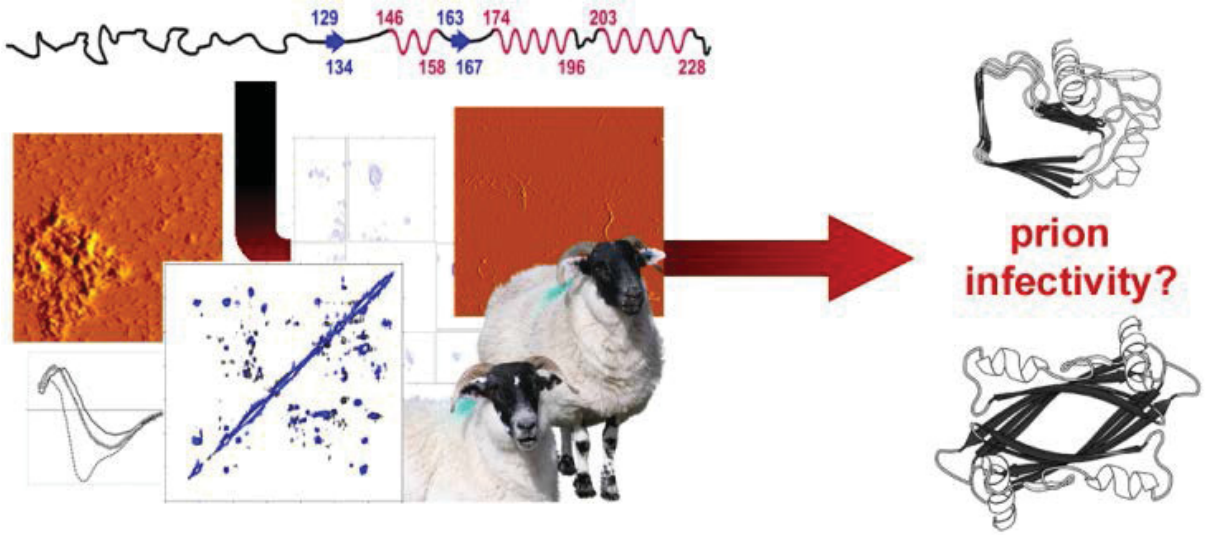

Graphical abstract

2.1.8 Double-strand DNA end-binding and sliding of the toroidal CRISPR- associated protein Csn2.

Publiziert in: Nucleic Acids Research

Impact Factor: 8,278

Eigenanteil an der Publikation: 20 %

Durchführung und Auswertung von AFM, Mitverfassen des Manuskripts.

Published online 26 April 2013 *Nucleic Acids Research, 2013, Vol. 41, No. 12* **6347–6359**
doi:10.1093/nar/gkt315

Double-strand DNA end-binding and sliding of the toroidal CRISPR-associated protein Csn2

Zihni Arslan[1], Reinhild Wurm[1], Oleksandr Brener[1,2], Philipp Ellinger[3], Luitgard Nagel-Steger[1,2], Filipp Oesterhelt[1], Lutz Schmitt[3], Dieter Willbold[1,2], Rolf Wagner[1], Holger Gohlke[4], Sander H. J. Smits[3] and Ümit Pul[1,*]

[1]Institut für Physikalische Biologie, Heinrich-Heine-Universität, Universitätsstr. 1, 40225 Düsseldorf, Germany, [2]ICS-6, Forschungszentrum Jülich, 52425 Jülich, Germany, [3]Institut für Biochemie, Heinrich-Heine-Universität, Universitätsstr. 1, 40225 Düsseldorf, Germany and [4]Institut für Pharmazeutische und Medizinische Chemie, Heinrich-Heine-Universität, Universitätsstr. 1, 40225 Düsseldorf, Germany

Received February 13, 2013; Revised April 4, 2013; Accepted April 5, 2013

ABSTRACT

The adaptive immunity of bacteria against foreign nucleic acids, mediated by CRISPR (clustered regularly interspaced short palindromic repeats), relies on the specific incorporation of short pieces of the invading foreign DNA into a special genomic locus, termed CRISPR array. The stored sequences (spacers) are subsequently used in the form of small RNAs (crRNAs) to interfere with the target nucleic acid. We explored the DNA-binding mechanism of the immunization protein Csn2 from the human pathogen *Streptococcus agalactiae* using different biochemical techniques, atomic force microscopic imaging and molecular dynamics simulations. The results demonstrate that the ring-shaped Csn2 tetramer binds DNA ends through its central hole and slides inward, likely by a screw motion along the helical path of the enclosed DNA. The presented data indicate an accessory function of Csn2 during integration of exogenous DNA by end-joining.

INTRODUCTION

Clustered regularly interspaced short palindromic repeats (CRISPR) and CRISPR-associated (Cas) proteins constitute a prokaryotic adaptive immunity system to prevent viral infections or the invasion by mobile DNA elements (1–3). The immunization is achieved by the specific storage of foreign nucleic acid sequences as 'portraits' of the targets, which are later used in the form of small RNAs for the specific recognition and inactivation of the invading DNA. Ten CRISPR-Cas systems have been described, which differ in the organization of the CRISPR operon, constituted by a set of diverse CRISPR-associated genes (*cas*) and the CRISPR arrays (4). The *cas* genes encode the protein components of the system, which exhibit various biochemical activities (5).

The mechanism of the CRISPR-mediated immunity is divided into three stages (2,6). The first stage describes the immunization of the host cells by the integration of foreign DNA-derived spacer sequences into the CRISPR array (adaptation stage). The second stage comprises the transcription of the CRISPR array to the precursor CRISPR RNA (pre-crRNA), the expression of Cas proteins and the processing of the pre-crRNA to small crRNAs (expression/processing stage). In the third stage, the crRNA-loaded Cas protein complexes screen the foreign DNA for spacer-matching sequences and initiate the nucleolytic hydrolysis of the target DNA (interference stage). According to the recent classification of the different CRISPR-Cas systems, three major types (type I, II and III) have been defined (4), which exhibit mechanistic variability in the maturation of the crRNAs and the inactivation of the target nucleic acids (7–15).

The type II CRISPR-Cas systems, mainly found in pathogenic bacteria (16), consist of the CRISPR array, the *cas* genes encoding for the proteins Cas9, Cas1, Cas2 and Csn2 (in type II-A) or Cas4 (in type II-B) and a gene for the trans-encoded crRNA (tracrRNA). The tracrRNA contains sequence elements complementary to the repeat of the pre-crRNA (11). The RNA duplex formation of the tracrRNA and the pre-crRNA mediates the maturation of the crRNAs by RNaseIII and the Cas9 protein (11,17). Loaded with the tracrRNA:crRNA duplex, the Cas9 protein introduces double-strand DNA breaks at the spacer-matching protospacer region (12). Several studies have shown that the Cas9 protein along with designed crRNA:tracrRNA is active in eukaryotic cells and can be used for multiplex genome editing in bacteria and eukaryotes (18–23). Moreover, engineered Cas9 protein with inactivated nuclease domains has been used for sequence-specific control of transcription in *Escherichia coli* and eukaryotic cells (24).

*To whom correspondence should be addressed. Tel: +49 211 81 14945; Fax: +49 211 81 15167; Email: pul@hhu.de

6348 Nucleic Acids Research, 2013, Vol. 41, No. 12

The activities of the proteins Cas1, Cas2 and Csn2 are dispensable for maturation of the crRNAs and the cleavage of the target DNA, and thus are likely required in the immunization stage (10,11). The nucleases Cas1 and Cas2 are involved in incorporation of new spacer sequences into the CRISPR array (25–27). Little is known about the function of the Csn2 protein; although early studies showed that a knockout of the *csn2* gene prevents the development of phage-insensitive mutants by an uptake of new spacer sequences (7,28), the role of the Csn2 protein during immunization is unknown. The structures and DNA-binding activities of Csn2 proteins from *Enterococcus faecalis*, *S. agalactiae* and *Streptococcus pyogenes* have been analyzed independently (29–31). These Csn2 proteins are ring-shaped homotetramers, and the structure of a protomer consists of a 'head' and a 'leg' domain. Whereas the leg domain consists of a pair of long stretched helices that form the interface for the tetrameric assembly, the function of the head domain is still unclear. More recently, based on the crystal structure of the Cas protein Stu0660 from *Streptococcus thermophilus*, a second Csn2 protein family has been proposed, which shares no sequence similarity to Csn2 proteins; however, its members have a similar tetrameric ring-shaped structure (32). All Csn2 proteins exhibit Ca^{2+}-dependent double-stranded DNA (dsDNA)-binding activities without any notable sequence dependence. The tetrameric structure contains a large positively charged central hole of ~4 nm in diameter, which is stabilized by Ca^{2+}-ions bound to the helices in the leg domain. This hole is large enough to encircle the dsDNA. An alternative DNA binding mode has been suggested by molecular dynamics simulations, which revealed that the Csn2 tetramers can adopt a conformation with a groove outside the ring that could interact with the dsDNA (30).

To elucidate the role of the Csn2 protein in the CRISPR immunization stage, we have analyzed the DNA-binding mechanism of Csn2 from the human pathogen *S. agalactiae* in detail, using different biochemical techniques, atomic force microscopy (AFM) and molecular dynamics (MD) simulations. We provide evidence that Csn2 binds to the ends of linear dsDNA and moves inward through rotation-coupled translocation. The encircling of the dsDNA by Csn2 tetramers was probed by capping the DNA ends of Csn2–DNA complexes with streptavidin, keeping the Csn2 rings arrested on the DNA. The MD simulations give mechanistic insights at the molecular level how a Csn2 ring may rotate along the helical path of the DNA in a Ca^{2+}-dependent manner. The data suggest that Csn2 is a DNA end-loading toroidal protein, whose function is directly related to DNA end metabolism. Csn2 thus resembles proteins involved in the repair of dsDNA breaks and recombination.

MATERIALS AND METHODS

Purification of Csn2

Streptococcus agalactiae Csn2 protein was expressed and purified as previously described (30).

Preparation of relaxed plasmid DNA for competition experiments

Relaxation of supercoiled plasmid DNA was performed with *E. coli* Topoisomerase I (New England Biolabs, NEB). Supercoiled pUC18-1 plasmid DNA (33) was extracted and purified from *E. coli* cells grown to stationary phase in YT medium. Ten micrograms of supercoiled plasmid DNA were incubated in 1 × NEBuffer 4 (50 mM potassium acetate, 20 mM Tris acetate, pH 7.9, 10 mM magnesium acetate, 1 mM DTT) and 1 $\mu g\,ml^{-1}$ bovine serum albumin in a total volume of 30 µl. Five units *E. coli* Topoismerase I were added and the reaction mixture was incubated for 1 h at 37°C to allow complete relaxation. After extraction with phenol/chloroform and ethanol precipitation, the DNA was resuspended in deionized water (Millipore). The relaxation was verified on a 1% agarose gel. DNA bands were stained with ethidium bromide and visualized under UV light.

Analyses of protein–DNA interaction by electrophoretic mobility shift assays

The 155 bp DNA fragment was obtained by *Eco*RI-*Dra*I digestion of the plasmid pUC18-1. DNA fragments were purified by agarose gel electrophoresis and end labeled by Klenow (Promega) incorporation of [α-^{32}P]-dATP. Binding reaction mixtures contained 2 nM DNA, 10 mM $CaCl_2$, 20 $ng\,\mu l^{-1}$ heparin and indicated concentrations of Csn2 or unlabeled plasmid DNA (supercoiled, relaxed or linearized) as given in the individual experiments. After incubation for 15 min at room temperature, the complexes were separated from free DNA on native 5% (w/v) Tris/glycine polyacrylamide gels. DNA bands were visualized by autoradiography.

Preparation of DNA for AFM

The pCR001 plasmid (5125 bp) used in the AFM analyses was constructed by ligation of *cas1-cas2* genes into the *Nde*I-*Pac*I cleaved pACYCDuet-1 vector (Novagen). The insert with *cas1-cas2* genes were obtained by PCR from genomic DNA of *E. coli* MG1655 using the following primers: forward 5′-GAATGCCATATGACCTGGC TTCCCCTTAAT-3′ and reverse 5′-CCGACCTTAATTA ACATTTCCTTATTATTAAAGATCAGCT-3′.

The plasmid pCR001 was extracted and purified from *E. coli* cells grown to stationary phase in YT medium with the Qiagen Plasmid Midi Kit. To obtain relaxed DNA, 10 µg of the supercoiled plasmid was treated with *E. coli* Topoisomerase I as described above. Linear plasmid DNA used in the AFM analyses was produced by cleavage with the restriction enzyme *Ecl136*II. After relaxation or linearization reactions, the DNA was extracted with phenol/chloroform, purified with PCR purification Kit (Qiagen) and precipitated with ethanol. The relaxed and linearized DNA probes were resuspended in deionized water (Millipore).

Atomic force microscopic (AFM) analyses of Csn2–DNA complexes

Linearized or relaxed pCR001 was incubated with the Csn2 protein in the presence of 2 mM $CaCl_2$ in a total

volume of 5 µl. The DNA and protein concentrations are given in the individual experiments. The samples were incubated 10 min at room temperature to allow complex formation and diluted with 95 µl of adsorption buffer (5 mM $CaCl_2$, 2 mM Tris–HCl, pH 8.0, 10 mM NaCl). Forty-microliter aliquots of the samples were immediately transferred to freshly cleaved mica. After 1 min incubation the mica surface was washed three times with 100 µl deionized water (Millipore). Excess water was dried with compressed N_2. Imaging of Csn2–DNA complexes was performed with Nanowizard II (JPK Instruments AG, Berlin) in intermittent contact in air, using standard silicon cantilevers (OLYMPUS OMCL-AC160).

Biotinylation of dsDNA fragment and Csn2 binding studies

The 256 bp DNA fragment was obtained by *Eco*RI-*Bam*HI digestion of the plasmid pUC18-1. After purification of the DNA fragments by agarose gel electrophoresis, the biotinylation of the ends was achieved by Klenow incorporation of Biotin-11-dUTP. Ten microgram of the DNA fragment was incubated with 5 U Klenow (Promega), each 0.2 mM dCTP, dGTP, dATP and Biotin-11-dUTP (GeneOn) in 1 × Klenow buffer (Promega, 50 mM Tris–HCl, pH 7.2, 10 mM $MgSO_4$ and 100 µM DTT) in a total volume of 50 µl for 1 h at room temperature. After extraction with phenol/chloroform and ethanol precipitation, the DNA was dissolved in 10 µl TE buffer.

The binding studies with the biotinylated DNA were performed by sequential incubation of 168 ng of the biotinylated DNA in the presence of 7.2 mM $CaCl_2$ with 4.7 µg Csn2, 14 mM ethylene glycol tetraacetic acid (EGTA) and/or 2 µg streptavidin (Sigma-Aldrich) in a total volume of 14.4 µl. The volumes of the binding reaction without EGTA or streptavidin were adjusted by addition of deionized water (Millipore). The incubation of the samples occurred in three steps, each for 15 min at room temperature. The complexes were separated from free DNA on a native 2% Tris/Acetate agarose gel. The bands were visualized by ethidium bromide staining.

MD simulations

MD simulations were performed with the AMBER 11 suite of programs (34) together with the force field as described by Cornell *et al.* (35) using modifications suggested by Simmerling *et al.* (36). To generate a starting structure of Csn2 binding to dsDNA, canonical B-DNA of 36 bp length (sequence: 5′-GTTTTAGAGCTGTGCTG TTTCGAATGGTTCCAAAAC-3′) was inserted into the central hole of tetrameric Csn2 such that the DNA is perpendicular to a least-squares fit plane through the protein atoms and that Csn2 is displaced by ~6 Å from the center of the DNA along the double strand. The tetrameric Csn2 was taken from Ellinger *et al.* (30) (PDB code: 3QHQ), including the Ca^{2+}-ions. In addition, a starting structure of Csn2 binding to dsDNA without Ca^{2+}-ions was generated. The starting structures were placed into octahedral periodic boxes of TIP3P water molecules (37). The distance between the edges of the water box and the closest atom of the solutes was at least 11 Å, resulting in system sizes of ~186 000 atoms. The systems were minimized by 50 steps of steepest descent minimization followed by 450 steps of conjugate gradient minimization. The particle mesh Ewald method (38) was used to treat long-range electrostatic interactions, and bond lengths involving bonds to hydrogen atoms were constrained using SHAKE (39). The time-step for all MD simulations was 2 fs, with a direct-space, non-bonded cutoff of 8 Å. Applying harmonic restraints with force constants of 5 kcal mol^{-1} $Å^{-2}$ to all solute atoms, canonical ensemble (NVT)-MD was carried out for 50 ps, during which the system was heated from 100 to 300 K. Subsequent isothermal isobaric ensemble (NPT)-MD was used for 150 ps to adjust the solvent density. Finally, the force constants of the harmonic restraints on solute atom positions were gradually reduced to zero during 100 ps of NVT-MD. The following NVT-MD at 300 K with a time constant of 10 ps for heat-bath coupling was used for analysis, with conformations extracted every 20 ps. The simulation lengths amount to 100 ns of which the first 30 ns were discarded. Each simulation was repeated once with varied starting velocities, resulting in four independent simulations in total.

For analyzing the trajectories, conformations were superimposed with respect to the phosphorous atoms of the dsDNA or the C_α atoms of Csn2. The conformational variability of Csn2 binding to dsDNA agrees with that observed in MD simulations of Csn2 alone (30). For determining the translocation along the dsDNA, the distance between the center of the dsDNA and the average coordinates of the C_α atoms of all four helices H5 was computed. For determining the rotation of Csn2 relative to the dsDNA, the angle defined by the point triple (average coordinates of the phosphorous atoms of the five most central nucleotides on one strand; average coordinates of the phosphorous atoms of the five most central nucleotides on the other strand; average coordinates of the C_α atoms of one pair of helices H5 located in one of the legs of the tetrameric structure) was computed. For determining the kink angle of the dsDNA, the angle defined by the point triple (average coordinates of the phosphorous atoms of the five outermost base pairs at one end of the DNA; average coordinates of the phosphorous atoms of the five most central base pairs of the DNA; average coordinates of the phosphorous atoms of the five outermost base pairs at the other end of the DNA) was computed.

RESULTS

Binding of Csn2 requires free DNA ends

The Csn2 tetramers from *S. agalactiae* are stable in the range of pH 7.0–9.0, a wide range of ionic strengths as well as in the presence of Ca^{2+}-chelating EGTA (30). Owing to the high stability of the ring-shaped Csn2 tetramers, it is unlikely that the quaternary structure can be opened wide enough to bind and enclose dsDNA as it is known to occur in several DNA-enclosing proteins (40,41). Therefore, if the Csn2 tetramers encircle the dsDNA the

6350 Nucleic Acids Research, 2013, Vol. 41, No. 12

tetramers should bind DNA by threading onto the DNA ends. In contrast, a binding of the DNA outside the central hole will be independent on the presence of free DNA ends. To distinguish between these two alternative DNA-binding modes, we performed electrophoretic mobility shift assays (EMSAs) and tested whether the binding of Csn2 requires free DNA ends.

First, we incubated a 155 bp ^{32}P-radiolabeled DNA fragment with increasing amounts of Csn2 and separated the protein–DNA complexes on a 5% native Tris/glycine polyacrylamide gel. As can be seen in Figure 1A, Csn2 formed one complex band with an estimated apparent $K_{0.5}$ value between 30 and 60 nM (Figure 1A, lanes 3 and 4). The declining mobility of the complex band with increasing protein concentration indicates the binding of multiple Csn2 molecules to the DNA fragment. To test a putative requirement for a free DNA end for the interaction, we performed competition experiments with unlabeled plasmid DNA, either in closed circular or linearized form. As shown in Figure 1B (lanes 3–6), the complex formation of Csn2 with the linear radiolabeled DNA was challenged with increasing concentrations of the linearized pUC18-1 plasmid. However, the same plasmid in supercoiled or relaxed form almost did not compete for binding of Csn2 (Figure 1B, lanes 7–14; Figure 1C, lanes 19–22). This indicates that free DNA ends are necessary for Csn2-binding and supports the threading of dsDNA into the central channel of the Csn2 tetramers.

To further evaluate the dependence of the Csn2–DNA interaction on free dsDNA ends, we repeated the competition experiments with the plasmid DNA cleaved by restriction enzymes at two sites, with the aim to double the concentration of the DNA ends. The competition efficiency was higher with DNA cleaved with double cutters *Pvu*II or *Ava*II compared with the *Sca*I-linearized DNA at the same final competitor concentration (Figure 1C, lanes 7–14). Moreover, plasmid DNA cleaved with *Hae*III at 12 sites reduced the binding to the radiolabeled DNA already at the lowest competitor concentration tested (Figure 1C, lanes 15–18). Thus, the challenging efficiency depended on the concentration of free DNA ends at equal total competitor DNA concentration. The appearance of three intermediate complexes during the decay of the Csn2–DNA complexes is consistent with a binding of multiple Csn2 tetramers to the 155 bp dsDNA, and suggests a sliding of the bound proteins along the DNA after loading the DNA from its ends.

Cleavage of the pUC18-1 plasmid with the restriction enzymes *Sca*I, *Pvu*II and *Hae*III produces blunt ends, while cleavage with *Ava*II gives 5′-overhangs of three bases. The comparable challenging extent of the *Pvu*II- and *Ava*II-cleaved DNA demonstrated that the DNA end-binding activity of Csn2 is not restricted to blunt ends but short 5′-protruding DNA ends are also bound by Csn2 (Figure 1C, lanes 7–14). The ability of Csn2 to bind dsDNA with 3′- and/or 5′-overhangs was further examined with different synthetic DNA substrates

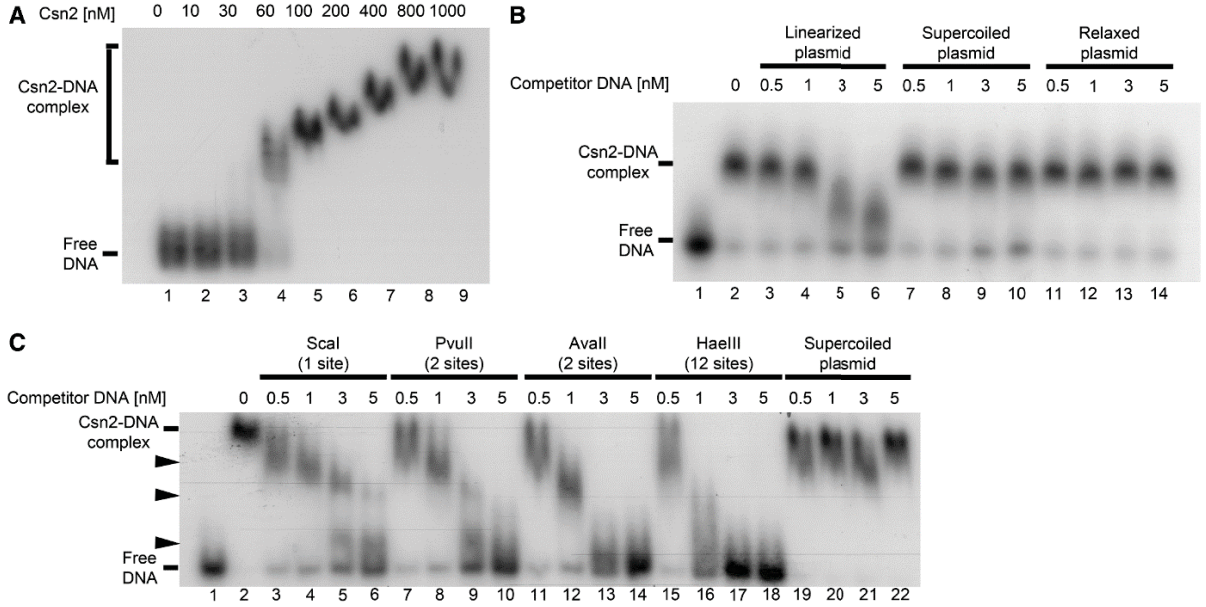

Figure 1. Electrophoretic mobility shift assays of a radiolabeled 155 bp DNA fragment with Csn2 either in the absence (**A**) or in the presence of competitor DNA (**B** and **C**) are presented. In each reaction 2 nM ^{32}P-labeled DNA, 20 ng/µl heparin, and 10 mM $CaCl_2$ were employed. (A) Titration of Csn2 in the range of 0 to 1 µM is shown. (B) Csn2 binding to the radiolabeled DNA fragment was competed with indicated amounts of 2915 bp unlabeled plasmid DNA either in *Sca*I-linearized (lanes 3–6), supercoiled (lanes 7–10) or in relaxed (lanes 11–14) form. The concentration of Csn2 was constant at 60 nM in lanes 2–14. Lanes 1 and 2 show the control reactions, performed either in the absence of Csn2 (lane 1) or in the absence of competitor DNA (lane 2). (C) The same competition experiment as in (B) but with *PvuII*-, *AvaII*-, or *HaeIII*-cleaved competitor plasmid. The numbers of cleavage sites of the different endonucleases are given in the brackets. The black arrowheads indicate intermediate Csn2-DNA complexes, resulting from decomposition of the fully occupied complexes.

Nucleic Acids Research, 2013, Vol. 41, No. 12 **6351**

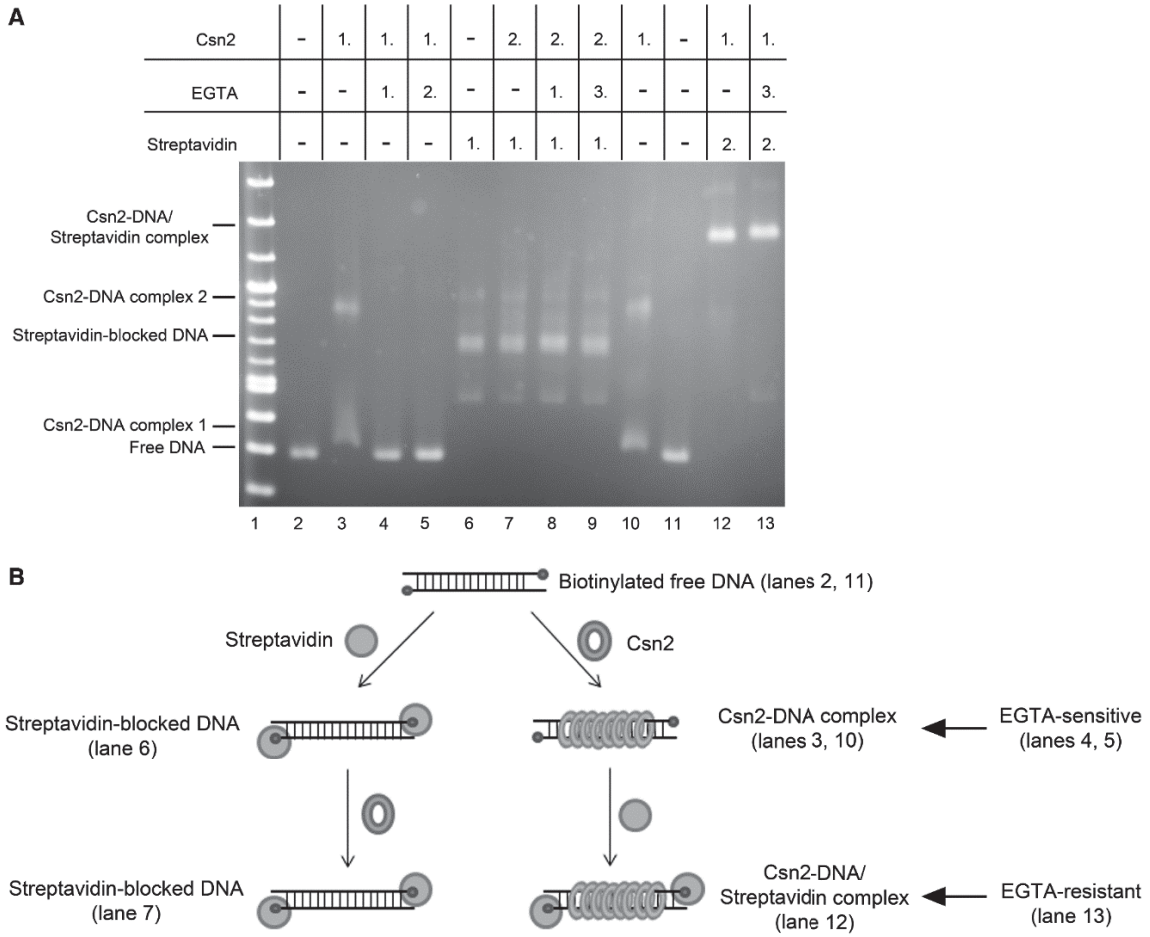

Figure 2. (**A**) Binding analyses of Csn2 in the presence and absence of EGTA and free DNA ends on 2% Tris-acetate agarose gel. In each lane 168 ng linear DNA and 7.2 mM $CaCl_2$ were employed. The numbers above the lanes indicate the order of addition of streptavidin (2 µg), Csn2 (4.7 µg), or EGTA (14 mM) in a total volume of 14.4 µl. Lanes 2–5: Influence of EGTA on Csn2-DNA interaction is shown. Lanes 6–9: 168 ng of the end-biotinylated DNA fragment were incubated first with streptavidin to block the DNA ends. Lanes 10 and 11: Streptavidin was added after binding of Csn2. After separation of the complexes the agarose gel was stained with ethidium bromide. (**B**) Schematic presentation of the binding analysis, shown in (A).

(Supplementary Figure S1). Csn2 did not form complexes with single-stranded DNA (ssDNA) (Supplementary Figure S1A and B, lanes 1–3). However, the hybridization of complementary oligonucleotides to ssDNA restored the Csn2–DNA interaction (Supplementary Figure S1A and B, lanes 4–6). Moreover, Csn2 formed faint complex bands with a DNA substrate that contains a 36-bp dsDNA region flanked by 29 or 34 nt ssDNA tails (Supplementary Figure S1B, lanes 7–9). These results indicate that Csn2 is in principle able to enter dsDNA regions by threading ssDNA tails in its central hole.

Dissociation of Csn2 occurs at the DNA ends: evidence for encircling the DNA by Csn2 rings

The crystal structure of the Csn2 from *S. agalactiae* revealed three Ca^{2+}-ions bound to the leg domain of each protomer (30). These ions have also been found in the crystal structures of Csn2 proteins from *E. faecalis* and *S. pyogenes* (29,31). The loss of one of the Ca^{2+}-ions within one protomer of Csn2 resulted in a reorientation of α-helices in the leg domain, which form the inner rim of the central hole (30) (Supplementary Figure S2). Thus, the Ca^{2+}-ions are considered to be important for the stabilization of the tetramer conformation that is able to bind the dsDNA (29–31).

Because capturing the Ca^{2+}-ions by EGTA did not disassemble the tetramers but abolished their DNA-binding activity (30,31), we suggested that in the presence of EGTA the conformation of the central hole becomes disordered, resulting in weakened interactions of the tetramers with the DNA backbone and leading to the dissociation of the sliding rings from the DNA ends. If this were the case, the obstruction of the DNA ends of

6352 Nucleic Acids Research, 2013, Vol. 41, No. 12

Csn2–DNA complexes should result in arrested Csn2 rings on the DNA, and the complexes should not dissociate in the presence of EGTA. To test this, we attached biotin to both ends of a dsDNA fragment, allowing the blocking of both DNA-termini with streptavidin.

Incubation of Csn2 with biotinylated dsDNA led to the formation of two complex bands, demonstrating that biotin itself did not interfere with Csn2 binding (Figure 2A, lanes 2, 10). As shown previously (29–31), in the presence of EGTA the complex formation was completely inhibited (Figure 2, lane 4). To test whether EGTA causes the dissociation of DNA-bound Csn2 molecules, we incubated the DNA with Csn2 in the presence of Ca^{2+} for 15 min and then added EGTA to the binding reaction followed by incubation for additional 15 min. Indeed, the lack of Csn2–DNA complexes indicated the decomposition of the complexes in the presence of EGTA (Figure 2A, lane 5).

As expected, the tethering of streptavidin to the DNA ends inhibited the binding of Csn2 (Figure 2A, lanes 6 and 7), consistent with the requirement of free DNA ends for Csn2 binding. In contrast, adding streptavidin after the binding of Csn2 resulted in supershifted Csn2-DNA/streptavidin complexes (Figure 2A, lane 12). Moreover, the Csn2 proteins in these complexes were captured on the DNA because adding EGTA did not lead to a decay of the complexes (Figure 2A, lane 13). Thus, both the association as well as the dissociation of Csn2 occurs at the DNA ends, indicating a sliding activity of the Csn2 rings (Figure 2B). In the absence of Ca^{2+}-ions, the tetramers slip down from the DNA ends, likely due to weakened electrostatic interactions between the distorted α-helices of the ring channel and the phosphate backbone of the DNA helix.

AFM of Csn2–DNA complexes

To confirm the DNA end requirement and to probe a binding of multiple Csn2 molecules, which would confirm a sliding activity of the Csn2 rings, we imaged the Csn2–DNA complexes by AFM in intermittent contact mode in air.

The AFM analyses were performed with the 5125 bp plasmid pCR001 as a substrate, either in linearized or relaxed circular form. AFM images of equal amounts of both DNA forms (each 1.3 nM) in the absence of Csn2 are shown Figure 3A and B. Some of the molecules of both DNA forms contained nodes, likely due to a crossover of DNA helices or a distortion/kinking of the DNA during the drying process of the probe on the mica surface (Figure 3B). AFM images of the same DNA mixture in the presence of 176 nM Csn2 showed the formation of protein–DNA complexes (Figure 3C–F). In average the ratio of the heights and widths of bound Csn2 and free DNA (Csn2-DNA/DNA) were 4.2 and 1.3, respectively. In contrast, the ratio of heights and widths of the DNA nodes relative to straight DNA were in average 1.9 and 1.5, respectively. Thus, these DNA nodes, which were also observed in the protein–free sample (Figure 3B), were not considered as protein–DNA complexes.

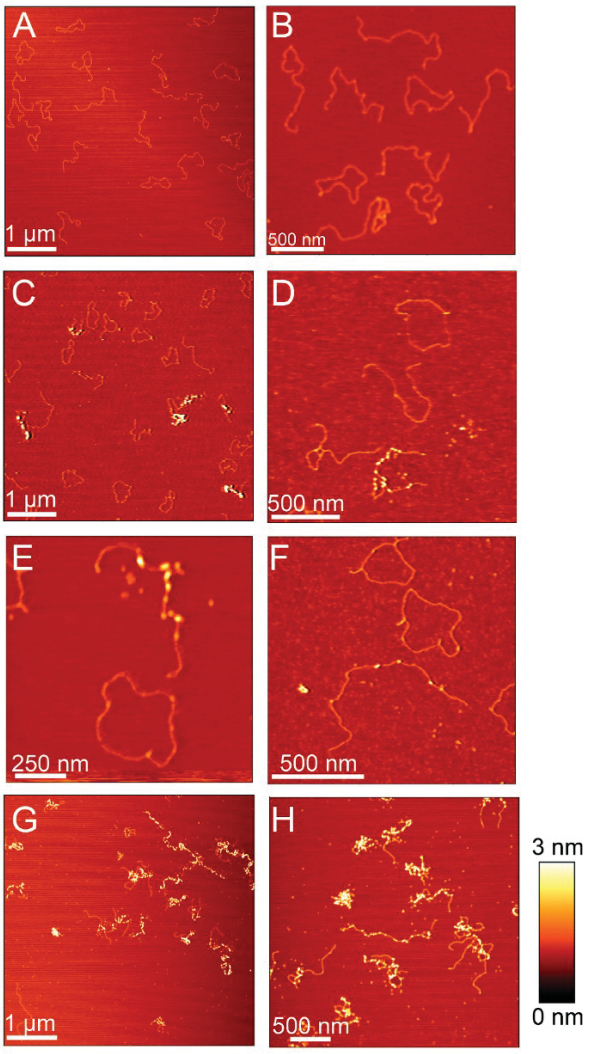

Figure 3. Representative AFM images of 5125 bp plasmid DNA in the absence or presence of Csn2 are shown. (**A**) and (**B**) show images of 1.3 nM relaxed and 1.3 nM linear plasmid DNA in the absence of Csn2; (**C–F**) images of equal amounts of relaxed and linear plasmid DNA (each 1.3 nM) incubated with 176 nM Csn2; (**G**) and (**H**) images of 2.6 nM linear plasmid DNA incubated with 800 nM Csn2. The relative color scale range is 0–3 nm in all images.

Csn2 was exclusively associated with linear DNA (Figure 3C–F), consistent with its DNA end-dependent–binding activity as observed in the mobility shift assays. The binding was not restricted to the DNA ends but internal sites along the entire DNA fragment were also occupied by several Csn2 proteins (Figure 3D–F), indicating a sliding activity of the tetramers after initial binding at the DNA ends. Moreover, the binding of Csn2 seems to be highly cooperative, as some linear DNA molecules were free of any protein, whereas others were bound by several Csn2 proteins in the same sample (Figure 3D–F). Such an apparent cooperative binding

Nucleic Acids Research, 2013, Vol. 41, No. 12 **6353**

activity is also known for the 'recombination associated protein' RdgC from *E. coli*, a ring-shaped DNA-binding protein with preference for DNA ends (42). As control, incubation of Csn2 with the relaxed plasmid in the absence of linear DNA confirmed that Csn2 does not bind to circular DNA (Supplementary Figure S3).

At higher Csn2 concentration, highly condensed nucleoprotein complexes were observed, likely caused by clustering of multiple Csn2 proteins and DNA-dependent self-association of DNA-bound Csn2 (Figure 3G and H). The formation of these higher-order nucleoprotein complexes should not be caused by an unspecific aggregation of the protein, as previous study has shown that Csn2 exists as stable tetramer in solution (30). To further evaluate the DNA end-dependence and to exclude an unspecific aggregation of Csn2 in the presence of DNA, we analyzed the elution profile of Csn2 in the presence of linear or closed circular plasmid DNA by size exclusion chromatography (Figure 4). Incubation of Csn2 with the linear DNA caused a co-elution of the entire Csn2 tetramers in the void fraction (Figure 4C). In contrast, the same DNA in supercoiled form did not change the elution profile of the tetrameric Csn2 (Figure 4D). The results are consistent with a selective binding of the Csn2 tetramers to the linear dsDNA and exclude an unspecific protein aggregation in the presence of DNA.

MD simulations reveal Ca^{2+}-dependent coupled translocation-rotation motions of Csn2 and kinking of the DNA

To further study Csn2 binding to DNA and the sliding activity of the tetramers, we performed two independent all-atom MD simulations of 100 ns length each of the tetrameric Csn2 with dsDNA of 36 bp length bound within the central hole. The sequence of the dsDNA corresponds to the CRISPR repeat sequence of the type II-A CRISPR system of *S. agalactiae*. Although we do not have an indication for a sequence-specific binding of Csn2, a bioinformatics analysis revealed a correlation between the presence of the *csn2* gene and a particular CRISPR repeat sequence (43).

The simulations reveal sliding motions of Csn2 along the DNA of a magnitude of >10 Å (Figure 5A), which is equivalent to about one-third of the B-DNA pitch. The motion pattern shows both inward and outward movements accompanied by repeated changes in the direction of motion, as expected for a process driven by thermal energy. Yet, during the last 70 ns of the simulations, the Csn2 molecules prefer to be more closely located to the center of the DNA: although distances up to 12 Å away from the center are observed during the simulations (Figure 5A), the combined likelihood from both trajectories of Csn2 being within 6 Å of the center is 66%. Thus, with the present length of the simulations, no preference for Csn2 to move toward one of the DNA ends could be detected.

The sliding motions of Csn2 are weakly ($r^2 = 0.21$) but significantly ($P < 0.001$) correlated to a rotation of the protein around the DNA (Figure 5B, D), as found for both independent MD simulations (data for the second simulation is shown in Supplementary Figure S4). The slope of the correlation line is ~13°/Å, which is only slightly larger than the turn angle per 1 Å rise of ~11° for B-DNA (44). The N-termini of helices H3 are likely responsible for this screw motion as the two helices within one dimer of Csn2, first, are almost perfectly collinearly oriented, second, are tilted by ~30° with respect to the axis of the dsDNA binding within the central hole and, third, possess a Lys (K78) at the N-terminus (Figure 5D). Taken together, this allows the pair of helices H3 of one dimer of Csn2 to fit with their N-termini in between the phosphate backbones of the major groove, while the helix pair of the other dimer is closer to the phosphate backbone of the minor groove. Therefore, on sliding, Csn2 must rotate around the dsDNA for helices H3 need to follow the course of the phosphate backbones, ultimately leading to a screw motion.

To probe the effect of removing Ca^{2+}-ions on Csn2 binding to the DNA, the above MD simulations were repeated without Ca^{2+}. No gross structural distortions of the tetrameric state of Csn2 were observed (Supplementary Figure S5), in agreement with the observed high stability of Csn2 even in the presence of EGTA (30). No release of Csn2 from the DNA was observed either, which is not surprising given the limited size of the water box enclosing the Csn2–DNA complex in the simulation that prevents a slipping down of Csn2. However, in contrast to the simulations with Ca^{2+}, no correlation between a sliding motion of Csn2 and its rotation could be detected in either one of the simulations ($r^2 < 0.07$). Thus, the absence of Ca^{2+} apparently disturbs the screw motion of Csn2, pointing to weakened interactions between Csn2 and DNA.

Both MD simulations furthermore reveal weak ($r^2 = 0.31$) or very weak ($r^2 = 0.06$) but significant ($P < 0.001$) correlations between the translocation of Csn2 from the DNA center and DNA bending in that a large kink angle in the DNA is preferentially observed if Csn2 moves toward a DNA end (Figure 5C and E). The DNA bending is fostered by the insertion of the N-terminus of at least one helix H3 of one of the Csn2 dimers into the major groove, and interactions between the phosphate backbones of the minor groove at two positions with Lys-rich loops between β4 and H2 of the other dimer, respectively (Figure 5E). As no correlation could be detected when plotting the kink angle against the distance of Csn2 from one end of the DNA, no indication was found either that the bending occurs preferentially at one end (and thus at a specific sequence) of the DNA.

DISCUSSION

In this study, we have characterized the DNA end-binding activity of the Cas protein Csn2 and investigated the structure of the Csn2–DNA complexes by atomic force microscopic imaging and MD simulations. Our results assign Csn2 as a new member of the class of multimeric toroidal proteins involved in DNA end-metabolism and indicate a pivotal role of Csn2 as an accessory protein

6354 Nucleic Acids Research, 2013, Vol. 41, No. 12

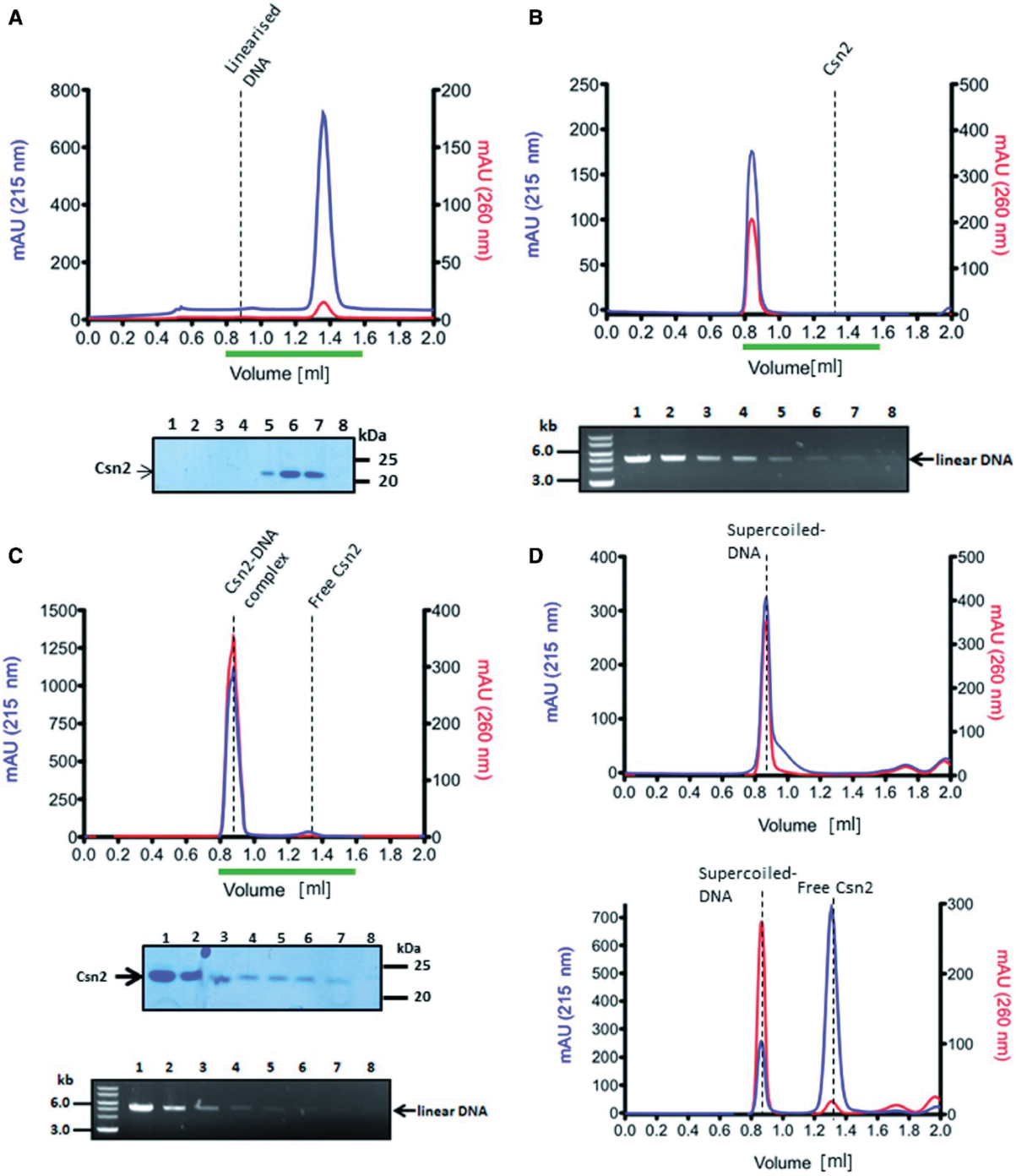

Figure 4. Analytical gel filtration analysis of Csn2 and Csn2-DNA complexes performed with a Superdex 200 PC 3.2/30 column is shown. Elution profiles of 20 µM Csn2 (**A**), 30 nM linearized pCR001 plasmid (**B**) and Csn2-DNA complexes (**C**) are shown. In (**D**) the elution profiles of 30 nM supercoiled pCR001 alone (upper part) or in the presence of 20 µM Csn2 (lower part) are shown. 100 µl fractions were collected starting at an elution volume of 0.8 ml. Aliquots of the fractions 1 to 8, indicated by the green lines below the elution profiles, were analyzed on 10% SDS gels (A, C) and on 1% agarose gels (B, C).

Nucleic Acids Research, 2013, Vol. 41, No. 12 **6355**

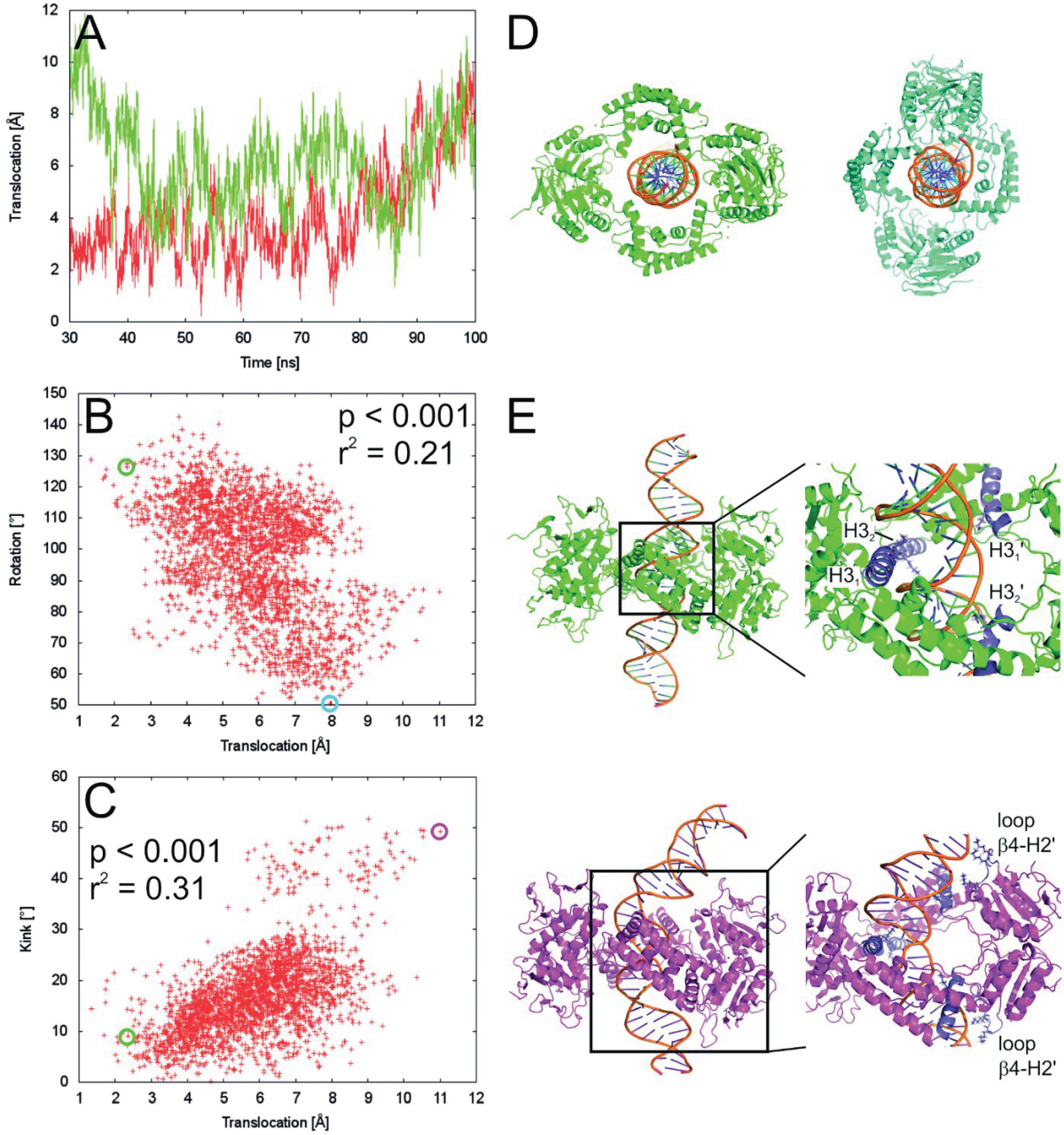

Figure 5. (**A**) Movement of Csn2 along the DNA determined from two independent MD simulations (red and green lines, respectively) over a time course of 70 ns. A translocation value of zero refers to Csn2 being centered on the DNA; translocation values >0 indicate a shift of Csn2 toward the termini of the DNA. (**B**) Coupled motions of translocation and rotation of Csn2 when moving along the DNA over the last 50 ns of the MD simulation. To determine the rotational motion, all conformations of the trajectories were aligned with respect to the phosphorous atoms of the DNA. (**C**) Coupling between DNA bending as determined by a kink angle and the translocation of Csn2 along the DNA over the last 50 ns of the MD simulation. (**D**) View along the DNA axis on Csn2-DNA conformations extracted from the MD trajectory at 50.3 ns (green) and 97.3 ns (cyan). The complexes were aligned with respect to the phosphorous atoms of the DNA and display a rotation of ~75° of Csn2 during a translocation of ~5.7 Å. In panel B, the respective data points are marked by circles. (**E**) Side view on Csn2-DNA complexes extracted from the MD trajectory at 50.3 ns (green) and 98.5 ns (magenta). The complexes display a kinking of the DNA by ~40° during a translocation of Csn2 of ~8.7 Å. In the close-up figures, helices H3 and loops β4-H2 are colored in blue, and Lys residues in these structural elements are depicted as sticks; unprimed labels mark helices and loops that belong to one dimer, primed labels mark objects that belong to the other dimer. In panel C, the respective data points are marked by circles.

6356 Nucleic Acids Research, 2013, Vol. 41, No. 12

during the integration of spacer sequences into the CRISPR array.

Csn2 tetramers bind at dsDNA ends and slide inward along the DNA

The toroidal structure of the DNA-binding protein Csn2 in different studies led to the suggestion that it binds to DNA through its positively charged central hole and encloses the DNA, although alternative binding mechanisms were also considered (29–31). Furthermore, the crystal structure of the Cas protein Stu0660 of the *S. thermophilus* has revealed the presence of a second group of the Csn2 protein family (Stu0660-like Csn2), the members of which share no sequence similarity but have a highly similar tetrameric structure (32). In contrast to the canonical Csn2 proteins, the Csn2-like Stu0660 protein has an extended C-terminal domain and binds to dsDNA without the need of Ca^{2+}-ions. Moreover, due to the lack of a mobility shift with a circular DNA, the authors suggested that Stu0660 'does not or barely' binds to circular DNA but selectively to linear dsDNA (32). Our study is consistent with this suggestion and clearly demonstrates that the Csn2 tetramer binds DNA through its positively charged central hole from the DNA ends and then slides inward along the DNA.

The sliding activity of Csn2 tetramers is not energy-dependent and thus likely not a directed translocation but rather a thermal energy-driven random walk fostered by electrostatic interactions between positively charged amino acids of Csn2 and the negatively charged phosphate backbone of the DNA. MD simulations revealed a rotation of Csn2 when moving along the helical axis of the DNA, similar to a rotation-coupled sliding of the sliding clamp PCNA (45), endonuclease EcoRV (46) or human oxoguanine DNA glycosylase 1 (47). One-dimensional diffusion of DNA-binding proteins is considered to facilitate finding of the specific binding sites (48). Although we have no evidence for a sequence-specific interaction *in vitro*, the reported correlation of the presence of the *csn2* gene and a particular CRISPR repeat sequence (43) could point to a specific role of Csn2 at the repeat sequence. The MD simulations were performed with the CRISPR repeat sequence, and one of the simulations indicated a bending of the DNA preferentially when Csn2 was located at an end. AFM is in principle suitable to study protein-induced DNA bending (49); however, the predicted Csn2-induced kinking is located at the ends of the DNA, and thus difficult to detect with AFM. Therefore, the structural deformation of the DNA ends on Csn2-binding, as proposed by the MD simulations, needs further experimental validation.

The cooperative binding of Csn2, observed in the EMSA and AFM analyses, indicates that multiple Csn2 tetramers are needed at the DNA ends to form stable Csn2–DNA complexes. We suggest that the binding of the first Csn2 tetramer at one DNA end is stabilized by loading of additional tetramers onto the same DNA end, which could impede a slipping down of the initially bound tetramers from the DNA end. This is consistent with the observation that the dissociation of Csn2–DNA complexes occurs through slipping down of the sliding tetramers at the DNA termini (Figure 2). In addition, at high concentrations, Csn2 tends to cluster along the DNA, leading to highly condensed nucleoprotein complexes. This apparent DNA-dependent self-association of the tetramers could point to a physical contact of the tetramers, contributing to the cooperative DNA end-loading of Csn2, as known for the Ku protein (50). The heterodimeric Ku protein forms a ring-like structure, binds preferentially at DNA ends, encircles the DNA (51), can slide along the DNA and promotes looped DNA structures (52). Moreover, it tends to cluster along the DNA as visualized by AFM (53). The DNA-binding properties of Ku are thus similar to the features of Csn2 observed in this study. The function of Ku *in vivo* is to mediate the formation of DNA end-synapsis and recruitment of recombination proteins to allow the repair of double-strand DNA breaks (54).

DNA end-metabolism and spacer integration

A series of multimeric ring-shaped proteins is known, which meet different functions in DNA metabolism, such as replication, transcription, recombination or DNA repair (40,41). In principle, there are three general ways how the DNA can get encircled by a ring-shaped protein: the quaternary structure can be opened wide enough to bind and enclose the DNA [e.g. RdgC (55)], the ring-shaped structure gets directly assembled around the DNA [e.g. PCNA (56)] or the DNA end has to pass through the central hole of the protein [e.g. Ku protein (51)]. In the latter case, the function of the protein is directly linked to DNA ends. Thus, the results presented here strongly suggest that the biological function of the CRISPR adaptation protein Csn2 is related to free DNA ends, which are likely formed during spacer acquisition.

The study of Yosef *et al.* (27) characterized a minimal requirement for spacer integration in type I-E CRISPR systems, and demonstrated the involvement of leader DNA and the nucleases Cas1 and Cas2 in the immunization process. The uptake of new spacers at the leader proximal end is also observed for other CRISPR subtypes, and together with the universality of Cas1 and Cas2, it seems that the main principle mechanism for spacer acquisition is similar in the different CRISPR subtypes. However, some of the CRISPR-Cas subtypes require in addition to Cas1 and Cas2 the proteins Csn2 or Cas4 for the acquisition of new spacer sequences. The Cas4 protein is proposed to be a subunit of the multiprotein complex Cascis (CRISPR-associated complex for the integration of spacers), mediating the CRISPR-mediated immunization (57). A recent study of the Cas4 protein from *Sulfolobus solfataricus* demonstrated that it contains a 5′–3′ DNA exonuclease activity, implying the requirement of DNA end modification/resection during integration of new spacer sequences into the CRISPR array (58). Moreover, the crystal structure of the Cas4 protein from *S. solfataricus* has been deposited in PDB database, showing that the Cas4 protein forms, like Csn2, a ring-shaped structure (PDB ID: 4IC1). Thus, the structural

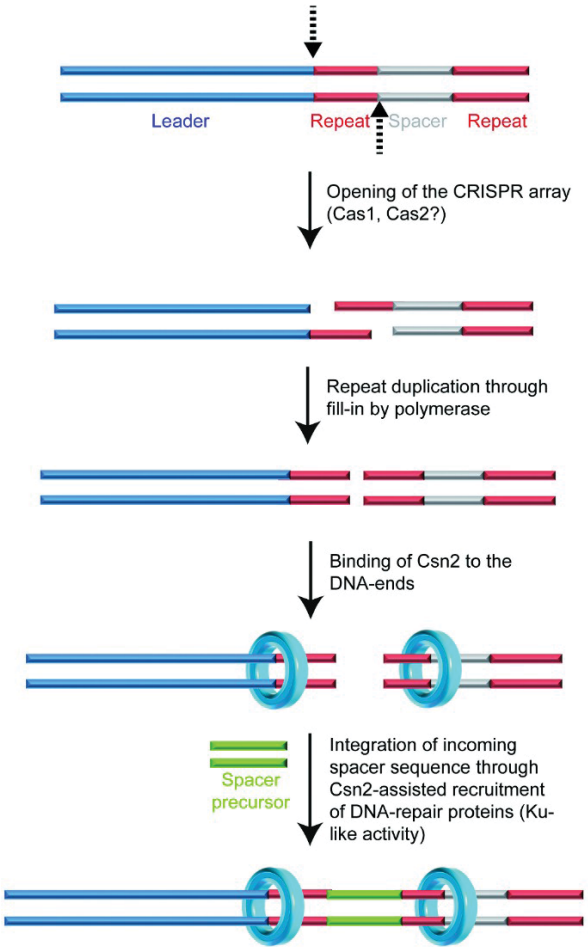

Figure 6. A model for the proposed function of Csn2 DNA end-binding in spacer integration is shown. The leader proximal repeat sequence serves as template for duplication of the repeat sequence (25,26,64), suggesting a cleavage at the leader-repeat and repeat-spacer borders (indicated by the dashed arrows). Complementary strand synthesis and binding of Csn2 to the DNA ends could assist in the integration of new spacer DNA fragments through holding the DNA ends together, while simultaneously recruiting DNA-repair proteins and protecting the double-stranded DNA breaks from exonucleolytic degradation.

similarity of Cas4 to AddB, its RecB-like exonuclease activity (58) and the DNA end-binding of Csn2 presented in this study are in agreement with DNA end-processing steps during the spacer integration. Another indication for the participation of DNA end-processing proteins in the adaptation stage is the genetic association of *nurA* and *herA* genes with type III-A CRISPR operons in Thermoproteales (59), encoding for an exonuclease–helicase complex involved in DNA end-resection (60).

The lack of enzymatic activity of Csn2 suggests that Cas4 and Csn2 are likely not functional homologs. However, the conserved co-localization within the type II systems and the DNA end-related activities of both proteins indicate that they are involved in DNA end-resection processes during integration of spacers. The reported protein–protein interaction of Cas1 with RecB in *E. coli* (61) and the AddB-like structure and activity of the Cas4 protein (58) could support an involvement of DNA repair systems during the uptake of CRISPR spacer sequences. The study of Chayot *et al.* (62) has demonstrated that the insertion of non-related exogenous sequences in *E. coli* depends on the RecBCD complex. The role of RecBCD is to process the DNA ends exonucleolytically on the 3′-end to produce microhomology with the incoming DNA, a mechanism termed alternative end-joining (A-EJ) (62). A similar mechanism could be catalyzed by Cas4 in type II-B or AddAB proteins in type II-A systems lacking Cas4.

The DNA end-binding activity of Csn2 suggests that it has a function as accessory protein on DNA ends. Csn2 could fulfill a task analogous to Ku during acquisition of exogenous DNA by non-homologous end-joining, by binding to the double-strand breaks to hold the ends together and/or by recruiting recombination proteins (63) (Figure 6). Alternatively, the DNA end binding activity of Csn2 could be related to the nuclease activity of Cas9, introducing specific double-strand DNA breaks into the target DNA (12,17). It is possible that after recognition and cleavage of the foreign DNA by Cas9-tracrRNA:crRNA ribonuleoprotein complex, Csn2 proteins are loaded at the DNA ends, e.g. to mark the foreign DNA as a substrate for new spacer sequences and/or to recruit the nucleases for specific generation of new spacer precursors. Indeed, such a coupling of the CRISPR interference with the immunization stage has been described to occur in the type I-E systems, known as 'primed acquisition' of spacer sequences (25). Although our analyses do not directly address the mechanisms of CRISPR spacer integration, the DNA end-binding of the adaptation protein Csn2 and the structure of the Csn2–DNA complexes resemble known recombination proteins acting on DNA end-metabolism. Therefore, we propose that the integration of new spacer DNA may occur by a recombination mechanism similar to non-homologous end-joining.

SUPPLEMENTARY DATA

Supplementary Data are available at NAR Online: Supplementary Figures 1–5.

ACKNOWLEDGEMENTS

We thank Britta Ries and Andre Abts for assistance during the experiments. S.S. acknowledges the continuing support from the Heinrich Heine University. H.G. is grateful to the 'Zentrum für Informations- und Medientechnologie' (ZIM) at the Heinrich Heine University for computational support. We gratefully thank the members of the DFG Research unit FOR 1680 for helpful discussions.

FUNDING

Deutsche Forschungsgemeinschaft (DFG) [PU 435/1-1]; Strategischer Forschungsfonds at the Heinrich Heine University (to Ü.P.); initiative 'Fit for Excellence' at the Heinrich Heine University (to H.G.). Funding for open access charge: Institutional funds and Strategischer Forschungsfonds of the Heinrich Heine University.

Conflict of interest statement. None declared.

REFERENCES

1. Bhaya,D., Davison,M. and Barrangou,R. (2011) CRISPR-Cas systems in bacteria and archaea: versatile small RNAs for adaptive defense and regulation. *Annu. Rev. Genet.*, **45**, 273–297.
2. Al-Attar,S., Westra,E.R., van der Oost,J. and Brouns,S.J. (2011) Clustered regularly interspaced short palindromic repeats (CRISPRs): the hallmark of an ingenious antiviral defense mechanism in prokaryotes. *Biol. Chem.*, **392**, 277–289.
3. Wiedenheft,B., Sternberg,S.H. and Doudna,J.A. (2012) RNA-guided genetic silencing systems in bacteria and archaea. *Nature*, **482**, 331–338.
4. Makarova,K.S., Haft,D.H., Barrangou,R., Brouns,S.J., Charpentier,E., Horvath,P., Moineau,S., Mojica,F.J., Wolf,Y.I., Yakunin,A.F. *et al.* (2011) Evolution and classification of the CRISPR-Cas systems. *Nat. Rev. Microbiol.*, **9**, 467–477.
5. Makarova,K.S., Grishin,N.V., Shabalina,S.A., Wolf,Y.I. and Koonin,E.V. (2006) A putative RNA-interference-based immune system in prokaryotes: computational analysis of the predicted enzymatic machinery, functional analogies with eukaryotic RNAi, and hypothetical mechanisms of action. *Biol. Direct.*, **1**, 7.
6. van der Oost,J., Jore,M.M., Westra,E.R., Lundgren,M. and Brouns,S.J. (2009) CRISPR-based adaptive and heritable immunity in prokaryotes. *Trends Biochem. Sci.*, **34**, 401–407.
7. Barrangou,R., Fremaux,C., Deveau,H., Richards,M., Boyaval,P., Moineau,S., Romero,D.A. and Horvath,P. (2007) CRISPR provides acquired resistance against viruses in prokaryotes. *Science*, **315**, 1709–1712.
8. Brouns,S.J., Jore,M.M., Lundgren,M., Westra,E.R., Slijkhuis,R.J., Snijders,A.P., Dickman,M.J., Makarova,K.S., Koonin,E.V. and van der Oost,J. (2008) Small CRISPR RNAs guide antiviral defense in prokaryotes. *Science*, **321**, 960–964.
9. Westra,E.R., van Erp,P.B., Kunne,T., Wong,S.P., Staals,R.H., Seegers,C.L., Bollen,S., Jore,M.M., Semenova,E., Severinov,K. *et al.* (2012) CRISPR immunity relies on the consecutive binding and degradation of negatively supercoiled invader DNA by Cascade and Cas3. *Mol. Cell*, **46**, 595–605.
10. Sapranauskas,R., Gasiunas,G., Fremaux,C., Barrangou,R., Horvath,P. and Siksnys,V. (2011) The *Streptococcus thermophilus* CRISPR/Cas system provides immunity in *Escherichia coli*. *Nucleic Acids Res.*, **39**, 9275–9282.
11. Deltcheva,E., Chylinski,K., Sharma,C.M., Gonzales,K., Chao,Y., Pirzada,Z.A., Eckert,M.R., Vogel,J. and Charpentier,E. (2011) CRISPR RNA maturation by trans-encoded small RNA and host factor RNase III. *Nature*, **471**, 602–607.
12. Jinek,M., Chylinski,K., Fonfara,I., Hauer,M., Doudna,J.A. and Charpentier,E. (2012) A programmable dual-RNA-guided DNA endonuclease in adaptive bacterial immunity. *Science*, **337**, 816–821.
13. Hale,C.R., Majumdar,S., Elmore,J., Pfister,N., Compton,M., Olson,S., Resch,A.M., Glover,C.V. III, Graveley,B.R., Terns,R.M. *et al.* (2012) Essential features and rational design of CRISPR RNAs that function with the Cas RAMP module complex to cleave RNAs. *Mol. Cell*, **45**, 292–302.
14. Hale,C.R., Zhao,P., Olson,S., Duff,M.O., Graveley,B.R., Wells,L., Terns,R.M. and Terns,M.P. (2009) RNA-guided RNA cleavage by a CRISPR RNA-Cas protein complex. *Cell*, **139**, 945–956.
15. Jore,M.M., Lundgren,M., van Duijn,E., Bultema,J.B., Westra,E.R., Waghmare,S.P., Wiedenheft,B., Pul,U., Wurm,R., Wagner,R. *et al.* (2011) Structural basis for CRISPR RNA-guided DNA recognition by Cascade. *Nat. Struct. Mol. Biol.*, **18**, 529–536.
16. Haft,D.H., Selengut,J., Mongodin,E.F. and Nelson,K.E. (2005) A guild of 45 CRISPR-associated (Cas) protein families and multiple CRISPR/Cas subtypes exist in prokaryotic genomes. *PLoS Comput. Biol.*, **1**, e60.
17. Gasiunas,G., Barrangou,R., Horvath,P. and Siksnys,V. (2012) Cas9-crRNA ribonucleoprotein complex mediates specific DNA cleavage for adaptive immunity in bacteria. *Proc. Natl Acad. Sci. USA*, **109**, E2579–E2586.
18. Jinek,M., East,A., Cheng,A., Lin,S., Ma,E. and Doudna,J. (2013) RNA-programmed genome editing in human cells. *Elife*, **2**, e00471.
19. Cho,S.W., Kim,S., Kim,J.M. and Kim,J.S. (2013) Targeted genome engineering in human cells with the Cas9 RNA-guided endonuclease. *Nat. Biotechnol.*, **31**, 230–232.
20. Jiang,W., Bikard,D., Cox,D., Zhang,F. and Marraffini,L.A. (2013) RNA-guided editing of bacterial genomes using CRISPR-Cas systems. *Nat. Biotechnol.*, **31**, 233–239.
21. Hwang,W.Y., Fu,Y., Reyon,D., Maeder,M.L., Tsai,S.Q., Sander,J.D., Peterson,R.T., Yeh,J.R. and Joung,J.K. (2013) Efficient genome editing in zebrafish using a CRISPR-Cas system *Nat. Biotechnol.*, **31**, 227–229.
22. Mali,P., Yang,L., Esvelt,K.M., Aach,J., Guell,M., DiCarlo,J.E., Norville,J.E. and Church,G.M. (2013) RNA-guided human genome engineering via Cas9. *Science*, **339**, 823–826.
23. Cong,L., Ran,F.A., Cox,D., Lin,S., Barretto,R., Habib,N., Hsu,P.D., Wu,X., Jiang,W., Marraffini,L.A. *et al.* (2013) Multiplex genome engineering using CRISPR/Cas systems. *Science*, **339**, 819–823.
24. Qi,L.S., Larson,M.H., Gilbert,L.A., Doudna,J.A., Weissman,J.S., Arkin,A.P. and Lim,W.A. (2013) Repurposing CRISPR as an RNA-guided platform for sequence-specific control of gene expression. *Cell*, **152**, 1173–1183.
25. Datsenko,K.A., Pougach,K., Tikhonov,A., Wanner,B.L., Severinov,K. and Semenova,E. (2012) Molecular memory of prior infections activates the CRISPR/Cas adaptive bacterial immunity system. *Nat. Commun.*, **3**, 945.
26. Swarts,D.C., Mosterd,C., van Passel,M.W. and Brouns,S.J. (2012) CRISPR interference directs strand specific spacer acquisition. *PLoS One*, **7**, e35888.
27. Yosef,I., Goren,M.G. and Qimron,U. (2012) Proteins and DNA elements essential for the CRISPR adaptation process in *Escherichia coli*. *Nucleic Acids Res.*, **40**, 5569–5576.
28. Deveau,H., Barrangou,R., Garneau,J.E., Labonte,J., Fremaux,C., Boyaval,P., Romero,D.A., Horvath,P. and Moineau,S. (2008) Phage response to CRISPR-encoded resistance in *Streptococcus thermophilus*. *J. Bacteriol.*, **190**, 1390–1400.
29. Nam,K.H., Kurinov,I. and Ke,A. (2011) Crystal structure of clustered regularly interspaced short palindromic repeats (CRISPR)-associated Csn2 protein revealed Ca2+-dependent double-stranded DNA binding activity. *J. Biol. Chem.*, **286**, 30759–30768.
30. Ellinger,P., Arslan,Z., Wurm,R., Tschapek,B., MacKenzie,C., Pfeffer,K., Panjikar,S., Wagner,R., Schmitt,L., Gohlke,H. *et al.* (2012) The crystal structure of the CRISPR-associated protein Csn2 from *Streptococcus agalactiae*. *J. Struct. Biol.*, **178**, 350–362.
31. Koo,Y., Jung,D.K. and Bae,E. (2012) Crystal structure of *Streptococcus pyogenes* Csn2 reveals calcium-dependent conformational changes in its tertiary and quaternary structure. *PLoS One*, **7**, e33401.
32. Lee,K.H., Lee,S.G., Eun Lee,K., Jeon,H., Robinson,H. and Oh,B.H. (2012) Identification, structural, and biochemical characterization of a group of large Csn2 proteins involved in CRISPR-mediated bacterial immunity. *Proteins*, **80**, 2573–2582.
33. Pul,U., Wurm,R. and Wagner,R. (2007) The role of LRP and H-NS in transcription regulation: involvement of synergism, allostery and macromolecular crowding. *J. Mol. Biol.*, **366**, 900–915.
34. Case,D.A., Cheatham,T.E. III, Darden,T., Gohlke,H., Luo,R., Merz,K.M. Jr, Onufriev,A., Simmerling,C., Wang,B. and Woods,R.J. (2005) The Amber biomolecular simulation programs. *J. Comput. Chem.*, **26**, 1668–1688.

35. Cornell,W.D., Cieplak,C.I., Bayly,I.R., Gould,I.R., Merz,K.M., Ferguson,D.M., Spellmeyer,D.C., Fox,T., Caldwell,J.W. and Kollman,P.A. (1995) A second generation force field for the simulation of proteins, nucleic acids, and organic molecules. *J. Am. Chem. Soc.*, **117**, 5179–5197.
36. Simmerling,C., Strockbine,B. and Roitberg,A.E. (2002) All-atom structure prediction and folding simulations of a stable protein. *J. Am. Chem. Soc.*, **124**, 11258–11259.
37. Jorgensen,W.L., Chandrasekhar,J., Madura,J. and Klein,M.L. (1983) Comparison of simple potential functions for simulating liquid water. *J. Chem. Phys.*, **79**, 926–935.
38. Darden,T., York,D. and Pederson,L. (1993) Particle Mesh Ewald—a Nlog(N) method for Ewald sums in large systems. *J. Chem. Phys.*, **98**, 10089–10092.
39. Ryckaert,J.P., Ciccotti,G. and Berendsen,H.J.C. (1977) Numerical-Integration of Cartesian Equations of Motion of a System with Constraints: Molecular Dynamics of n-Alkanes. *J. Comput. Phys.*, **23**, 327–341.
40. Hingorani,M.M. and O'Donnell,M. (1998) Toroidal proteins: running rings around DNA. *Curr. Biol.*, **8**, R83–R86.
41. Hingorani,M.M. and O'Donnell,M. (2000) A tale of toroids in DNA metabolism. *Nat. Rev. Mol. Cell. Biol.*, **1**, 22–30.
42. Tessmer,I., Moore,T., Lloyd,R.G., Wilson,A., Erie,D.A., Allen,S. and Tendler,S.J. (2005) AFM studies on the role of the protein RdgC in bacterial DNA recombination. *J. Mol. Biol.*, **350**, 254–262.
43. Kunin,V., Sorek,R. and Hugenholtz,P. (2007) Evolutionary conservation of sequence and secondary structures in CRISPR repeats. *Genome Biol.*, **8**, R61.
44. Saenger,W. (1984) *Principles of Nucleic Acid Structure*. Springer-Verlag, New York.
45. Kochaniak,A.B., Habuchi,S., Loparo,J.J., Chang,D.J., Cimprich,K.A., Walter,J.C. and van Oijen,A.M. (2009) Proliferating cell nuclear antigen uses two distinct modes to move along DNA. *J. Biol. Chem.*, **284**, 17700–17710.
46. Dikic,J., Menges,C., Clarke,S., Kokkinidis,M., Pingoud,A., Wende,W. and Desbiolles,P. (2012) The rotation-coupled sliding of EcoRV. *Nucleic Acids Res.*, **40**, 4064–4070.
47. Blainey,P.C., Luo,G., Kou,S.C., Mangel,W.F., Verdine,G.L., Bagchi,B. and Xie,X.S. (2009) Nonspecifically bound proteins spin while diffusing along DNA. *Nat. Struct. Mol. Biol.*, **16**, 1224–1229.
48. von Hippel,P.H. and Berg,O.G. (1989) Facilitated target location in biological systems. *J. Biol. Chem.*, **264**, 675–678.
49. Dame,R.T., van Mameren,J., Luijsterburg,M.S., Mysiak,M.E., Janicijevic,A., Pazdzior,G., van der Vliet,P.C., Wyman,C. and Wuite,G.J. (2005) Analysis of scanning force microscopy images of protein-induced DNA bending using simulations. *Nucleic Acids Res.*, **33**, e68.
50. Ma,Y. and Lieber,M.R. (2001) DNA length-dependent cooperative interactions in the binding of Ku to DNA. *Biochemistry*, **40**, 9638–9646.
51. Walker,J.R., Corpina,R.A. and Goldberg,J. (2001) Structure of the Ku heterodimer bound to DNA and its implications for double-strand break repair. *Nature*, **412**, 607–614.
52. Dynan,W.S. and Yoo,S. (1998) Interaction of Ku protein and DNA-dependent protein kinase catalytic subunit with nucleic acids. *Nucleic Acids Res.*, **26**, 1551–1559.
53. Cary,R.B., Peterson,S.R., Wang,J., Bear,D.G., Bradbury,E.M. and Chen,D.J. (1997) DNA looping by Ku and the DNA-dependent protein kinase. *Proc. Natl Acad. Sci. USA*, **94**, 4267–4272.
54. Feldmann,E., Schmiemann,V., Goedecke,W., Reichenberger,S. and Pfeiffer,P. (2000) DNA double-strand break repair in cell-free extracts from Ku80-deficient cells: implications for Ku serving as an alignment factor in non-homologous DNA end joining. *Nucleic Acids Res.*, **28**, 2585–2596.
55. Briggs,G.S., Yu,J., Mahdi,A.A. and Lloyd,R.G. (2010) The RdgC protein employs a novel mechanism involving a finger domain to bind to circular DNA. *Nucleic Acids Res.*, **38**, 6433–6446.
56. Kong,X.P., Onrust,R., O'Donnell,M. and Kuriyan,J. (1992) Three-dimensional structure of the beta subunit of E. *coli* DNA polymerase III holoenzyme: a sliding DNA clamp. *Cell*, **69**, 425–437.
57. Plagens,A., Tjaden,B., Hagemann,A., Randau,L. and Hensel,R. (2012) Characterization of the CRISPR/Cas subtype I-A system of the hyperthermophilic crenarchaeon *Thermoproteus tenax*. *J. Bacteriol.*, **194**, 2491–2500.
58. Zhang,J., Kasciukovic,T. and White,M.F. (2012) The CRISPR associated protein cas4 Is a 5′ to 3′ DNA exonuclease with an iron-sulfur cluster. *PLoS One*, **7**, e47232.
59. Bernick,D.L., Cox,C.L., Dennis,P.P. and Lowe,T.M. (2012) Comparative genomic and transcriptional analyses of CRISPR systems across the genus Pyrobaculum. *Front. Microbiol.*, **3**, 251.
60. Blackwood,J.K., Rzechorzek,N.J., Abrams,A.S., Maman,J.D., Pellegrini,L. and Robinson,N.P. (2012) Structural and functional insights into DNA-end processing by the archaeal HerA helicase-NurA nuclease complex. *Nucleic Acids Res.*, **40**, 3183–3196.
61. Babu,M., Beloglazova,N., Flick,R., Graham,C., Skarina,T., Nocek,B., Gagarinova,A., Pogoutse,O., Brown,G., Binkowski,A. *et al.* (2011) A dual function of the CRISPR-Cas system in bacterial antivirus immunity and DNA repair. *Mol. Microbiol.*, **79**, 484–502.
62. Chayot,R., Montagne,B., Mazel,D. and Ricchetti,M. (2010) An end-joining repair mechanism in *Escherichia coli*. *Proc. Natl Acad. Sci. USA*, **107**, 2141–2146.
63. Doherty,A.J. and Jackson,S.P. (2001) DNA repair: how Ku makes ends meet. *Curr. Biol.*, **11**, R920–R924.
64. Goren,M.G., Yosef,I., Auster,O. and Qimron,U. (2012) Experimental definition of a clustered regularly interspaced short palindromic duplicon in *Escherichia coli*. *J. Mol. Biol.*, **423**, 14–16.

SUPPLEMENTARY DATA

Double-strand DNA end binding and sliding of the toroidal CRISPR-associated protein Csn2

Zihni Arslan[1], Reinhild Wurm[1], Oleksandr Brener[1,2], Philipp Ellinger[3], Luitgard Nagel-Steger[1,2], Filipp Oesterhelt[1], Lutz Schmitt[3], Dieter Willbold[1,2], Rolf Wagner[1], Holger Gohlke[4], Sander H.J. Smits[3] and Ümit Pul[1,*]

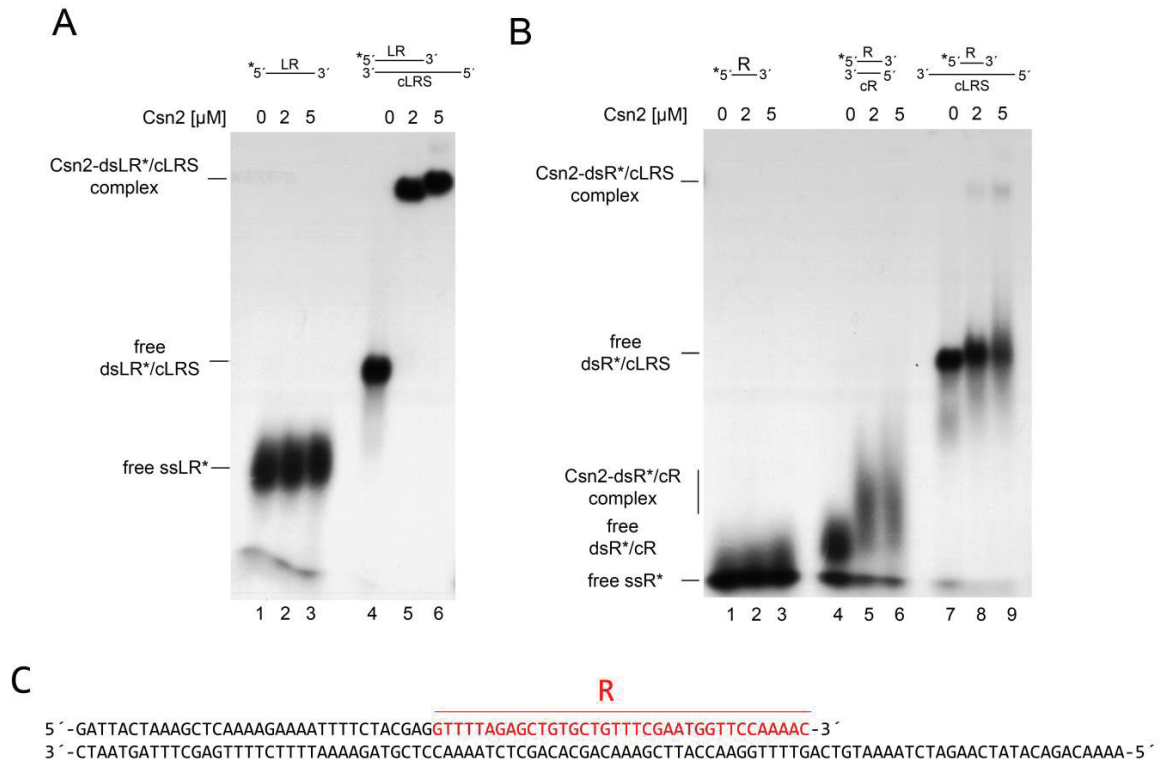

Figure S1: Csn2 binds to dsDNA with single-stranded DNA tails

Electrophoretic mobility shift assays of Csn2 with ssDNA or dsDNA are shown. (A) 5´-labeled ssLR oligonucleotide (70 nt in length) was incubated with 0 (lane 1), 2 µM (lane 2) or 5 µM (lane 3) Csn2. No complexes are formed with ssLR DNA. The ssLR oligonucleotide was hybridized with 100 nt complementary oligonucleotide cLRS to generate dsDNA with 5´-overhang. The dsLR/cLRS DNA was incubated with 0 (lane 4), 2 µM (lane 5) or 5 µM (lane 6) Csn2. Unbound DNA and Csn2-DNA complexes are indicated on the left. Asterisks indicate the labeled DNA strand. (B) Similar analyses as shown in (A) with either ssR* oligonucleotide (36 nt), dsR*/cR DNA or dsR*/cLRS (3´ and 5´ overhangs) are presented. (C) The upper strand corresponds to the sequence of the ssLR oligonucleotide. The sequence of the ssR oligonucleotide is colored in red. The lower strand corresponds to the sequence of the cLRS oligonucleotide.

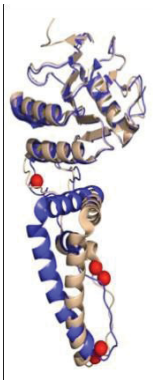

Figure S2: Superposition of the two Csn2 monomers (PDB ID: 3QHQ) (30)
Superposition of two Csn2 protomers is shown. The lack of Ca^{2+} at the linker domain of one protomer leads to conformational change of the α-helices in the leg domain (30).

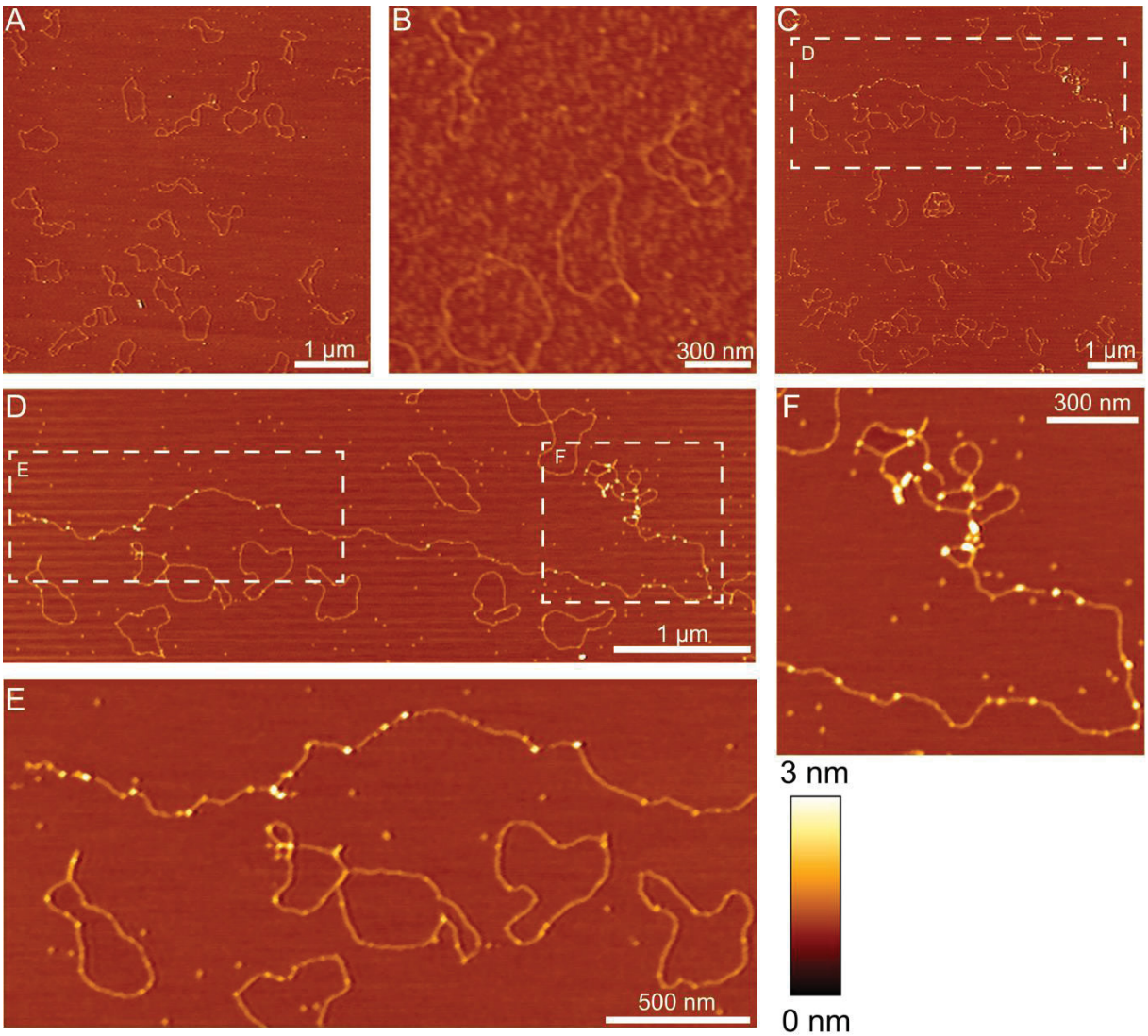

Figure S3: Csn2 does not bind to closed circular DNA.

AFM images of circular plasmid DNA incubated with Csn2 are presented. 2.6 nM of 5125 bp relaxed plasmid DNA was incubated with 176 nM Csn2. No accumulation of Csn2 on the closed circular plasmid was observed (A-E). Several Csn2 proteins are associated with a long linear DNA fragment (roughly more than 8 µm in length, corresponding to 24 kbp), likely a co-purified chromosomal DNA fragment (C-F). The DNA end segments of this linear DNA were occupied by Csn2 (D-F). The relative color scale range is 0 to 3 nm in all images.

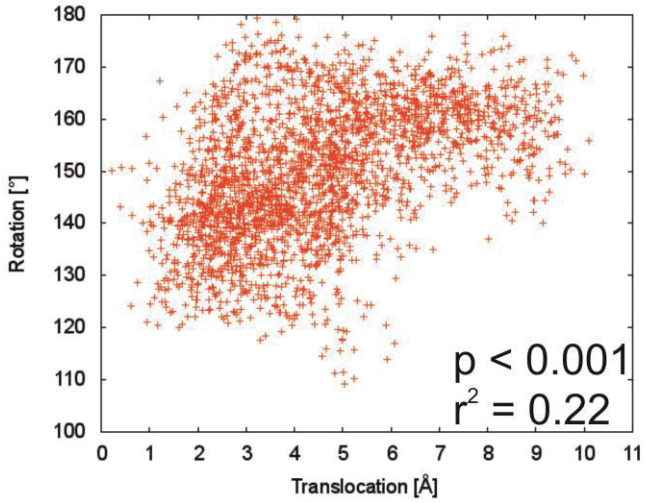

Figure S4: Coupled motions of translocation and rotation of Csn2 when moving along the DNA over the last 50 ns of the second MD simulation.
To determine the rotational motion, all conformations of the trajectories were aligned with respect to the phosphorous atoms of the DNA. Note that, while the magnitude of the slope of the correlation line (~9°/Å) is similar to the one determined for the first simulation (Figure 6B), its sign is opposite. This is because the translocation is symmetric with respect to the DNA center, and Csn2 moves in opposite directions in both simulations.

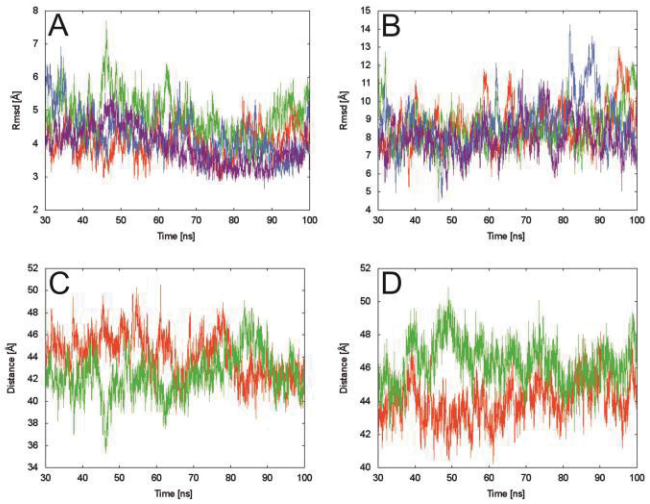

Figure S5: Root mean-square deviations and pore movements during molecular dynamics simulations of Csn2-DNA complexes

(A) Rmsd of Cα atoms of Csn2 with respect to the crystal structure after aligning the protein with respect to the Cα atoms. Red and green lines: two independent simulations of Csn2-DNA complexes with Ca^{2+} ions; magenta and blue lines: two independent simulations of Csn2-DNA complexes without Ca^{2+} ions. (B) Rmsd of phosphorous atoms of DNA with respect to an ideal B-DNA after aligning the DNA with respect to the phosphorous atoms. See panel A for the color code. (C) Distance between the average coordinates of the Cα atoms of the two 3_{10} helices located in the head domains of Csn2 on one side of the tetramer. See panel A for the color code. (D) Distance between the average coordinates of the Cα atoms of the two pairs of H5 helices; each pair of helices is located in one of the legs of the tetrameric structure. See panel A for the color code.

2.1.9 Publizierte Patente

Mittel zur Behandlung der Alzheimerschen Demenz

Veröffentlichungsnummer: WO2011DE00389 20110409

Auch veröffentlicht unter: DE20101019336 20100505, DE102010019336 (A1)

Veröffentlichungsdatum: 10.11.2011

Erfinder: Susanne Aileen Funke, Luitgard Nagel-Steger, Dirk Bartnik, Oleksandr Brener, Torsten Sehl, Katja Wiesehan, Dieter Willbold.

Zusammenfassung:

Die Erfindung betrifft Mittel zu Behandlung der Alzheimerschen Demenz. Erfindungsgemäß wird ein Peptid nach Sequenz Nr. 1 zur Verfügung gestellt, welches an Aβ-Oligomere anbindet und so zur Heilung oder Linderung der Alzheimerschen Demenz führt.

In weiteren Ausgestaltungen der Erfindungen werden Peptide bereitgestellt, welche eine Sequenz Nr. 1 enthalten jedoch über vor geschaltete Sequenzabschnitte verfügen, die eine Sekretion des Peptids ermöglichen. Zum Zweck der Gentherapie werden entsprechende DANN-Sequenzen und Vektoren insbesondere nach den Sequenzen 3 bis 6 zur Verfügung gestellt.

Hybrid-Verbindung, deren Verwendung und Verfahren zu deren Herstellung

Veröffentlichungsnummer: WO2011147797 A2

Auch veröffentlicht unter: DE102010017130A1, WO2011147797A3

Veröffentlichungsdatum: 01.12.2011

Erfinder: Thomas Schrader, Julia März-Beberich, Andreas Müller-Schiffmann, Carsten Korth, Susanne Aileen Funke, Luitgard Nagel-Steger, Dirk Bartnik, Oleksandr Brener, Dieter Willbold, Anselm Horn, Heinrich Sticht.

Zusammenfassung:

Die Erfindung betrifft eine Hybrid-Verbindung basierend auf Aminopyrazolderivaten und Peptiden zur Verwendung als Therapeutikum bei der Behandlung von Krankheiten, bei denen eine aberrante Proteinaggregation oder -multimerisierung bzw. eine Proteinfehlfaltung eine Rolle spielt. Ferner betrifft die Erfindung ein Verfahren zur Herstellung dieser Verbindungen.

Polymere, enthaltend multivalente Amyloid-beta-bindende D-Peptide und deren Verwendung

Veröffentlichungsnummer: WO2013150127A2

Auch veröffentlicht unter: WO2013150127A3, DE102012102998 (A1)

Veröffentlichungsdatum: 10.11.2013

Erfinder: Dieter Willbold, Susanne Aileen Funke, Oleksandr Brener, Luitgard Nagel-Steger, Dirk Bartnik.

Zusammenfassung:

Gegenstand der Erfindung sind neue multivalente Amyloid-Beta-bindende polymere Substanzen, bestehend aus mehreren miteinander verbundenen Substanzen, die für sich bereits Amyloid-Beta-bindende Eigenschaften haben, sowie die Verwendung dieser im Folgenden „Polymere" genannten Substanzen insbesondere in der Medizin.

Neue, von D3 abgeleitete D-enantiomere Peptide und deren Verwendung

Veröffentlichungsnummer: DE201210108598

Auch veröffentlicht unter: WO2014041115A2

Veröffentlichungsdatum: 10.11.2013

Erfinder: Susanne Aileen Funke, Oleksandr Brener, Dieter Willbold, Dirk Bartnik, Luitgard Nagel-Steger, Antonia Nicole Klein.

Zusammenfassung:

Die vorliegende Erfindung betrifft neue, D-enantiomere A-Beta-Oligomerbindende Peptide, Homologe, Fragmente, Teile und Polymere davon sowie deren Verwendung.

2.2 Nicht publizierte Ergebnisse

In diesem Kapitel werden nicht publizierte Ergebnisse beschrieben, die eine wichtige Rolle für das Design der Wirkstoffe gegen Aβ-Oligomere und die Charakterisierung ihres Einflusses auf die Aβ spielen.

Das mit Spiegelbild-Phagen-Display selektierte D-Peptid D3 (D3-Sequenz: rprtrlhthrnr) diente als Basis für weitere Wirkstoffentwicklung. Der Einfluss dieses Liganden auf unterschiedliche Aβ-Spezies wurde mit Hilfe von einer Dichtegradientenzentrifugation (DGZ) mit anschließender Fraktionierung des Gradienten und Analyse dieser Fraktionen auf Aβ-Gehalt mittels SDS-PAGE untersucht (siehe Kapitel 2.1.1). Wie in der Abbildung 15 zu sehen ist, reduziert D3 in substöchiometrischen Konzentrationen (80 µM Aβ und 20 µM D3) die Menge von Aβ-Oligomeren in Fraktionen 4-6 des Gradienten im Vergleich zu Kontrolle. In äquimolaren Konzentrationen eliminiert D3 diese Oligomere vollständig (siehe Kapitel 2.1.1). In den betroffenen Fraktionen befinden sich Aβ-Aggregate, die einen s-Wert zwischen 5 S und

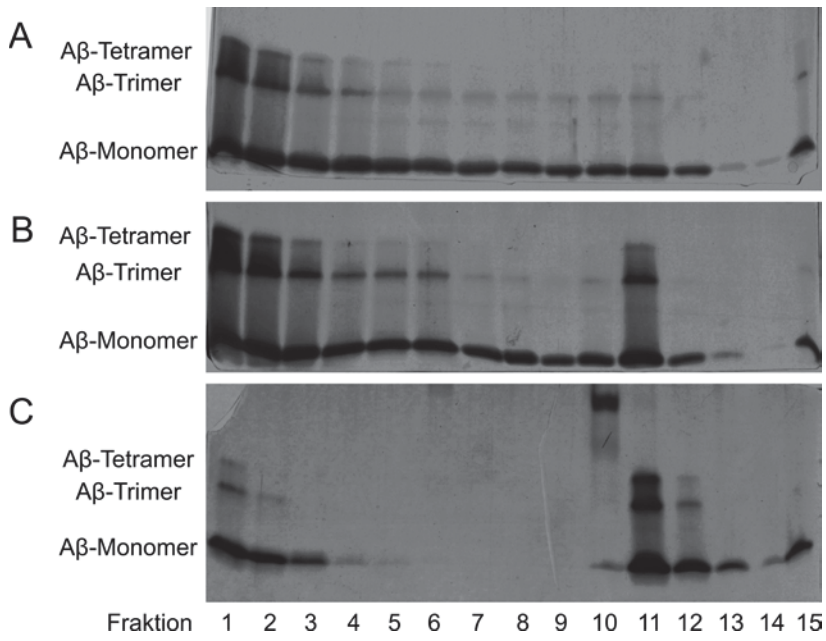

Abbildung 15 – Charakterisierung des Einflusses von D3 und D3D3 auf die Aβ-Aggregatgrößenverteilung mit einem Dichtegradienten

Der Iodixanol-Dichtegradient wurde mit 100 µl einer 80 µM Aβ-Lösung entweder ohne Ligand (A) oder mit einem Zusatz von 20 µM D3 (B), mit 10 µM D3D3 (C) überschichtet und anschließend 3 h lang bei 4 °C mit 259.000 x g zentrifugiert. Nach der Zentrifugation wurde der Gradient von oben nach unten fraktioniert. Die Fraktionen wurden mittels SDS-PAGE mit Silberfärbung analysiert. D3 reduziert Aβ-Oligomere in den Fraktionen 4-6 und komplexiert diese zu hochmolekularen Komplexen in den Fraktionen 11-12 (B). D3D3 eliminiert Aβ-Oligomere in den fraktionen 4-6 vollständig.

7 S sowie ein entsprechendes Molekulargewicht zwischen 66 und 150 kDa haben können (siehe Kapitel 2.1.4). D3 reagiert mit Aβ-Oligomeren in diesem Größenbereich zu hochmlekularen Komplexen, die ein Molekulargewicht von einem Megadalton oder mehr haben. Diese Komplexe sind in den Fraktionen 11 bis 15 des Gradienten zu finden. In diesem Bereich ist die Dichte des Gradienten fast so hoch wie die eines Proteins. Der prozentuelle Anteil des Iodixanols (Dichtegradientenmaterial) beträgt in diesen Fraktionen 28,5 bis 64,5 %. Koppelt man D3 mit einem FITC-Fluoreszenzfarbstoff, kann man seine Verteilung im Gradienten mittels Fluoreszenzdetektion m essen. D3 ohne Aβ verteilt sich aufgrund des kleinen Molekulargewichts bzw. s-Wertes in den oberen Fraktionen 1-4 oder nur geringfügig in den Fraktionen 5-7 (Daten nicht gezeigt). Nach der Reaktion mit Aβ wird D3 auch in den Fraktionen 11-14 detektiert (Abbildung 16). Es kann nur komplexiert mit Aβ so tief in den Dichtegradienten eindringen.

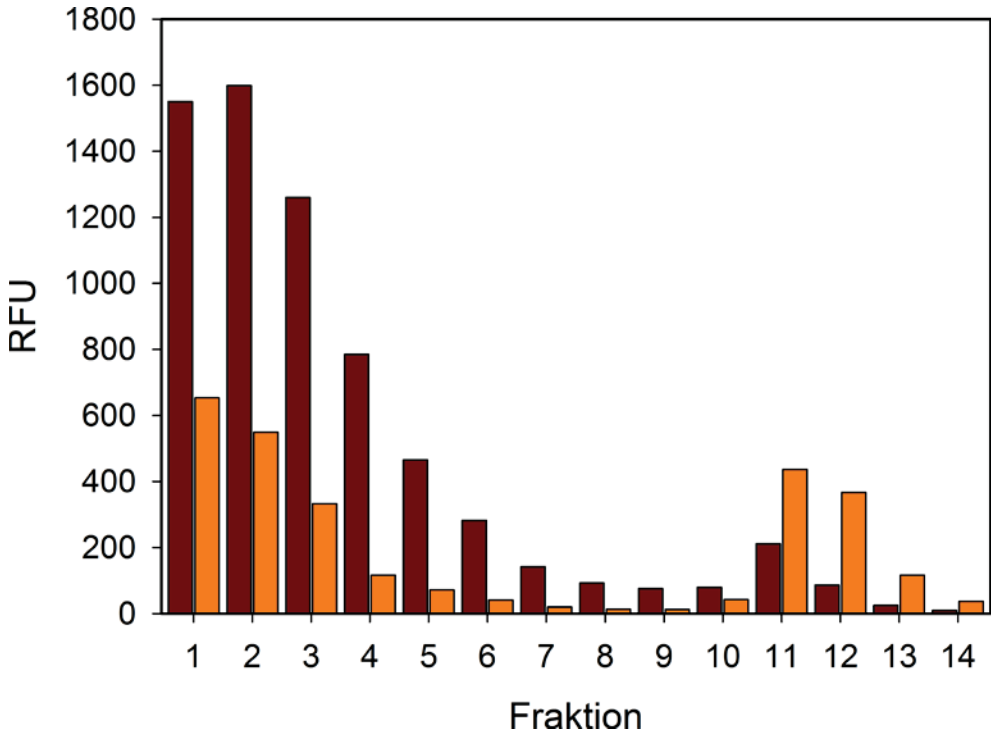

Abbildung 16 – Charakterisierung der Verteilung von D3-FITC und D3D3-FITC nach einer Reaktion mit Aβ-Aggregaten in einem Dichtegradienten

Der Iodixanol-Dichtegradient wurde mit 100 µl einer 80 µM Aβ-Lösung entweder mit einem Zusatz von 20 µM D3-FITC (rot) oder 10 µM D3D3-FITC (orange) überschichtet und anschließend 3 h lang bei 4 °C mit 259.000 x g zentrifugiert. Nach der Zentrifugation wurde der Gradient von oben nach unten fraktioniert. Die Fraktionen wurden mittels Fluoreszenzmessung analysiert. Ungebundenes D3 oder D3D3 kann sich auf Grund seines s-Wertes nur in oberen Fraktionen wiederfinden. Die Fluoreszenzintensität in den Fraktionen 10-14 zeigt die relative mit Aβ-Oligomeren komplexierte Menge von D3 (rot) oder D3D3(orange).

Das *„Head to Tail“*-D3-Dimer (D3D3) zeigte eine höhere Wirksamkeit bezüglich der Aβ-Oligomer-Reduktion als D3. 10 µM D3D3 konnten Aβ-Oligomere in den Fraktionen 5-9 eliminieren, was mit der doppelten Konzentration von D3 nicht erreicht werden konnte (Abbildung 15).

Der qualitative Effekt von D3D3 auf Aβ blieb jedoch gleich wie bei D3. Entsprechend der verstärkten Eliminierung von Aβ-Oligomeren durch D3D3 ist auch der Anteil an hochmolekularen Komplexen in den Fraktionen 11-14 gestiegen. Auch die in den Fraktionen 11-14 gemessene Fluoreszenzintensität ist nach dem Einsatz von D3D3-FITC höher als bei D3-FITC (Abbildung 16).

Anhand der Abbildung 15 kann man erkennen, dass Aβ in SDS-Gelen in mehreren Banden vorliegt. Die tri- und tetramere Banden sind typisch für Aβ, wenn es in höheren

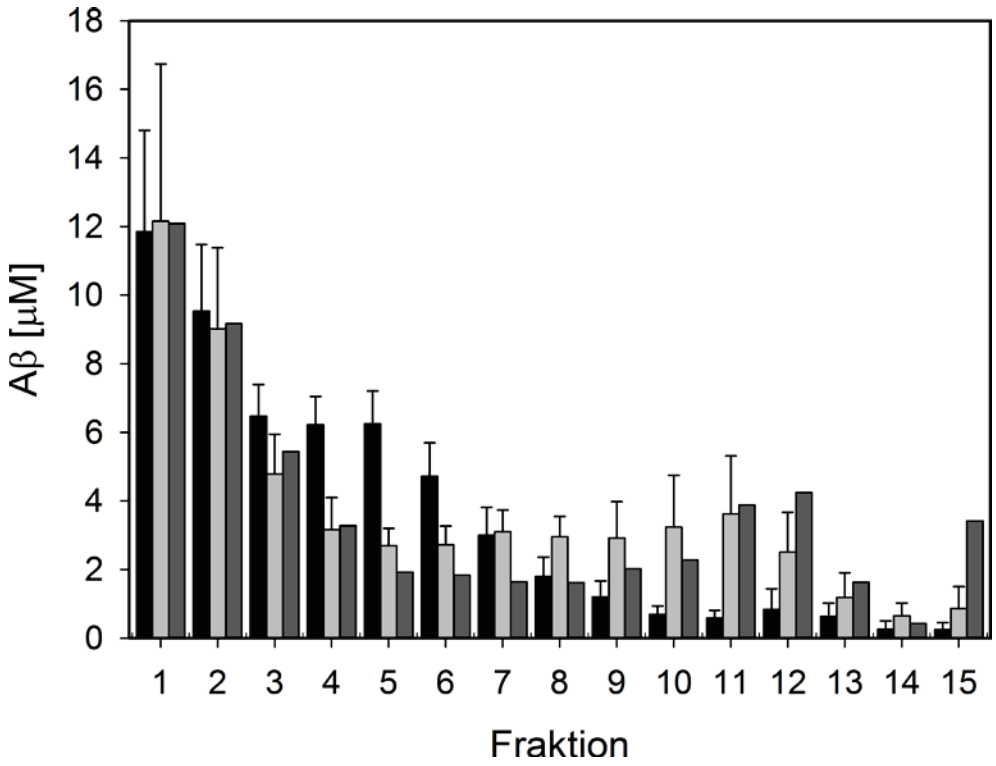

Abbildung 17 – Vergleich des Einflusses von D3 und D3D3 auf die Aβ-Aggregatgrößenverteilung mittels QIAD

Der Iodixanol-Dichtegradient wurde mit 100 µl einer 80 µM oligomer-haltigen Aβ-Lösung entweder ohne Ligand (schwarz, 11 gemittelte Proben) oder mit einem Zusatz von 20 µM D3 (hellgrau, 4 gemittelte Proben), mit 5 µM D3D3 (dunkelgrau, 2 gemittelte Proben) überschichtet und anschließend 3 h lang bei 4 °C mit 259.000 x g zentrifugiert. Nach der Zentrifugation wurde der Gradient von oben nach unten fraktioniert. Die Fraktionen wurden mittels Umkehrphasen-HPLC analysiert. D3 reduziert Aβ-Oligomere in den Fraktionen 4-6 zu ca. 50 % und komplexiert diese zu hochmolekularen Komplexen in den Fraktionen 10-15. 5 µM D3D3 reduzieren Aβ-Oligomere stärker als 20 µM D3.

Konzentrationen vorliegt. Es handelt sich hierbei um bekannte SDS-induzierte Artefakte (siehe Kapitel 1.3.2 und 1.3.3). In der Abbildung 15c ist in der 10. Fraktion noch eine weitere höhermolekulare Bande zu sehen.

Die Aussagekraft der SDS-PAGE-Analytik von fraktionierten Aβ-Spezies war nicht bei allen Tests zufriedenstellend. Es wurde ein neues Verfahren zur quantitativen Charakterisierung amyloider Peptide und/oder Proteine in einer Probe entwickelt (*assay for quantitating the efficacy of Aβ oligomer removal*: QIAD) (siehe Kapitel 2.1.4).

Bei diesem Verfahren werden mit DGZ fraktionierte Aβ-Aggregate mittels analytischer Umkehrphasen-HPLC quantifiziert. Es wurden auch neue Bedingungen für die Vorbereitung der Aβ-Oligomer-haltigen Probe gefunden, sodass der durchschnittliche oligomere Anteil (Aβ-

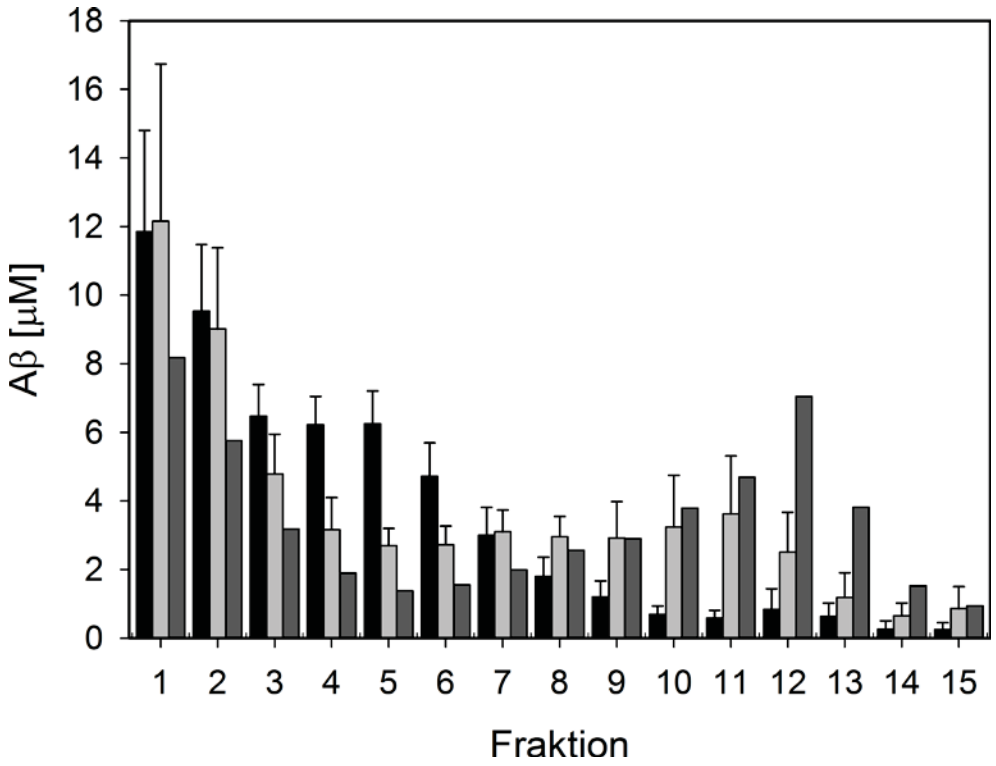

Abbildung 18 – Vergleich des Einflusses von D3 und RD2 auf die Aβ-Aggregatgrößenverteilung mittels QIAD

Der Iodixanol-Dichtegradient wurde mit 100 µl einer 80 µM oligomer-haltigen Aβ-Lösung entweder ohne Ligand (schwarz, 11 gemittelte Proben) oder mit einem Zusatz von 20 µM D3 (hellgrau, 4 gemittelte Proben), mit 20 µM RD2 (dunkelgrau, 2 gemittelte Proben) überschichtet und anschließend 3 h lang bei 4 °C mit 259.000 x g zentrifugiert. Nach der Zentrifugation wurde der Gradient von oben nach unten fraktioniert. Die Fraktionen wurden mittels Umkehrphasen-HPLC analysiert. D3 reduziert Aβ-Oligomere in den Fraktionen 4-6 zu ca. 50 % und komplexiert diese zu hochmolekularen Komplexen in den Fraktionen 10-15. Die Effektivität von RD2 bezüglich der Aβ-Oligomer-Reduktion ist höher als die von D3.

Oligomere in den Fraktionen 4-6) über 30 % betrug und keine oder fast keine höhermolekularen Aggregate in der Aβ-Kontrolllösung vorlagen.

Eine statistische Auswertung von 11 unabhängigen Experimenten ohne Ligandenzusatz zeigte eine hohe Reproduzierbarkeit (siehe Kapitel 2.1.4). Die Aufsummierung der in den einzelnen Fraktionen detektierten Mengen an Aβ ergab Werte oberhalb von 95 % der ursprünglich auf den Dichtegradienten aufgetragenen Menge und damit eine für dieses System außergewöhnlich hohe Wiederfindungsrate. In der Abbildung 17 ist der Einfluss von 20 µM D3 und 5 µM D3D3 auf eine 80 µM oligomerreiche Aβ-Probe zu sehen. Bei diesen Bedingungen reduziert D3 den Aβ-Oligomer-Anteil in den Fraktionen 4-6 um ca. 50 %. Der Einsatz von nur 5 µM D3D3 übertrifft diesen Effekt. Es ist auch gut erkennbar, dass Aβ-Monomere in den Fraktionen 1-3 weder von D3 noch von D3D3 beeinflusst werden. Aufgrund fehlender Trennleistung der DGZ kann nicht ausgeschlossen werden, dass neben den Monomeren auch kleinere Oligomere in diesen Fraktionen vorhanden sind.

Unter Beibehaltung der Zusammensetzung wurde die D3-Aminosaürensequenz variiert. Auf diese Weise wurde ein weiterer Wirkstoff designt. Dieser Wirkstoff wurde RD2 genannt. Die Aminosaürensequenz von RD2 ist ptlhthnrrrrr.

Der Einfluss von RD2, getestet mit QIAD-Verfahren, auf die Aβ-Aggregation erwies sich als sehr ähnlich zu dem von D3, er reduziert Aβ-Oligomere in den Fraktionen 4-6 und komplexiert diese zu hochmolekularen Komplexen. RD2 reduziert jedoch stärker Aβ-Oligomere in den Fraktionen 4-6 und auch Aβ-Monomere in den Fraktionen 1-2 als D3 bei gleicher Konzentration (siehe Abbildung 18). Da der Einfluss von RD2 auf die Aβ-Aggregatverteilung nur zwei Mal getestet wurde, können keine Aussagen über die Signifikanz der beobachteten Unterschiede bezüglich der Verstärkung der Aβ-Oligomer-reduzierenden Eigenschaften von RD2 gegenüber D3 getroffen werden. Die Tendenz ist jedoch deutlich.

Nach dem erfolgreichen Testen von RD2 und D3D3 wurden auch Heterodimere von RD2 und D3 hergestellt. Diese wurden genauso wie D3D3 „*Haed to Tail*“ verknüpft. Es wurden beide möglichen Varianten RD2D3 und D3RD2 getestet. Mit der Idee die für die Bindung notwendige Struktur durch eine Zyklisierung zu stabilisieren, wurde auch ein zyklisches RD2D3 Heterodimer erstellt. Die Zyklisierung erfolgte durch die Amidbindung der C- und N-Termini des Peptids.

Diese Peptidwirkstoffe wurden 5 µM im QIAD-Verfahren getestet. Keiner von ihnen konnte eine höhere Effektivität bei der Aβ-Oligomer-Reduktion als D3D3 zeigen (Abbildung 19) (für die Definition der Aβ-Oligomer-Reduktion siehe Kapitel 2.1.4). Die Einflüsse dieser Wirkstoffe auf den Aβ-Oligomer-Gehalt in einer Probe sind kaum zu unterscheiden. Eine

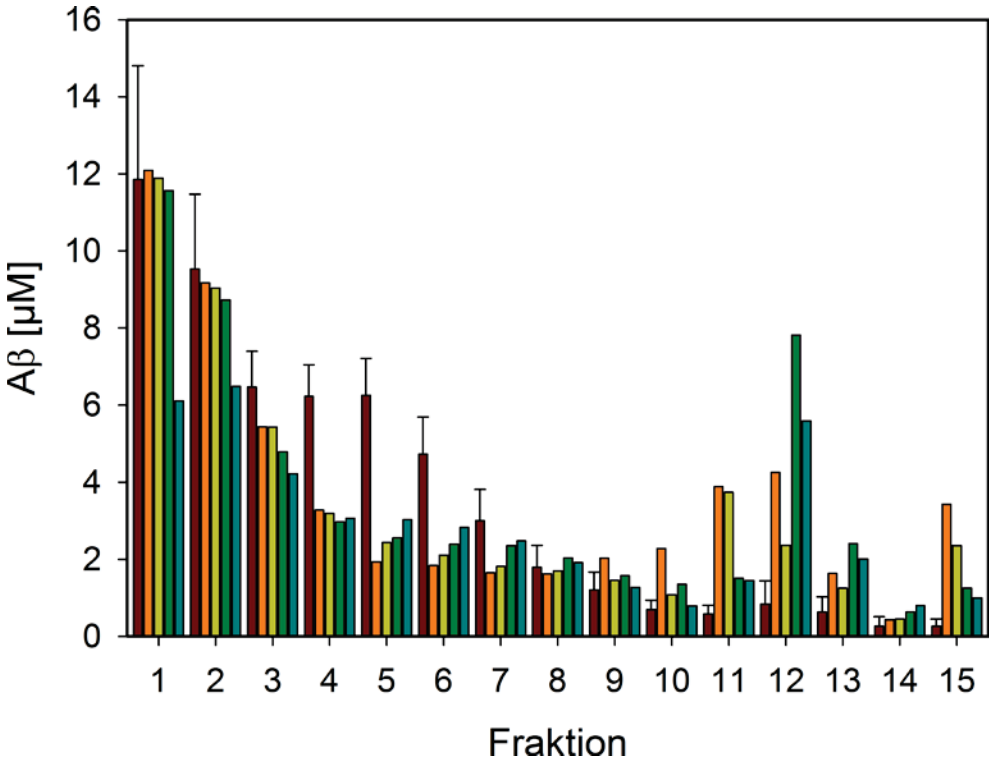

Abbildung 19 – Vergleich des Einflusses von D3D3, D3RD2, RD2D3 und cRD2D3 auf die Aβ-Aggregatgrößenverteilung mittels QIAD

Der Iodixanol-Dichtegradient wurde mit 100 µl einer 80 µM oligomer-haltigen Aβ-Lösung entweder ohne Ligand (rot, 11 gemittelte Proben) oder mit einem Zusatz von 5 µM D3D3 (orange, 2 gemittelte Proben), mit 5 µM D3RD2 (hellgrün, 2 gemittelte Proben), 5 µM RD2D3 (dunkelgrün, 2 gemittelte Proben), 5 µM cRD2D3 (blau, 2 gemittelte Proben) überschichtet und anschließend 3 h lang bei 4 °C mit 259.000 x g zentrifugiert. Nach der Zentrifugation wurde der Gradient von oben nach unten fraktioniert. Die Fraktionen wurden mittels Umkehrphasen-HPLC analysiert. Alle Wirkstoffe reduzieren Aβ-Oligomere in den Fraktionen 4-6 und komplexieren diese zu hochmolekularen Komplexen in den Fraktionen 10-15. Die Effektivität von diesen Wirkstoffen bezüglich der Aβ-Oligomer-Reduktion ist in etwa gleich.

Ausnahme stellt das zyklische RD2D3 (cRD2D3) dar. Im Gegensatz zu anderen Wirkstoffen reduziert es deutlich auch die Menge von Aβ-Monomeren. Da auch hier nur eine Doppelbestimmung durchgeführt wurde, kann man keine Aussage über die Signifikanz treffen. Die Hypothese durch eine Zyklisierung die für die Bindung notwendige Struktur zu stabilisieren wurde auch im Falle von D3 aufgestellt. Auch hier wurde die Zyklisierung durch die Peptidbindung der C- und N-Termini erreicht. Da alle hier beschriebene Peptidwirkstoffe einen amidierten C-Terminus besitzen, verlieren sie durch die Zyklisierung im Vergleich zum linearen Peptid eine positive Nettoladung des N-Terminus. Um diese zu kompensieren, wurde auch ein zyklisches D3 mit einem zusätzlichen Arginin am Ende der Sequenz designt. Dieser Wirkstoff wurde cD3r bezeichnet. Das zyklische D3 ohne diese kompensatorische Ladung erhielt die Kennzeichnung cD3z (*zero*).

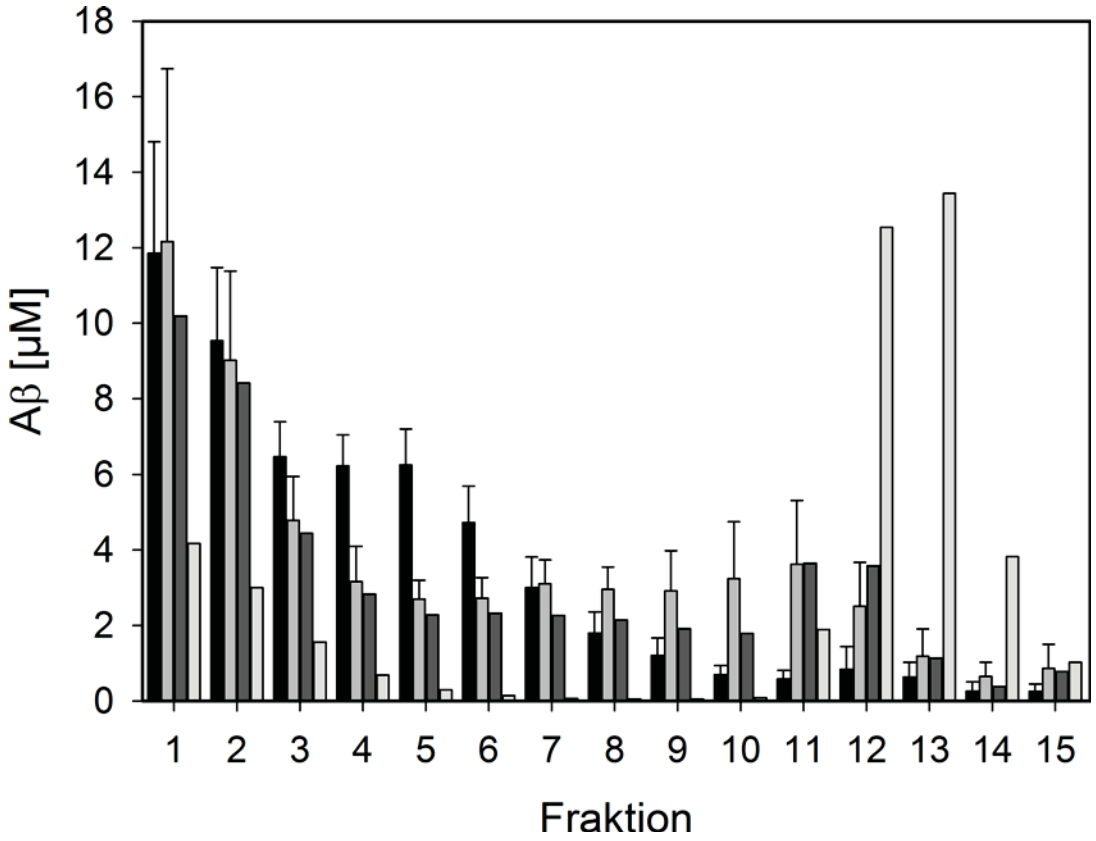

Abbildung 20 – Vergleich des Einflusses von D3, cD3z und cD3r auf die Aβ-Aggregatgrößenverteilung mittels QIAD

Der Iodixanol-Dichtegradient wurde mit 100 µl einer 80 µM oligomer-haltigen Aβ-Lösung entweder ohne Ligand (schwarz, 11 gemittelte Proben) oder mit einem Zusatz von 20 µM D3 (hellgrau, 4 gemittelte Proben), mit 20 µM cD3z (dunkelgrau, 2 gemittelte Proben), mit 20 µM cD3r (weiß-grau, 2 gemittelte Proben) überschichtet und anschließend 3 h lang bei 4 °C mit 259.000 x g zentrifugiert. Nach der Zentrifugation wurde der Gradient von oben nach unten fraktioniert. Die Fraktionen wurden mittels Umkehrphasen-HPLC analysiert. D3 reduziert Aβ-Oligomere in den Fraktionen 4-6 zu ca. 50 % und komplexiert diese zu hochmolekularen Komplexen in den Fraktionen 10-15. Die Effektivität von cD3z bezüglich der Aβ-Oligomer-Reduktion ist in etwa gleich wie die von D3, cD3r eliminiert die Oligomere fast vollständig.

Auch zyklische D3-Derivate zeigen im QIAD-Verfahren eine ähnliche Wirkung auf Aβ-Spezies wie D3. Zwischen der Wirkung von cD3z und D3 kann man so gut wie keine Unterschiede beobachten. Das cD3r reduziert Aβ-Oligomere aber auch Aβ-Monomere deutlich stärker als D3 (Abbildung 20). Der Einsatz von 20 µM cD3r eliminiert fast vollständig Aβ-Oligomere in den Fraktionen 4-6. Die gleiche Menge von D3 führt zu einer Aβ-Oligomer-Reduktion von nur ca. 50 %.

3 Diskussion

Der Schwerpunkt dieser Arbeit ist die Charakterisierung und gezielte Eliminierung von toxischen Proteinaggregaten. Unterschiedliche Publikationen auf dem AD-Forschungsgebiet legen nahe, dass für die Entwicklung und Pathogenese der AD Aβ-Oligomere verantwortlich sind. Trotz aller Erkenntnisse und Bemühungen gibt es heutzutage keine wirksame Therapie, die die Ursachen und nicht nur die AD-Symptome behandelt. Die Entwicklung wirkungsvoller Therapeutika gegen die AD wäre also von großer Bedeutung. Da Aβ-Oligomere die Ursache der AD-Pathogenese darstellen, wäre ein Wirkstoff gegen diese Spezies der logischste und vielversprechendste Ansatz Wirkstoffe zu entwickeln, die später in AD-Tiermodellen auf ihre Wirksamkeit getestet und bei einem Erfolg in klinischen Studien eingesetzt werden können. Die meisten entwickelten Wirkstoffe werden in erster Linie auf ihre Eigenschaft amyloide Strukturen zu reduzieren selektiert (O'Hare et al. 2013). Diese Selektionen werden mittels Thioflavin-T- oder Thioflavin-S-Fluoreszenzmessungen durchgeführt, weil sich die Technik als Hochdurchsatzverfahren einsetzen lässt. Diese zeigen meistens jedoch den relativen Anteil an Fibrillen in analysierter Probe. Techniken, die auf die Aβ-Oligomer-Reduktion zielen, basieren entweder auf einer indirekten Bestimmung der Aβ-Oligomer-Konzentration in einer Probe (z.B. über die Quantifizierung der Monomer-Zu- oder Abnahme (Cheng and van Breemen 2005)) oder auf nur semiquantitativen und/oder Epitop-abhängigen Verfahren wie ELISA.

Die Entwicklung einer Methode, die eine quantitative Bestimmung der Reduktion oder Eliminierung bestimmter Aβ-Oligomere möglich macht, ist also ein wichtiger Schritt für die Entwicklung von Wirkstoffen gegen die AD. Die Überprüfung der Aussagekräftigkeit dieser Technik erfolgte durch *in vivo* Tests von mit ihrer Hilfe selektierten Wirkstoffen.

3.1 Untersuchung des Einflusses Aβ-bindender Liganden auf die Aβ-Aggregatgrößenverteilung

Als Leitstrukturen für diese Arbeit dienten ein mit Phagen-Display bzw. mit Spiegelbild-Phagen-Display selektiertes L- und D-Peptid (L3 und D3), welche an Aβ binden. Diese Aβ-Liganden entstammen Vorarbeiten unserer Arbeitsgruppe ((van Groen et al. 2008) und Kapitel 2.1.2). Mit Hilfe der Dichtegradientenzentrifugation (DGZ) konnten Aβ-Gemische fraktioniert werden. Der Aβ-Gehalt in jeder Fraktion wurde mittels SDS-PAGE bestimmt. Eine

Herausforderung stellte dabei die Vorbereitung einer Aβ-Oligomer-haltigen Probe, da Aβ schnell und auf unterschiedlichen Wegen aggregiert. Mithilfe der DGZ lassen sich die relativen Mengen an Monomeren und kleinen Oligomeren, mittleren Oligomeren und großen Aggregaten mit fibrillärer oder amorpher Struktur, welche in einer Aβ-Lösung vorliegen, bestimmen. Frischgelösten Aβ besteht hauptsächlich aus Monomeren und kleinen Oligomeren, Aggregate in den unteren Gradientenfraktionen fehlen vollständig. Durch Variation der Vorinkubationsbedingungen konnten Aggregatgrößenverteilungen mit verringertem Monomeranteil und deutlich erhöhtem Oligomeranteil erzielt werden, in der große Aggregate noch nicht nachweisbar sind. Derart vorinkubierte Aβ-Lösungen wurden verwendet, um den Einfluss von D3 und L3 auf Aβ-Oligomere zu testen. Die Untersuchung der mit D3 oder L3 inkubierten Aβ-Lösungen mittels DGZ mit anschließender SDS-PAGE-Analyse zeigte, dass sowohl D3 als auch L3 Aβ-Oligomere bestimmter Größe konzentrationsabhängig reduzieren, bzw. in äquimolarer Konzentration vollständig eliminieren (siehe Kapitel 2.1.1 und 2.1.2). Beide Wirkstoffe modulierten also die Aβ-Aggregation sehr ähnlich, obwohl sie unterschiedliche Aminosäurezusammensetzung und Sequenz haben und aus unabhängigen Selektionen stammen. Gemeinsam haben sie einen hohen Arginin-Gehalt und einen fast identischen isoelektrischen Punkt, der im basichen Bereich liegt, und somit eine starke positive Ladung im neutralen pH. Man kann also annehmen, dass die beobachtete, Aβ-Oligomer-reduzierende Wirkung dieser Wirkstoffe stark von elektrostatischen Wechselwirkungen mit Aβ abhängt. Dabei könnten diese Kationen auf unterschiedliche Weise wirken: entweder durch eine direkte Bindung an Aβ oder eine Veränderung der Lösungseigenschaften, die sich aggregationsbeschleunigend auf das aggregierende Peptid auswirkt. Dies wäre z.B. dank der chaotropen Wirkung der Arginine möglich, da Chaotrope die Wasserstoffbrücken-Bildung bei Proteinen reduzieren (Hofmeister 1888). Arginine haben auch die Eigenschaft die Oberflächenspannung einer Lösung zu erhöhen. Je höher die Oberflächenspannung, desto schneller aggregiert das Aβ. Die Aggregationsbeschleunigung von Aβ ist besonders stark ausgeprägt, wenn der Ligand an das Zielmolekül binden kann und die Oberflächenspannung erhöht (Gibson and Murphy 2005).

Durch Fluoreszenzmarkierung des D3 mit FITC konnte gezeigt werden, dass die eliminierten Aβ-Oligomere mit D3 zu hochmolekularen, nicht amyloiden Komplexen reagieren (siehe Abbildungen 15 und 16 und Kapitel 2.1.1). Des Weiteren zeigten Peptide, die entweder die C- oder N-terminale Hälfte des D3 darstellen, auch beim Einsatz in hohen Konzentrationen (160 µM) keinen modulierenden Effekt auf die Aβ-Aggregation (Daten nicht gezeigt), obwohl der Einfluss dieser D3-Fragmente auf die Lösungseigenschaften gleich oder stärker als der von D3 sein sollte. Die Bedeutung dieser elektrostatischen

Wechselwirkungen, die eine direkte Bindung von D3 an Aβ voraussetzen, wurde auch mit MD-Simulationen bestätigt (siehe Kapitel 2.1.1 und 2.1.6). Die Entstehung von hochmolekularen Komplexen bei der Reaktion von D3 und Aβ kann also nicht durch die Lösungseffekte erklärt werden. Eine andere Erklärungsmöglichkeit für diese Reaktion wäre, dass D3 mehrere, aber mindestens zwei Bindestellen hätte. Diese unterschiedlichen Bindestellen des D3 binden je ein Zielmolekül. Auf diese Weise könnte D3 Aβ-Oligomere quervernetzen und zu beobachteten hochmolekularen Komplexen reagieren lassen.

D3 führte auch zu einer Verbesserung kognitiver Fähigkeiten in einem AD-Mausmodell (siehe Kapitel 2.1.1). Diese Ergebnisse stimmen mit den in der Literatur beschriebenen Zusammenhängen und aufgestellten Hypothesen überein, dass eine Eliminierung von Aβ-Oligomeren, zu einer Heilung der AD führen soll. Man kann jedoch nicht ausschließen, dass der *in vivo* Effekt von D3 auf seiner Eigenschaft die Bildung großer amorpher Aggregate zu beschleunigen beruht. Die amorphen Aggregate könnten durch Anregung von Clearance-Mechanismen leicht abgebaut werden. Dies hätte eine Reduktion amyloider Strukturen im Hirngewebe zu Folge und würde zu einer Verbesserung der Kognition führten. Die D3-Eigenschaft amyloide Strukturen umzuformen liegt wahrscheinlich auch der *in vivo* beobachteten Plaque-Reduktion zu Grunde. Diese Zusammenhänge wären mit Hilfe der Amyloid-Kaskaden-Hypothese erklärbar (siehe Kapitel 1.3.1). Sie würden aber nicht in den Kontext der aktuellen Erkenntnisse über die Entwicklung der AD passen, laut denen die senilen Plaques ein Symptom und nicht die Ursache der AD sind. Die Schlüsselrolle bei der Pathogenese der AD spielen Aβ-Oligomere (siehe Kapitel 1.3.2).

Aβ-Oligomere, die durch den Einsatz von D3 oder L3 eliminiert wurden, weisen einen s-Wert von 5 bis 7 S, was einem Molekulargewicht von 66 bis 150 kDa entspricht. Oligomere dieser Art standen zum Zeitpunkt der Entstehung dieser Ergebnisse weniger im Mittelpunkt der AD-Forscher-Aufmerksamkeit als kleinere Aβ-Oligomere (z.B. Dodecamere) (Selkoe 2008). Doch auch einige andere Arbeitsgruppen berichteten über ähnliche Aβ-Oligomere (Hepler et al. 2006).

Während dieser Arbeit wurde die Hypothese aufgestellt, dass die D3-Eigenschaft, *in vitro* Aβ-Oligomere zu eliminieren, für die beobachtete *in vivo* Wirksamkeit von Bedeutung ist. Um diese Hypothese zu überprüfen und effizientere Wirkstoffe gegen Aβ-Oligomere und somit die AD zu entwickeln, wurden unterschiedliche D3-Derivate designt.

3.2 Design von D3-Derivaten und Untersuchung ihres Einflusses auf die Aβ-Aggregatgrößenverteilung

Bei der Derivatisierung von D3 wurden unterschiedliche Ansätze getestet. D3 wurde dimerisiert, zyklisiert, mit bereits untersuchten Verbindungen hybridisiert und seine Aminosäuresequenz wurde unter Beibehaltung der Zusammensetzung variiert. Bei der Hybridverbindung von D3 und einem β-Faltblatt brechenden Molekül mit der Kennzeichnung Trimer-Aminopyrazol, das bereits untersucht und charakterisiert wurde (Rzepecki et al. 2004), gelang es einen Effekt zu erzielen, der mehr als die Summe einzelner Verbindungen war (siehe Kapitel 2.1.3). Dies kann damit erklärt werden, dass wenn einer der Liganden der Hybridverbindung an das Zielmolekül bindet, automatisch auch der zweite Ligand sich in der Nähe der Bindungsstelle befindet. Somit erhöht sich die lokale Konzentration der Wirkstoffe am Target. Diese Theorie wird auch durch die Aβ-Oligomer-reduzierende Wirkung von D3D3, einem „Head to Tail" Dimer des D3, bestätigt. Die Wirkung von D3D3 auf Aβ-Oligomere ist signifikant stärker als die einer doppelten Konzentration von D3 (siehe Kapitel 2.1.4).

Die Hypothese des Quervernetzens von Aβ-Oligomeren bedingt durch vermeintlich mehrere Bindestellen von D3 und seiner Derivate steht im Widerspruch mit der höheren Effektivität von D3D3, die durch die Erhöhung der lokalen Wirkstoffkonzentration am Target erklärt werden sollte. Wenn für die Reaktion von Aβ-Oligomeren mit D3-Derivaten mehrere Aβ-Oligomere notwendig sind, kann man die Konzentrationserhöhung der Bindestellen nur an einem Aβ-Oligomer (für ein Wirkstoffmolekül gesehen) nicht erklären. Die Ergebnisse zeigen jedoch eindeutig, dass sogar 5 µM D3D3 einen stärkeren Effekt auf Aβ-Oligomere als 20 µM D3 hat (Abbildung 17). Eine weitere Theorie über den Wirkungsmechanismus von D3-Derivaten könnte diesen Widerspruch beseitigen. So könnten D3 und D3D3 durch die Bindung an ein Aβ-Oligomer dessen strukturelle Änderungen hervorrufen. Der Komplex dieser Moleküle wäre einer Art Aggregationskeim oder Reaktionskatalysator, der einen Lawineneffekt für eine weitere aber begrenzte Anzahl von Aβ-Oligomeren hervorruft. Hierbei könnte vielleicht auch die o.g. chaotrope Wirkung von Argininen eine Rolle spielen. Setzt man diese Theorie voraus, würden D3 oder D3D3 ein gebundenes Aβ-Oligomer unterschiedlich stark umstrukturieren. D3 würde also die Struktur eines Oligomers nicht vollständig umformen. Dafür sind eventuell mehrere D3-Moleküle notwendig. Es wäre auch vorstellbar, dass diese Reaktion eine kinetische Komponente hat. Genauer, die Umstrukturierung wäre relativ langsam und D3 würde abdissoziieren, bevor die Strukturänderung vollendet ist. D3D3 hat aber eine höhere Avidität, kann also länger am Target bleiben. Der Effekt der höheren Avidität wäre auch mit der Quervernetzungstheorie durch multiple Bindestellen von D3 und D3D3 zu vereinen.

Wäre der Aβ-Oligomer/D3-Komplex nur dann stabil oder die Reaktion dieser Edukte irreversibel, wenn bereits mehr als ein Oligomer komplexiert ist, könnte D3 einfach abdissoziieren bevor ein weiteres Aβ-Oligomer andocken kann.

Beim Design von RD2 wurden die o.g. Hypothesen berücksichtigt und angenommen, dass elektrostatische Wechselwirkungen zwischen D3 und Aβ eine entscheidende Rolle für die Reaktion dieser Moleküle spielen und dass D3 mehr als eine (wahrscheinlich zwei) Bindestellen hat. Als Bindemotiv wird die abwechselnde Reihenfolge von Arginin (r) und einer beliebigen anderen Aminosäuren (x) postuliert. D3 weist genau zwei solche Motive auf. Es wurde angenommen, dass das Motiv rxrx auch bei x = r möglich ist, da die Seitenketten der benachbarten Aminosäuren in entgegengesetzte Richtungen zeigen. Betrachtet man also nur die Argininseitenketten, ergibt sich auch bei einer rrrr Sequenz ein rxrx Motiv der Seitenketten. Durch die Positionierung von allen Argininen am C-Terminus des Wirkstoffs wurde erhofft, dass die zwei hypothetischen Bindestellen lokal „konzentriert“ werden und somit die Komplexierung von Aβ-Oligomeren durch diesen Wirkstoff wahrscheinlicher wird. Da die restlichen Aminosäuren eventuell bei hydrophoben und hydrophilen Wechselwirkungen zwischen D3 und Aβ-Oligomeren wichtig wären (siehe Kapitel 2.1.6), wurde ihre Sequenz nach der Arginin-Umstellung möglichst unverändert gelassen. So entstand die Sequenz von RD2: ptlhthnrrrrr (D3-Sequenz: rprtrlhthrnr).

Die aufgestellten im letzten Absatz geschilderten Hypothesen konnten zunächst nur bedingt überprüft werden, da das oben beschrieben DGZ-System gekoppelt mit SDS-PAGE nur leichte Tendenzen im Vergleich der RD2- und D3-Wirkung auf Aβ-Oligomere zeigen konnte. Nach der Entwicklung des QIAD-Verfahrens (siehe Kapitel 2.1.4) konnte gezeigt werden, dass RD2 in der Tat bei gleicher Konzentration Aβ-Oligomere effektiver als D3 reduziert (Abbildung 18). Ein Nebeneffekt des RD2 war der Einfluss auf Aβ-Monomere, deren Konzentration in keiner Weise von D3 beeinflusst aber von RD2 leicht reduziert wurde.

Die oben aufgestellten Hypothesen über die Reaktionsmechanismen von D3 und D3D3 lassen sich mit diesem Ergebnis nicht definitiv bestätigen, werden jedoch auch nicht widerlegt. Die erhöhte Effektivität der Aβ-Oligomer-Reduktion von RD2 könnte am besten mit der oben beschriebenen Theorie der chaotropen Arginin-Wirkung erklären. Wenn die im Kapitel 2.1.6 dargelegten MD-Simulationen den realen Bindemechanismen von D3 und RD2 entsprechen und somit die Arginine wirklich die entscheidende Rolle bei der Bindung an Aβ spielen, wären im Falle von RD2 die Argininseitenketten, die nicht in der Bindung involviert sind räumlich näher am Target als im Falle von D3 und würden so einen stärkeren chaotropen Effekt auf das gebundene Aβ-Oligomer ausüben.

Nach dem erfolgreichen Testen von D3D3 und RD2 wurde versucht, die Vorteile beider Wirkstoffdesign-Wege zu kombinieren. Heterodimere von D3 und RD2 wurden entworfen und mit QIAD getestet. Dabei wurden beide möglichen Varianten dieses Heterodimers berücksichtigt (RD2D3 und D3RD2). Der Einfluss der beiden auf die Aβ-Oligomer-Reduktion war zu dem von D3D3 sehr ähnlich. Die Unterschiede waren so gering, dass sie im Schwankungsbereich liegen. Es widerspricht der Erwartung, dass zumindest ein der Heterodimere eine stärkere modulierende Wirkung der Aβ-Aggregation zeigen sollte. Eventuell erreichte dieser Weg der D3-Optimierung sein Limit.

D3 weist mit seinen 12 Aminosäuren eine gewisse Flexibilität auf. Es wurde die Hypothese aufgestellt, dass die Bindestelle(n) des D3 eventuell eine gewisse Zeit benötigt, um die für die Bindung notwendige Konformation zu finden. Das könnte vermieden werden, wenn die richtige Struktur stabilisiert wäre. Dies sollte durch eine Zyklisierung, die über die Peptidbindung zwischen dem C- und N-Terminus hergestellt wird, erreicht werden. Da bei dieser Art der Zyklisierung auch die N-terminale positive Ladung verloren geht, wurde auch ein zyklisches D3 mit einem zusätzlichen Arginin am Ende seiner Sequenz eingefügt hergestellt und getestet.

Zyklisches D3 ohne die kompensatorische Ladung (cD3z) zeigte verglichen mit D3 beim QIAD-Verfahren keine Unterschiede bezüglich der Aβ-Aggregation-Modulierung. Zyklisches D3 mit zusätzlichen Arginin (cD3r) zeigte dagegen eine viel stärkere Reduktion von sowohl Aβ-Oligomeren als auch Aβ-Monomeren (Abbildung 20). Der Einfluss von 20 µM cD3r liegt im gleichen Bereich wie der von 10 µM D3D3. Diese Ergebnisse zeigen, dass die extra eingefügte kompensatorische Ladung für die Reaktion mit Aβ-Oligomeren sehr wichtig ist. Es wurde allerdings nicht überprüft, ob der Effekt vom zusätzlichen Arginin dem von einem Lysin gleich wäre. Möglicher Weise spielen auch hierbei die chaotropen Eigenschaften der Arginine eine Rolle. Der Aβ-Oligomer-reduzierende Effekt konnte also in der Tat durch die Stabilisierung der D3-Struktur um das Vielfache erhöht werden. Es ist jedoch auch möglich, dass durch das zusätzliche Arginin eine weitere Bindestelle kreiert wurde. Legt man die Strukturstabilisierung dem beobachteten Effekt zu Grunde, so scheint die Strukturstabilisierung die gleiche Auswirkung auf die Aβ-Oligomer-Reduktion wie die Verdopplung von D3 zu haben.

Bei gleicher Effektivität der Aβ-Oligomer-Reduktion hätte cD3r möglicherweise Vorteile bei einem Einsatz in vivo, da es fast zweimal kleiner als D3D3 oder ein RD2D3 Heterodimer ist. Man erhielte bei einem *in vivo* Einsatz von gleicher Dosis (mg/kg) von cD3r und D3D3 eine doppelt so starke Aβ-Oligomer-Reduktion im Fall von cD3r.

3.3 Vor- und Nachteile des DGZ-SDS-PAGE- und QIAD-Systems

Mit Hilfe des DGZ-SDS-PAGE-Systems gelang es die qualitativen Aspekte des Einflusses von D3 und D3-Derivaten auf die Aβ-Aggregatgrößenverteilung zu demonstrieren und auch ein begrenztes Ranking von D3-Derivaten bezüglich ihrer Eigenschaft Aβ-Oligomere zu reduzieren zu erstellen. Bei D3-Derivaten mit geringen Unterschieden in ihrer Wirkung, ließen sich mit dem System im besten Falle nur leichte vergleichende Tendenzen feststellen.

Zu den Vorteilen der Auftrennung einer Aβ-Lösung mittels DGZ zählen: keine Wechselwirkung von Aβ mit einer Matrix, an welcher Aβ „kleben“ bleiben kann; geringer Einfluss vom Dichtegradientenmaterial Iodixanol auf Proteinstrukturen, keine Bindung des Iodixanols an Proteine (Graham 2002, Jacobsen et al. 1995); eine sehr hohe Dichte, nahe der Proteindichte, in den unteren Fraktionen des Gradienten, wodurch die Pelletierung sehr großer Aggregate wie Fibrillen verhindert wird und die Möglichkeit unterschiedliche Aβ-Spezies für weitere Analysen zu präparieren. Die Nachteile dieser Auftrennungsmethode lassen sich folgend zusammenfassen. Mit der verwendeten Zusammenstellung des Dichtegradienten (siehe Kapitel 2.1.4) lassen sich keine Moleküle auftrennen, die einen s-Wertunterschied von ungefähr kleiner 2 S aufweisen. Wobei auch Moleküle mit diesem s-Wertunterschied eine überlappende Zone im Gradienten haben. In der unteren Hälfte des Gradienten muss dieser Unterschied noch viel größer sein. Im unteren Viertel des Gradienten lassen sich Protein- und/oder Peptidkomplexe fast gar nicht auftrennen. Das Iodixanol absorbiert sehr stark im UV-Bereich und macht somit viele spektroskopische Techniken nutzlos bei der Analyse der Dichtegradienten-Fraktionen.

Die Quantifizierung von fraktionierten Aβ-Spezies mittels SDS-PAGE und Silberfärbung erlaubt zwar die Aussagen über die relative Verteilung von Aβ-Aggregaten im Dichtegradienten und ist unabhängig von der Epitop-Zugänglichkeit oder dem Epitop-Blocking, ist aber im besten Falle nur semiquantitativ aufgrund der Silberfärbungsigenschaften. Des Weiteren bildet Aβ in SDS-Gelen mehrere Banden, was die Auswertung zusätzlich erschwert. Manchmal entstehen auch höhermolekulare Aβ-Banden die nur bedingt oder gar nicht ins Gel einwandern (siehe Abbildung 15).

Aus diesem Grunde wurde nach einer Möglichkeit gesucht, die Aβ-Quantifizierung in Dichtegradienten-Fraktionen auf einem anderen Wege durchzuführen. Eine große Schwierigkeit dabei war die UV-absorbierende Eigenschaft des Iodixanols. Dieses musste von Aβ abgetrennt werden. Da das Iodixanol und Aβ sich stark in ihren hydrophob-hydrophilen Eigenschaften unterscheiden, konnte dies erfolgreich mittels der Umkehrphasen-HPLC erreicht werden (siehe Kapitel 2.1.4). Dabei konnte der separat eluierende Aβ-Peak bei 214 nm

detektiert und integriert werden. Da die HPLC-Läufe unter vollständig denaturierenden Bedingungen stattfinden, ist die Quantifizierung von Aβ komplett unabhängig von dessen Aggregatzustand oder von Epitop-Zugänglichkeit und kann für die ganze Palette der Aβ-Spezies oder Aβ/Ligand-Komplexe eingesetzt werden.

Die Kombination der Auftrennung von Aβ-Spezies mittels DGZ mit anschließender Quantifizierung der Aβ-Konzentrationen in Dichtegradienten-Fraktionen mittels HPLC erhielt die Bezeichnung „Verfahren zur quantitativen Charakterisierung amyloider Peptide und/oder Proteine in einer Probe“ oder „*quantitative determination of interference with aggregate size distribution*“ (QIAD). Das QIAD Verfahren ist deutlich sensitiver gegenüber Liganden induzierte Veränderungen der Aβ-Aggregatgrößenverteilungen als die DGZ mit anschließender SDS-PAGE. Da QIAD eine minimale Nachweisgrenze von ca. 20 nM Aβ aufweist, wurde es bei diesem *in vitro*-Test möglich auch mit viel geringeren, für *in vivo* mehr relevanten Aβ–Konzentrationen zu arbeiten. Im QIAD lässt sich die Menge an im Gradienten wiedergefundenen Aβ quantifizieren und mit der eingesetzten Aβ-Menge vergleichen. Dies ist fürs Experimentieren mit Aβ von großer Bedeutung, da Aβ die Eigenschaft besitzt sich an Oberflächen anzulagern und in Form großer Aggregate schlecht pipettierbar wird. Die bestimmten Wiederfindungsraten im QIAD waren sehr hoch (siehe Kapitel 2.1.4). Das spricht auch für den Einsatz der DGZ, da fast das ganze eingesetzte Aβ-Material in Lösung blieb. Dank statistischer Auswertung der Aβ-Aggregatverteilung wurde auch die Vorbereitung einer Aβ-Oligomer-reichen Probe optimiert und die Wahrscheinlichkeit der Fehlschlüsse durch Schwankungen der Aβ-Oligomer-Mengen in einer Probe reduziert werden. Die Kombination all dieser Faktoren ermöglichte eine hohe Reproduzierbarkeit beim Experimentieren mit Aβ-Oligomeren.

Mittels QIAD konnte nicht die Verteilung von D3-Derivaten im fraktionierten Dichtegradienten bestimmt und quantifiziert werden. Dies lag an der sehr hydrophilen Natur dieser Wirkstoffe. Sie eluierten zusammen mit dem auch stark hydrophilen Iodixanol. Da das Iodixanol im UV-Bereich absorbiert, überschattete es die D3-Derivate. Sollten in diesem System Wirkstoffe mit anderen z.B. hydrophoberen Eigenschaften getestet werden, wäre es möglich auch sie zu quantifizieren.

Als größter QIAD-Vorteil kann seine Vorhersagekraft für *in vivo*-Tests gewertet werden. Dies wurde anhand von D3 und D3D3 demonstriert. Die signifikant höhere Effektivität von D3D3 gegenüber D3 getestet mit QIAD, ließ sich ebenfalls im Tiermodell aufgrund verbesserter kognitiver und motorischer Fähigkeiten wiederfinden. Diese Ergebnisse legten nahe, dass mit dem entwickelten *in vitro* Testsystem die Wirksamkeit von Wirkstoffen, welche Aβ-Oligomere als Target haben, im Tiermodell vorhergesagt werden kann.

3.4 Aβ-Oligomer-Charakterisierung

Die mit DGZ fraktionierten Aβ-Oligomere konnten mit anderen biophysikalischen und biochemischen Methoden untersucht werden. Vom größten Interesse waren dabei Aβ-Oligomere, die durch D3 und seine Derivate eliminiert werden. Mittels einer Dichtegradientenkalibrierung wurde ihr s-Wert zwischen 5 und 7 S geschätzt. Die Größe und Form dieser Partikel konnte näher mit AFM untersucht werden. Dabei stellte es sich heraus, dass die in Verbindung mit Aβ-Oligomeren allgemein verwendete Abbildungstechnik (*tapping mode* luftgetrockneter Probe) wenig geeignet für die Bestimmung der realen Aβ-Oligomer-Größen ist. Dies liegt daran, dass Aβ-Oligomere, die oft eine gerinde Stabilität aufweisen, an Luft denaturieren oder durch den mechanischen Einfluss der AFM-Spitze beschädigt werden. Dabei spielen auch andere AFM-Artefakte eine Rolle (E. Ukraintsev 2012). Deswegen wurde im Laufe diese Arbeit ein Abbildungsverfahren in Puffer, also den nativen Bedingungen am nächsten kommend, entwickelt. Mit diesem Verfahren ließ sich die Höhe von Aβ-Oligomeren viel exakter bestimmen. Dadurch wurde die Abschätzung der Form dieser Partikel in Lösung und eine relativ genaue Kalkulation ihrer Volumina möglich. So konnte bestimmt werden, dass diese Aβ-Oligomere aus ca. 23 monomeren Einheiten bestehen (siehe Kapitel 2.1.4). Diese Kalkulation hat eine gewisse Ungenauigkeit, da auch beim entwickelten Abbildungsverfahren Aβ-Oligomere durch den mechanischen Einfluss der AFM-Spitze verschoben oder beschädigt werden konnten. Des Weiteren üben sich auf die Bestimmung der Partikeldimensionen das Rauschen und Spitzendimensionen-Variation negativ aus. Dennoch konnten die Höhen und Breiten dieser Aβ-Oligomere auf weniger als 1 nm genau bestimmt (mit dem vom Hersteller angegebenen mittleren Spitzenradius) und gezeigt werden, dass diese Aβ-Oligomere eine spheroidale Form haben. Es ist möglich, dass die charakterisierten Partikel eine Kugelform haben, wenn sie frei in der Lösung vorliegen, und nur nach Bindung der Oberfläche oder nach dem Einfluss der AFM-Spitze eine spheroidale Form annehmen.

Die Sekundärstruktur der mit DGZ präparierten Aβ-Oligomere konnte nicht ohne weiteres bestimmt werden, da das Dichtegradientenmaterial Iodixanol stark im UV-Bereich absorbiert und somit den Einsatz der Circulardichroismus- (CD) Spektroskopie unmöglich macht. Aβ-Oligomere konnten mittels Größenausschlusschromatographie von Iodixanol abgetrennt werden. Das anschließend gemessene CD-Spektrum zeigte, dass die aus den Dichtegradienten-Fraktionen präparierten Aβ-Oligomere überwiegend aus β-Faltblättern bestehen (siehe Kapitel 2.1.4). Ein Test mit Thioflavin-T (ThT), einem Indikator für amyloide Strukturen, die einen hohen β-Faltblattanteil aufweisen, zeigte jedoch, dass diese Aβ-Oligomere ThT-negativ sind. Eine Erklärung dafür ist, dass Aβ-Oligomere keine 5 bis 6 β-Faltblätter in einer Reihe haben,

die für eine ThT-Bindung notwendig sind (Groenning 2010).

Mittels MTT-Assay konnte die Toxizität der präparierten Aβ-Oligomere auf *Brain-derived neurotrophic factor* (BDNF) differenzierte humane Neuroblastom-Zellen demonstriert werden. Diese Zellen weisen einige Eigenschaften vollständig ausdifferenzierter Neuronen aus (Agholme et al. 2010, Jamsa et al. 2004). Sie exprimieren bereits einige Rezeptoren, darunter auch PrP^c, und können das zelleigene Tau-Protein hyperphosphorylieren. Diese Komponenten sind auch in der Entwicklung der AD von großer Bedeutung (siehe Einleitung). Es wäre also vorstellbar, dass die getesteten Aβ-Oligomere ihre Toxizität über die in der Entwicklung der AD bedeutungsvollen Mechanismen vermittelten.

Die Relevanz der in dieser Arbeit charakterisierten Aβ-Oligomere für die *in vivo*-Situation wird in erster Linie durch die Korrelation der QIAD-Ergebnisse und den Effekten von D3 und D3D3 in Tiermodellen bestätigt. Dabei ist es wichtig, dass der Einfluss dieser Wirkstoffe auf AD-Symptome in unterschiedlichen Tiermodellen demonstriert werden konnte (siehe Kapitel 2.1.1 und 2.1.4). Auch in der Literatur wird eine wichtige Rolle von Aβ-Oligomeren ähnlicher Größe für die Pathogenese der AD beschrieben. Mittels Immunkopräzipitation wurde gezeigt, dass das humane PrP^c an Aβ-Oligomere ähnlicher Größe aus *post mortem* AD-Hirnen bindet (Dohler et al. 2014)(ZITAT). Die postulierten Bindestellen des PrP^c ähneln in ihren Motiven der positiven Ladungen stark denen von D3 und seinen Derivaten (Fluharty et al. 2013). Dies lässt die Schlussfolgerung zu, dass das PrP^c und D3-Derivate gleiche oder ähnliche Aβ-Oligomere als Bindepartner haben könnten. Somit wären eventuell in dieser Arbeit charakterisierten Aβ-Oligomere mit der in Literatur beschriebenen *in vivo* Aβ-Spezies zu verbinden, die über das PrP^c die AD-Symptome auslösen (Gimbel et al. 2010, Lauren et al. 2009, Lesne S. E. 2013). Dieser Zusammenhang ließe sich auch auf ein weiteres in der Literatur beschriebenes Peptid übertragen. Dieses Peptid stellt einen Sequenzabschnitt des *pericentriolar material-1* (PMC-1) Proteins dar und weist auch eine Ähnlichkeit der positiven Ladungsmotive zu D3-Derivaten auf (Chakravarthy et al. 2014)(zitat chakravarthy). Dieses Peptid bindet an Aβ-Aggregate aus *post mortem* AD-Hirnen.

4 Ausblick

Die in dieser Arbeit gezeigten Ergebnisse geben den Anstoß zu einigen weiterführenden Fragestellungen. Ist eine weitere Optimierung von D3-Derivaten bezüglich ihrer Aβ-Oligomer-reduzierenden Wirkung möglich? Eventuell kann mit einem weiteren Vervielfachen von D3 oder RD2 eine noch effektivere Eliminierung von Aβ-Oligomeren erreicht werden. Man würde Homo- und Heterotrimere oder Tetramere des D3 und RD2 testen. Da diese Moleküle aus 36 bzw. 48 Aminosäuren bestehen würden und ein Molekulargewicht von ca. 4,5 oder 6 kDa hätten, wäre der Einsatz dieser Verbindungen als therapeutisch wirksamer Substanzen fraglich. Die Strukturstabilisierung von D3 erwies sich als eine sehr effektive Strategie, um die Wirkung dieses Wirkstoffes zu optimieren. Da ein aus 12 oder mit einer kompensatorischen Ladung aus 13 Aminosäuren bestehendes Peptid immer noch eine gewisse Flexibilität aufweist, wäre es vorstellbar, dass eine weitere Struktureinengung, z.B. durch Herstellung eines D3 mit Zweiring-Struktur (sogenannte *bicycles*), eine noch stärkere Aβ-Oligomer-Reduktion zu Folge hätte.

Man könnte auch Aβ-Oligomer-bindenden Sequenzen von PrP^c und PMC-1, die nanomolar an Aβ-Oligomere binden, als Grundlage für eine neue Peptid-Wirkstoffentwicklung nehmen oder diese mit D3 oder RD2 kombinieren. Mit dem Ziel kleinere Wirkstoffe zu entwerfen, kann RD2 N-terminal verkürzt werden, da alle Arginine sich am C-Terminus befinden und einige der restlichen Aminosäuren eventuell nicht in die Bindung oder/und den Wirkungsmechanismus mitinvolviert sind. Wegen der Ähnlichkeit der postulierten D3 und PrP^c Bindemotive stellt sich auch die Frage, ob sie einen ähnlichen Einfluss auf Aβ-Oligomere ausüben könnten. Falls ja, könnte man eventuell den *in vivo* D3-Wirkungsmechanismus dank den bereits gewonnen Informationen über des PrP^c erforschen. Eine wichtige Frage wäre, wie nun der Aβ/D3- oder Aβ/D3-Derivat-Komplex strukturell aufgebaut ist und wie die Bindestellen dieser Wirkstoffe ausschauen. Binden alle D3-Derivate gleich oder doch unterschiedlich an Aβ-Oligomere? Diese Fragen könnten mit hochauflösenden Techniken wie NMR geklärt werden. Dabei wäre für den Einsatz von Flüssig-NMR wichtig zu verhindern, dass diese Komplexe weiter quervernetzen und somit zu groß für eine Untersuchung mittels Flüssig-NMR werden. Alternativ könnten die hochmolekularen Komplexe mit Festkörper-NMR untersucht werden.

Die Präparation von Aβ-Oligomeren mittels DGZ hat sich als sehr nützlich für weitere Charakterisierungen dieser Spezies erwiesen. Man könnte trotz der geringen Stabilität dieser Moleküle versuchen, ihre hochaufgelöste Struktur zu bestimmen. Aβ-Oligomere können

entweder mithilfe eines chemischen Crosslinkers quervernetzt, tiefgefroren oder pelletiert mit weiteren Techniken wie Flüssig- NMR, Festkörper-NMR, Cryo-EM, SANS oder SAXS untersucht werden. Es lohnt sich aber auch weiter nach Bedingungen zu suchen, bei denen Aβ-Oligomere ohne weitere Eingriffe über einen längeren Zeitraum stabil bleiben.

5 Zusammenfassung

In dieser Arbeit wurde die Charakterisierung und gezielte Eliminierung von toxischen Proteinaggregaten, am Beispiel der für die Pathogenese der Alzheimer-Krankheit (AD) verantwortlichen Amyloid-β (Aβ) Oligomere, behandelt. Als Wirkstoffkandidaten dienten zunächst mit Phagen-Display bzw. mit Spiegelbild-Phagen-Display auf Aß-Bindung selektierte L- und D-Peptide (L3 und D3).

Eine Fraktionierung der mit D3 oder L3 inkubierten Aβ-Lösungen mittels Dichtegradientenzentrifugation (DGZ) und nachfolgender Analyse durch SDS-PAGE zeigte, dass D3 in der Lage ist, in substöchiometrischer Konzentration den Gehalt von Aβ-Oligomeren bestimmter Größe zu reduzieren. In äquimolarer Konzentration von D3 oder L3 werden Aß-Oligomere vollständig eliminiert. Durch Fluoreszenzmarkierung des D3 mit FITC konnte gezeigt werden, dass die eliminierten Aβ-Oligomere mit D3 zu hochmolekularen Komplexen reagieren. Diese Komplexe sind nicht amyloid. Da D3 auch zu einer Verbesserung der kognitiven Fähigkeiten in einem AD-Mausmodell führte, wird vermutet, dass seine Eigenschaft *in vitro* Aβ-Oligomere zu eliminieren, auch für die beobachtete *in vivo* Wirksamkeit von Bedeutung ist.

Um diese Hypothese zu überprüfen und effizientere Wirkstoffe gegen Aβ-Oligomere und somit gegen AD zu entwickeln, wurden unterschiedliche D3-Derivate entworfen. Gleichzeitig wurde das auf der DGZ basierende Testsystem zu einem quantitativen Assay mit hoher Reproduzierbarkeit und Wiederfindungsrate für das eingesetzte Aβ weiterentwickelt, mit dem der Einfluss der D3-Derivate auf die Aß-Aggregatgrößenverteilung untersucht werden konnte. Dazu wurde die auf einer DGZ basierende Fraktionierung der Aβ-Aggregate mit einer Umkehrphasen-HPLC-Analytik unter vollständig denaturierenden Bedingungen kombiniert.

Mit diesem Testsystem wurden nun viele D3-Derivate auf die Verringerung von Aβ-Oligomeren getestet. Ein „*Head to Tail*“ Dimer des D3 (D3D3) erwies sich im Vergleich zu D3 als effektiver bezüglich dieser Eigenschaft, wodurch die Hypothese, dass D3D3 dank der höheren Avidität eine höhere Wirksamkeit zeigen sollte, bestätigt wurde. Die höhere Effektivität von D3D3 gegenüber D3 ließ sich ebenfalls im Tiermodell aufgrund verbesserter kognitiver und motorischer Fähigkeiten wiederfinden. Diese Ergebnisse legten nahe, dass mit dem entwickelten *in vitro* Testsystem die Wirksamkeit von Wirkstoffen, welche Aβ-Oligomere als Target haben, im Tiermodell vorhergesagt werden kann.

Mit diesem Verfahren gelang es weitere Derivate des D3, welche neben der Dimerisierung,

gezielte Sequenzänderungen, auch Zyklisierungen und kovalente Kopplungen an andere Wirkstoffkandidaten erzeugt wurden, erfolgreich für weitere Charakterisierungen im Tiermodell vorzuselektieren. Die durch Zugabe von D3 und seinen Derivaten eliminierten Aβ-Oligomere wurden biophysikalisch und biochemisch charakterisiert. So konnte gezeigt werden, dass diese Moleküle für humane Neuroblastom-Zellen toxisch sind, überwiegend aus β-Faltblättern bestehen, sich jedoch strukturell von Fibrillen unterscheiden. Ein im Laufe dieser Arbeit etabliertes AFM-Abbildungsverfahren von Aβ-Oligomeren in Lösung zeigte, dass diese Oligomere aus ca. 23 Monomer-Einheiten bestehen.

6 Summary

This dissertation is about the characterization and specific removal of toxic protein aggregates demonstrated on Amyloid-β (Aβ) oligomers, which play a central role in the pathogenesis of Alzheimer's disease (AD). L- and D-peptide (L3 and D3) active agents, which were selected by phage or mirror-image phage display respectively and bind Aβ, provided a basis for further development of active agents.

The study of the influence of L3 and D3 on the distribution of Aβ aggregates was performed by combining density gradient centrifugation (DGC) and SDS-PAGE analysis. It revealed that both D3 and L3 reduce the amount of Aβ oligomers of a specific size and remove these oligomers completely at equimolar ratios. By D3 coupled with the fluorescence label FITC could be demonstrated that Aβ oligomers removed by D3 react with this active agent to complexes with high molecular weights. The fact D3 could also improve performance of transgenic AD mice allowed formation of a hypothesis that the property to remove Aβ oligomers *in vitro* could correlate with the effect of D3 *in vivo*.

Different D3 derivatives were designed to test this hypothesis and to create more effective active agents. Simultaneously the test system based on DGC was upgraded. Consequently an assay for quantitating the efficacy of Aβ oligomer removal (QIAD) was established. This assay enables beside of the quantitative analysis and statistical approaches high reproducibility and recovery rates by dealing with Aβ. QIAD represents a combination of separation and fractionation of different Aβ aggregates by DGC with reversed phase HPLC under completely denaturing conditions. D3D3 is a “head to tail” dimer of D3. It was designed under the assumption that the doubling of its avidity improves its properties according the removal of Aβ oligomers more than a double. This assumption could be proven by QIAD. It was demonstrated that D3D3 is superior to D3 in animal models, too. D3D3 improved the cognitive and motoric performance of AD mice significantly stronger than the same amount of D3. These results demonstrate that QIAD allows an *in vitro* prediction of the efficacy of active agents *in vivo*. The assay will help to avoid testing of ineffective compounds in expensive and time consuming *in vivo* assays or even in clinical trials.

It was possible to select also other derivatives of D3, which reveal a high propensity to remove Aβ oligomers. Beyond these are cyclic, homo- and heterodimeric, scrambled and hybrid derivatives of D3.

The target Aβ oligomers, removed by D3 and its derivatives, were characterized by biophysical

and biochemical technics. It could be demonstrated that these oligomers are toxic to human neuroblastoma cells and consist predominantly of β-sheets, but their structure differs from the fibrils one. AFM imaging of Aβ oligomers in solution, which was established during this thesis, reveals that the characterized Aβ oligomers consist of approximately 23 monomeric units.

7 Literaturverzeichnis

Agholme L, Lindstrom T, Kagedal K, Marcusson J, Hallbeck M. 2010. An in vitro model for neuroscience: differentiation of SH-SY5Y cells into cells with morphological and biochemical characteristics of mature neurons. J Alzheimers Dis 20: 1069-1082.

Ahmed M, Davis J, Aucoin D, Sato T, Ahuja S, Aimoto S, Elliott JI, Van Nostrand WE, Smith SO. 2010. Structural conversion of neurotoxic amyloid-beta(1-42) oligomers to fibrils. Nat Struct Mol Biol 17: 561-567.

Alzheimer. 1907. Über eine eigenartige Erkrankung der Hirnrinde. Allgemeine Zeitschrift für Psychiatrie und psychisch-gerichtliche Medizin. 64: 3.

Balducci C, et al. 2010. Synthetic amyloid-beta oligomers impair long-term memory independently of cellular prion protein. Proc Natl Acad Sci U S A 107: 2295-2300.

Barrow CJ, Yasuda A, Kenny PT, Zagorski MG. 1992. Solution conformations and aggregational properties of synthetic amyloid beta-peptides of Alzheimer's disease. Analysis of circular dichroism spectra. J Mol Biol 225: 1075-1093.

Bell KF, Zheng L, Fahrenholz F, Cuello AC. 2008. ADAM-10 over-expression increases cortical synaptogenesis. Neurobiol Aging 29: 554-565.

Benilova I, De Strooper B. 2013. Neuroscience. Promiscuous Alzheimer's amyloid: yet another partner. Science 341: 1354-1355.

Berthelot K, Cullin C, Lecomte S. 2013. What does make an amyloid toxic: morphology, structure or interaction with membrane? Biochimie 95: 12-19.

Bitan G, Teplow DB. 2004. Rapid photochemical cross-linking--a new tool for studies of metastable, amyloidogenic protein assemblies. Acc Chem Res 37: 357-364.

Bitan G, Fradinger EA, Spring SM, Teplow DB. 2005. Neurotoxic protein oligomers--what you see is not always what you get. Amyloid 12: 88-95.

Brookmeyer R, Johnson E, Ziegler-Graham K, Arrighi HM. 2007. Forecasting the global burden of Alzheimer's disease. Alzheimers Dement 3: 186-191.

Busciglio J, Gabuzda DH, Matsudaira P, Yankner BA. 1993. Generation of beta-amyloid in the secretory pathway in neuronal and nonneuronal cells. Proc Natl Acad Sci U S A 90: 2092-2096.

Cabrita LD, Dobson CM, Christodoulou J. 2010. Protein folding on the ribosome. Curr Opin Struct Biol 20: 33-45.

Caughey B, Lansbury PT. 2003. Protofibrils, pores, fibrils, and neurodegeneration: separating the responsible protein aggregates from the innocent bystanders. Annu Rev Neurosci 26: 267-298.

Chakravarthy B, Ito S, Atkinson T, Gaudet C, Menard M, Brown L, Whitfield J. 2014. Evidence that a synthetic amyloid-ss oligomer-binding peptide (ABP) targets amyloid-ss deposits in

transgenic mouse brain and human Alzheimer's disease brain. Biochem Biophys Res Commun 445: 656-660.

Cheng X, van Breemen RB. 2005. Mass spectrometry-based screening for inhibitors of beta-amyloid protein aggregation. Anal Chem 77: 7012-7015.

Chiti F, Dobson CM. 2006. Protein misfolding, functional amyloid, and human disease. Annu Rev Biochem 75: 333-366.

Cochran AG, Skelton NJ, Starovasnik MA. 2001. Tryptophan zippers: stable, monomeric beta -hairpins. Proc Natl Acad Sci U S A 98: 5578-5583.

Cohen AS, Calkins E. 1959. Electron microscopic observations on a fibrous component in amyloid of diverse origins. Nature 183: 1202-1203.

De Strooper B, et al. 1999. A presenilin-1-dependent gamma-secretase-like protease mediates release of Notch intracellular domain. Nature 398: 518-522.

Dobson CM. 2003. Protein folding and misfolding. Nature 426: 884-890.

Dohler F, Sepulveda-Falla D, Krasemann S, Altmeppen H, Schluter H, Hildebrand D, Zerr I, Matschke J, Glatzel M. 2014. High molecular mass assemblies of amyloid-beta oligomers bind prion protein in patients with Alzheimer's disease. Brain 137: 873-886.

E. Ukraintsev AK, H. Kozak, Z. Remeš and B. Rezek. 2012. Artifacts in Atomic Force Microscopy of Biological Samples. Pages 30 - 54. Atomic Force Microscopy Investigations into Biology - From Cell to Protein: InTech.

Farris W, et al. 2007. Loss of neprilysin function promotes amyloid plaque formation and causes cerebral amyloid angiopathy. Am J Pathol 171: 241-251.

Ferri CP, et al. 2005. Global prevalence of dementia: a Delphi consensus study. Lancet 366: 2112-2117.

Findeis MA, et al. 1999. Modified-peptide inhibitors of amyloid beta-peptide polymerization. Biochemistry 38: 6791-6800.

Finder VH, Vodopivec I, Nitsch RM, Glockshuber R. 2010. The recombinant amyloid-beta peptide Abeta1-42 aggregates faster and is more neurotoxic than synthetic Abeta1-42. J Mol Biol 396: 9-18.

Fluharty BR, et al. 2013. An N-terminal fragment of the prion protein binds to amyloid-beta oligomers and inhibits their neurotoxicity in vivo. J Biol Chem 288: 7857-7866.

Frydman-Marom A, Rechter M, Shefler I, Bram Y, Shalev DE, Gazit E. 2009. Cognitive-performance recovery of Alzheimer's disease model mice by modulation of early soluble amyloidal assemblies. Angew Chem Int Ed Engl 48: 1981-1986.

Gellermann GP, Byrnes H, Striebinger A, Ullrich K, Mueller R, Hillen H, Barghorn S. 2008. Abeta-globulomers are formed independently of the fibril pathway. Neurobiol Dis 30: 212-220.

Gervais F, et al. 2007. Targeting soluble Abeta peptide with Tramiprosate for the treatment of brain amyloidosis. Neurobiol Aging 28: 537-547.

Gibson TJ, Murphy RM. 2005. Design of peptidyl compounds that affect beta-amyloid aggregation: importance of surface tension and context. Biochemistry 44: 8898-8907.

Gilman S, et al. 2005. Clinical effects of Abeta immunization (AN1792) in patients with AD in an interrupted trial. Neurology 64: 1553-1562.

Gimbel DA, Nygaard HB, Coffey EE, Gunther EC, Lauren J, Gimbel ZA, Strittmatter SM. 2010. Memory impairment in transgenic Alzheimer mice requires cellular prion protein. J Neurosci 30: 6367-6374.

Glenner GG, Wong CW. 1984. Alzheimer's disease: initial report of the purification and characterization of a novel cerebrovascular amyloid protein. Biochem Biophys Res Commun 120: 885-890.

Golde TE, Petrucelli L, Lewis J. 2010. Targeting Abeta and tau in Alzheimer's disease, an early interim report. Exp Neurol 223: 252-266.

Gong Y, Chang L, Viola KL, Lacor PN, Lambert MP, Finch CE, Krafft GA, Klein WL. 2003. Alzheimer's disease-affected brain: presence of oligomeric A beta ligands (ADDLs) suggests a molecular basis for reversible memory loss. Proc Natl Acad Sci U S A 100: 10417-10422.

Graeber MB, Kosel S, Egensperger R, Banati RB, Muller U, Bise K, Hoff P, Moller HJ, Fujisawa K, Mehraein P. 1997. Rediscovery of the case described by Alois Alzheimer in 1911: historical, histological and molecular genetic analysis. Neurogenetics 1: 73-80.

Graham JM. 2002. OptiPrep density gradient solutions for macromolecules and macromolecular complexes. ScientificWorldJournal 2: 1547-1550.

Groenning M. 2010. Binding mode of Thioflavin T and other molecular probes in the context of amyloid fibrils-current status. J Chem Biol 3: 1-18.

Haass C, Selkoe DJ. 2007. Soluble protein oligomers in neurodegeneration: lessons from the Alzheimer's amyloid beta-peptide. Nat Rev Mol Cell Biol 8: 101-112.

Hardy JA, Higgins GA. 1992. Alzheimer's disease: the amyloid cascade hypothesis. Science 256: 184-185.

Harrison RS, Sharpe PC, Singh Y, Fairlie DP. 2007. Amyloid peptides and proteins in review. Rev Physiol Biochem Pharmacol 159: 1-77.

Hepler RW, et al. 2006. Solution state characterization of amyloid beta-derived diffusible ligands. Biochemistry 45: 15157-15167.

Hiltunen M, van Groen T, Jolkkonen J. 2009. Functional roles of amyloid-beta protein precursor and amyloid-beta peptides: evidence from experimental studies. J Alzheimers Dis 18: 401-412.

Hofmeister. 1888. Zur Lehre von der Wirkung der Salze. Arch. Exptl. Pathol. Pharmakol. 24: 247.

Huang SM, et al. 2006. Neprilysin-sensitive synapse-associated amyloid-beta peptide oligomers impair neuronal plasticity and cognitive function. J Biol Chem 281: 17941-17951.

Igbavboa U, Sun GY, Weisman GA, He Y, Wood WG. 2009. Amyloid beta-protein stimulates trafficking of cholesterol and caveolin-1 from the plasma membrane to the Golgi complex in mouse primary astrocytes. Neuroscience 162: 328-338.

Iwatsubo T, Odaka A, Suzuki N, Mizusawa H, Nukina N, Ihara Y. 1994. Visualization of A beta 42(43) and A beta 40 in senile plaques with end-specific A beta monoclonals: evidence that an initially deposited species is A beta 42(43). Neuron 13: 45-53.

Jacobsen PB, Blindheim L, Skotland T. 1995. Bioanalytical methods for iodixanol and their application to studies on metabolism and protein binding. Acta Radiol Suppl 399: 61-66.

Jahn TR, Radford SE. 2005. The Yin and Yang of protein folding. FEBS J 272: 5962-5970.

Jakes R, Novak M, Davison M, Wischik CM. 1991. Identification of 3- and 4-repeat tau isoforms within the PHF in Alzheimer's disease. EMBO J 10: 2725-2729.

Jamsa A, Hasslund K, Cowburn RF, Backstrom A, Vasange M. 2004. The retinoic acid and brain-derived neurotrophic factor differentiated SH-SY5Y cell line as a model for Alzheimer's disease-like tau phosphorylation. Biochem Biophys Res Commun 319: 993-1000.

Jan A, Adolfsson O, Allaman I, Buccarello AL, Magistretti PJ, Pfeifer A, Muhs A, Lashuel HA. 2011. Abeta42 neurotoxicity is mediated by ongoing nucleated polymerization process rather than by discrete Abeta42 species. J Biol Chem 286: 8585-8596.

Juhasz G, Marki A, Vass G, Fulop L, Budai D, Penke B, Falkay G, Szegedi V. 2009. An intraperitoneally administered pentapeptide protects against Abeta (1-42) induced neuronal excitation in vivo. J Alzheimers Dis 16: 189-196.

Kaether C, Haass C, Steiner H. 2006. Assembly, trafficking and function of gamma-secretase. Neurodegener Dis 3: 275-283.

Karran E, Mercken M, De Strooper B. 2011. The amyloid cascade hypothesis for Alzheimer's disease: an appraisal for the development of therapeutics. Nat Rev Drug Discov 10: 698-712.

Klyubin I, et al. 2005. Amyloid beta protein immunotherapy neutralizes Abeta oligomers that disrupt synaptic plasticity in vivo. Nat Med 11: 556-561.

Kuroda Y, Kidokoro S, Wada A. 1992. Thermodynamic characterization of cytochrome c at low pH. Observation of the molten globule state and of the cold denaturation process. J Mol Biol 223: 1139-1153.

Lambert MP, et al. 1998. Diffusible, nonfibrillar ligands derived from Abeta1-42 are potent central nervous system neurotoxins. Proc Natl Acad Sci U S A 95: 6448-6453.

Lammich S, Kojro E, Postina R, Gilbert S, Pfeiffer R, Jasionowski M, Haass C, Fahrenholz F. 1999. Constitutive and regulated alpha-secretase cleavage of Alzheimer's amyloid precursor protein by a disintegrin metalloprotease. Proc Natl Acad Sci U S A 96: 3922-3927.

Lauren J, Gimbel DA, Nygaard HB, Gilbert JW, Strittmatter SM. 2009. Cellular prion protein mediates impairment of synaptic plasticity by amyloid-beta oligomers. Nature 457: 1128-1132.

Leach A, Jhoti H. 2007. Structure-based Drug Discovery: Springer.

Leissring MA, Farris W, Chang AY, Walsh DM, Wu X, Sun X, Frosch MP, Selkoe DJ. 2003. Enhanced proteolysis of beta-amyloid in APP transgenic mice prevents plaque formation, secondary pathology, and premature death. Neuron 40: 1087-1093.

Lesne S, Koh MT, Kotilinek L, Kayed R, Glabe CG, Yang A, Gallagher M, Ashe KH. 2006. A specific amyloid-beta protein assembly in the brain impairs memory. Nature 440: 352-357.

Lesne SE. 2013. Breaking the Code of Amyloid- Oligomers. Int J Cell Biol 2013: 950783.

Lien S, Lowman HB. 2003. Therapeutic peptides. Trends Biotechnol 21: 556-562.

Lin H, Bhatia R, Lal R. 2001. Amyloid beta protein forms ion channels: implications for Alzheimer's disease pathophysiology. FASEB J 15: 2433-2444.

Lue LF, Kuo YM, Roher AE, Brachova L, Shen Y, Sue L, Beach T, Kurth JH, Rydel RE, Rogers J. 1999. Soluble amyloid beta peptide concentration as a predictor of synaptic change in Alzheimer's disease. Am J Pathol 155: 853-862.

Luo Y, Bolon B, Damore MA, Fitzpatrick D, Liu H, Zhang J, Yan Q, Vassar R, Citron M. 2003. BACE1 (beta-secretase) knockout mice do not acquire compensatory gene expression changes or develop neural lesions over time. Neurobiol Dis 14: 81-88.

Madsen U, Krogsgaard-Larsen P, Liljefors T. 2002. Textbook of Drug Design and Discovery: CRC Press.

Manfredi R, Sabbatani S. 2006. A novel antiretroviral class (fusion inhibitors) in the management of HIV infection. Present features and future perspectives of enfuvirtide (T-20). Curr Med Chem 13: 2369-2384.

Marambaud P, et al. 2002. A presenilin-1/gamma-secretase cleavage releases the E-cadherin intracellular domain and regulates disassembly of adherens junctions. EMBO J 21: 1948-1956.

Masters CL, Simms G, Weinman NA, Multhaup G, McDonald BL, Beyreuther K. 1985. Amyloid plaque core protein in Alzheimer disease and Down syndrome. Proc Natl Acad Sci U S A 82: 4245-4249.

McLaurin J, et al. 2006. Cyclohexanehexol inhibitors of Abeta aggregation prevent and reverse Alzheimer phenotype in a mouse model. Nat Med 12: 801-808.

McLean CA, Cherny RA, Fraser FW, Fuller SJ, Smith MJ, Beyreuther K, Bush AI, Masters CL. 1999. Soluble pool of Abeta amyloid as a determinant of severity of neurodegeneration in Alzheimer's disease. Ann Neurol 46: 860-866.

Mehta NM, Malootian A, Gilligan JP. 2003. Calcitonin for osteoporosis and bone pain. Curr Pharm Des 9: 2659-2676.

Mueller-Steiner S, et al. 2006. Antiamyloidogenic and neuroprotective functions of cathepsin B: implications for Alzheimer's disease. Neuron 51: 703-714.

Muller U, Winter P, Graeber MB. 2013. A presenilin 1 mutation in the first case of Alzheimer's disease. Lancet Neurol 12: 129-130.

Naslund J, Haroutunian V, Mohs R, Davis KL, Davies P, Greengard P, Buxbaum JD. 2000.

Correlation between elevated levels of amyloid beta-peptide in the brain and cognitive decline. JAMA 283: 1571-1577.

Nordberg A. 2004. PET imaging of amyloid in Alzheimer's disease. Lancet Neurol 3: 519-527.

O'Hare E, et al. 2013. Orally bioavailable small molecule drug protects memory in Alzheimer's disease models. Neurobiol Aging 34: 1116-1125.

Podlisny MB, Ostaszewski BL, Squazzo SL, Koo EH, Rydell RE, Teplow DB, Selkoe DJ. 1995. Aggregation of secreted amyloid beta-protein into sodium dodecyl sulfate-stable oligomers in cell culture. J Biol Chem 270: 9564-9570.

Poduslo JF, Curran GL, Kumar A, Frangione B, Soto C. 1999. Beta-sheet breaker peptide inhibitor of Alzheimer's amyloidogenesis with increased blood-brain barrier permeability and resistance to proteolytic degradation in plasma. J Neurobiol 39: 371-382.

Portelius E, Westman-Brinkmalm A, Zetterberg H, Blennow K. 2006. Determination of beta-amyloid peptide signatures in cerebrospinal fluid using immunoprecipitation-mass spectrometry. J Proteome Res 5: 1010-1016.

Portelius E, Price E, Brinkmalm G, Stiteler M, Olsson M, Persson R, Westman-Brinkmalm A, Zetterberg H, Simon AJ, Blennow K. 2011. A novel pathway for amyloid precursor protein processing. Neurobiol Aging 32: 1090-1098.

Puchtler H, Sweat F. 1965. Congo red as a stain for fluorescence microscopy of amyloid. J Histochem Cytochem 13: 693-694.

Robakis NK, Ramakrishna N, Wolfe G, Wisniewski HM. 1987. Molecular cloning and characterization of a cDNA encoding the cerebrovascular and the neuritic plaque amyloid peptides. Proc Natl Acad Sci U S A 84: 4190-4194.

Ross CA, Poirier MA. 2004. Protein aggregation and neurodegenerative disease. Nat Med 10 Suppl: S10-17.

Roychaudhuri R, Yang M, Hoshi MM, Teplow DB. 2009. Amyloid beta-protein assembly and Alzheimer disease. J Biol Chem 284: 4749-4753.

Rushworth JV, Griffiths HH, Watt NT, Hooper NM. 2013. Prion protein-mediated toxicity of amyloid-beta oligomers requires lipid rafts and the transmembrane LRP1. J Biol Chem 288: 8935-8951.

Rzepecki P, Nagel-Steger L, Feuerstein S, Linne U, Molt O, Zadmard R, Aschermann K, Wehner M, Schrader T, Riesner D. 2004. Prevention of Alzheimer's disease-associated Abeta aggregation by rationally designed nonpeptidic beta-sheet ligands. J Biol Chem 279: 47497-47505.

Saido TC, Iwatsubo T, Mann DM, Shimada H, Ihara Y, Kawashima S. 1995. Dominant and differential deposition of distinct beta-amyloid peptide species, A beta N3(pE), in senile plaques. Neuron 14: 457-466.

Schenk DB, Seubert P, Grundman M, Black R. 2005. A beta immunotherapy: Lessons learned for potential treatment of Alzheimer's disease. Neurodegener Dis 2: 255-260.

Schumacher TN, Mayr LM, Minor DL, Jr., Milhollen MA, Burgess MW, Kim PS. 1996. Identification of D-peptide ligands through mirror-image phage display. Science 271: 1854-1857.

Selkoe DJ. 2001a. Presenilin, Notch, and the genesis and treatment of Alzheimer's disease. Proc Natl Acad Sci U S A 98: 11039-11041.

—. 2001b. Alzheimer's disease: genes, proteins, and therapy. Physiol Rev 81: 741-766.

—. 2008. Soluble oligomers of the amyloid beta-protein impair synaptic plasticity and behavior. Behav Brain Res 192: 106-113.

Seubert P, et al. 1992. Isolation and quantification of soluble Alzheimer's beta-peptide from biological fluids. Nature 359: 325-327.

Shafrir Y, Durell S, Arispe N, Guy HR. 2010. Models of membrane-bound Alzheimer's Abeta peptide assemblies. Proteins 78: 3473-3487.

Sipe JD, Cohen AS. 2000. Review: history of the amyloid fibril. J Struct Biol 130: 88-98.

Skelton NJ, et al. 2001. Structure-function analysis of a phage display-derived peptide that binds to insulin-like growth factor binding protein 1. Biochemistry 40: 8487-8498.

Soscia SJ, et al. 2010. The Alzheimer's disease-associated amyloid beta-protein is an antimicrobial peptide. PLoS One 5: e9505.

Soto C, Estrada LD. 2008. Protein misfolding and neurodegeneration. Arch Neurol 65: 184-189.

Soto C, Sigurdsson EM, Morelli L, Kumar RA, Castano EM, Frangione B. 1998. Beta-sheet breaker peptides inhibit fibrillogenesis in a rat brain model of amyloidosis: implications for Alzheimer's therapy. Nat Med 4: 822-826.

Suh YH, Checler F. 2002. Amyloid precursor protein, presenilins, and alpha-synuclein: molecular pathogenesis and pharmacological applications in Alzheimer's disease. Pharmacol Rev 54: 469-525.

Sun N, Funke SA, Willbold D. 2012. Mirror image phage display--generating stable therapeutically and diagnostically active peptides with biotechnological means. J Biotechnol 161: 121-125.

van Groen T, Wiesehan K, Funke SA, Kadish I, Nagel-Steger L, Willbold D. 2008. Reduction of Alzheimer's disease amyloid plaque load in transgenic mice by D3, A D-enantiomeric peptide identified by mirror image phage display. ChemMedChem 3: 1848-1852.

Vlieghe P, Lisowski V, Martinez J, Khrestchatisky M. 2010. Synthetic therapeutic peptides: Science and market. Drug Discovery Today 15: 17.

Walsh DM, Selkoe DJ. 2007. A beta oligomers - a decade of discovery. J Neurochem 101: 1172-1184.

Wang J, Dickson DW, Trojanowski JQ, Lee VM. 1999. The levels of soluble versus insoluble brain Abeta distinguish Alzheimer's disease from normal and pathologic aging. Exp Neurol

158: 328-337.

Welander H, Franberg J, Graff C, Sundstrom E, Winblad B, Tjernberg LO. 2009. Abeta43 is more frequent than Abeta40 in amyloid plaque cores from Alzheimer disease brains. J Neurochem 110: 697-706.

Westlind-Danielsson A, Arnerup G. 2001. Spontaneous in vitro formation of supramolecular beta-amyloid structures, "betaamy balls", by beta-amyloid 1-40 peptide. Biochemistry 40: 14736-14743.

Wiesehan K, Willbold D. 2003. Mirror-image phage display: aiming at the mirror. Chembiochem 4: 811-815.

Winklhofer KF, Tatzelt J, Haass C. 2008. The two faces of protein misfolding: gain- and loss-of-function in neurodegenerative diseases. EMBO J 27: 336-349.

Wolynes PG, Onuchic JN, Thirumalai D. 1995. Navigating the folding routes. Science 267: 1619-1620.

Zhao G, Tan J, Mao G, Cui MZ, Xu X. 2007. The same gamma-secretase accounts for the multiple intramembrane cleavages of APP. J Neurochem 100: 1234-1246.

Zhao LN, Long H, Mu Y, Chew LY. 2012. The Toxicity of Amyloid beta Oligomers. Int J Mol Sci 13: 7303-7327.

Zou K, Gong JS, Yanagisawa K, Michikawa M. 2002. A novel function of monomeric amyloid beta-protein serving as an antioxidant molecule against metal-induced oxidative damage. J Neurosci 22: 4833-4841.

Zwanzig R, Szabo A, Bagchi B. 1992. Levinthal's paradox. Proc Natl Acad Sci U S A 89: 20-22.